FUNCTIONAL POLYMER FILM ROLL-TO-ROLL MANUFACTURING BY FIELD ASSISTED ALIGNMENT OF NANOPARTICLES/PHASES IN THICKNESS "Z" DIRECTION

A Dissertation

Presented to

The Graduate Faculty of The University of Akron

In Partial Fulfillment

of the Requirements for the Degree

Doctor of Philosophy

Yuanhao Guo

December, 2016

FUNCTIONAL POLYMER FILM ROLL-TO-ROLL MANUFACTURING BY FIELD ASSISTED ALIGNMENT OF NANOPARTICLES/PHASES IN THICKNESS "Z" DIRECTION

Yuanhao Guo

Dissertation

Approved:	Accepted:
Advisor Dr. Mark D. Soucek	Department Chair Dr. Sadhan C. Jana
Committee Member Dr. Miko Cakmak	Dean of College Dr. Eric J. Amis
Committee Member Dr. David S. Simmons	Dean of Graduate School Dr. Chand Midha
Committee Member Dr. Abraham Joy	Date
Committee Member Dr. Alper Buldum	

ABSTRACT

Roll-to-roll nanomanufacturing is the next generation processing technique with advantages of high throughput and low cost, beneficial for manufacturing functional materials for flexible electrons, medical device and filtration applications. Roll-to-roll processing combining external electric field to organize nanoparticles in polymer films provides a unique processing path fabricate the nanocomposites with directionally ordered structures which exhibit significantly enhanced properties in field direction.

The first part of this study presents a simple, low cost and commercially viable method to manufacture multifunctional nanocomposites with directionally ordered structures. The manufacturing of poly(dimethylsiloxane) (PDMS) film with “Z” aligned graphite nanoparticles by application of electric field is achieved continuously on a roll-to-roll processing line. The “Z” aligned nanocomposite films exhibit significantly enhanced dielectric permittivity, electrical and thermal conductivity through the thickness direction.

The second study develops a novel roll-to-roll processing method for “Z” alignment of barium titanate ($BaTiO_3$) nanoparticles in polystyrene (PS)/toluene solution systems, which broadens the choice of polymers to use as matrix to manufacture functional films with anisotropic structure. This is accomplished by applying electric field to a two-layer solution film cast on a carrier: the top layer is a sacrificial layer contacting the electrode and the bottom one is the composite layer. The “Z” aligned nanocomposite films show substantially increased dielectric permittivity for enhancing the performance of capacitors.

The third study proposes a three-layer wound dressing with “Z” aligned superabsorbent particles by using the processing method developed in previous study. This resulting wound dressing preferentially expands in thickness direction after absorbing water, thus reducing the lateral stress between the dressing and wound. The aligned wound dressings could achieve up to 33% smaller lateral expansion than the film with random particles. Compared to irregular shape particles, rod-like particles with higher aspect ratio are more effective to improve anisotropic swelling and reduce lateral expansion.

The final study demonstrates the formation of dispersed and bicontinuous morphology of PS and PMMA blends with the interface coated by silica nanoparticles modified with PS-r-PMMA copolymer. The effect of the solvent evaporation rate, blend compositions, particle loading and size on the resulting morphology is systematically investigated. The vertical alignment of PMMA phase with dense nanoparticle coated interface by the application of electric field is investigated. The effect of dielectric constant of nanoparticles on their reorganization at the interface under electric field demonstrated.

DEDICATION

This dissertation is lovingly dedicated to my beloved parents Xuekun Guo and Wenjuan Wu for their unconditional support, encouragement and love.

ACKNOWLEDGEMENTS

First, I would like to thank my advisor, Distinguished Professor, Dr. Miko Cakmak, for his guidance, patience, encouragement, mentorship and support throughout my five years in Akron, Ohio. He trained me not only the cutting-edge techniques but also the attitude to explore the fundamental and details of every scientific research topic. His creativity, ambition and persistence to science and engineering will encourage and urge me to improve myself to higher level in my future life and research. I would like to thank my co-advisor, Dr. Mark Soucek, for his help and support. I would like to express my sincere thanks to the committee members, Dr. David Simmons, Dr. Abraham Joy and Dr. Alper Buldum, for their valuable time, discussion and encouragement.

I would like to thank to the all the group members in Professor Cakmak's research group. My special thanks go to Enmin Wang, Dr. Saurabh Batra, Dr. Yuwei Chen, Dr. Emre Unsal, Dr. Cheng Qu, Dr. Tsang Min Huang, Dr. Isil Nugay, Fanhui Jiang, Fang Peng and other colleagues in the department for their advice and helps. I am also grateful to all my friends, especially Zhe Qiang, Guopeng Fu, Chao Yi, Senglong Gu and Qianghe Wang for their encouragement in both research and life

Finally, I would like dedicate this work to the most important people in my life, my parents who unconditionally support, encourage and love me during difficult times no matter how far they are from me. I am so fortunate to have such loving and caring parents and I owe everything to them. There are not enough words to express my love for them. I also would like to thank Qianhui Liu for her understanding, help and encouragement.

TABLE OF CONTENTS

Page

LIST OF TABLES

LIST OF FIGURES

Figure Page

LIST OF SCHEMES

CHAPTER I

INTRODUCTION

Incorporating functional nanomaterials into polymer is one of the most promising approaches to fabricate multifunctional nanocomposites with tailorable mechanical,[1] thermal[2] and electrical properties.[3] Polymer based nanocomposites have been actively explored to replace traditional metal materials in emerging areas due to their lightweight, flexibility, high mechanical strength, superior manufacturing and low processing cost. With explosive growth of nanoscience and nanotechnology, the multifunctional polymer nanocomposites have a prosperous future in broad applications, such as light weight structures,[1] energy storage,[4] flexible electronics[5] and biomedical applications.[6]

The methods of adjusting compositions, interfaces and structures are commonly used to tailor or optimize the properties of multifunctional nanocomposites. Ordered structures are more preferential for nanocomposites because it can promote the properties more effectively, and the properties can be tailored by controlling the degree of ordering. The ordered structures of nanocomposite films can be achieved by self-assembly, patterned substrate, imprint technique and external field assisted assembly. The external field assisted assembly of nanoparticles or phases is a very effective method to create long range ordered structures for nanocomposite films.

External electric field is one of the most commonly used methods to create ordered structures for polymer nanocomposite, liquid crystals, polymer blends and block copolymers. The electric field assisted assembly of nanomaterials has been developed in laboratory scale for applications of flexible electronics, filtration, fuel cells, photovoltaics etc. And large scale nanomanufacturing capability of product will be demanded in the next decades. Roll-to-roll processing is one of important industrial manufacturing techniques fabricating coating, film and devices in high volume manufacturing involving a flexible substrate which is transferred between two drums. Benefiting from the continuous production, roll to roll processing can lower the cost of manufacturing, increase the volume rates of production and process efficiency through sequential application of successive layers on a web. More importantly, additive and subtractive process can be built on roll to roll processing line to build structures in continuous manner since it’s a substrate based manufacturing technique. Therefore, a novel roll to roll processing line built on with external electric field, magnetic field and thermal gradient zone was developed in our laboratory to manufacture the polymer based nanocomposites with ordered structures. This roll to roll line was designed to used doctor blade, slot die or flow coating to cast liquid polymer composite film on a flexible substrate. The cast liquid film is then transported by the carrier into the electric field zone which consisting of a parallel electrode sitting on the top of the film. The electric field zone is capable to provide ±15 kV voltages in direct current (DC), alternating current (AC) and biased AC mode. Under the high electric field strength, the ordered structures of nanoparticles, phases and domains can be created for nanocomposite films.

Previous studies focused on developing nanocomposites with thermal[7] or UV curable[8] resins as the matrix materials due to the ease of utility in continuous processes. The electric field assisted ordered structures are frozen in the matrix materials cured by thermal heat or UV light. However, the top electrode was adhered to the film after solidifying due to direct contact in these studies which limit the continuous processing. An air gap is introduced between film and top electrode to solve this problem to achieve continuous manufacturing. Moreover, there are several limitations for the thermoset system: (1) the matrix materials can only be thermoset materials; (2) the viscosity of the fluid may be too high for the particles to move to achieve the alignment at high loading of particles; (3) the matrix needs to be transparent to UV light which is difficult at high particle loading. The fluid may not be transparent when the refractive index contrast (difference) of matrix and particle is large. Thus a new system is needed for thermoplastic polymers to broaden the choice of materials for matrix. The system of thermoplastic polymer/solvent solution is another alternative, because it is ease of adjustment of the viscosity by modifying the particle/polymer concentration. Moreover, more diverse choices of thermoplastic materials with excellent performance can be chosen for the matrix materials such as polyvinylidene fluoride (PVDF), polyethylenimine (PEI) and polyimide (PI).

The goal of this research is to develop multifunctional nanocomposites with ordered structures and solve various processing challenges for roll to roll continuous manufacturing of nanocomposites with ordered structures. This research also develops a new processing method to create ordered structures for thermoplastic polymers/solvent system. By using this newly developed method, multifunctional nanocomposites for applications of capacitors, wound dressing and filtration are fabricated. The work presented here should provide a new processing system to develop multifunctional nanocomposites with more broad choices of materials.

Chapter II provides fundamental mechanisms of film formation, chain orientation and phase separation by solvent evaporation and the technique of electric field assisted assembly of nanoparticles and phases.

Chapter III introduces a roll to roll continuous process to manufacture large-scale multifunctional thermosets films with electric field assisting graphite nanoparticle organization in the thickness direction (“Z” direction). The kinetics of “Z” alignment was studied by tracking the real-time optical light transmission response to electric field as the nanocolumlar organization under the electric field creates particle depletion zones and hence creating transparency. Benefiting from the anisotropic structure of aligned particle chains, the electrical and thermal properties of the nanocomposites were dramatically enhanced through the thickness direction as compared to the nanocomposites containing the same particle loading without alignment. This roll to roll electric field continuous process provides a simple, low cost and commercially viable method to manufacture multifunctional nanocomposites.

Chapter IV describes a newly developed roll to roll processing method for “Z” alignment of nanoparticles in thermoplastic/solvent solution under mesh-plate electric field, which significantly broadens the choices of polymer matrix from thermoset to thermoplastic polymers. A two-layer solution film is cast on a carrier: top sacrificial layer contacting the electrode and the bottom layer of polymer solution dispersed with $BaTiO_3$ particles. The kinetics of particle alignment and chain buckling is studied by measuring the real time optical light transmission during electric field application and drying steps. The enhancement of dielectric permittivity of resulting films with “Z” alignment particles is shown.

Chapter V designs a three-layer wound dressing film containing wound contact layer, absorbing layer and backing layer. The absorbing layer contains “Z” aligned superabsorbent particles by external electric field during film formation in order to minimize the lateral swelling during exudate absorbing process, thus eliminating the lateral stress on the wound. The reduced lateral expansion of aligned wound dressing is shown. The effect of particle shape on anisotropic swelling is also investigated.

Chapter VI demonstrates the formation of bicontinuous polystyrene (PS)/ poly(methyl methacrylate) (PMMA) polymer blends with silica particles coated at the interface during solvent evaporation. The effect of the rate of solvent evaporation, blend compositions, particle loading and size on the resulting morphology is systematically investigated. The electric field induced alignment of vertical PMMA domains with particles coated interface is shown. The effect of dielectric constant of nanoparticles on the organization of nanoparticles at the interface is also demonstrated.

CHAPTER II

BACKGROUND AND LITERATURE REVIEW

2.1 High dielectric materials

The fundamentals and applications of high dielectric permittivity (high-k) materials are discussed in details below.

2.1.1 Dielectric permittivity and polarization

The capacitance for parallel plate capacitor with free space and dielectric material as insulator (Figure 2.1) is given by equation 2.1 and 2.2 respectively.

$$C = \frac{\epsilon_0 A}{d} \tag{2.1}$$

$$C' = \frac{\varepsilon' A}{d} \tag{2.2}$$

$$\varepsilon_r = \frac{C'}{C} = \frac{\varepsilon'}{\epsilon_0} \tag{2.3}$$

where C is capacitance, ε_0 is the absolute permittivity of the free space ($8.854 * 10^{-12}$ F/m), ε' is the absolute dielectric permittivity of dielectric material, A is the electrode area, d is the gap between two electrode, and ε_r is called relative dielectric permittivity. Compared to the capacitor with vacuum, the capacitance of the capacitor with dielectric material is increased by a factor of ε_r, and the value of ε_r is called as the dielectric constant or relative dielectric permittivity, which can be calculated as equation 2.3.

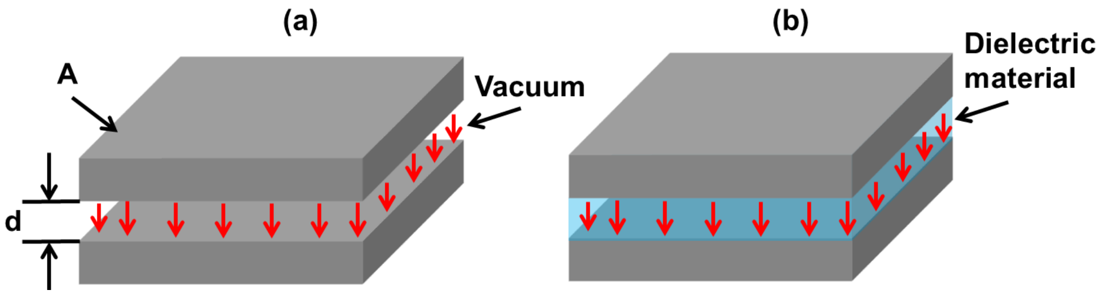

Figure 2.1 The structure of plate capacitor: (a) with vacuum, (b) with dielectric material between two conductive electrodes with area of A and separation of d.

The charge storage is due to the polarization of the medium under electric field where the positive and negative charges are displaced away from the equilibrium position. Polarization can be divided into four mechanisms: (1) electric polarization, (2) ionic polarization, (3) orientation polarization and (4) interfacial polarization.[9] When an atom is composed of electron cloud and atomic nucleus in an external electric field, the induced dipole will be developed due to the separation of electron center (negative charge) from the atomic nucleus center (positive charge), which is electric polarization. For ionic crystals, there is no net polarization due to the same magnitude of dipole moment for positive and negative dipole. However, the net polarization is no longer zero in the presence of electric field due to the displacement of positive and negative ions under field, which is ionic polarization.[10] Some materials have permanent dipoles within the structure, but the molecules are still randomly oriented due to the thermal agitation. If an electric field is applied, the permanent dipoles are oriented and aligned in the direction of electric field, which is orientation polarization. In order to achieve the orientation polarization, the dipole must have enough energy to overcome the thermal energy under electric field, thus the orientation polarization is temperature dependent. In case of composites, the interfacial polarization occurs due to the accumulation of the positive charges at the interface and remains negative charge in the bulk.[10]

2.1.2 High dielectric permittivity materials

High dielectric permittivity materials are highly demanded for electronic applications including actuators,[11, 12] organic field-effect transistors,[13, 14] electrical stress control applications[15, 16] and high-charge storage devices.[17-20] For example, the high-k materials play an essential role in electrical stress control as demonstrated in Figure 2.2.[7] The electric field concentrates at cut back point of shield layer leading to the stress field beyond the shield layer. The electric field stress concentrated at the cut back point may cause the breakdown of air eventually leading to the surface discharge and insulation failure of the cable. To reduce the surface electrical stress and keep the electrical stress below the breakdown voltage of air, high-k material is needed to cover the cut back point. Ceramics such as barium titanate (BT),[21] calcium copper titanate (CCTO),[22] and lead zirconate titanate (PZT)[23] are the most commonly used materials as high-k materials due to their high dielectric permittivity. However, their drawbacks of mechanical brittleness, low breakdown strength and high temperature processing condition limit their applications.[18] Polymers have advantages in energy storage applications due to their mechanical flexibility, high breakdown strength and ease of processing. Nevertheless, most polymers have their limitations in energy storage applications due to low dielectric permittivity, so high electric field (i.e. E> 500 MV/m) is needed to achieve high energy density.[19, 24]

One of the promising methods to prepare high-k material is to include the ceramics into the polymer matrix. The CCTO particle/polyimide (PI) nanocomposites with 40 vol% loading prepared by in-situ polymerization method show dielectric permittivity as high as 49.1, which is 14 time higher than the pure PI.[25] Compared to the dielectric permittivity of perovskite ceramics, up to several thousand, the dielectric permittivity of the composite is still too low due to the interface structure.[26] Much effort has been made to enhance the dielectric permittivity of the polymer/ceramic composite, including eliminating the voids in polymer composites,[27] doping metal oxide on surface of ceramic particles,[28] aligning particles in thickness direction by dielectrophoretic assembly.[29, 30] The effect of the structure of ceramic materials in polymer matrix on the dielectric permittivity of composites is discussed in detail below.

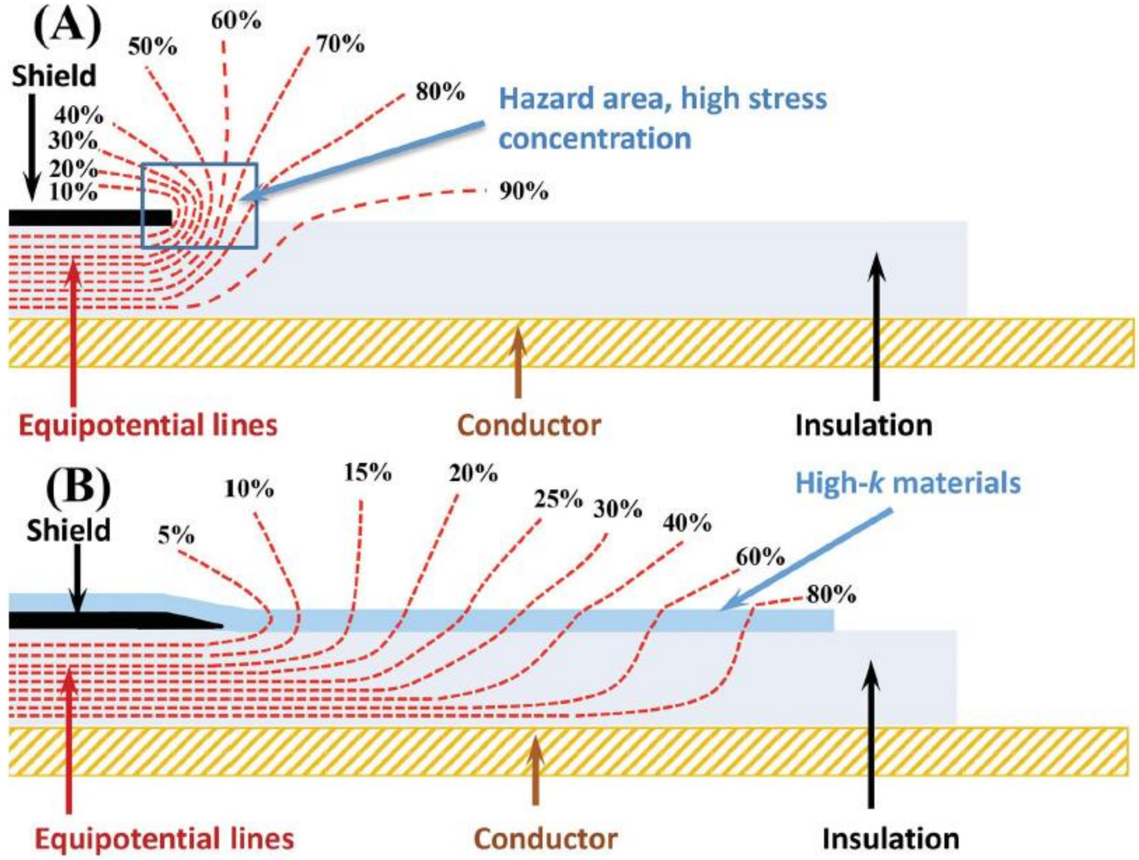

Figure 2.2 Electric stress and potential distribution at cable terminations without (A) and with (B) high- k material. The dashed lines are equipotential lines.[11] (Reprinted with permission from Ref. 11)

The dielectric permittivity of polymer matrix nanocomposites is dependent on the concentration of the filler and the dielectric permittivity of the filler and matrix. The dielectric permittivity of composites is limited by the structure extremity of involved two phases, as shown in Figure 2.3. The dielectric permittivity of the composites with parallel and series model[31] is shown equation 2.4 and 2.5, respectively.

$$\varepsilon_{c,max} = \varepsilon_m \phi_m + \varepsilon_p \phi_p \tag{2.4}$$

$$\varepsilon_{c,min} = \frac{\varepsilon_m \varepsilon_p}{\varepsilon_m \phi_p + \varepsilon_p \phi_m} \tag{2.5}$$

where ε_m and ε_p is dielectric permittivity of matrix and particle, respectively, ϕ_m and ϕ_p is concentration of matrix and particles, respectively.

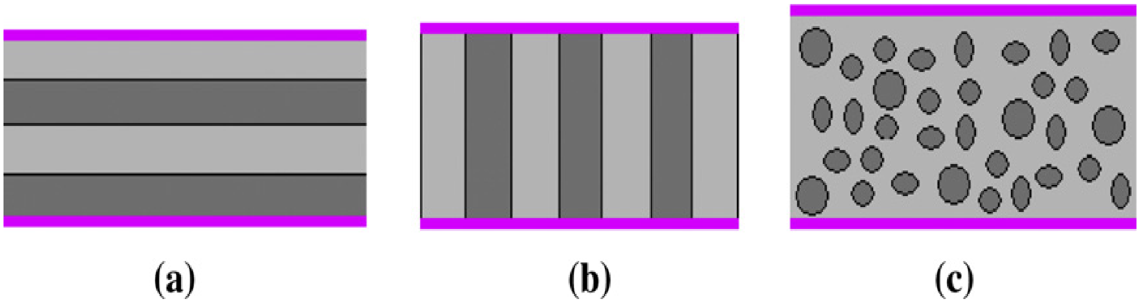

Figure 2.3 (a) series model, (b) parallel model and (c) random mixing model for composites.

The series model predicts the lowest and the parallel model predicts the highest dielectric permittivity for the nanocomposites as shown in Figure 2.4. For particles that are random in the matrix, the dielectric permittivity of the composites locates between these two limits. Maxwell mixing rule (equation 2.6) gives the predicted value:

$$\varepsilon_c = \varepsilon_m \left[\frac{2\varepsilon_m + \varepsilon_p + 2\phi_p(\varepsilon_p - \varepsilon_m)}{2\varepsilon_m + \varepsilon_p - \phi_p(\varepsilon_p - \varepsilon_m)}\right] \tag{2.6}$$

Although the addition of ceramic particles with high dielectric permittivity enhances the dielectric permittivity dramatically, the dielectric permittivity of the composites cannot exceed 100 even with 75 vol% particle content.[32, 33] With such high particle content, the polymer composites films lose high flexibility, mechanical performance and low cost of production.

One of the promising approaches to achieve better enhancement of the dielectric permittivity for polymer matrix with much less ceramic particle loading is aligning the particles to form pearl chain structure in the thickness "Z" direction under electric field. Tomer[34] studied the composites of barium titanate ($BaTiO_3$) particles aligned in silicon elastomer by dielectrophoretic assembly and reported 120% improvement of dielectric permittivity after alignment. The composites with aligned structure of $(Ba_{0.55}Sr_{0.45})TiO_3$ has 3 time higher dielectric permittivity than sample with random particles[35]. Tang[30] found out that the alignment of PZT nanowires in "Z" direction can enhance the energy density up to 51.6% greater than the nanocomposites with random nanowires at 20 vol% particles.

The aligned dielectric particles form columns along "Z" direction, and these columns create a similar structure as the parallel model, which can increase the dielectric permittivity for composites close to the upper limit. However, the measured dielectric permittivity of composite with aligned particles is smaller than the value predicted by the parallel model. The particles forming chains are closer to each other than the random particles, so the interaction between particles increases[36]. The gap among particles filled with polymer with low dielectric permittivity causes the measured value smaller than the value predicted by parallel model. This system can be modeled by the one dimensional chains of particles separated by polymer gap[35, 37] as shown Figure 2.5. In a single chain, the dielectric permittivity can be predicted by the series model. Therefore, the dielectric permittivity of the composite can be predicted by the following equation[35, 37]:

$$\varepsilon_c = \varepsilon_m \phi_m + \phi_p \left[\frac{g\varepsilon_m \varepsilon_p}{g\varepsilon_m + \varepsilon_p}\right] \tag{2.7}$$

where g is the ratio of the particle size and the average inter-particle distance.

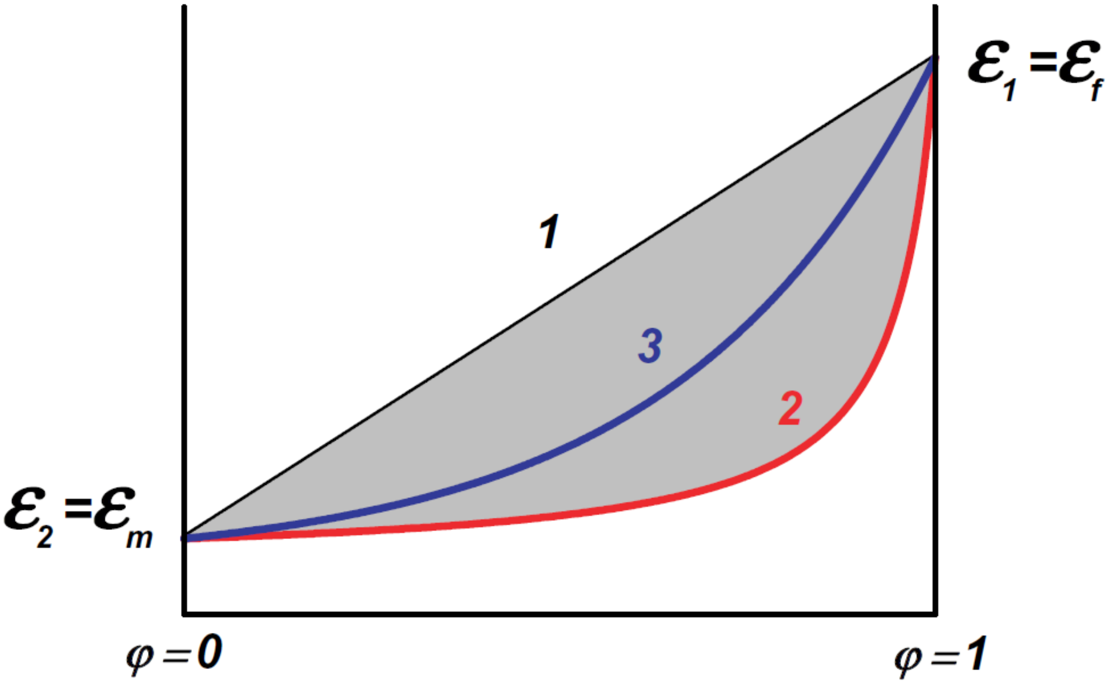

Figure 2.4 Schematic of effect dielectric constant of a mixture/composite versus the composition: 1-parallel connection, 2-series connection; 3-real composite with random particles.[38] (Reprinted with permission from Ref. 38)

In the long range, the pearl chain length is not as long as the thickness of the film, so there are large gaps between the pearl chains, which also leads to the smaller value of dielectric permittivity than upper limit. On the other hand, since the value of g has a large numerical value, the dielectric permittivity of composite with aligned pearl-chain is larger than that of composites with random particles. Bowen reports that the dielectric permittivity of aligned composites generally 2-3 times larger than randomly dispersed sample when g=14.3.

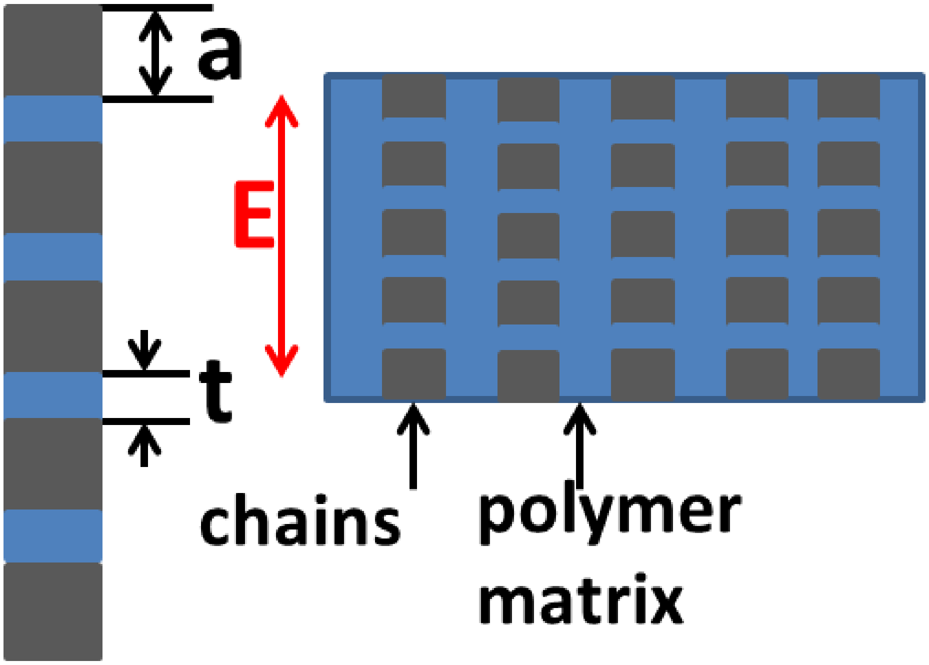

Figure 2.5 Schematic of one dimensional model.

Another effective method to achieve high dielectric permittivity of polymer composite film with very low loading of particles is to use electrically conductive particles based on the percolation theory. Very high dielectric permittivity ranging from several hundred to millions has been achieved for percolated composites with different conductive particles including metal, carbon nanotubes and graphene etc. Fan[17] reported that dielectric permittivity of poly(vinylidene fluoride)(PVDF)/graphene composite could be up to more than 200 at 1000Hz with 1.01 vol%, and the dielectric loss was 0.48. As the concentration of graphene increased further beyond the percolation, the dielectric permittivity of composites increased exponentially to extremely high value of 4.5×10^7 at 1000 Hz while the dielectric loss was as high as 229 at this concentration. This nanocomposite with high dielectric permittivity and dielectric loss can be used as electromagnetic wave absorption.

When the concentration of the conductive particles is close to the percolation threshold, the composites has an insulation-conductive transition behavior. The percolation transition is a transition of isolated fillers into continuous cluster throughout the system formed by fillers contacting each other as the concentration increases.[20] The dielectric permittivity of the composites can be expressed in a classic explicit law[18]:

$$\frac{\varepsilon_c}{\varepsilon_m} = (f_c - f_{filler})^{-q} \quad \text{for} \quad f_{filler} < f_c \qquad (2.8)$$

where f_c is the percolation threshold, and q is the critical exponent, in the range 0.8 to 1.

The critical change of the dielectric permittivity near the percolation is due to the micro-capacitor network.[20, 39] The micro-capacitor is formed by the neighboring conductive particles and a thin layer of polymer between them. The significant increase of dielectric permittivity of the composites contributed by all the micro-capacitors is correlated with a significant intensity increase of local electric field near the percolation threshold. The migration and accumulation of charge carriers at the interface of matrix and conductive fillers are promoted by the increase of local electric field intensity. The charges generated by surface plasma resonance or by charge injection from electrode are accumulated at the interface of polymer and conductive fillers due to their different relaxation times. As the particle concentration increases, the accumulated charges at the interface are relaxed by tunneling (when the neighboring particle distance is within tunneling range) or by ohmic conduction (when the particles have direct contact with each other).[40] Thus the significantly enhanced dielectric permittivity of polymer/conductive particle composites is attributed to the interfacial polarization.

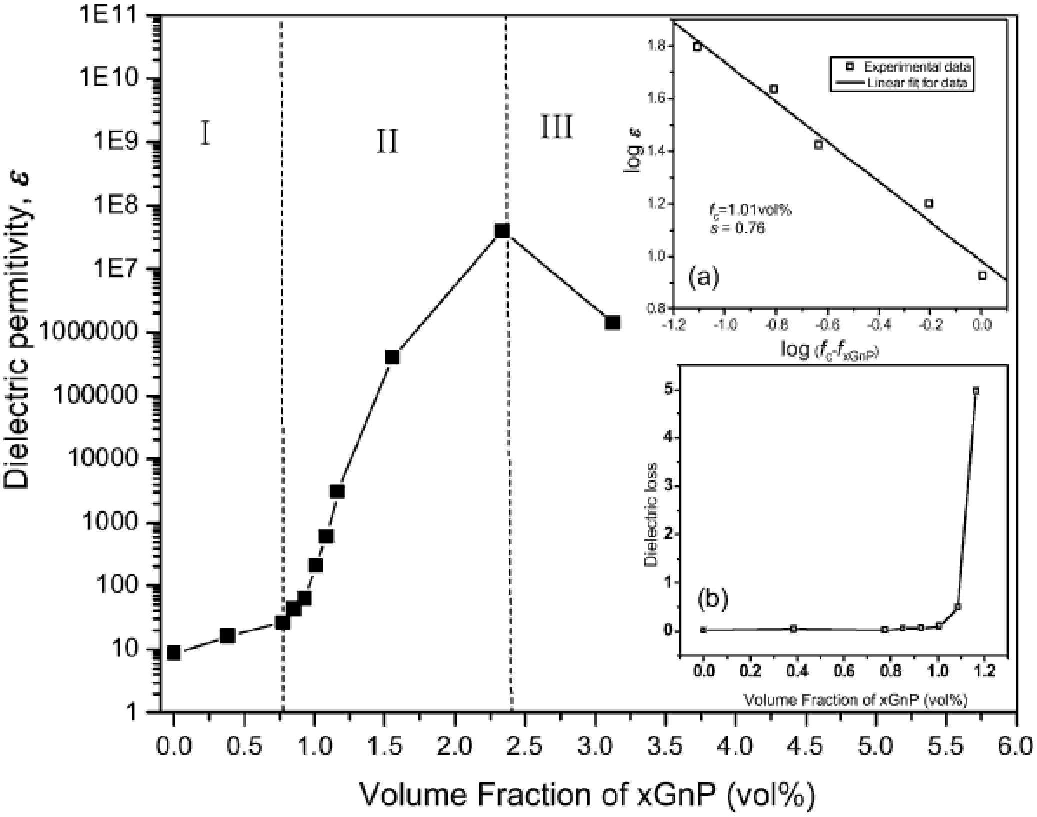

Figure 2.6 Dielectric constant of the PVDF/xGnP nanocomposites as a function of the xGnP volume fraction, measured at 1000 Hz. Inset a) shows the best fits of the conductivity to Equation 2.8. Inset b) shows the loss tangent as a function of xGnP volume fraction.[17] (Reprinted with permission from Ref. 17)

High dielectric permittivity at much lower particle loading is achieved by using the conductive particles than ceramic particles. Since the conductive particles in previous studies are randomly dispersed in polymer matrix, there is a potential to achieve higher dielectric permittivity with much lower loading of filler thus retaining the flexibility of polymer and lowering the cost. One way to reduce this critical concentration is to use electric field to form “nanocolumns” of conductive nanoparticles chains in the field direction in polymer matrix. For instance, electric field aligned epoxy/graphite flakes composite films exhibit up to 7-8 orders of magnitude higher of electric conductivity than randomly dispersed composites.[41] Since the percolation behavior of dielectric permittivity follows the percolation behavior of electrical conductivity for most of polymer/conductive particle composites,[42, 43] enhanced dielectric permittivity is also expected by the alignment of the conductive particles. The fundamental mechanism of electric field assisted assembly of ceramic particles, conductive particles and phase will be discussed in detail. To prepare the polymer based composite film with best quality, the fundamental of film processing, film formation will be described below.

2.2 Polymer film processing

Polymers or polymer based nanocomposite films are gaining increased popularity and enjoying worldwide growth due to their extensive applications in the fields of packaging, electronics, pharmacy and optics.[44-46] There are many methods to manufacture polymer or polymer nanocomposite films including film blowing, hot melt cast film extrusion, spray coating and solution casting method for thermoplastic polymers, ultraviolet curing and thermal curing for thermoset polymers.

Film blowing is a process of forcing the polymer melts through a tubular die, blowing air to inflate the polymer melts into a cylinder, cooling the film in air, and drawing down the tubular film.[47] Hot melt cast film extrusion technique is widely used in industrial manufacturing due to its single process step, higher production capacity, and lower cost compared to film blowing. The cast film line is usually composed of gravimetric feeding system, extruder, filtration system, flat die system, cooling unit, automatic gauge control system, corona treatment and winder.[48] In a typical film extrusion, the polymer material is provided by the gravimetric feeding system, then melted and mixed in the extruder. The polymer melts are extruded through the flat die system, and the molten curtain enters the highly polished cooled rolls to freeze the film. The orientation of molecular chains and thickness of the film can be controlled by the rotation speed of rollers. Then the film is passed downstream where edge trimming and corona treatment is applied if needed, and the final film is winded into rolls.[49] Spray coating is suitable for low viscosity polymer solutions and the process includes liquid atomization, in-flight droplet evaporation, spreading, drying and adhesion on the substrate.[50] Solvent solution casting method is a process of dissolving of thermoplastic polymer in organic solvent, die or blade casting on the substrate followed by evaporation of the solvent. It is widely used for fabricating high quality films with uniformity, clarity, flexibility and controlled thickness. UV curing is a conversion of liquid resins with acrylate double bonds or epoxy group into solid films via free radical or cationic polymerization activated by UV light energy. UV curing is becoming more and more popular due to its high process speed, and the liquid film can be cured in seconds, which is much faster than other methods. Thermal curing is similar as UV curing but activated by heat energy instead of UV light and its curing speed is relative slower than UV curing, ranging from minutes to hours.

Solution casting method is the main method to fabricate the nanocomposite films in this dissertation, so the fundamental simulation of drying, orientation of molecular chains during drying, and the techniques for solution casting will be discussed below.

2.2.1 Solution casting process

The advantages of the solution casting films are uniform thickness distribution, optimum optical purity, high optical transparency, low haze and virtually in-plane isotropic orientation.[51] Owing to all these excellent properties, the solvent cast films can be used as photographic film, optical polarizers,[52] compensation or retardation film,[53] and electronic applications.[54, 55] Some high temperature polymers such as polyimide film with excellent electrical stability at high temperature can only be achieved by solution casting process but not the melting extrusion method. Polyimide film is produced by casting poly (amide carboxylic)/ dimethylacetamide and cross linking with acetic anhydride subsequently.[55] In a typical process of solvent casing, the polymers are dissolvent in volatile solvents or solvent mixtures to form a homogeneous solution with a reasonable viscosity. Doctor blade die or slot die are usually used to cast the solution into a liquid film with a desired thickness on a supporting substrate. There are varieties of materials used for supporting substrate: copper, stainless steels, polytetrafluoroethylene (PTFE) films, siliconized paper, polyester film and other polymer films.[51] The cast liquid film goes into the oven to remove the solvent, and the drying condition is controlled by heating via supporting film heater, heating via radiation, and air stream drying. The drying condition is important to fabricate films with high quality, such as temperature, air flow speed and solvent loading in the air. There are two steps for the solvent to evaporate from the cast film. The first step happens as the solvent concentration is still high, and the diffusion rate of solvent is also high, so the solvent evaporates rapidly. As residual solvent in the film becomes very low, the solvent content of the surface is close to zero and the diffusion rate of the residual solvent to the surface can be 1000 times slower than before, which is the controlling factor for solvent evaporation. The drying process for solvent cast films is very complex and the detailed mathematical modeling is discussed below.

2.2.2 Mathematical modeling of the drying process

The drying process of solvent cast film is a thermal diffusion process of polymers and solvent in the solution film related to the mass and heat diffusion. The 3D governing equations for the kinetics of concentration and temperature evolution for drying process were developed by Shams E.[56]

$$\rho_1 \frac{d\varphi}{dt} = \nabla \cdot \{ \alpha \left(\frac{\partial \mu}{\partial \varphi}\right)_T \nabla \varphi + [\alpha \left(\frac{\partial \mu}{\partial T}\right)_\varphi + \beta] \nabla T \} \qquad (2.9)$$

$$\rho c_P \frac{dT}{dt} = -\nabla \cdot \{ \left(\mu + \frac{\beta}{\alpha} T\right) J_1 - (\gamma - \frac{\beta^2}{\alpha} T) \nabla T \} \qquad (2.10)$$

where ρ_1 and φ is the mass density and volume fraction of the solvent respectively; t time; T temperature; ρ and c_P are mass density and isobaric specific heat capacity of the polymer solution respectively. J_1 is the non-convective mass flux of the solvent and μ is the exchange chemical potential of the components and are given by

$$J_1 = -\alpha \left(\frac{\partial \mu}{\partial \varphi}\right)_T \nabla \varphi - \left[\alpha \left(\frac{\partial \mu}{\partial T}\right)_\varphi + \beta\right] \nabla T \qquad (2.11)$$

$$\mu = \frac{\mu_1}{M_1} - \frac{\rho_2}{\rho_1} \frac{\mu_2}{M_2} \qquad (2.12)$$

where μ_1 and μ_2 are the chemical potentials of solvent and polymer respectively; M_1 and M_2 are molar mass of solvent and polymer respectively and ρ_2 is the mass density of polymer. To preserve the positive definiteness of entropy production, the phenomenological coefficients restricted by constraints: α, β and γ should satisfy the following conditions:

$$\alpha > 0, \gamma > 0, \beta < \sqrt{\alpha \gamma T^{-1}} \qquad (2.13)$$

where $\alpha(\partial\mu/\partial\varphi)_T$, $\alpha(\partial\mu/\partial\varphi)_\varphi+\beta$ and $\gamma-\beta^2 T/\alpha$ are mutual diffusion coefficient, thermal diffusion coefficient and thermal conductivity, respectively. To satisfy the constraint $\beta < \sqrt{\alpha \gamma T^{-1}}$, β is made as zero, mutual diffusion coefficient α and thermal conductivity γ is given by[56]

$$\alpha = \frac{D_0 \rho_1 M_1 \varphi (1-\varphi)}{RT} \qquad (2.14)$$

$$\gamma = \gamma_0 \frac{T_b^{6/5}}{M_1 T_c^{1/6}} \frac{(1-T_r)^{0.38}}{{T_r}^{1/6}} \qquad (2.15)$$

where D_0 and γ_0 are two constant parameters, T_b and T_c are boiling and critical points of the solvent and T_r is the reduced temperature.

In his study, the above governing equations were used to numerically simulate the drying process of a solvent cast polymer solution film on a glass substrate and the whole system is exposed to a laminar air flow at temperature T_∞ as shown in Figure 2.7.Since the dimension of solvent cast film in the plane of surface is larger than the thickness in several orders of magnitude, the diffusion is considered as a 1D process to a good approximation.

The film drying process is a moving boundary problem, so the surface position of the film w(t) is not known a priori. The equation of this moving boundary were derived with regard to the conservation of polymer mass during the drying process as below[56]

$$\frac{dw(t)}{dt} = -\frac{C_s}{\rho_1} \tag{2.16}$$

where C_s is the evaporating solvent flux.

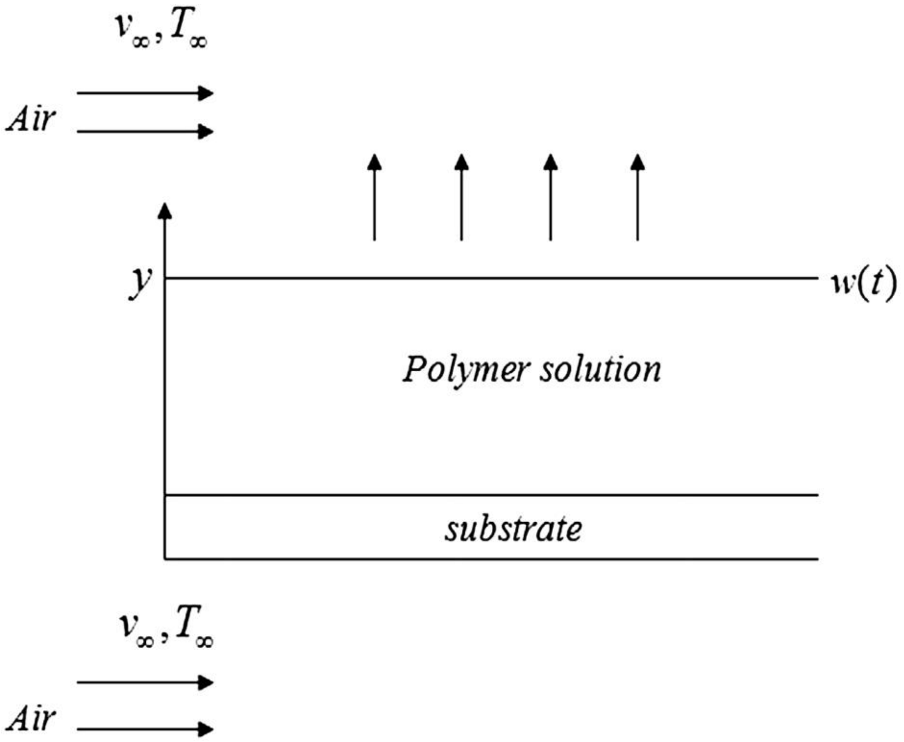

Figure 2.7 Schematic drawing of film drying process.[56] (Reprinted with permission from Ref. 56)

A system of coupled nonlinear partial differential equations is formed from the governing mass diffusion and heat conduction equations. By plugging J_1 from Eq. (2.11) into Eq. (2.10) and letting β be zero, the 1D evaporation problem can be expressed below:

$$\rho_1 \frac{d\varphi}{dt} = \frac{\partial}{\partial y}\{\alpha \left(\frac{\partial \mu}{\partial \varphi}\right)_T \frac{\partial \varphi}{\partial y} + \alpha(\frac{\partial \mu}{\partial T})_\varphi \frac{\partial T}{\partial y}\} \tag{2.17}$$

$$\rho c_P \frac{dT}{dt} = \frac{\partial}{\partial y}\{\alpha\mu \left(\frac{\partial \mu}{\partial \varphi}\right)_T \frac{\partial \varphi}{\partial y} + (\alpha\mu \left(\frac{\partial \mu}{\partial \varphi}\right)_\varphi + \gamma) \frac{\partial T}{\partial y}\} \tag{2.18}$$

One initial condition and two boundary conditions are needed to solve Equations above. The initial conditions are fulfilled by starting with uniform concentration and temperature profiles

$$\varphi(y, t=0) = \varphi_0 \tag{2.19}$$

$$T(y, t=0) = T_0 \tag{2.20}$$

Boundary conditions at the surface w(t) of the solution are[56]

$$(J_1)_{w(t)} - c_1(w(t), t)\frac{dw(t)}{dt} = C_s \tag{2.21}$$

$$(J_q)_{w(t)} = < h > (T - T_\infty) + \Delta H_v C_s \tag{2.22}$$

where <h> and ΔH_v are the averaged heat transfer coefficient and heat of evaporation of solvent, respectively[57]. Boundary conditions at the substrate for the mass and heat equations are

$$J_1 = 0 \tag{2.23}$$

$$J_q = -k\frac{\partial T_{sub}}{\partial y} \tag{2.24}$$

where k and T_{sub} are the thermal conductivity and absolute temperature of substrate respectively. Transient heat conduction in the substrate along with the associated initial and boundary conditions are given by

$$\frac{\partial T_{sub}}{\partial t} = \kappa\frac{\partial^2 T_{sub}}{\partial y^2} \tag{2.25}$$

$$T_{sub}(y, t=0) = T_0 \tag{2.26}$$

$$< h > (T_\infty - T_{sub}) = -k\frac{\partial T_{sub}}{\partial y} \tag{2.27}$$

where κ is the thermal diffusivity of the substrate. The boundary condition at the interface between substrate and polymer solution is satisfied by a continuity condition in temperature. An explicit finite difference scheme was used to solve the system of partial differential equations (9) and (10) considering the initial and boundary conditions described above. φ, t^* and ξ are volume fraction of the solvent, dimensionless time and dimensionless length. $\xi=0$ shows the substrate and $\xi= 1$ represents the evaporating surface at t=0. In case of T=318.15 K, V=1.2 m/s and initial solvent concentration is 0.8, the calculated concentration and temperature profiles is showing Figure 2.8 and 2.9. Before evaporation happens, the solvent concentration is constant 0.8 throughout the thickness direction of cast film. Once solvent starts evaporating, the solvent concentrations increases decreases dramatically on top surface of the film while increase slightly near the substrate in Figure 2.8, so the drying rate is solvent evaporation controlled. The solvent concentration on top surface is much lower than bottom surface which explains the formation of skin layer on top surface during drying. As the evaporation proceeds, the solvent concentration on bottom surface starts decreasing and the top surface deceases at much lower rate, and the drying rate is diffusion controlled. Eventually, the solvent concentration is at very low level and there's no solvent gradient in thickness direction. In case of film temperature, there's a temperature gradient observed: colder on top surface and warmer on bottom surface due to faster evaporation on the top surface showing in Figure 2.9. The temperature first decreases at the beginning of drying due to the evaporation and then increases asymptotically to the set drying temperature.

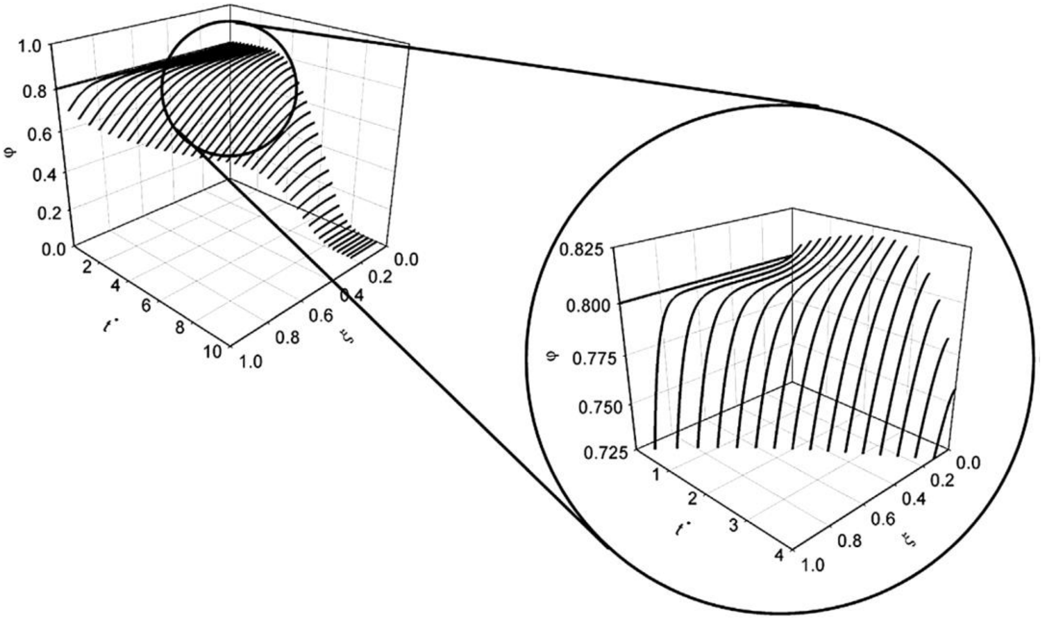

Figure 2.8 Concentration profile for film evaporation process.[56] (Reprinted with permission from Ref. 56)

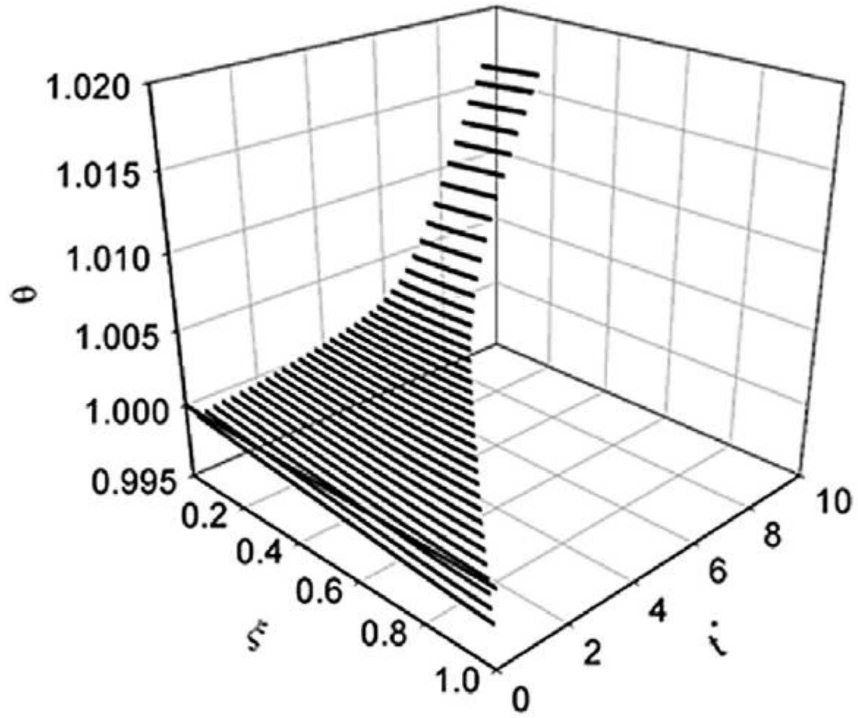

Figure 2.9 Temperature profile for film evaporation process.[56] (Reprinted with permission from Ref. 56)

2.2.3 Molecular orientation induced by solvent evaporation

The solvent cast polymer solution film undergoes constrained volume shrinkage due to solvent evaporation, because the film sticks to the substrate, resulting in one dimensional thickness reduction.[58] The constrained volume shrinkage induces the development of in-plane stress[59], which leads to the most of polymer chains lying in the plane of the film naturally.[60] In an unconstrained polymer solution drying, the film has a three dimensional volumetric shrinkage which does not lead to any orientation. The in-plane orientation of the polymer chains cause the out of plane birefringence, so the orientation level of the polymer molecular chains can be characterized by birefringence technique if refractive index difference (intrinsic birefringence) between parallel and perpendicular to the polymer chain is not zero. D. Luca[61, 62] investigated the effect of solvent cast conditions such as film thickness, polymer molecular weight, casting solvent, temperature on the molecular orientation by measuring birefringence. It was found out that the birefringence increased with decreasing film thickness due to faster drying rate for thinner film. The birefringence decreases with increasing temperature due to the ambient temperature is closer to the glass transition temperature. The drying process can be regarded as freezing the molecular conformations when the glass transmission of film passes the substrate or ambient temperature. The closer substrate temperature to the glass transmission temperature, the slower the freezing and the more time for the molecular chains to relax resulting lower birefringence. The birefringence increases with polymer molecular weight because of more molecular entanglement and slower drying rate. The birefringence was measured after film was totally dried, so we miss the information of molecular orientation during drying. Recent, a custom built measurement system was developed in Dr. Cakmak's research group to track the real-time change of weight, thickness, in-plane and out of plane birefringence of the solvent cast film during drying.[63] It was found out that the weight and thickness decreases and level off beyond a critical time after solvent evaporation. The in-plane birefringence almost remains zero during drying indicating that the polymer chains are randomly distributed in the plane. However, the out of plane birefringence remains zero during initial drying and increases sharply to a very high value as the weight and thickness approached to the plateau indicating the polymer chains are oriented parallel to the film plane.[64] Moreover, the out of plane birefringence gradient along the thickness direction of the film was investigated caused by the drying gradient along thickness direction.[65] Higher birefringence was observed on the substrate-solution film interface at earlier stage due to the casting procedures. As the solvent evaporates, the birefringence gradient profile was reversed and the air-solution film interface had higher birefringence. After a critical time, highly oriented layer was formed at the air-solution film interface, and this layer developed through the whole thickness as the solvent evaporates.

2.2.4 Phase separation of polymer blends solution during drying

The thermodynamics and kinetics of phase solution of polymer blends solution during solvent evaporation are introduced below.

2.2.4.1 Thermodynamics of polymer blends

Since the phase separation mechanism of ternary solution is complicated, the introduction begins with the binary solution. The necessary but not sufficient thermodynamic condition for the binary system involving polymer or solvent to be homogenous mixture is that the Gibbs free energy of this mixture, $\Delta G_{m,}$ must be negative. ΔG_m as a functional of polymer ratio at different temperature is shown in the upper part of Figure 2.10. At temperature T_1, the curve of ΔG_m has concave shape with one minimum value over the whole polymer ratio range ($\partial^2\Delta G_m/\partial\Phi^2>0$), meaning any phase separation will cause the increase of ΔG_m which is not preferential, so the system at T1 is completely miscible over the whole range of polymer ratio. Therefore, the necessary and sufficient conditions for homogeneous mixtures are $\Delta G_m<0$ and $\partial^2\Delta G_m/\partial\Phi^2>0$. At temperatures of T_2 and T_3, the system is partially miscible because it only meets condition of $\Delta G_m<0$ but $\partial^2\Delta G_m/\partial\Phi^2<0$ in some range due to two local minima. In order minimize the Gibbs free energy ΔG_m of the system, the system will phases separate into two phases with each of them having the concentration determined by the tangent points on the on ΔG_m curve and these two points are called binodal points expressed below

$$(\partial\Delta \mathrm{G}_m/\partial\Phi)_{phase\ 1} = (\partial\Delta \mathrm{G}_m/\partial\Phi)_{phase\ 2} \tag{2.28}$$

The volume ratio of rich and minor phases at binodal points can be predicted by the lever rule. The curve connected by all these binodal points at different temperatures is binodal curve as shown in the lower part of Figure 2.10. There're two inflection points between two minima and maxima where $\partial^2\Delta G_m/\partial\Phi^2=0$, which is called spinodal points, and the curve connection these points at different temperatures is the spinodal curves. In the phase diagram, the binodal and spinodal curve meet at a critical point where $\partial^3\Delta G_m/\partial\Phi^3=0$. There are three regions of different degree of miscibility in the phase diagram (1) the stable single phase regions above the binodal curve in Figure 2.10, (2) the metastable region between the binodal and spinodal curves and (3) unstable region where the system spontaneously phase separated. At T_4, the Gibbs free energy of the mixture is positive so the system is completely immiscible over the whole range of polymer ratio.

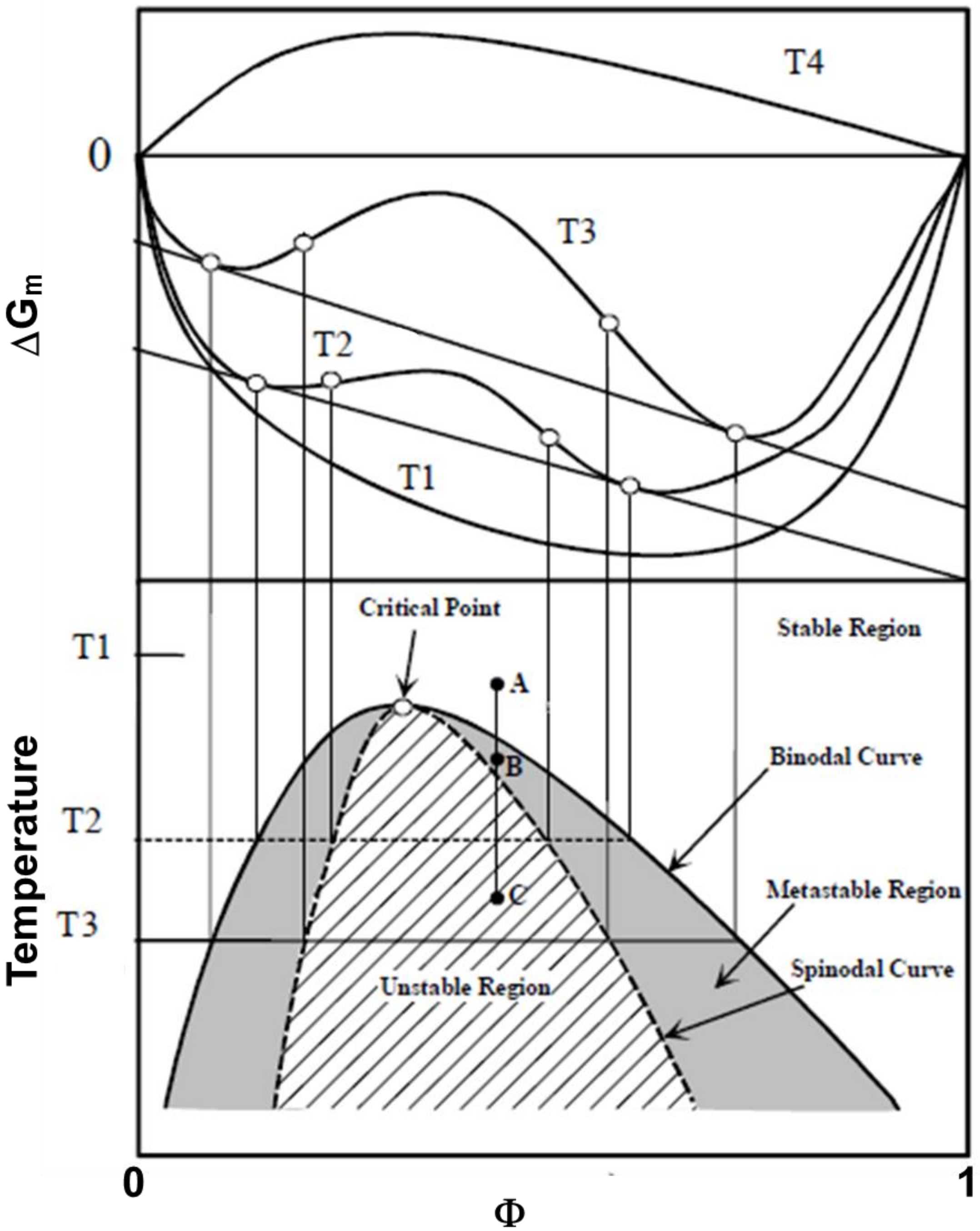

Figure 2.10 Schematic diagram of Gibbs free energy of mixing and phase diagram as a function of polymer concentration.[66] (Reprinted with permission from Ref. 66)

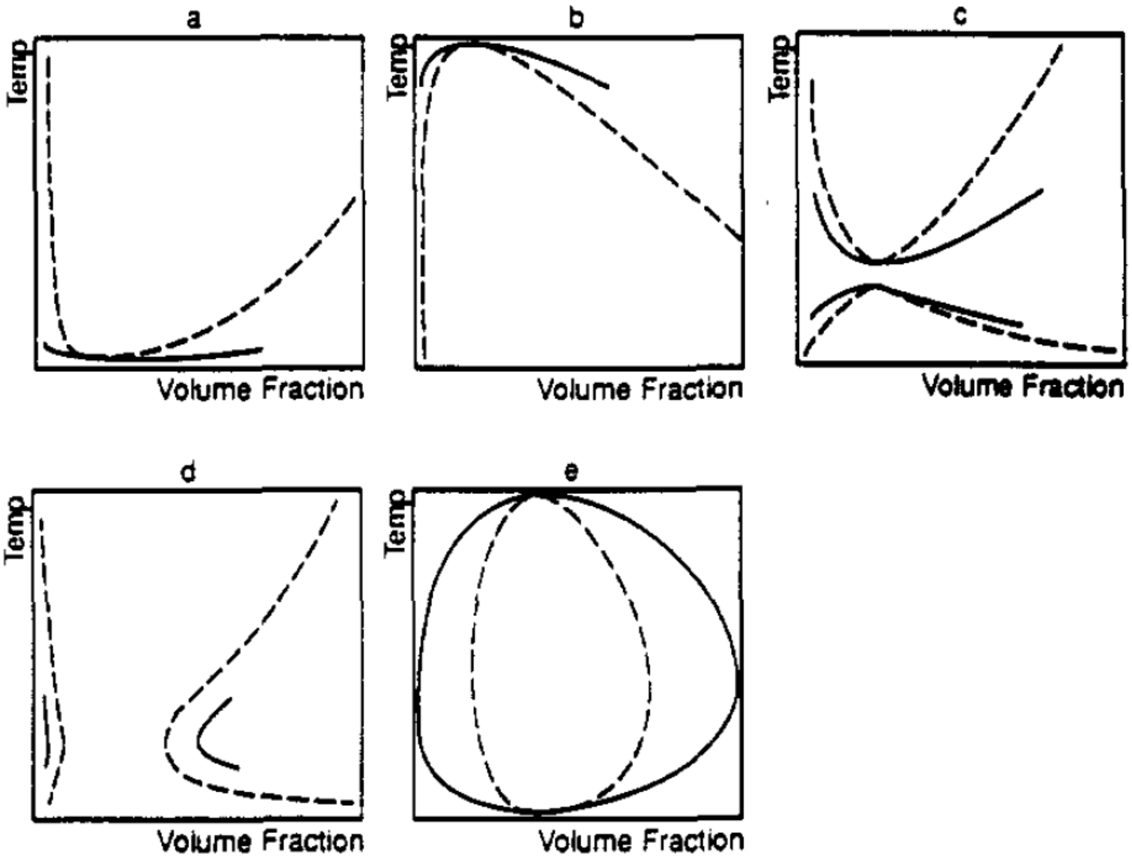

Figure 2. 11 Phase diagrams of hypothetical polymer blends. The solid line is the binodal and the broken line is the spinodal. The diagrams are of the form (a) LCST, (b) UCST, (c) combined LCST and UCST, (d) hourglass, and (e) closed loop.[67] (Reprinted with permission from Ref. 67)

For binary system such as polymer solution or polymer blends, there're five types of phase diagrams observed most commonly including upper critical solution temperature (UCST), lower critical solution temperature (LCST), combined UCST and LCST, hourglass and closed loop shaped phase diagrams showing in Figure 2.11.[67] If the miscibility of mixture as shown in the Figure 2.10 increases with the temperature, the system change from two phases to one phase as the temperature increases, which is UCST. Polystyrene in cyclohexane exhibits UCST phase diagram.[68] On the contrary, the system such as polystyrene in benzene[68] with decreasing miscibility as the temperature increases shows a lower critical solution temperature (LCST). Some binary systems such as polystyrene in acetone may show different phases diagrams depending on the molecular weight: (1) a combined UCST and LCST phase diagram for polystyrene with lower molecular weight of 4800 and 10,300 (2) hourglass shape phase diagram for polystyrene with higher molecular weight of 19,800 and 50,000.[69] Poly(vinyl alcohol)/water system was found to have a closed-loop phase diagram.[70]

2.2.4.2 Kinetic of phase separation

Phase separation is the process of a mixture with single phase moving to metastable or unstable region caused by a change of temperature, pressure or composition. The mechanism of phase separation is substantially different for moving from one phase region to metastable region and unstable region resulting from nucleation and growth and spinodal decomposition respectively showing in Figure 2.12.

(a) Nucleation and growth mechanism

When a polymer solution is forced to jump from the single phase region into metastable region, the system may stay at a single phase or undergo phase separation. This is attributed to the fact that the Gibbs free energy of this system is at local but not global minimum. Therefore, the system is stable to the small fluctuations of concentration caused by the change of temperature or pressure. If the fluctuation is large enough to form nucleating clusters, the phases separate and grow spontaneously, so this phase separation process is called nucleation-growth decomposition. These nucleating clusters have similar composition as the new phases. The formation of nucleating clusters requires the activation energy ΔE_{aN}, which depends on the gradient of free energy of mixture and the interfacial tension (γ_{12}) which is given by the equation below:

$$\Delta E_{aN} = -\frac{4\pi}{3} {R_N}^3 \Delta G_m + 4\pi {R_N}^2 \gamma_{12} \tag{2.29}$$

where ΔGm is the supersaturation degree related Gibbs free energy, γ_{12} is the interfacial tension between nucleating clusters and their surroundings, R_N is the diameter of nucleating cluster.

The activation energy as a functional of the diameter of nucleating cluster R_N is shown in Figure 2.13. The activation energy ΔE_{aN} shows a maximum value (ΔE^*) at critical radius R^* of nucleating cluster. If the diameter of cluster is smaller than R^*, it will be dissolved back into the solution to form single phase. If the diameter of cluster is larger than R^*, the growth process will start spontaneously. The critical value of ΔE^* and R^* is given below:

$$\Delta E^* = \frac{16\pi {\gamma_{12}}^3}{3 {\Delta G_m}^2} \tag{2.30}$$

$$R^* = \frac{2\gamma_{12}}{\Delta G_m} \tag{2.31}$$

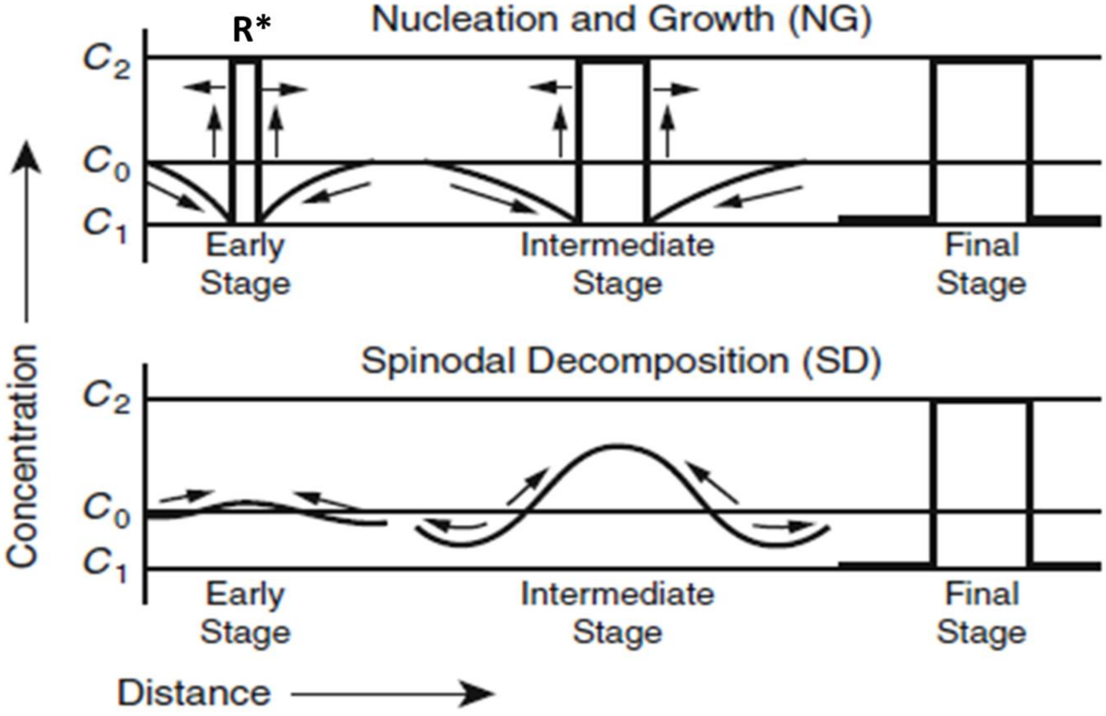

Figure 2.12 Schematic representation of the density fluctuations during the spinodal decomposition mechanism (SD, bottom) and the nucleation and growth (NG, top).[71] (Reprinted with permission from Ref. 71)

The rate of nucleation of N nucleation clusters during time t can be described using an Arrhenius equation in equation below:

$$\frac{dN}{dt} = k_N \exp\left(-\frac{\Delta E^*}{k_B T}\right) \tag{2.32}$$

where k_N is pre-exponential factor, k_B is Boltzmann constant ,T is temperature.

The growth is diffusion controlled, so it is proportional to the concentration gradient towards the nucleating cluster. As shown in Figure 2.12, there are three stages of phase separation process: early, intermediate, and late/final. The upper and lower limits of concentration are determined by the tie-line limits intersection of the binodal. Once the nucleation cluster with diameter of R^* forms in the early stages, the growth starts spontaneously due to the concentration gradient in the intermediate stage. The new phase has a concentration of C2 with a sharp interface with its surroundings. As a result, the phase separation based on the nucleation mechanism usually leads to island/matrix morphology.

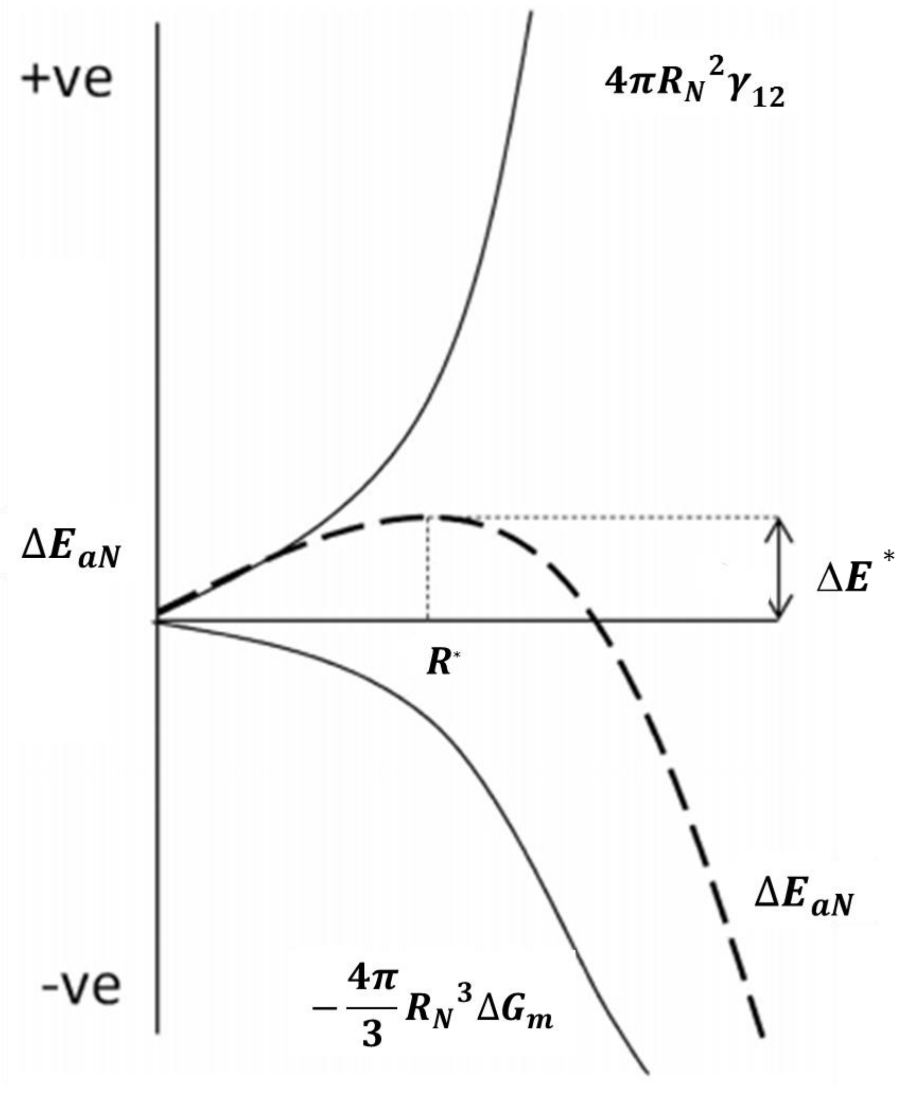

Figure 2.13 Activation energy diagram for nucleation explaining the existence[72]

(Reprinted with permission from Ref. 72)

(b) Spinodal decomposition

When the polymer solution is forced to jump from the stable region to unstable region, the long range phase separation starts spontaneously according to the spinodal decomposition mechanism due to the delocalized concentration fluctuation. In spinodal decomposition, the fluctuation of concentration results in the decrease of free energy in the system and triggers a long-wave fluctuation through the solution as shown in Figure 2.12. There's no sharp interface forming in the early and intermediate stages for spinodal decomposition compared to nucleation growth mechanism. The wavelength doesn't change but the amplitude increases with time during the early stage of spinodal decomposition, which is explain by Cahn and Hilliard theory.

The concentration fluctuation described by Cahn-Hilliard[73] theory is below

$$\frac{\partial c(x,t)}{\partial t} = M\nabla^2 \times \{(\frac{\partial \mathrm{f}[(\mathrm{c}(\mathrm{x},\mathrm{t}))]}{\partial \mathrm{c}})_T + \mathrm{r}_{\mathrm{ri}}^2 \mathrm{k}_\mathrm{B} \mathrm{T} \nabla^2 \mathrm{c}(\mathrm{x},\mathrm{t})\} \tag{2.33}$$

where c(x,t) is the concentration field, M is the mobility, f is the free energy density as a function of concentration, r_{ri} is range of effective integration. Since the concentration fluctuations are small relative to the overall concentration during the early stage of spinodal decomposition, the linearized diffusion equation can be described below by neglecting the concentration dependencies:

$$\frac{\partial c(x,t)}{\partial t} = M[(\frac{\partial^2 \mathrm{f}}{\partial \mathrm{c}^2})_T \nabla^2 c + \mathrm{r}_{\mathrm{ri}}^2 \mathrm{k}_\mathrm{B} \mathrm{T} \nabla^2 \mathrm{c}] \tag{2.34}$$

Then the equation above is written as a Fourier series

$$\delta c_k(t) = \delta c_k(0) \exp[R(k)t] \tag{2.35}$$

where k is the wave vector and R(k) is amplification factor. The amplification factor as a function of wave vector is shown in Figure 2.14. If the system is quenched into unstable regions ($\partial^2 f/\partial c^2<0$), the amplification factor is positive, on the other hand, if the system is quenched into metastable region ($\partial^2 f/\partial c^2>0$), it is negative. The critical wave vector is defined below:

$$k_c = \sqrt{-\left(\frac{\partial^2 \mathrm{f}}{\partial \mathrm{c}^2}\right)_T \frac{1}{\mathrm{r}_{\mathrm{ri}}^2 \mathrm{k_B T}}} \tag{2.36}$$

The amplification factor increases exponentially as $k<k_c$, and decay exponentially as $k>k_c$. It grows at the maximum rate if $k_m=k_c/\sqrt{2}$. Since the amplification factor increases with wave vector exponentially, there's a sharp maximum at $k= k_m$. Therefore, all the concentration waves other than those at k_m can be neglected and the system has a fixed wavelength at $\lambda_m=2\pi/k_m$.[74] However, the linearized Cahn-Hilliard theory is only valid during the initial stage of spinodal decomposition when the deviations of concentration compared to the mean are small.

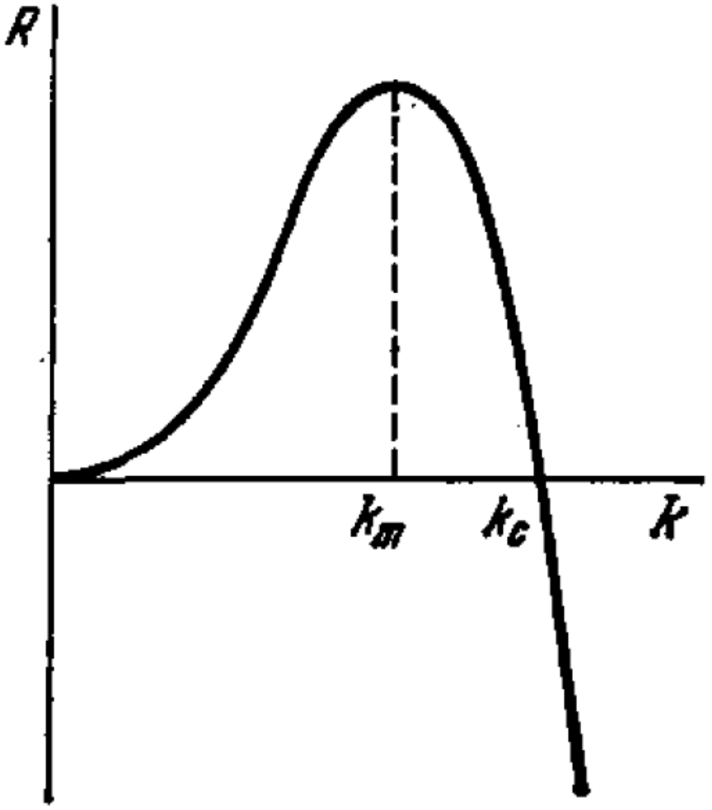

Figure 2.14 Amplification factor as a function of wave number.[74](Reprinted with permission from Ref. 74)

In the intermediate stage, the linear theory above in no longer valid, and the non-linear effects will dominate the phase separation which can be predicted by the Langer-Bar-Miller theory. It predicts that the wavelength of the sinusoidal concertation wave increases instead of staying at a stagnant value as predicted in linear theory, which leads to the growth of domain size.[75] The amplitude of scattering peak grows till it reaches the equilibrium concentration. In the late stage of spinodal decomposition, coarsen behavior of domain occurs and the domains may grow to a size much larger than microscopic length. The peak wave vector K, can be described in power law: $k_m \sim t^{-\Theta}$, with Θ=1/3 for solid binary mixture and Θ=1/d for fluid system, where d is the dimension of the system. The morphology of domains formed by spinodal decomposition is usually bicontinuous structure, but this bicontinuous morphology may break up to form droplet structure.

2.2.4.3 Phase equilibria in ternary system: polymer A/polymer B/solvent

The phase behavior becomes more complicated with the introduction of a third component. Since the ternary systems studied in this dissertation focus on the phase behavior of polymer A/polymer B/solvent system, so the kinetic of phase separation for this system will be described below. During solvent evaporation, the concentration of polymer increases and the phase separation occurs according to the mechanism of nucleation-growth or spinodal decomposition. Figure 2.15 shows the typical phase diagram for ternary solution where the dot curve is binodal line and the solid curve is the spinodal line. Point P and Q is the state of the solution at different concentration during evaporation.

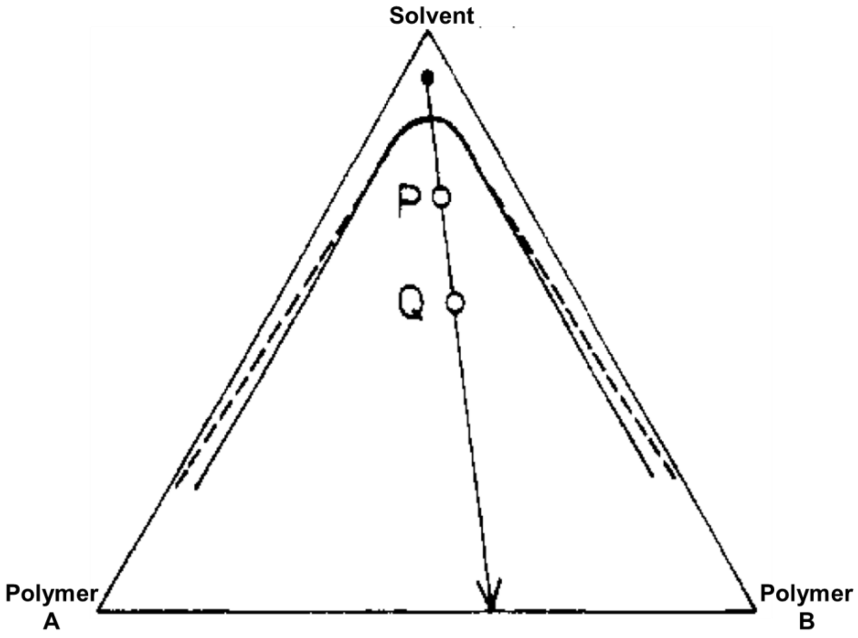

Figure 2.15 Ternary phase diagram of polymer A/polymer B/solvent system. The arrow indicates the drying process.[76] (Reprinted with permission from Ref. 76)

The free energy of mixing for the ternary polymer solution consisting of polymer A, polymer B and solvent is described in the Flory-Huggins expression:[77]

$$\frac{\Delta G_m}{RT} = \sum_i \frac{\Phi_i}{v_i} ln \Phi_i + \sum_{i<j} x_{ij} \Phi_i \Phi_j \tag{2.37}$$

where i= A, B and S (A is polymer A, B is polymer B and S is solvent), Φ_i is the volume fraction v_i is the molar volume, and χ_{ij} is the interaction parameter. The blend ratios of the polymer are defined as θ_A and θ_B according to Scott's procedures, and the volume fraction of total polymer Φ_p is expressed below:

$$\theta_A = \Phi_A / (\Phi_A + \Phi_B) \tag{2.38}$$

$$\theta_B = \Phi_B / (\Phi_A + \Phi_B) \tag{2.39}$$

$$\Phi_P = \Phi_A + \Phi_B = 1 - \Phi_S \tag{2.40}$$

The second derivation of free energy with respect to θ_A is expressed below:

$$\frac{\partial^2 \Delta G_m}{\partial {\theta_A}^2} = RT\,\Phi_P\left(\frac{1}{v_A\theta_A}+\frac{1}{v_B\theta_B}-\frac{2\chi_{AB}\Phi_P}{v_A}\right) = -2RT\,\frac{\chi_{AB}}{v_A}\,\Phi_P(\Phi_P-{\Phi_P}^s) \quad (2.41)$$

where ${\Phi_P}^s$ is the spinodal volume fraction of polymer blends where $\partial^2\Delta G_m/\partial{\theta_A}^2=0$. λ_m is the wavelength of the concentration fluctuation having the highest growth rate, and R_m is the maximum fluctuation growth rate constant.

$$\lambda_m = 4\pi[-(\frac{\partial^2 G}{\partial{\theta_A}^2})/4\kappa]^{-1/2} = 2\pi l[3(\Phi_P-{\Phi_P}^s)]^{-1/2} \quad (2.42)$$

$$R_m = \frac{M(\frac{\partial^2 G}{\partial{\theta_A}^2})^2}{8\kappa} = \frac{3RT}{l^2}M\,\frac{\chi_{AB}}{V_A}\,\Phi_P(\Phi_P-{\Phi_P}^s)^2 \quad (2.43)$$

where κ is the gradient energy constant according to J. Aartsen, l is a range of polymer-polymer interaction.[78] Figure 2.16 shows the effect of polymer concentration Φ_p on λ_m and R_m. The phase separation starts to occur at lower concentration near point P for lower evaporation rate of solvent resulting in larger λ_m. In contrast, the phase separation occurs at higher concentration near point Q for higher evaporation rate resulting in smaller λ_m, and then the fluctuation will be frozen as solvent evaporates leading to shorter periodic distance in the bicontinuous structure.[76]

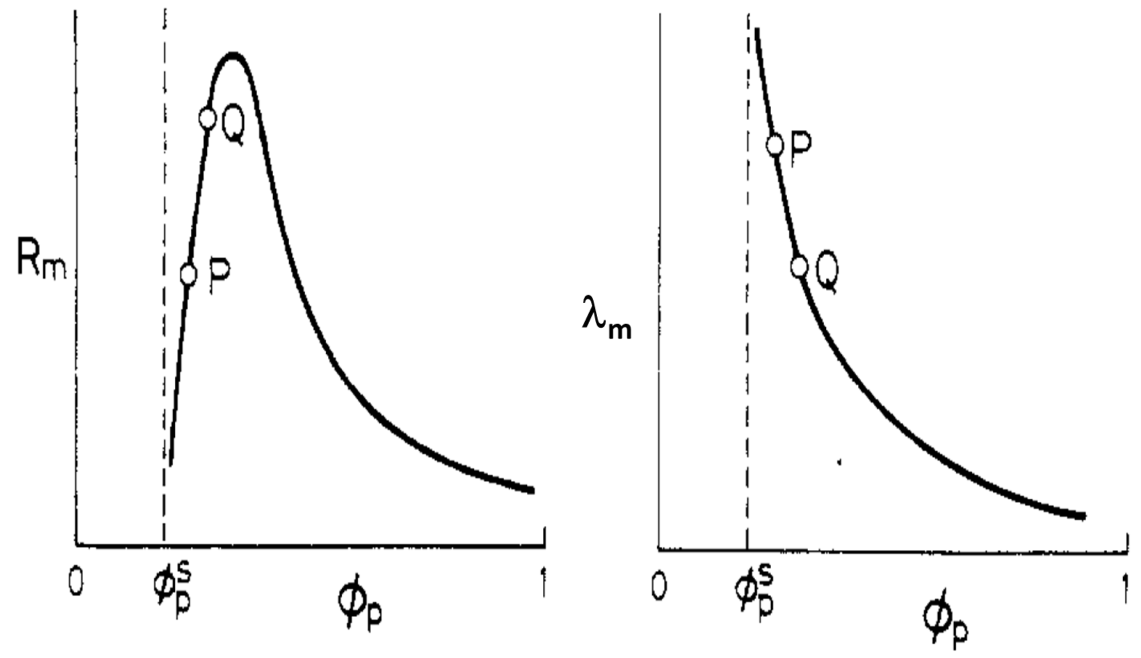

Figure 2.16 Concentration dependence of R_m, and λ_m. Calculated from eq. 2.42 and 2.43.[76] (Reprinted with permission from Ref. 76)

Figure 2.17 shows the concentration dependence of R_m on various factors such as the polymer-polymer interaction parameter, blend ratio and degree of polymerization. The spinodal polymer volume concentration $\Phi_P{}^s$ is proportional to $\chi_{AB}{}^{-1}$ for symmetric polymer pair ($v_A = v_B$), thus $\Phi_P{}^s$ decreases and the R_m-Φp curve shifts from (ii) to (i) as χ_{AB} increases. Therefore, the higher χ_{AB} is the less possibility to form bicontinuous structure and the higher possibility to form drop/matrix structure. The larger of the deviation of polymer blend ratio from the symmetry, the smaller of the product of $\theta_A\theta_B$, which results in larger $\Phi_P{}^s$ and shifts the curve from (i) to (ii). Since $R_m \sim N^{-4}$, the curve shifts from (ii) to (iii) for polymers with higher molecular weight. Thus the ternary solution has less phase-separated structure if the polymer has very high molecular weight.

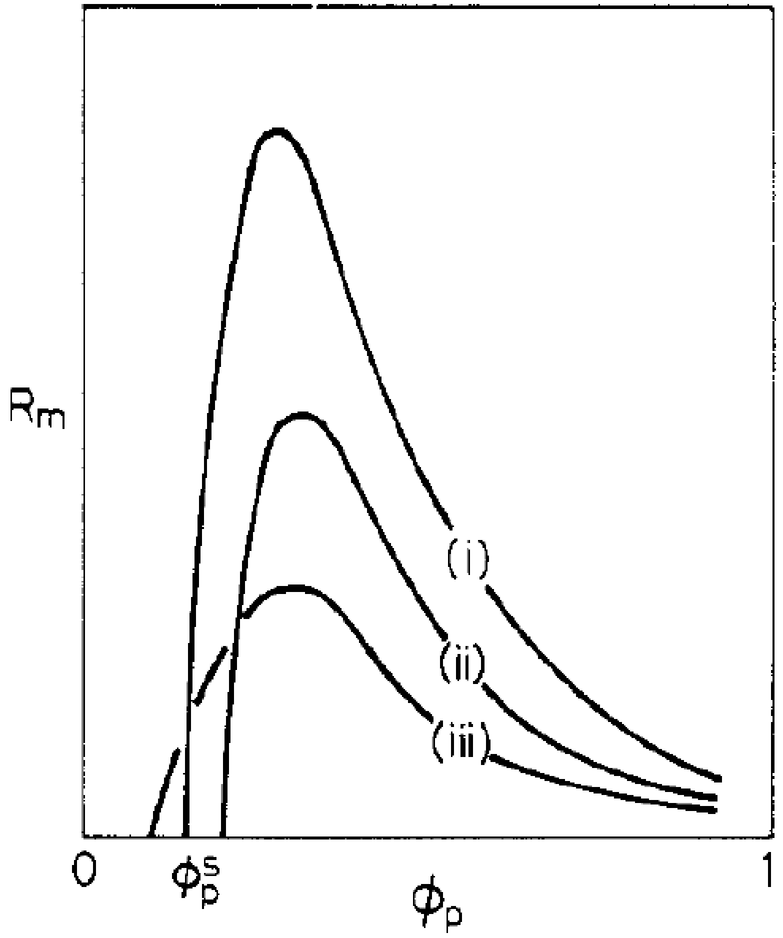

Figure 2.17 Concentration dependence of Rm, showing the effects of χ_m, blend ratio $\theta_A\theta_B$, and degree of polymerization N: (i) larger χ_m, $\theta_A\cong\theta_B$; (ii) small χ_m, $\theta_A<\theta_B$; (iii) large N.[76]

(Reprinted with permission from Ref. 76)

2.2.4.4 Phase separation of polymer blends with nanoparticles

The nanoparticles tend to be absorbed at the interface of two immiscible fluids if they have equal affinity to each component. It was first known since early 20th century as Pickering emulsions by using colloids to stabilize the emulsions for low molecular weight liquids. The liquid-liquid interface can be created by mechanical or ultrasound agitation and phase separation. If the liquid undergoes nucleation-growth phase separation, Pickering emulsions are expected to form. If the liquid forms bicontinuous structure with large interfacial area by spinodal decomposition, the chemically neutral colloids are absorbed to form a mono-layer of particles at the interface to freeze the structure, which is known as bicontinuous interfacially jammed emulsion gels (bijels). Dr. Cates first reported bijels in 2005 by computational simulation of the formation of solid-like liquid materials with continuous domains maintained by a jammed layer of colloid particles.[79] Figure 2.18 shows the sequence of bijels structure forming. The two liquids are colored in yellow and blue, and particles are green. The spinodal phase separation induced bicontinuous domains coarsen to reduce the interfacial energy. As coarsening proceeds, the interface absorbs and sequesters the colloid particles by sweeping the fluid phases. Shortly thereafter the bijels of 2,6-lutidine/water/ fluorescent silica colloids[80] and alcohol/oil/silica colloids[81] were formed experimentally.

Recent studies have developed polymer blends in both dispersed and bicontinuous structures with the particles packed densely at the interface. Therefore, the concepts of Pickering emulsion and bijels have been extended from low molecular fluids to polymer systems. The polydimethylsiloxane (PDMS) and polyisobutylene (PIB) blends with 7/3 ratio phase separated into droplet/matrix morphology according to nucleation and growth mechanism.[82] The addition of silica particles suppressed or slowed down coalescence because silica nanoparticles were accumulated at interface. The Janus particles of triblock terpolymer polystyrene-block-polybutadiene-block-poly(methylmethacrylate) (SBM) were found densely packed at the interface of Poly(2,6-dimethyl-1,4-phenylene ether) (PPE) and poly(styrene-co-acrylonitrile) (SAN).[83] Owing to this Pickering effect, the coarsening of the droplet was suppressed due to the stearic repulsion of Janus particles. The SBM Janus particles also stabilized the dispersed and bicontinuous morphologies of PS and PMMA blends via densely assembling at the interface. The bicontinuous structure of PMMA and SAN blends with PMMA modified silica particles coated interface was investigated by Composto as shown in Figure 2.19.[84] As the particles loading increased from 2 to 10 wt.%, the domain size was reduced from ~400nm to ~200nm.

The interfacially jammed nanoparticles act as excellent compatibilizers for polymer blends to reduce the phase separated domain size for both dispersed and bicontinuous domains, which is beneficial for improving the mechanical and optical properties. Furthermore, if selectively etching one of the phases, porous materials with partially exposed nanoparticle at the surface of the channels can be fabricated. The porous polymer materials act as the scaffold to support the nanoparticle to have high surface exposure area. The catalytic nanoparticles can catalyze the reaction of gas or liquid passing through the channels of porous materials, which promising for filtration and catalyst applications.

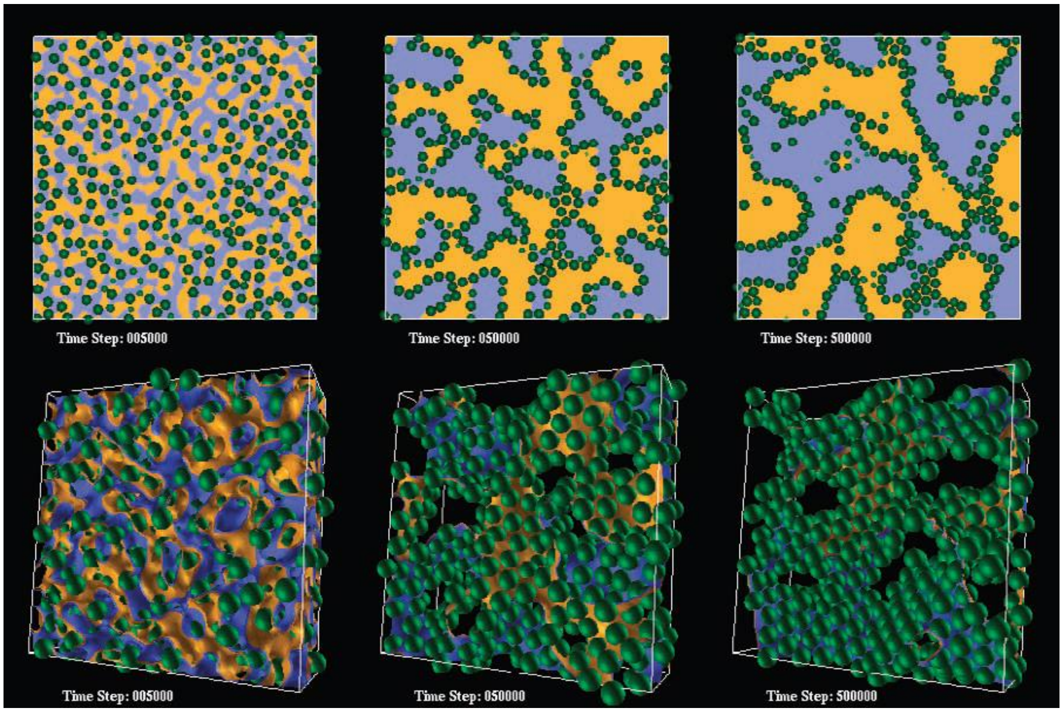

Figure 2.18 Time evolution of monodisperse neutrally wetting colloidal particles at volume fraction of 20% in a binary solvent following a quench.[79] (Reprinted with permission from Ref. 79)

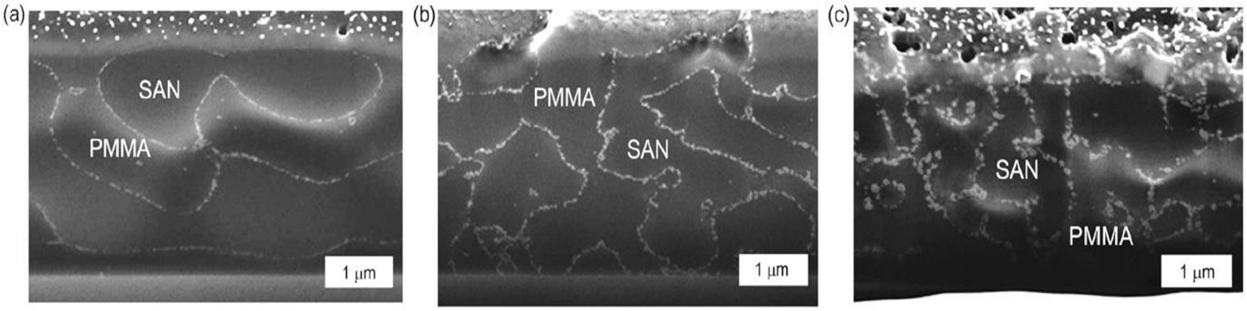

Figure 2.19 Cross-sectional SEM images of 2.5 mm thick PMMA : SAN films with (a) 2 wt% NP, (b) 5 wt% NP and (c) 10 wt% NP. Films are annealed at 195 oC for 24 h and exhibit a bicontinuous structure. As loading increases, the domain size decreases.[84] (Reprinted with permission from Ref. 84)

2.2.5 Roll to roll process for functional polymer films

The roll to roll process, as known as web processing, is one of the industrial manufacturing techniques to fabricate coating, film and devices in high volume manufacturing. It involves a flexible substrate which is transferred between two drums. The basic version of roll to roll processing line is composed of a loop of stainless steel belt wrapped over two drums with one of them connected to drive which can control the speed precisely and another one connected to a servo system to adjust the belt tension in order to ensure its constant flatness.[51] The belt needs an edge guide system to prevent the shift of belt during the operation by horizontal movement of the support drum. Many different support materials can be used as the substrate such as copper, PET films, silicon paper and other polymer films. Since roll to roll process is a substrate based manufacturing method, it provides a platform serving a full range of additive and subtractive process to build functional structures in a continuous way, [85] and these additional process can be vacuum, UV, thermal, external electric and magnetic field.[29, 64, 86] Roll to roll process has been to manufacture optical films, separation membranes, textiles, flexible solar panels, printed thin film batteries and flexible packaging of electronic component. Benefiting from the continuous production, roll to roll process can lower the cost of manufacturing, increase the volume rates of production and process efficiency through sequential application of successive layers on a web. Although the initial cost for setting up the system is high, it can be recovered by the economic advantages during production.

Roll to roll process provides a platform for a variety of techniques for nanomaterial fabrication such as external field assisted assembly, deposition, nanopatterning, imprint or soft lithography and laser ablation. Each technique will be discussed below:

a. External field

The application of external field such as electric field, magnetic field and thermal gradient zone on the roll to roll process line (Figure 2.20 a) has been developed by M. Cakmak,[86] which provides us a robust manner to manufacture multifunctional films including heat spreaders, ultrahigh density information storage systems, capacitors, fuel cell and battery membranes. This roll to roll process line can deposit liquid film on flexible substrate, and the nanoparticles in the liquid matrix can be organized into particle chains as it passes through the electric field zone as shown in Figure 2.20(b).[87] If the dispersed phase is diamagnetic or ferromagnetic particle, it can be aligned into columns as the film passes the magnetic zone as shown in Figure 2.20 (c).[88] Vertically oriented cylindrical PS-PMMA block copolymer nanostructure can be achieved as the block copolymer thin film pass through the thermal gradient zone. As shown in Figure 2.20(d), 92% vertical orientation factor can be achieved due to the sharp temperature gradient field with successful scale up on the roll to roll line.[89]

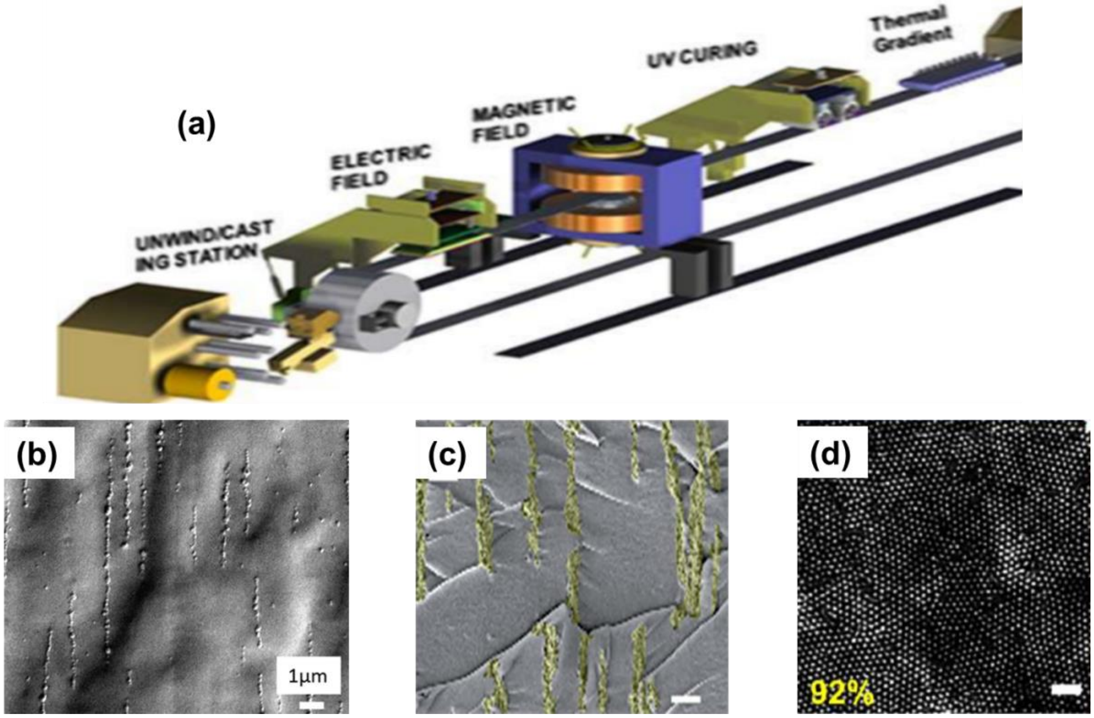

Figure 2.20 (a) roll to roll processing line combing electric field, magnetic field and thermal gradient zone,[86] (b) Aligned BaTiO$_3$ particles by E field[87] (c) Aligned Ni particles by magnetic field,[88] (d) morphology of PS-PMMA annealed in thermal gradient zone.[89] (Reprinted with permission from Ref. 86, 87, 88 and 89)

b. Deposition

Several deposition methods such as sputtering, evaporation, chemical vapor deposition (CVD) can be implanted on the roll to roll process line. Multilayer sputtering system can be easily achieved on roll to roll line as shown in Figure 2.21, where the entire line is loaded into vacuum to sputter different materials without inference among each different sputter source. As the substrate moves through the sputtering zone, the materials will be deposited on the substrate and the thickness of each material is affected by the process rate. While it is difficult for CVD to deposit multilayer in this method because the reactive gas barrier is needed within the vacuum system.

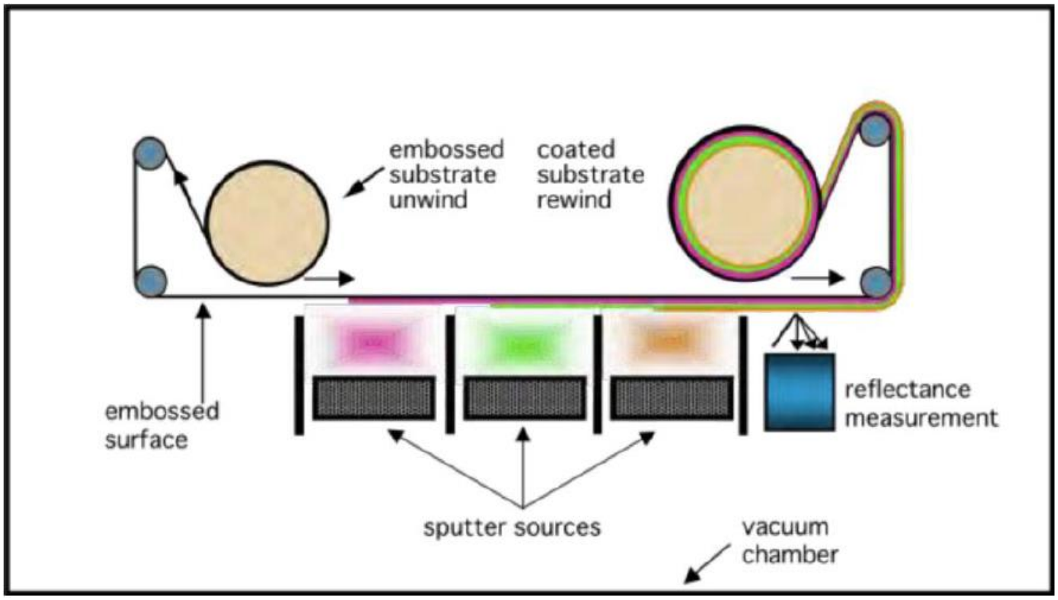

Figure 2.21 Inline vacuum coater and sputtering process.[90](Reprinted with permission from Ref. 90)

c. Nanopatterning

Roll to roll nanopatterning is a promising technique for high through nanopatterning for a wide range of device applications. The gravure printing, flexographic printing, and screen printing techniques are described below. Gravure printing is a type of printing process to engrave the image onto a carrier. The rotary patterned cylinder is coved with ink, and the excess ink is cleaned off by dr. blade leaving the cavities filled with ink as shown in Figure 2.22. The plate cylinder contacts with the compression cylinder to print the ink to the substrate. Gravure printing works well for low viscosity ink printing and high speed printing (up to 15m/s).[91] Flexographic printing transfers the ink via direct contact of the soft printing plate cylinder and substrate, whose ink is provided by anilox cylinder with engraved micro cavities on the surface (Figure 2.22). The ink on anilox roller is supplied by the fountain roller which is immersed in the ink batch. There’re two screen printing methods: flatbed screen printing and rotary screen printing. In flatbed screen printing, the squeegee swipe the ink on the mesh and the ink will penetrate into the opening of mesh. Then the mesh is lifted up leaving the patterns with same feature as the mesh opening on the substrate. The screen rotates at the same speed as the substrate and the ink is pushed through the opening of the mesh to the substrate. The printing speed can be larger than 100 m/min for rotary screen printing, and 0-35 m/min for the flatbed screen printing. [91]

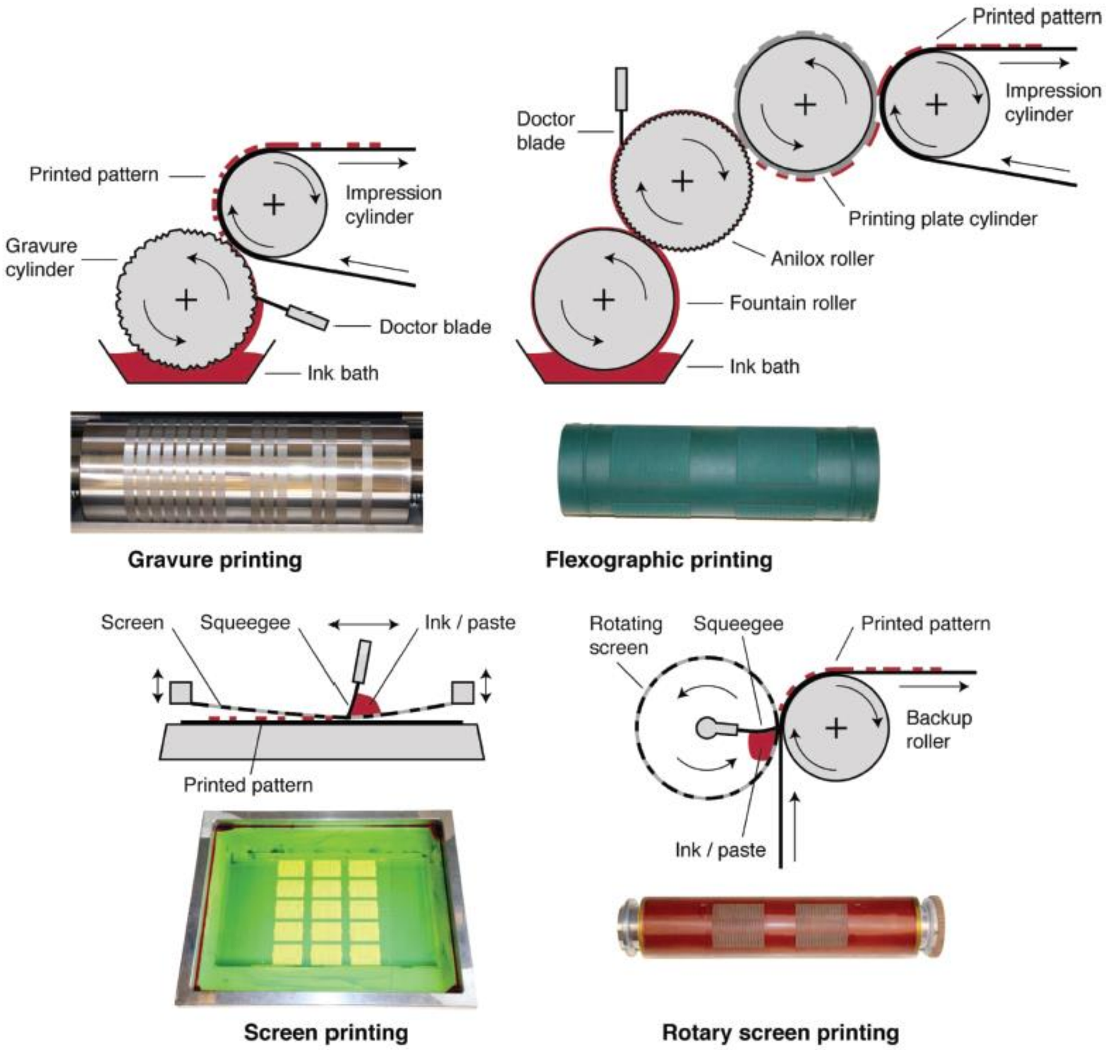

Figure 2.22 Schematic illustration of printing techniques with permanent printing forms, namely gravure printing, flexographic printing, and screen printing in flatbed or rotary design. Underneath each illustration is a picture of a corresponding printing form.[91] (Reprinted with permission from Ref. 91)

d. laser ablation

Laser ablation on roll to roll process line can produce ablated polyimide or PET substrate for flexible electronics. This technique can write on the polymer film directly using high power laser by breaking molecular bond into short units. The amount of material to be broken can be tailored by adjusting the energy density, wavelength and pulse width of laser.

2.3 Electric field assisted assembly

Functional polymer nanocomposite films with organized nanoparticle chains or phases can be manufactured on roll to roll processing line if an external electric field zone was implanted on it as stated in the section above. The orientation or alignment of dispersed phase or nanoparticles in the polymer matrix enhances the mechanical, thermal or electrical properties of resulting nanocomposite. In this section, the fundamental of particle or phase organization under electric field and previous studies will be described below.

2.3.1 Forces acting on a particle under electric filed

The particles are polarized to form “pearl chain” structures due to attractive electrostatic force. As the particles move under electric field, the hydrodynamic force resists the motion of the particles. During the drying of the casting film, the shrinkage forces forms dramatically at the end of the drying. All these forces are discussed in detail in the following.

A. Electrostatic forces.

a. non-conductive particles

Assuming that the electric field around the induced dipole doesn't affect the neighboring particles' field, the polarization of a particle is regarded as a point dipole locating at the center of the particle. Point-dipole approximation provides us a simple and reasonable method to analyze the inter-particle interaction forced in the dielectrophoresis.

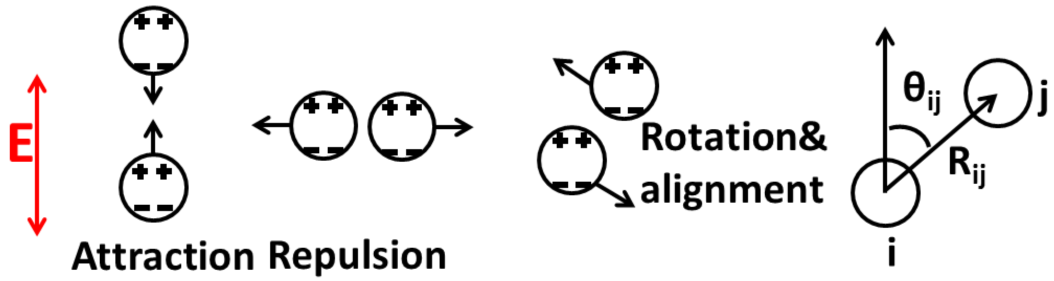

Figure 2.23 Electrostatic interaction between dipoles i and j in electric field.

As the electric field is applied to the composite solution in "Z" direction, the particles are polarized to form dipole as shown in Figure 2.23. If the angle between the line of particles' center and Z direction is 0 degree, the attracting force between the dipole can be expressed generally in the following equation:

$$F = \frac{3}{8}\pi\varepsilon_0\varepsilon_m d^2\beta^2 {E_0}^2 \left(\frac{d}{R_{ij}}\right)^4 \tag{2.44}$$

where ε_0 is the permittivity of the free space, ε_m is the dielectric constant of the matrix, d is the diameter of the particles, E_0 is the electric field strength, the R is the distance of two neighboring particles,[92] and Clausius-Mossotti factor $\beta = (\varepsilon_p - \varepsilon_m)/(\varepsilon_p + 2\varepsilon_m)$.

If the angle between the line of particles' center and Z direction is not 0, and the attractive force on the particle i at the origin of the spherical coordinate system by another particle j at (R_{ij}, θ_{ij}) (Figure 2.23) can be expressed as:[93]

$$F_{ij}^{el}\left(R_{ij}, \theta_{ij}\right) = \frac{3}{16}\pi\varepsilon_0\varepsilon_m d^2\beta^2 {E_0}^2 (\frac{d}{R_{ij}})^4[\left(3\cos^2\theta_{ij} - 1\right)e_r + (\sin 2\theta_{ij})e_\theta] \quad (2.45)$$

where e_r and e_θ are the unit vector in r and θ, respectively. If the diameter of the particles is different, only the magnitude of the attractive force alerts. This equation is valid if the dielectric constant is small (β→0) and the particles are separated greatly (R_{ij}/d→0).

When two particles with line of center parallel with electric field direction, the two particles will be attractive to each other. When the line of center of two particles is perpendicular to the electric field, they will repel to each other. When their line of center is at some angle with respect to the electric field, a torque will be acted on them to align them in the direction of electric field.[94]

If the highly polarized spheres are very close to another particle, equation becomes not accurate, because this case doesn't satisfy the point dipole assumption. In this case, the induced dipole creates disturbance field and this field can polarize another particle leading to electrostatic dipole beyond the dipole. Thus the magnitude of the attractive force will be much larger than the value predicted by equation 2.45. The attractive force can be given:

$$F_{ij}^{el}\left(R_{ij}, \theta_{ij}\right) =$$

$$\frac{3}{16}\pi\varepsilon_0\varepsilon_m d^2\beta^2 {E_0}^2(\frac{d}{R_{ij}})^4[\left(2f_{//}\cos^2\theta_{ij} - f_{\perp}\sin 2\theta_{ij}\right)e_r + (f_{\Gamma}\sin 2\theta_{ij})e_\theta] \quad (2.46)$$

where the $f_k$describes the effect of higher order multipole moments. $f_{//}$ and the electric field strength between the interparticle gap increases monotonically with $\varepsilon_p/\varepsilon_m$, so the attractive force between the nearly contacting spheres are very large.

b. Conductive particles in a matrix

If the particles are conductive, the free charges of particles will migrate to the particle/matrix interface. In DC field, the free charges accumulating at the interface screen the electric field in the particles, so the conductivity determines the polarization of the particles. In the AC field with high frequency, there’s no sufficient time for the free charges to respond, thus the polarization of the particles is controlled by the permittivity. In the medium frequency, the polarization of the particles is controlled by both permittivity and conductivity. The interaction force is a function of field frequency, permittivity and conductivity of both particles and matrix.

If the particles or the matrix is conductive, the absolute dielectric constant ε needs to be replaced by the complex permittivity $\varepsilon^* = \varepsilon - i\frac{\sigma}{\omega}$ where σ is the conductivity, ω=2πf, f being the frequency of the applied electric field.[95] The Clausius-Mossotti factor can be expressed as follow:

$$\beta^* = (\varepsilon_p^* - \varepsilon_m^*)/(\varepsilon_p^* + 2\varepsilon_m^*) \quad (2.47)$$

The Clausius-Mossotti factor is frequency dependent, and its value when the frequency is 0 and ∞ can be given as below:

$$\beta_0 = \frac{\sigma_p - \sigma_m}{\sigma_p + 2\sigma_m} \tag{2.48}$$

$$\beta_\infty = \frac{\varepsilon_p - \varepsilon_m}{\varepsilon_p + 2\varepsilon_m} \tag{2.49}$$

It can be concluded that at the low frequency limit of 0, the polarization is dominated by the conductivity ratio, and the polarization is determined by the dielectric constant ratio at the high-frequency limit of ∞.

The attractive force between the dipoles can be determined as: [94, 96]

$$F_{ij}^{el}(R_{ij}, \theta_{ij}) =$$

$$(f_{\Gamma} \sin 2\theta_{ij}) e_\theta] \qquad (2.50)$$

where $E_{rms} = E_0 / \sqrt{2}$, and the effective Clausius-Mossotti factor is

$$\beta_{eff}^2(w) = \beta_d^2 \frac{[(wt_{mw})^2 + \frac{\beta_c}{\beta_d}]^2 + (wt_{mw})^2 [1 - \frac{\beta_c}{\beta_d}]^2}{[1 + (wt_{mw})^2]^2} \tag{2.51}$$

where $\beta_d = (\varepsilon_p - \varepsilon_m)/(\varepsilon_p + 2\varepsilon_m)$, $\beta_c = (\sigma_p - \sigma_m)/(\sigma_p + 2\sigma_m)$, $t_{mw} = \varepsilon_0 \frac{\varepsilon_p + 2\varepsilon_m}{\sigma_p + 2\sigma_m}$

B. Hydrodynamic resistance

The electric field induced dipole-dipole attractive forces have to overcome the hydrodynamic resistance to make the motion and organization of the particles in the matrix possible. Particles are much larger than the molecules of the matrix, so the matrix can be regarded as a continuum. The Reynolds number is very small, because the particles are very small and the matrix is relatively viscous. Thus the hydrodynamic resistance can be described by the Stokes equations as follow:

$$F_i^{hyd} = -3\pi\eta_m dU \qquad (2.52)$$

where, η_m is the viscosity of the matrix and U is the shear rate of the ith particles.

C. Brownian forces

The particles experience the Brownian forces due to the thermal motion of the matrix, so the Brownian forces make the particles random in the matrix. The thermal force experienced by the particles is zero mean for long time scales. The Brownian force can be give as follow:

$$< F^B(t)F^B(t+t') \geq 12\pi\eta_m dkT\delta\delta(t') \qquad (2.53)$$

D. Short range of repulsive forces

The particles are not contacting each other, because the particles are separated to some distance by the repulsive force, including Born repulsion, steric or solvation forces. These short range repulsive forces are modeled as hard sphere interaction. The short range repulsive forces can be expressed in two forms:

$$F_1^{rep}(R_{ij}) = -F_0\exp[-100\left(\frac{R_{ij}}{d} - 1\right)]\, e_r \qquad (2.54)$$

$$F_2^{rep}(R_{ij}) = -F_0\left(\frac{R_{ij}}{d}\right)^{-n}\, e_r \qquad (2.55)$$

where $F_0 = \frac{3}{16}\pi\varepsilon_0\varepsilon_m d^2\beta^2{E_0}^2$, typically 5 < n < 37. The first equation is in exponential repulsion and the second one includes the power-law repulsion. Simulation results show that the pearl chains are thicker than one particles diameter (multi particle width columns) in the case of the exponential repulsion equation. On the contrast, the peal chains shows only single particle wide chains in the case of the inverse power law form if the exponent is small. For exponential repulsion system, there is a relative minimum in the potential energy alongside the strand. Nevertheless, there’s no minimum for the power law system with small exponent. If the exponent is sufficiently large for revealing the relative minima, multiple particles thick strands can be produced.

E. Stress induced by constrained drying

The polymer solution is deposited on a substrate, and the volume of this solution film will shrink due to the solvent evaporation. The area of the film is constrained on the substrate, so only the thickness shrinks. At the early stage of the drying, there’s no shrink stress which is relieved by the viscous flow of the polymer solution[97]. As more solvent evaporates, the film becomes solid enough to support the elastic stress. [98] The film stress starts grow after a critical point at which the glass transition temperature of the coating is equal to the drying temperature.[99] The stress in film can be calculated as[98]

$$\sigma = \frac{2E_s {t_s}^2}{(1-v_c)6\varepsilon t_c} \tag{2.56}$$

where σ is the film stress, E_s is the modulus of the substrate, t_s is the thickness of substrate, v_c is the Poisson’s ratio of the coating, t_c is the thickness of film and ε is a radius of the curvature.[99]

The drying of polymer solution is non-uniform in both vertical and lateral direction. For solution casting films, the edge of the solution film dries faster due to less resistance to vapor phase transport and relatively thinner thickness. [100] For the solution film in the dish or pocket cell, the center dries faster than the edge.[101] Out-of-plane compression[100] stress appears near the edge of the solution film for solution casting films.[102] As the solvent evaporates, the drying front grows towards to the center of the film. Thus the out-of-plane compression stress grows in the whole films during the drying, and it causes the pearl chain to tilt.

F. Total Forces acting on the particles

When the electric field is applied to the particle suspension, the total force acted on the particles includes electrostatic force, hydrodynamic resistance, Brownian forces and short range repulsive force. Whether the particles can form pearl chains depends on the electrostatic force is larger than all the resistance. The ratio of Brownian force to the electrostatic force is as follow:

$$\frac{F_B}{F_E} \sim 0\left(\frac{kT}{\varepsilon_0 \varepsilon_m d^3 \beta^2 {E_0}^2}\right) \tag{2.57}$$

So the Brownian force can be negligible compared to the electrostatic force.

Based on the point dipole model, the ratio of the electrostatic force to the hydrodynamic force is given:

$$\frac{F_E}{F_{hydro}} \sim \frac{\varepsilon_0 \varepsilon_m d \beta^2 {E_0}^2}{8 \eta U} \tag{2.58}$$

For the experiments in this work , ε_m=2.5, d=500nm, E_0=2kV/mm, U[103] is at the scale of 10μm/s. The calculated viscosity should be smaller than 0.5 Pa*s to make the electrostatic force larger than the hydrodynamic forces. This is not consistent with experiment results. The reason is that the point dipole model is only valid if $\frac{d}{R_{ij}} \rightarrow 0$ and β→0. The actual electrostatic force is much larger, because the local field strength is very large when the particles are nearly touching.

The ratio of the electrostatic force to the short range repulsive force is given as:

$$\frac{F_E}{F_{rep}} \sim \frac{2(\frac{d}{R_{ij}})^4}{\exp[-100\left(\frac{R_{ij}}{d}-1\right)]} \tag{2.59}$$

For this case, the ratio is around 0.35<1, which is due to the limitation of point dipole model. Zukoski[93] reported that the time needed to form pearl chains could be calculated by $t = \frac{16\eta}{\varepsilon_0 \varepsilon_m \beta^2 {E_0}^2}$, thus varying these parameters will affect the time it takes to obtain the chain structure, within the scale of 10-100ms.

2.3.2 Electric field assisted assembly of particles

Many studies have been carried out on the electric field assisted assembly of various particles or phase in thermoplastic or thermoset polymer matrix including particles with dielectric and electrically conductive particles. The typical procedures to prepare the nanocomposite with electric field assisted assembled particles are below. The particles are first uniformly distributed the polymer/solvent solutions, polymer melts and thermal or UV curable precursors by using high speed mixing, sonication or other dispersion methods. An insulating plane such as glass slide with two parallel electrodes is the most commonly used setup for electric field aligned. The composite solutions are poured into the gap between the two electrodes and the electric field is applied between them. The particles are generated with dielectric forces to overcome the drag force of viscous polymer medium and undergo two steps of motion under the electric field. The anisotropic particles rotate themselves with the long axis parallel to the electric field direction in most cases and attract each other to form particle chains in field direction. Since the particles are aligned into chain in the plane of the film rather than the thickness direction, the kinetic of the alignment can be easily observed by optical microscopy. The liquid polymer matrix needs to be solidified to freeze the structure of particle chains by solvent evaporation, cooling and UV or thermal curing methods.

2.3.2.1 Electric field alignment of dielectric particles

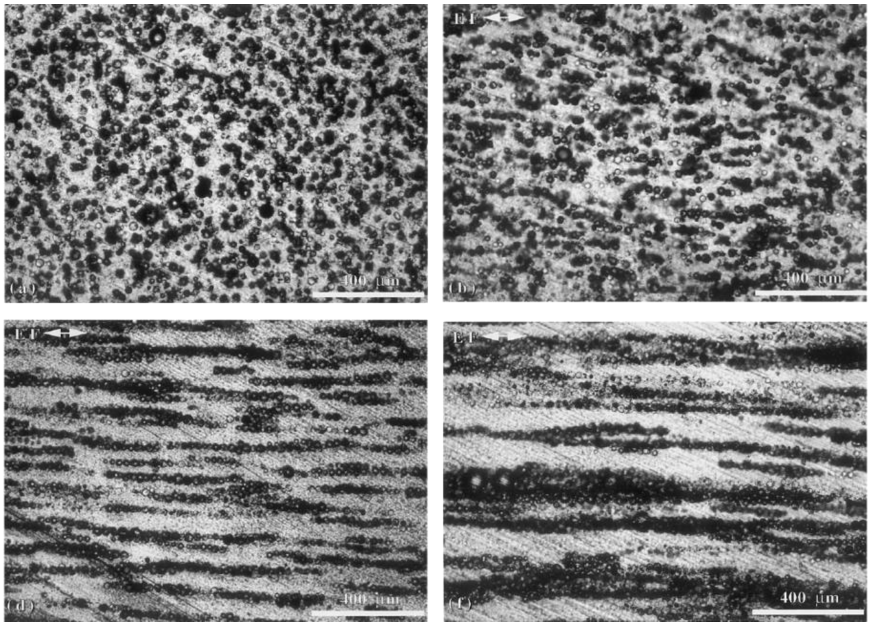

Figure 2.24 Optical micrographs of aligned glass spheres (10 vol%) with narrow size distribution, polymerized after: (a) 0 s, no alignment; exposed to electric field of 0.9 KV/mm for (b) 1 s and (c) for 1 min (d) for 4 min.[104] (Reprinted with permission from Ref. 104)

The dielectrophoretic force is proportional to the dielectric permittivity contrast between particles and matrix according to the equation 2.44, so strong electric field strength is needed for the alignment of dielectric particles with relatively low dielectric permittivity such as glass bubbles (dielectric permittivity is 6.9). E. Robertson[104] studied the alignment kinetics of glass bubbles with 25 µm diameter in photo curable matrix under 0.9kV/mm electric field strength by optical microscope as shown in Figure 2.24. It was clearly seen that the glass bubbles form very short chains after applying electric field 1s and the length of the chains grows and doubles after 1 minute. After 4 minutes, the single particle chain joins together into strings, so the alignment happens very fast under the electric field. Zhang[105] studied the alignment of glass bubble in polydimethylsiloxane (PDMS) in thickness direction and the aligned composites show enhanced compression modulus compared to the composites with random particle. The in-plane alignment of barium titanate particles with high dielectric permittivity (2000) in PDMS under electric field was also studied by E. Roberson. Relatively, and lower electric field strength (0.27 kV/mm) is needed to achieve the alignment of barium titanate particles due to its higher dielectric permittivity resulting in stronger dielectrophoretic forces. The particle chains also grow longer and coarsen thicker with the time of applying electric field. Batra[87] investigated the chaining and alignment of barium titanate nanoparticles in thickness direction of PDMS nanocomposite film by applying electric field. The barium titanate particles (100nm diameter) form discreet rows of particle chains in thickness direction instead of coarsened particle strings. The nanocomposites with aligned particle chains showed around 30% increase of dielectric permittivity than the random nanocomposites at the same loading of particles, which was useful for capacitor applications.

2.3.2.2 Electric field alignment of conductive particles

The dielectrophoretic force is proportional to the square of polarizability of the particle in the matrix which is given by the real part of Clausuis-Mossotti factor β ($0<\beta<1$) as mentioned above in equation 2.48. In the case of conductive particles such as gold and silver, $\beta=1$ due to zero internal electric field reduced by the redistribution of conduction bad electrons continually inside the particles.[106, 107] Therefore, the dielectrophoretic force that act on the conductive particles is much stronger than dielectric particles to make them easier to align into particle chains under the electric field. The gold colloid nanoparticles (25nm) were uniformly distributed in the matrix due to the repulsive interactions between them to prevent agglomeration as shown in Figure 2.25(a). After applying electric field, the dielectrophoretic force acting on the gold nanoparticle drives them to form gold microwires with 400 nm diameter and the particles are packed closely together as shown in Figure 2.25(b) and (c).[107]

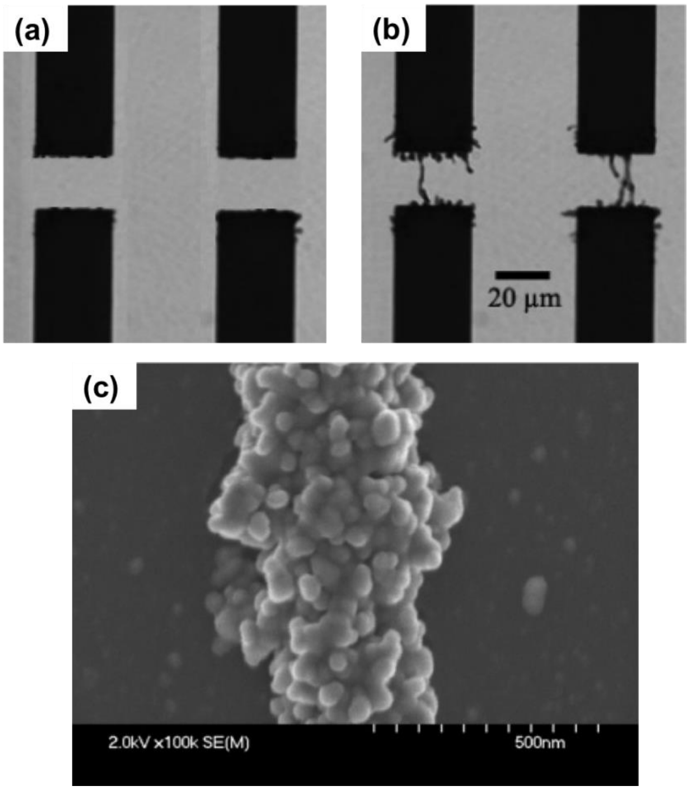

Figure 2.25 Gold microwires grown in a 20 μm electrode gap. (a) Before applying voltage, no wire growth (b) Applying voltage 7 V RMS results in the formation of wires, (c) SEM morphology of the wire grown from 25 nm diameter gold nanoparticles.[107] (Reprinted with permission from Ref. 107)

2.3.2.3 Effect of particle shape on the alignment

Previous work discussed above is all about the alignment of spherical particle under the electric field due to the dielectrophoretic force. However, particles with non-spherical shape such as rod, wires and flakes are also widely used to prepare nanocomposites. The principal axes of these particles with non-spherical shape must be parallel to the applied electric field direction so that the induced dipole moment is parallel to the field direction.

As a result, the non-spherical particles experience the orientation under the dielectrophoretic torque till stable state first, and then the particles are aligned into chains due to dipole-dipole interactions. In the presence of electric field, the spheroidal particles are induced dipoles as shown in Figure 2.26. If the dipole is very small compared to the scale of non-uniformity of applied electric field strength E_0, the dielectrophoretic force and toque can be approximated as follow:[108]

$$F \cong (p * \nabla)E_0 \tag{2.60}$$

$$T_q \cong p \times E_0 \tag{2.61}$$

$$p = \frac{4\pi abc}{3}(\varepsilon_p - \varepsilon_m)E^{-} \tag{2.62}$$

where F is dielectrophoretic force, p is dipole moment of spheroidal particle having semi-major axes a, b and c, E_0 is applied electric field strength, T_q is torque, E^- is the uniform electric field internal to the particle, which is not parallel to E_0 in general.

$$E_x^- = E_{0,x}/[1 + (\varepsilon_p - \varepsilon_m)L_x/\varepsilon_m] \tag{2.63}$$

where $L_x \equiv \frac{abc}{2}\int_0^\infty \frac{ds}{(s+a^2)R_s}$,where $R_s \equiv \sqrt{(s+a^2)(s+b^2)(s+c^2)}$. The internal field for y and z components has similar expression as in x direction. Equation 55 is substituted into equation 54 and 53, the torque in x component can be give below[108]

$$T_x = \frac{4\pi abc\left(\varepsilon_p - \varepsilon_m\right)^2 (L_z - L_y)E_{0,y}E_{0,z}}{3\varepsilon_m[1 + (\frac{\varepsilon_p - \varepsilon_m}{\varepsilon_m})E_y][1 + (\frac{\varepsilon_p - \varepsilon_m}{\varepsilon_m})E_z]} \tag{2.64}$$

To generalize, the electric field components are assumed all positive and a>b>c, in which case $0<L_x< L_y< L_z<1$. Therefore, $T_x<0$, $T_y>0$ and $T_z>0$, meaning that the dielectrophoretic torque tends to orient the principal axes of particle along the electric field direction.

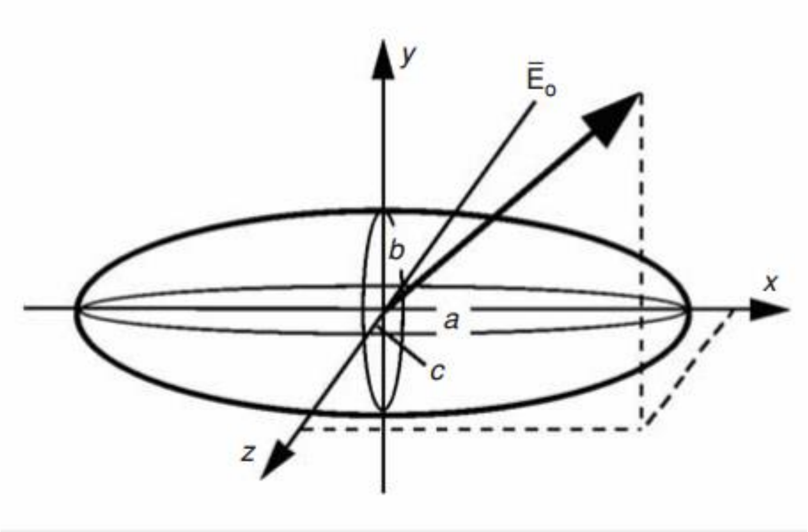

Figure 2.26 A spheroidal dielectric particle in a uniform electric field. The semimajor axes are a > b > c. The particle experiences an electrical torque that seeks to align the particle with any of the axes, but only alignment along the longest axis (a) is stable.[108] (Reprinted with permission from Ref. 108)

The alignment of plate-like particles with low dielectric permittivity such as montmorillonite clay particles were demonstrated by S. Batra.[109] The kinetic of particle orientation and alignment was characterized by real-time birefringence change due to clay's optical anisotropy upon applying electric field. At low voltage, the birefringence increased slowly and reached a plateau eventually due to the drag flow resistance of the resin. The rate of birefringence increase was much faster and the increases of birefringence happened immediately at high voltage. The orientation and alignment of clay particles were also observed by polarized optical microscopy with first order red wave plate. With the application of the electric field parallel to the slow axis of red wave plate, the color of clay particle changed from yellow to blue slowly due to the rotation of particles and the particles formed blue chains as shown in Figure 2.27. The electrically conductive flaky particles, graphene nanoplatelets, were vertically aligned in epoxy polymer under electric field.[41] The basal plane of graphene nanoplatelets was oriented along the electric field direction and then aligned into conductive chains in thickness direction. The nanocomposites with aligned graphene nanoplatelets showed significantly improved electrical and thermal properties with 7-8 orders of magnitude improvement of electrical conductivity and 60% increase of thermal conductivity in alignment direction.[41]

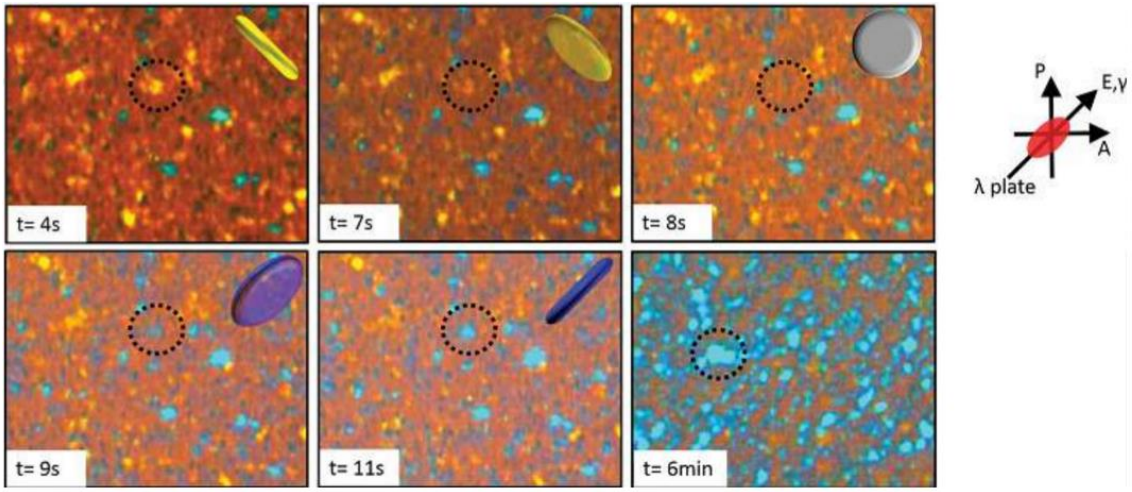

Figure 2.27 Time sequence images showing rotation of particles in the electric field (40 V/mm) with the electric field parallel to the slow axis of red wave λ plate.[109] (Reprinted with permission from Ref. 109)

Halloysite nanotubes, tubular clay mineral nanoparticles with low dielectric permittivity (ε=7.9),[110] were aligned in photo curable resin by the application of electric field. The kinetics of the orientation and alignment of halloysite nanotubes were characterized by real-time change of birefringence after applying electric field.[111] It was found that the orientation of the nanotubes takes place in less than 1s after applying electric field. The cross-sectional morphology showed that all the halloysite nanotubes were oriented with the long axis of the tube along the field direction, and the nanotubes were aligned to form chains in head and tail. The movement of lead zirconate titanate (PZT) fibers with high dielectric permittivity in thermal curable polyurethane under electric field was investigated by D. Ende.[36] Upon application of the electric field, the PZT fibers rotated with their long axes along electric direction then coalesced into chains. It was found out that the orientation angle of individual fibers inside the fiber chains increased with the aspect ratio of fibers because the low aspect ratio fibers connected to adjacent particle corner to corner resulting in off-axis. The single wall carbon nanotubes (SWNTs) with 2 nm diameter and 5-15 μm length dispersed DI water were exposed to electric field, and the SWNTs were rotated and aligned along electric field lines and connected two electrode as shown in Figure 2.28.[112] The device with dielectrophoresis aligned SWNTs can be used as a pH sensor due to the pH sensitive electrical conductivity of SWNTs.

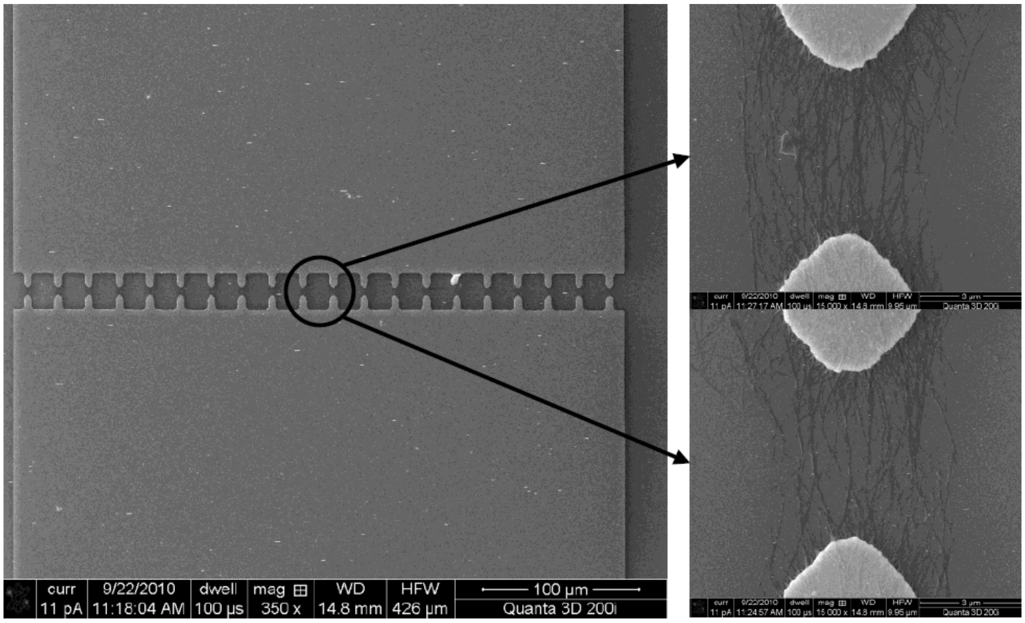

Figure 2.28 SEM images of the sensor structure and the dielectrophoretically aligned SWNTs.[112] (Reprinted with permission from Ref. 112)

2.3.3 Electric field assisted assembly of polymer blend

The phase morphology of polymer blends has great effect on the mechanical, electrical, thermal, chemical and other properties. If one phase is oriented to form anisotropic morphology, the polymer blends are expected to form anisotropic mechanical, electrical or optical properties. Electric field has been used to control the morphology by orienting one of the phases in many polymer blend systems including two[113, 114] or three phases system.[115, 116] One of the conclusions is that no apparent droplet deformation or orientation can be observed for a blend system in which there’s almost no dielectric constant mismatch between the dispersed phase and matrix such as polystyrene/polybutadiene/toluene system.[117]

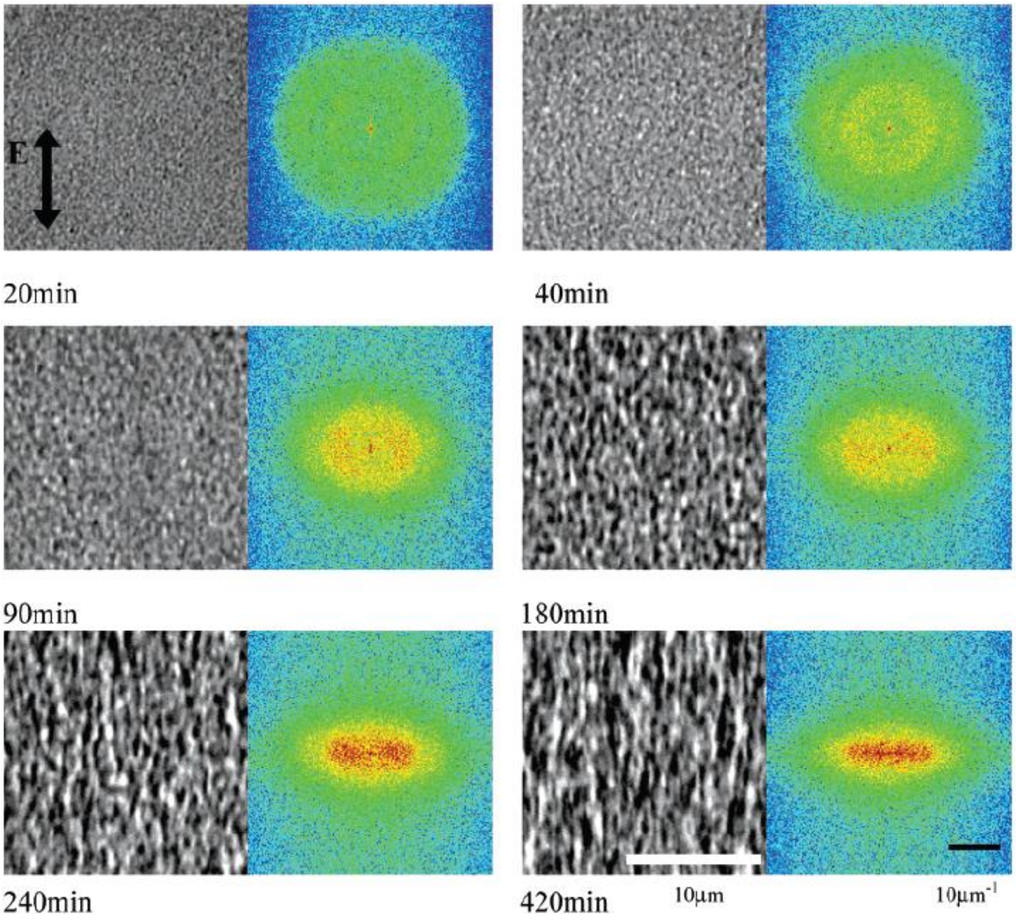

Figure 2.29 Time-evolution of phase-separated structures and corresponding 2D-FFT power spectra obtained for a P2CS/PVEM (30:70) blend containing $LiClO_4$ (0.5 wt. %) under an electric field (AC 11.2 kV/cm, f =10 Hz) at 118 °C.[118] (Reprinted with permission from Ref. 118)

The two phase blends of Poly(2-chlorostyrene) (P2CS)/poly(vinyl methyl ether) (PVME) with 30:70 ratio was applied to 11.2 kV/cm electric field at 118 ^{o}C to study the time-evolution of morphology as shown in Figure2.29.[118] In the early stage of phase separation, the morphology was isotropic evidenced by the circular shape of 2-dimensional Fourier transform (2D-FFT) spectra. After 90 minutes, the shape of

2D-FFT spectra started changing into ellipsoidal from circular indicating the formation of anisotropic morphology. The morphology of aligned patterns became more and more obvious and coarsened with time, and the size of ellipsoids decreased meaning that the anisotropic degree increased.

The three phase blends of 50/50 PS/PVA in toluene blend were applied with electric field during solvent evaporation at two different field strengths. At weak field 2.3 kV/cm, the prolate ellipsoids of dispersed PVA phase were aligned to form chains in electric field direction (Figure 2.30(a)), which was very similar as the morphology of aligned nanoparticles. As the field strength was increased to 4.5 kV/cm, the ellipsoids were deformed further and fused together to form cylinder structures as shown in Figure 2.30(b).[119] However, the PS-rich droplet in 10/90 PS/PVA blend in toluene were elongated perpendicular to the field direction, and the elongated ellipsoid started to break up under 8 kV/mm as shown in Figure 2.30(c).

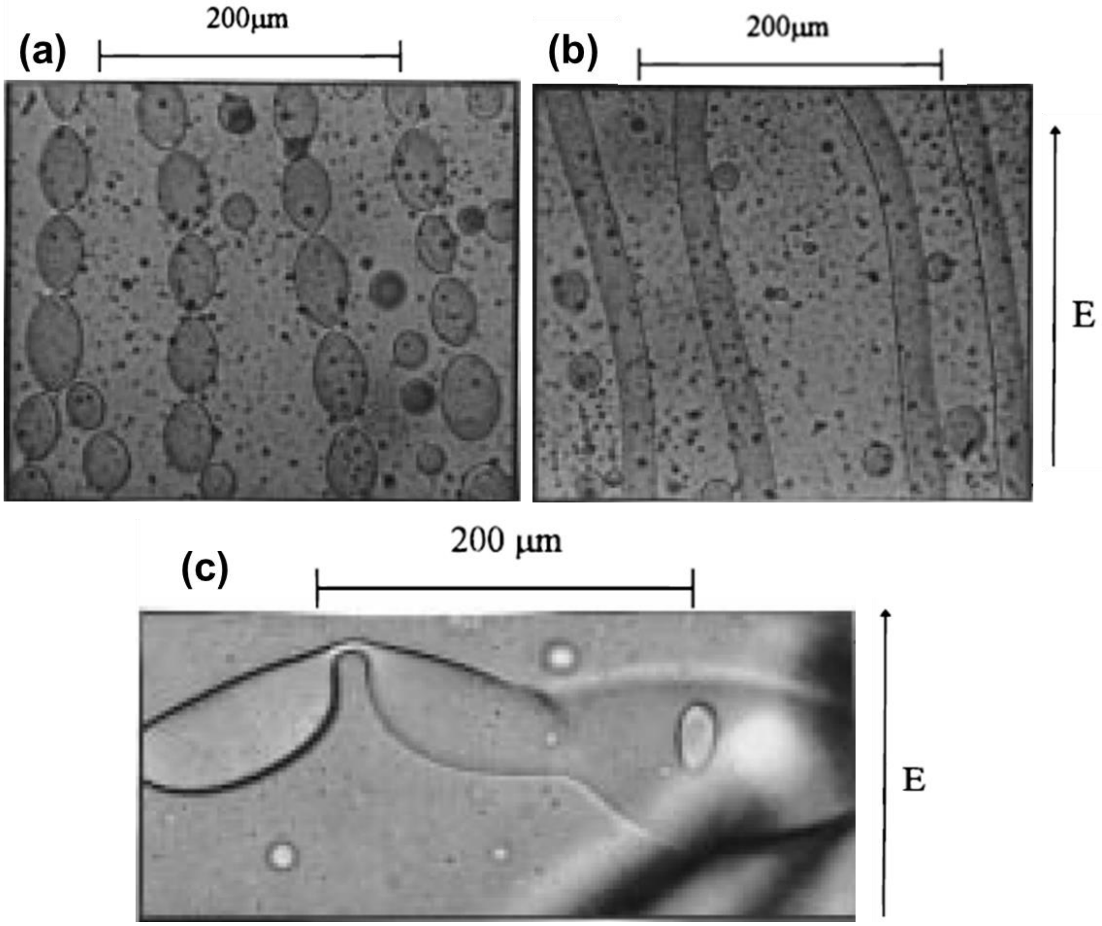

Figure 2.30 Electric-field-induced morphologies of 1/1 (w/w) PS/PVA in toluene during solvent evaporation: (A) at E=2.3 kV/cm; (B) at E=4.5 kV/cm, (c) Breakup of presumably PS-rich columns in a PVA-rich matrix at E= 8 kV/cm for 1/9 PS/PVA in toluene blend.[119] (Reprinted with permission from Ref. 119)

The difference of elongation direction was caused by the dielectric permittivity and conductivity difference between two polymers. The elongation of the dispersed droplet was along the electric field when the dispersed phase (PVA-rich) had higher dielectric permittivity and electrical conductivity than the matrix phase (PS) in the system discussed above. A discrimination function, Φ, was developed by Torza S. to predict the deformation direction of dispersed phase in three phases blend as below:[120]

$$\emptyset = S(R^2 + 1) - 2 + 3(SR - 1)(2M + 3)/(5M + 5) \qquad (2.65)$$

$$S = \frac{\varepsilon_m}{\varepsilon_p}, R = \frac{\sigma_m}{\sigma_p}, M = \frac{\eta_m}{\eta_p} \qquad (2.66)$$

where ε_m and ε_p, σ_m and σ_p, η_m and η_p are the dielectric permittivity, conductivities and viscosity of the matrix and dispersed phase, respectively. Thus the deformation direction can be predicted by the sign of Φ as follows: (1) the elongation is along the field direction to form prolate ellipsoid if $\Phi>0$, (2) there's no deformation for dispersed phase if $\Phi=0$, (3) the elongation is perpendicular to the field direction to form oblate ellipsoid if $\Phi<0$. As shown in Figure 2.31, the effect of dielectric permittivity and conductivity on the free charge distribution and deformation direction. There's no free charge distributed on the dispersed phase/matrix interface when $\Phi=0$, resulting in no deformation of droplet. When $SR < 1$, the hemisphere facing the negative electrode became negatively charged thus electric tangential stress inducing a pole-to-equator fluid deformation. The reverse happened when $SR > 1$, with opposite direction of electric tangential stress inducing an equator-to-pole fluid deformation.

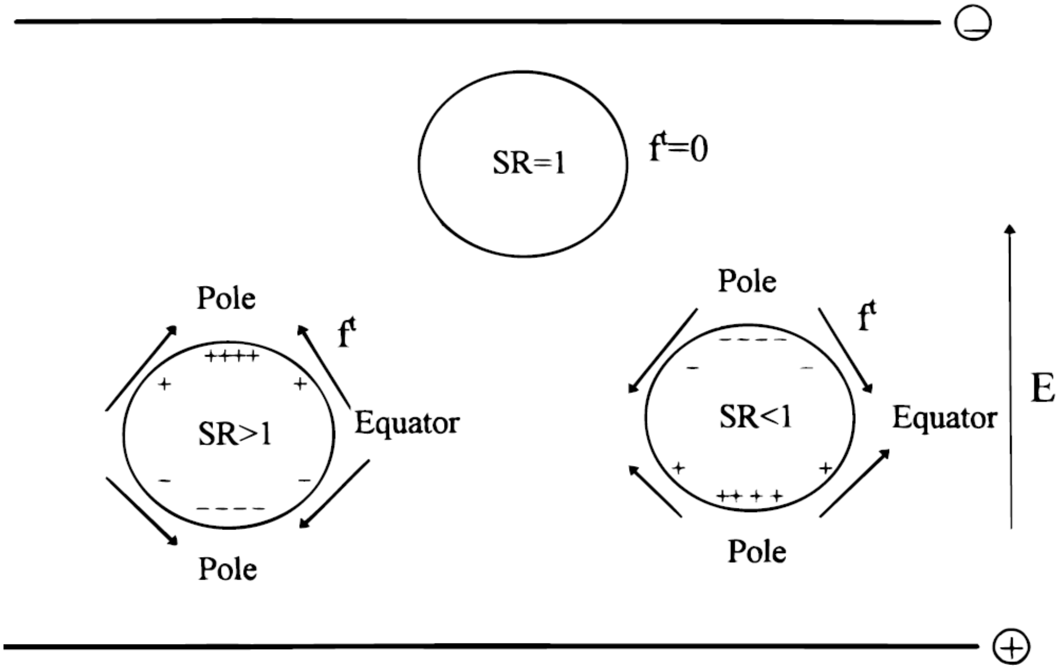

Figure 2.31 Instantaneous free charge distribution and the direction of the electric tangential stress at the interface in an electric field.[119] (Reprinted with permission from Ref. 119)

If the electric field strength was too high, the deformed ellipsoids started to break up as predicted by Carton and Krasucki.[121] The critical electric field strength of breakup of dispersed phase under strong electric field can be predicted as following equation:

$$E_{crit} = 600\left(\frac{2\pi\aleph}{\epsilon_m d}\right)^{\frac{1}{2}}\left(\frac{\epsilon_m}{\epsilon_m-\epsilon_p} - G_0\right)H_0 \tag{2.67}$$

$$G = \frac{1}{N^2-1}\left[\frac{N\cos^{-1}N}{(N^2-1)^{\frac{1}{2}}} - 1\right] \tag{2.68}$$

$${H_0}^2 = 2N^{1/3}A_0 \tag{2.69}$$

$$A_0 = 2N - 1 - N^{-2} \tag{2.70}$$

where E_{crit} is the critical electric field strength before break up, ℵ is the surface tension of droplet, d is the initial diameter, N is the ratio of major axis and minor axis of prolate spheroidal droplet. The major axis to minor axis ratio of droplet was shown in Figure 2.32 as a function of the expression$(\frac{\epsilon_m}{\epsilon_m-\epsilon_p} - G_0)H_0$. It was found out that, as this expression was beyond a critical value, N increased dramatically implying that the spheroidal droplet was not stable and could be broken up as the electric field strength was above the critical value.[121]

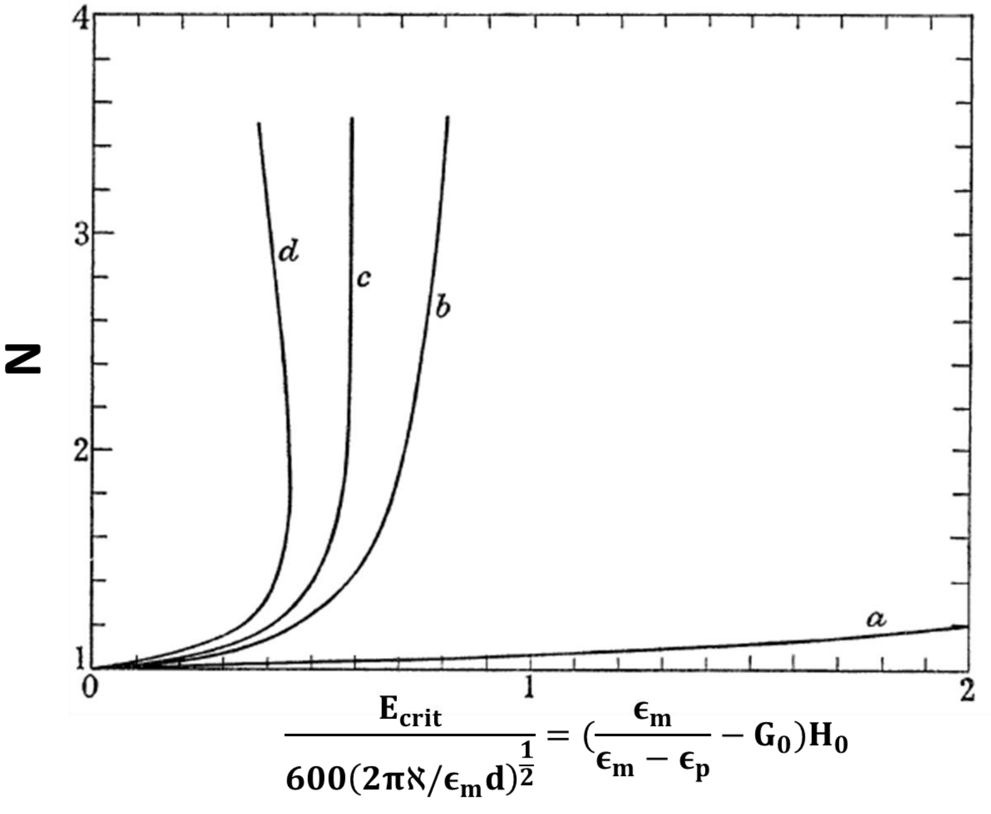

Figure 2.32 Elongation of dispersed phase under electric field. Curve (a) $\varepsilon_{p/}\varepsilon_m$ =0.5, (b) $\varepsilon_{p/}\varepsilon_m$ =11, (c) $\varepsilon_{p/}\varepsilon_m$ =21, (d) $\varepsilon_{p/}\varepsilon_m$ =∞.[121] (Reprinted with permission from Ref. 121)

CHAPTER III

ROLL TO ROLL CONTINUOUS MANUFACTURING MULTIFUNCTIONAL NANOCOMPOSITES BY ELECTRIC FIELD ASSISTED “Z” DIRECTION ALIGNMENT OF GRAPHITE FLAKES IN POLY(DIMETHYLSILOXANE)

A roll to roll continuous process was developed to manufacture large-scale multifunctional poly(dimethylsiloxane) (PDMS) films embedded with thickness direction (“Z” direction) aligned graphite nanoparticles by application of electric field. The kinetics of particle “Z” alignment and chain formation was studied by tracking the real-time change of optical light transmission through film thickness direction. Benefiting from the anisotropic structure of aligned particle chains, the electrical and thermal properties of the nanocomposites were dramatically enhanced through the thickness direction as compared to the nanocomposites containing the same particle loading without electrical field alignment. With 5 vol% graphite loading, 250 times higher electrical conductivity, 43 times higher dielectric permittivity and 1.5 times higher thermal conductivity was achieved in the film thickness direction after the particles were aligned under electrical field. Moreover, the aligned nanocomposites with merely 2 vol% graphite particles exhibit even higher electric conductivity and dielectric permittivity than the non-aligned nanocomposites at random percolation threshold (10 vol% particles), as the “electric field directed” percolation threshold concentration is substantially decreased using this process. As the graphite loading increases to 20 vol%, the aligned nanocomposites exhibit thermal conductivity as high as 6.05 W/m*K, which is 35 times of the thermal conductivity of pure matrix. This roll to roll electric field continuous process provides a simple, low cost and commercially viable method to manufacture multifunctional nanocomposites for applications as embedded capacitor, electromagnetic (EM) shielding and thermal interface materials.

3.1 Introduction

Multifunctionality in polymer based nanocomposites increasingly become essential for electronic applications. For instance, the applications of flexible displays[122], capacitive sensors[122], electromagnetic (EM) shielding[123], actuators,[11, 12] electrical stress control applications[15, 16] and high-charge storage devices[17-20] require electrically conductive polymer nanocomposites and high dielectric permittivity (high-k) materials. In addition, as the power density of electronics becomes higher, it can lead to overheating.[124] Efficient heat removal, herein, becomes crucial in order to retain the performance and reliability of electronics[125] and thus polymer nanocomposites with high thermal conductivity are needed for thermal interface material (TIM) to dissipate heat efficiently.

The inclusion of electrically conductive particles into polymer matrix may enhance the electrical conductivity, dielectric permittivity as well as thermal conductivity. For example, Dang et al.[42] fabricated poly(vinylidene fluoride) (PVDF)/Nickel (Ni) nanocomposites, and the electrical conductivity can reach 10^{-6} S/m at 100 Hz with 17 vol% of Ni particle. Its dielectric permittivity is increased to 400 at 100 Hz. Xue et al.[43] reported that PVDF/multi-walled carbon nanotube (MWCNT) nanocomposites with 6 vol% MWCNT can achieve about $5x10^{-4}$ S/m electrical conductivity and 1700 dielectric permittivity at 1 kHz. PVDF/exfoliated graphite nanoplate nanocomposites show $1.15x10^{-6}$ S/m electrical conductivity and about 2700 dielectric permittivity at 100 Hz with 1.01 vol% loading.[17] The electrical conductivity and dielectric permittivity of this nanocomposite film can even reach $2.3x10^{-3}$ S/m and $4.5x\ 10^{7}$ at 1 kHz with 2.4 vol% loading respectively, although the dielectric loss is also high (229).[17] With addition of 20 vol% loading of single wall carbon nanotube (SWNT), the thermal conductivity of high density polyethylene (HDPE) increases from 0.5 to 3.2 W/m*K.[126] Balandin et al.[127] prepared epoxy/graphene-multilayer graphene nanocomposites with 10 vol% loading, and the thermal conductivity can reach 5.1 W/m*K, which is 23 times higher than pure epoxy. Thus the inclusion of conductive nanoparticles into polymer is very effective way to prepare material with high dielectric permittivity, electrical and thermal conductivity.

Since the conductive particles in all the above studies were randomly dispersed in polymer matrix, they tend to be filled at high concentrations, typically beyond percolation threshold, to achieve meaningful enhancement in properties. At these higher loadings, other desired properties such as flexibility and transparency usually are detrimentally affected. One way to reduce this critical concentration is to use electric field to form "nanocolumns" of chains of nanoparticles in the field direction in polymer matrix. For instance, Knaapila[128] reported the use of electric field to align carbon nanocones in resin to form conductive chains, and the film exhibits at least 2-3 orders of magnitude enhancement in electrical conductivity along thickness direction compared with the film with random dispersed fillers. Electric field aligned epoxy/graphite flakes composite films exhibit up to 7-8 orders of magnitude higher of electric conductivity than randomly dispersed composites.[41] Since the percolation behavior of dielectric permittivity follows the percolation behavior of electrical conductivity for most of polymer/conductive particle composites,[42, 43] enhanced dielectric permittivity is also expected by the alignment of particles. In case of thermal conductivity, alignment of 5 vol% diamond particle in polysiloxane can achieve 145% enhancement of thermal conductivity, increasing from 0.128 to 0.301 W/m*K.[129] Therefore, the "Z" electric field assisted assembly of nanoparticles has significant effect on enhancing through-thickness dielectric permittivity, electrical and thermal conductivity. However, batch methods are used for most studies to fabricate nanocomposites with two electrodes contacting to the film directly, which is not suitable for mass production and industrial applications.

Aiming to manufacture nanocomposites with "Z" aligned nanoparticles in large scale, a roll to roll processing line equipped with an electric field zone assisting alignment was developed in our research group.[29, 86, 109, 130, 131] In this processing line, particles are aligned in polymer solution/precursor under the electric field as the cast UV curable monomer film containing nanoparticles passes through the electric field zone. The aligned particles are frozen by UV or thermal curing or solvent evaporation, and then the composite film moves out of electric field zone as the nanocomposite film continues along the film line. If a direct contact of top electrode with the composite film is used, this causes detachment difficulties following solidification. In order to eliminate this issue, an air gap between top electrode and film is introduced and this facilitated continuous manufacturing. Relatively low electric field is applied on the film compared to direct contacting method because the air gap acts as an insulating layer. Thus it's easier to achieve alignment for ceramic particles with high dielectric permittivity or electrically conductive particles.

In this paper, we report a new method of aligning graphite particles dispersed in PDMS by electric field. Graphite is used as the filler because it's electrically and thermally conductive. Moreover, it's naturally abundant and low cost carbon filler as compared with carbon nanotubes and graphene. The kinetic of "Z" alignment of graphite particles in PDMS precursor under electric field with air gap is studied by measuring optical light transmission and the aligned particles are frozen in the final film by thermal curing PDMS. The effect of aligned structures on the dielectric permittivity, electrical conductivity and thermal conductivity is investigated.

3.2 Materials and methods

The materials, batch method and roll to roll processing method are described in details as follow.

3.2.1 Materials

Natural graphite flaky nanoparticles (400nm-1μm) were obtained from US Research Nanomaterials, Inc. Polydimethylsiloxane (PMDS), Sylgard 184, was supplied by Dow Corning Co. and used as the matrix to prepare the nanocomposites. It is a thermally curable and solvent free resin, and can be cured in 20 minutes at 90 ^{o}C. Indium Tin Oxide (ITO) coated conductive glass purchased from Structure Probe, Inc. was used as electrode.

3.2.2 Batch production of nanocomposite film

The graphite nanoparticles were uniformly dispersed in the PDMS precursor by Thinky planetary centrifugal mixer. The curing agent was added to the dispersion with 1:10 ratio to the precursor. 15cm wide dr. blade was used to cast the suspension with 100 μm thickness on ITO coated glass (bottom electrode). The gap between the cast film and top ITO coated glass (top electrode) was controlled at 1 mm by using four spacers at the four corners of the ITO coated glass as shown in Figure 3.1. The AC electric field (100 Hz) was applied between the two electrodes for 40 mins and the film was heated to 90 ^{o}C by hot plate with the electric field on until the film was totally cured after 20 minutes.

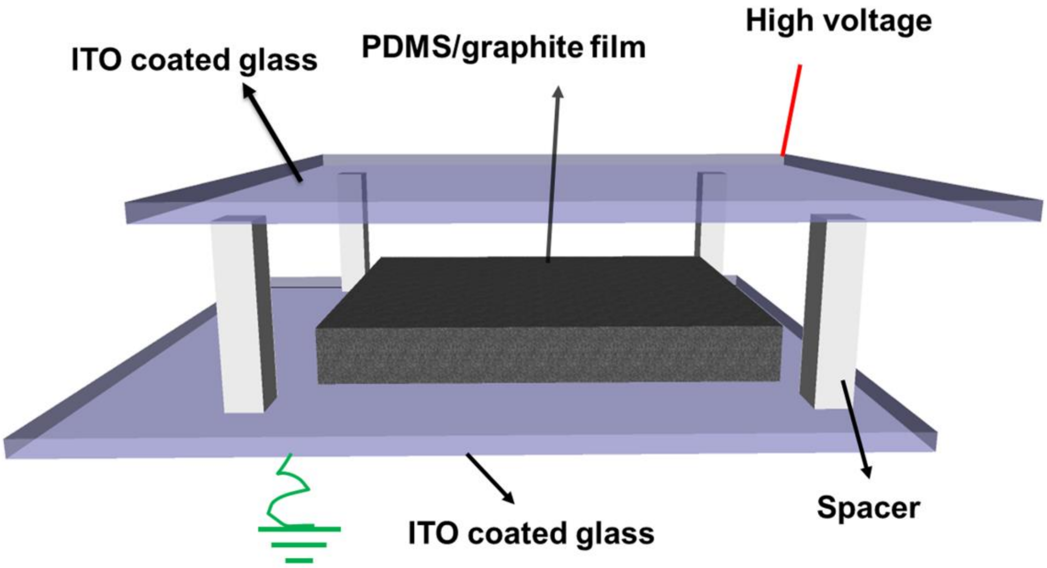

Figure 3.1 Set up for electric field assisted alignment with an air gap between the top electrode and film.

3.2.3 Roll to roll manufacturing of nanocomposite film

15 cm. wide dr. blade was utilized to cast the suspension on PET substrate on the roll to roll processing line assembled with electric field at speed of 50 cm/min. After the front of the film entering the electric zone, the speed was slowed down to 1 cm/min. The gap between the cast film and top electrode was set at 1mm. In electric field application portion of the R2R machine there are two temperature zones: (1) first cold zone maintained at room temperature; (2) the hot zone at 100 ^{o}C at downstream section of electric field. As the film passes through the electric zone, the graphite particles were aligned to form nanocolumnar chain structure in the first cold zone and the PDMS resin was cured the second hot zone

while preserving the nanostructure developed in the first zone and proceeded along the machine direction and collected continuously.

3.2.4 Characterization

The cross sectional morphology of PDMS/graphite nanoparticles nanocomposite films with and without alignment was characterized by SEM (JSM7401). The cured films were fractured in liquid nitrogen and sputter coated with silver before SEM characterization. The electrical conductivity, dielectric permittivity and dielectric loss were measured by 4192A LF impedance analyzer. 15mm × 15mm size of PDMS/graphite nanocomposite films were sputter coated with silver on both sides. The silver coated films were sandwiched by two electrodes to measure the capacitance with frequency sweeping from 1 kHz to 1MHz. According to the measured capacitance, the dielectric permittivity of film is calculated by the following equation:

$$\varepsilon_t = \frac{Cd}{\varepsilon_0 A} \tag{3.1}$$

where ε_t is the dielectric permittivity of film, C is the measured capacitance (Farads), d is the thickness (m) of film, ε_0 is the dielectric permittivity of free space (8.854×10^{-12} F*m^{-1}) and A is the area (m^2) of capacitor electrode. The PDMS/graphite nanoparticles nanocomposite film with 6 cm diameter and 1 mm thickness are used to measure the thermal conductivity by FOX 50 Series thermal conductivity analyzer.

3.3 Results and discussions

This section is divided into the kinetic of alignment, electrical conductivity, dielectric permittivity, thermal conductivity and roll to roll continuous processing.

3.3.1 The kinetic of alignment

The through thickness light transmission is low for the nanocomposite films with randomly distributed nanoparticle, as most of the light is scattered and/or absorbed by the randomly distributed highly absorbing fillers. If the nanoparticles are aligned into chains in "Z" direction to form "nanocolumnar" anisotropic structure, depletion zones are created between the columns allowing the light to pass through the depletion zones directly and the light that passes in the direction normal to the film increases in proportion to the formation of depletion zones. This allowed us to indirectly quantify the formation kinetics of the nanocolumnar chain structures.[29, 64, 88] A custom-built measurement system (Figure 3.2(a)) was developed in our group to track the real-time change of weight, thickness, birefringence, optical light transmission and temperature.[63] The blade cast PDMS/graphite film is sandwiched by two pieces of indium-tin oxide (ITO) coated glass with four spacers between them, which can create a 1mm thick air gap between the film and top ITO glass as shown in Figure 3.2(b).

The real time change of light transmission for 0.1v% graphite/PDMS composite film without and with electric field (500V) is shown in Figure 3.2(c). The light transmission value through the electrodes without the sample is defined as 100%. Prior to the application of external electrical field (in the first 60s), the light transmission is low as the randomly distributed graphite particles in PMDS at stage I scatter and absorb the incoming light. Once 500 V is applied, the light transmission shows a very sharp increase within several minutes, noted as stage II. This rapid increase of light transmission is caused by the formation of short particle chains of adjacent particles leaving particle depletion zones in between. At stage III, the light transmission increases at a lower rate, as these short particles chains grow into longer chains by attracting the free particles to create wider and more particle free depletion zones. At 2400s, the temperature (red line) of the film is increased to 85 ^{o}C by blowing hot air to cure PDMS while maintaining the electric field. During heating, the light transmission slightly increases as the lowering of viscosity at higher temperatures before the polymer matrix fully cured facilitate further refinement of nanocolumnar structures and the light transmission becomes constant thereafter. The light transmission for the film without applying high voltage (black line) remains nearly constant during the whole process.

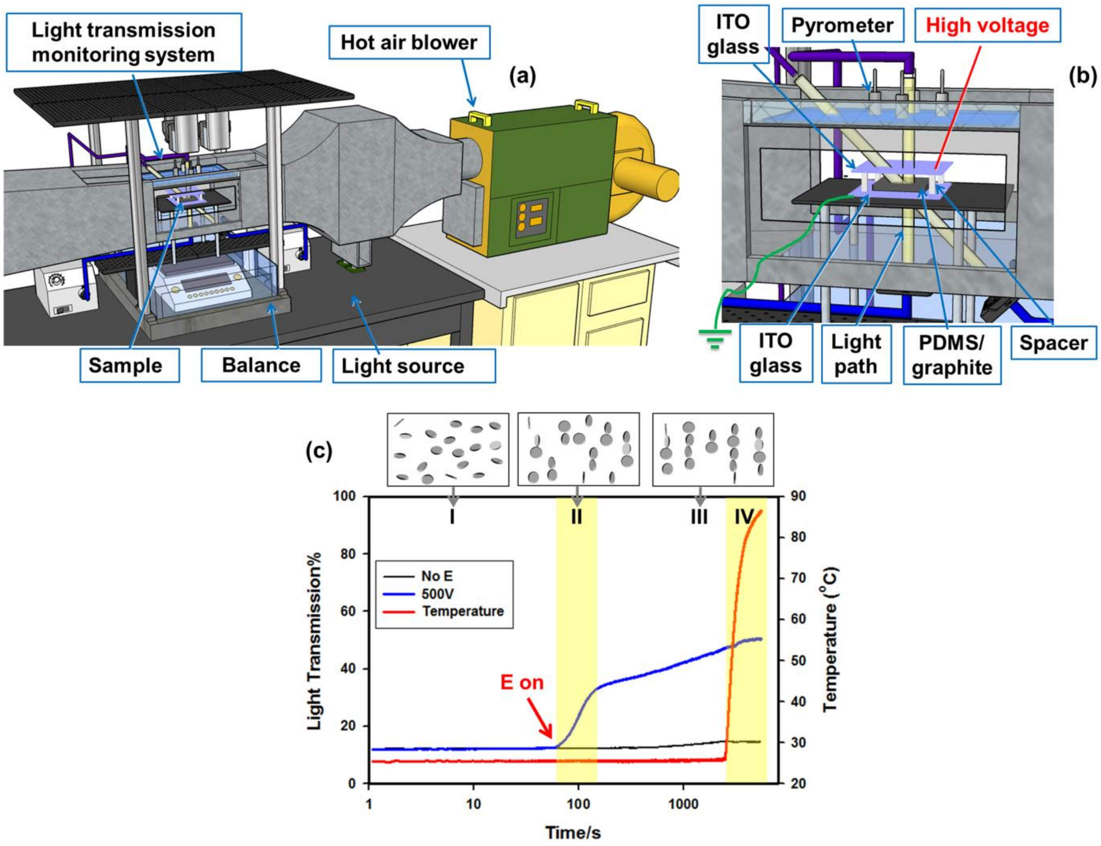

Figure 3.2 (a) Measurement system tracking real time change of weight, thickness, birefringence, light transmission and temperature, (b) Setup to measure the light transmission after applying electric field, (c) Real-time change of light transmission and temperature for 0.1vol% graphite/PDMS without and with high voltage (500V).

The effect of voltage on the light transmission for 0.1vol% graphite/PDMS film is shown in Figure 3.3(a). As expected, higher voltage leads to rapid increase of light transmission at stage II and the higher light transmission level at the end of stage II. With higher voltage, the particles undergo stronger dielectrophoretic force to overcome the viscous resistance of the matrix to form chains thus leading to a faster alignment and light transmission change. At stage III and IV, the light transmission increases to higher level at higher applied voltage. When applied voltage is higher than 1000V, the liquid film is attracted towards the top electrode, which means 1000V is the highest voltage and still safe condition for preparing the film.[132, 133] Similar four-stage behavior can also been seen for higher graphite loadings: 0.25 and 0.5 vol%, as demonstrated in Figure 3.3(b) and (c), respectively. Under the same applied voltage, the higher the graphite loading, the lower the rate of light transmission increase at stage II and III as well as the lower final value observed. The light transmission of the cured films with different loadings of graphite prepared under different voltages is summarized in Figure 3.3(d). The aligned films are more transparent than the film with random particles, and the light transmission increases with increasing applied voltages. When the applied voltage is 1000V, the light transmission was improved 2.9 times for the film with 0.1 vol% graphite, increasing from 16% to 62%. As the particle concentration increases, the light transmission decreases at same process conditions. When the particle loading is 0.5%, the light transmission increases from 1% to17%. Therefore, electrical field assisted alignment is also effective to achieve enhanced transparency along “Z” direction, and the light transmission can be tailored by adjusting applied voltages. For the nanocomposites with higher concentration of particles, the films become too opaque for the instrument to measure the light transmission.

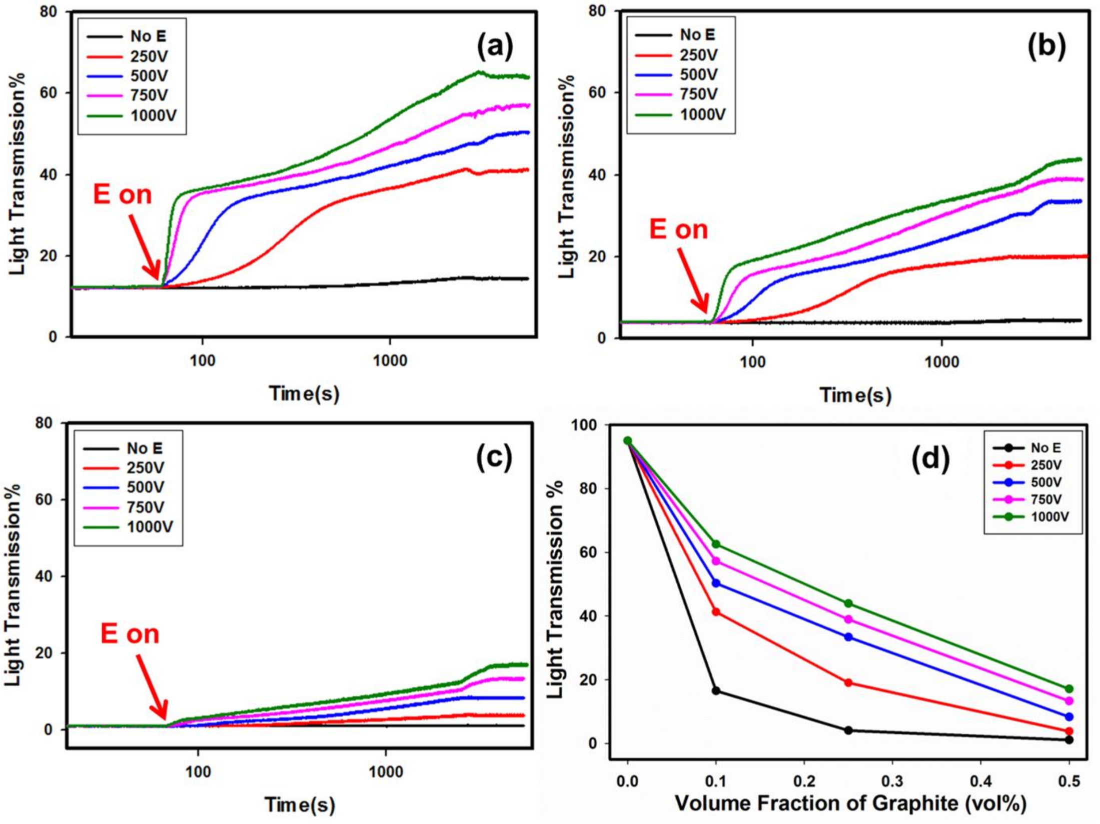

Figure 3.3 Effect of applied voltage on real-time light transmission change of PDMS/graphite film with different loadings: (a) 0.1 vol%, (b) 0.25 vol%, (c) 0.5 vol%, (d) effect of applied voltage and particle loading on light transmission of nanocomposite film after curing.

The effect of applied voltage on the particle alignment for 0.5 vol% graphite/PDMS nanocomposite film is also studied by SEM, as shown in Figure 3.4. The particles are colored yellow (false) to distinguish them from other features. The graphite particles are randomly distributed within the film without the application of electric field, as can be seen in Figure 3.4(a). Upon the application of 250V external electrical field along the thickness direction, graphite particles are aligned into short chains following the direction of the applied electrical field, as observed in Figure 3.4(b). As the applied voltage is increased up to 500V, 750V and 1000V, the particle chains also grew longer and the number of chains became fewer. As a consequence, the depletion zones between particle chains became wider at higher voltage, which is consistent with the higher light transmission values at higher voltages, as stated earlier. 1000V external electrical field is selected to study the effect of particle concentrations. The cross sections of aligned nanocomposites under 1000V external electrical field with different particle loadings are studied by SEM and shown in Figure 4. Below 10 vol% of particle loadings (Figure 3.5a-e), clear chain structures consist of graphite particles can be observed upon applied electrical field, whereas for samples containing higher than 10 vol% of particles, the anisotropic chain structures can be barely seen. Instead, vast aggregates of particles that are randomly dispersed within the PDMS matrix were observed due to the high viscosity and the frustrated particle structure forms at such high concentrations as the spatial density of particles became too high leading to interruption of alignment process.

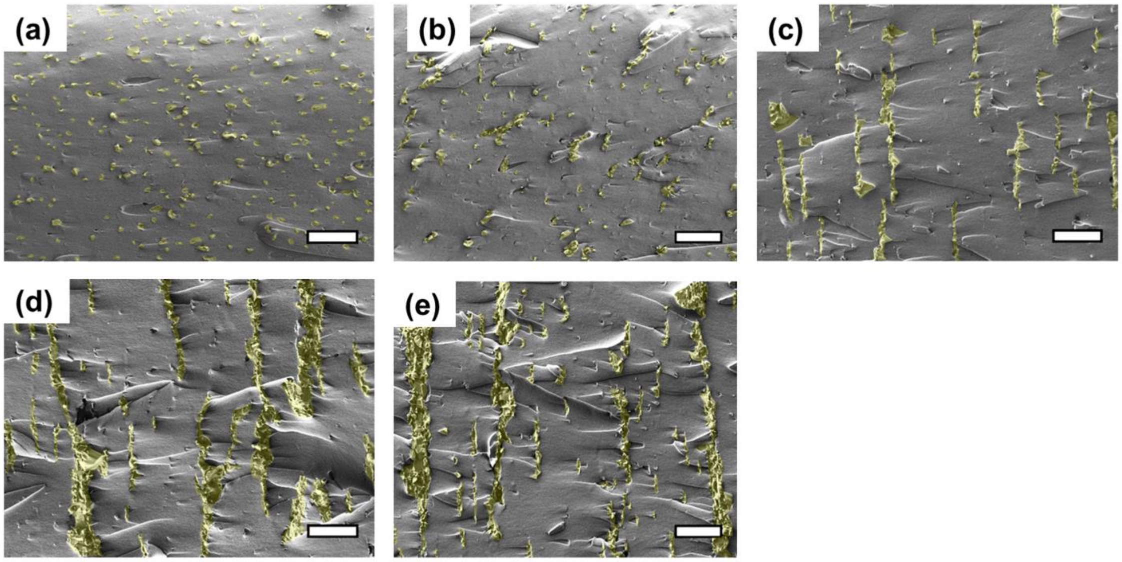

Figure 3.4 Cross sectional morphology of 0.5v% graphite/PDMS nanocomposites prepared under different voltages: (a) 0V, (b) 250V(c) 500V, (d) 750V, (e) 1000V (scale bar:20μm) (graphite particles are artificially colored to enhance the contrast).

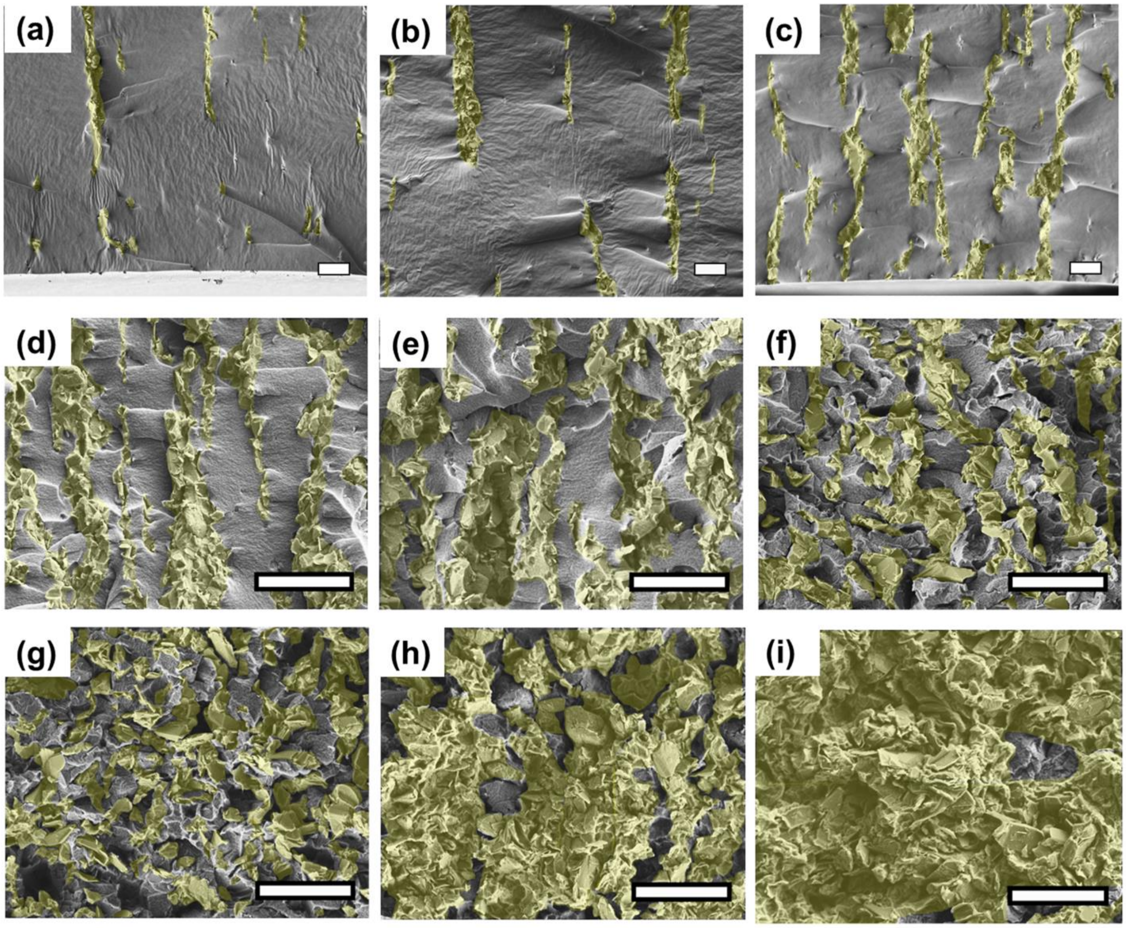

Figure 3.5 Cross sectional morphology of PDMS/graphite nanocomposites with different consternations after alignment: (a)0.25 v.%, (b) 0.5 v.%, (c) 1 v.%, (d) 2 v.%, (e) 5 v.%, (f) 10 v.%, (g) 15 v.%, (h) 20 v.%, (j) 25 v.% (scale bar:20µm) (graphite particles are artificially colored to enhance the contrast).

3.3.2 Electrical conductivity and dielectric permittivity

To study the effect of alignment on the electrical properties of resulting polymer nanocomposites, the electrical conductivity of cured PDMS/graphite nanocomposites with different particle loadings was measured along the thickness direction as a function of frequency at room temperature, as shown in Figure 3.6 It can be seen that the electrical conductivity of the nanocomposites increases with frequency and volume content of particles for both aligned and non-aligned samples. The electrical conductivity for the aligned nanocomposite (Figure 3.5b) has higher value than that of isotropic nanocomposite (Figure 3.5a) at same loading of particles. The electrical conductivity value at frequency 1000 Hz was summarized in Figure 3.7 as a function of graphite volume content. For the composites with randomly dispersed particles, the electrical conductivity increases mildly with particle concentration below ~10 vol.%, whereas this increase becomes significantly more rapid beyond 10 vol.%, as indicated by the black curve in Figure 3.7. When the particle content is relatively low, the conductive particles are separated by the insulating polymer matrix and the electrical conductivity is attributed to the tunneling effect (non-Ohmic conduction). As the loading of particles increases, the insulating polymer layer becomes thinner and hence the tunneling effect becomes more effective. As the volume content increases beyond a critical value, the conductive particles come to direct contact with each other, and an insulator-conductor transition can be observed.[134, 135] In the case of graphite nanoparticles, the critical content value lies in between 7.5% and 16%. This direct contact between conductive particles gives rise to percolation transition, which forms conductive networks through the film. This critical volume content of conductive particles is called percolation threshold, where Ohmic conduction occurs.[135] The conductivity of polymer/conductive particle nanocomposites near the percolation threshold can be described as below,

$$\sigma(f_g) \propto (f_c - f_g)^{-s}, \text{ when } f_g < f_c \tag{3.2a}$$

$$\sigma(f_g) \propto (f_g - f_c)^{t}, \text{ when } f_g > f_c \tag{3.2b}$$

where f_g is the volume content of graphite, f_c is the percolation threshold, s and t are the dimensionless parameters in the insulating and conducting regions, respectively.[136] The fitting results of experimental electrical conductivity data based on Equation 1a and 1b are given in the inset plots of Figure 3.7. It can be seen that the percolation threshold (f_c) is 10%, with t=3.43 and s=1.03. The critical exponent value in the insulator region, s=1.03, is very close to the universal values ($s_{un} \approx 0.8$~1 for 3D fillers in theory[136]). While the critical exponent, t=3.43, is larger than the universal values ($t_{un} \approx 1.6$~2 for 3D fillers in theory[136]) in conductor region but close to the value for PVDF/reduced graphene oxide system.[137] The discrepancy of the critical exponent in conductor region between graphite and universal value is attributed to the high aspect ratio of the two dimensional flaky graphite particles.

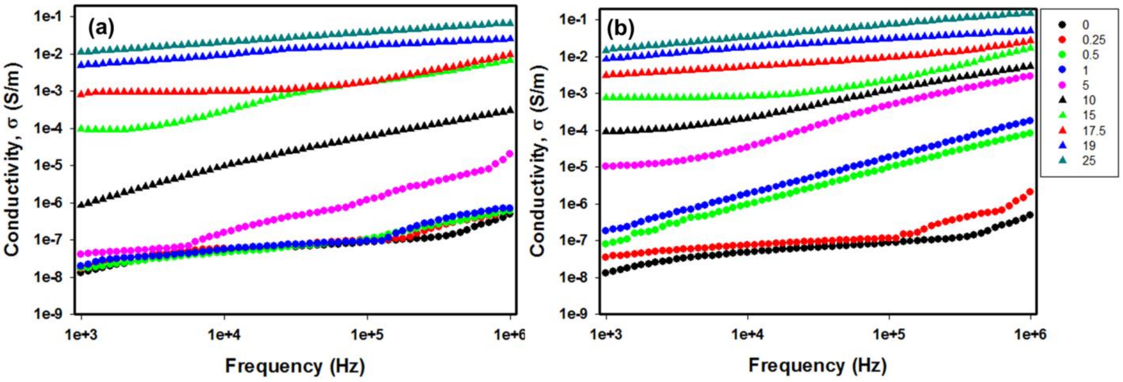

Figure 3.6 Dependence of electrical conductivity on frequency for PDMS/graphite nanocomposites at room temperature: (a) with random particles, (b) with aligned particles.

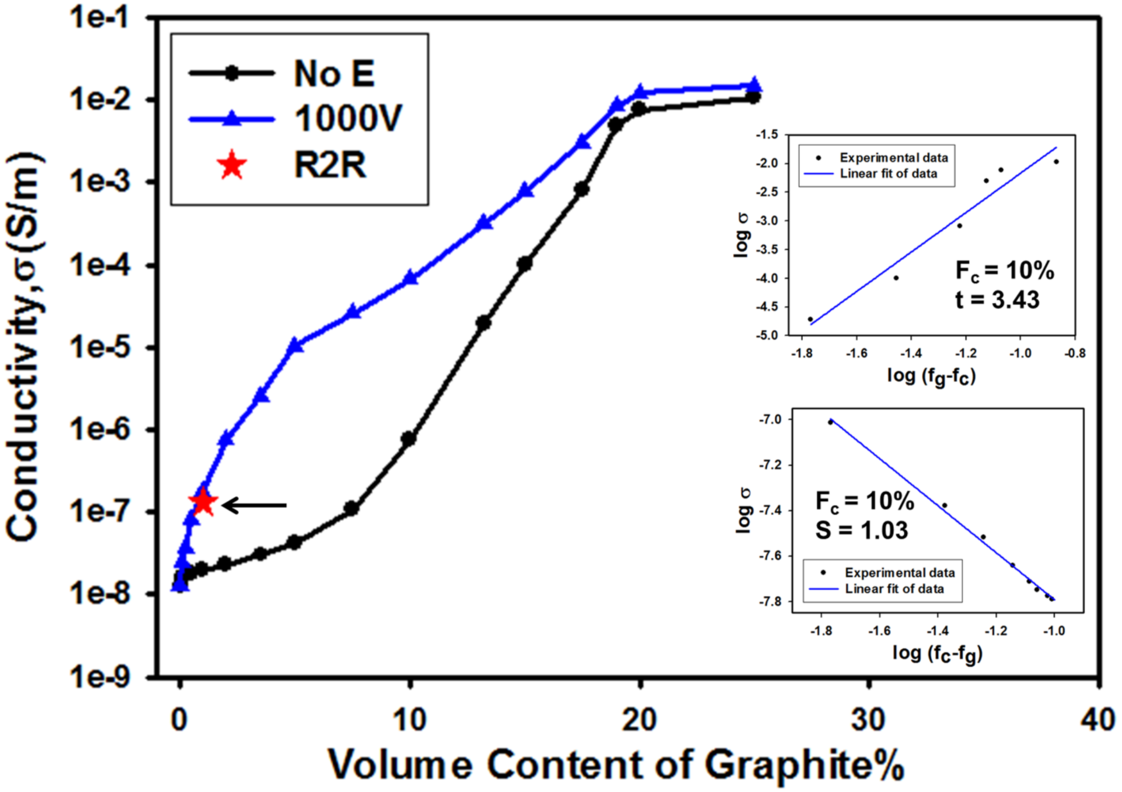

Figure 3.7 Effect of alignment on the electrical conductivity for nanocomposites as a function of volume content at room temperature and 1000 Hz. The insets show the best fits of the conductivity to Equation 3.2.

It can also be seen in Figure 3.7 that aligned nanocomposites (blue curve) exhibit higher electrical conductivity than non-aligned nanocomposites (black curve) for all particle concentrations (0.1-25 vol.%), and this gap of electrical conductivity between aligned and non-aligned samples is significantly greater at lower particle concentrations (below 10 vol.%). As the volume content is 5 vol%, the electrical conductivity of aligned nanocomposite shows largest enhancement and is more than 250 times higher than that of isotropic one. This is consistent with the SEM results in Figure 3.5, where the graphite particles are shown to form vertical chains instead of isolated particles in aligned samples, which induces much shorter distance between particles and thus higher conductivity. Moreover, the particles are aligned better at concentrations lower than 10 vol.% (Figure 3.5a-e), whereas aligned samples with higher concentrations exhibit poor alignment structures (Figure 3.5f-i), which results in the less significant difference of electrical conductivity at higher concentrations between aligned and non-aligned samples. It can also be noted in Figure 3.7 that the aligned sample with 2 vol% particles reaches the same electrical conductivity level of non-aligned nanocomposite with 10 vol% particles, which is the percolation threshold according to the fitting results. Namely, the alignment of embedded particles by external electrical field can significantly decrease the conductive percolation transition concentration. In addition, since the slope of the conductivity curve is reduced beyond 5% filler content, the films with intermediate conductivities may be more repeatedly produced. This is particularly important for electrostatic discharge film packaging applications for protection of sensitive electronics including hard disk heads.

The dielectric permittivity of nanocomposites as a function of frequency at room temperature is shown in Figure 3.8 The dielectric permittivity decreases with frequency and increases with the concentration of particles, and aligned samples (Figure 3.8b) show higher dielectric permittivity than non-aligned ones (Figure 3.8a) at given particle concentration. The values of dielectric permittivity at 1000Hz were summarized and plotted in Figure 3.9 for both aligned and non-aligned nanocomposite as a function of volume content. A very sharp increase of dielectric permittivity can be observed near the percolation threshold for the nanocomposites with random particle as shown in Figure 3.9 (black curve), which is similar to the percolation behavior of electrical conductivity. The dielectric permittivity increases dramatically to 88.4 as the particle concentration reaches the percolation threshold (10 vol%), which is around 40 times higher than the polymer matrix, pure PDMS (about 2.24). The change of the dielectric permittivity can be predicted by power law in equation 2 as below:

$$\varepsilon\left(f_g\right) \propto (f_c - f_g)^{-s}, \text{ when } \; f_g < f_c \tag{3.3}$$

where ε is the dielectric permittivity, f_c=10% and s=1.17 in this equation as given in the bottom inset plot of Figure 3.9. As the volume fraction increases further to 20 vol.%, the dielectric permittivity continues increasing exponentially to a giant value as high as 3.1×10^7 and the dielectric loss is also high as 212 due to increased electrical conductivity, as indicated by the top inset plot of Figure 3.9. The nanocomposites with both high dielectric permittivity and loss provide promising candidates for EM shielding applications.

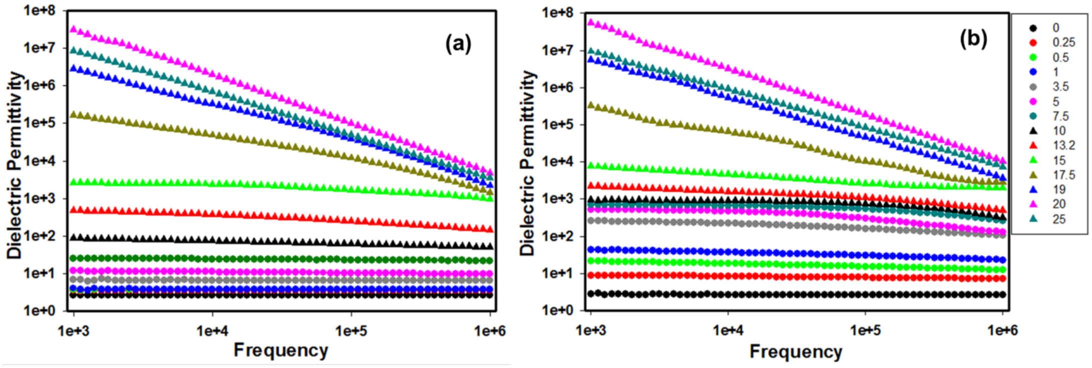

Figure 3.8 Dependence of dielectric permittivity on frequency for PDMS/graphite nanocomposites at room temperature with (a) random particles, (b) aligned particles.

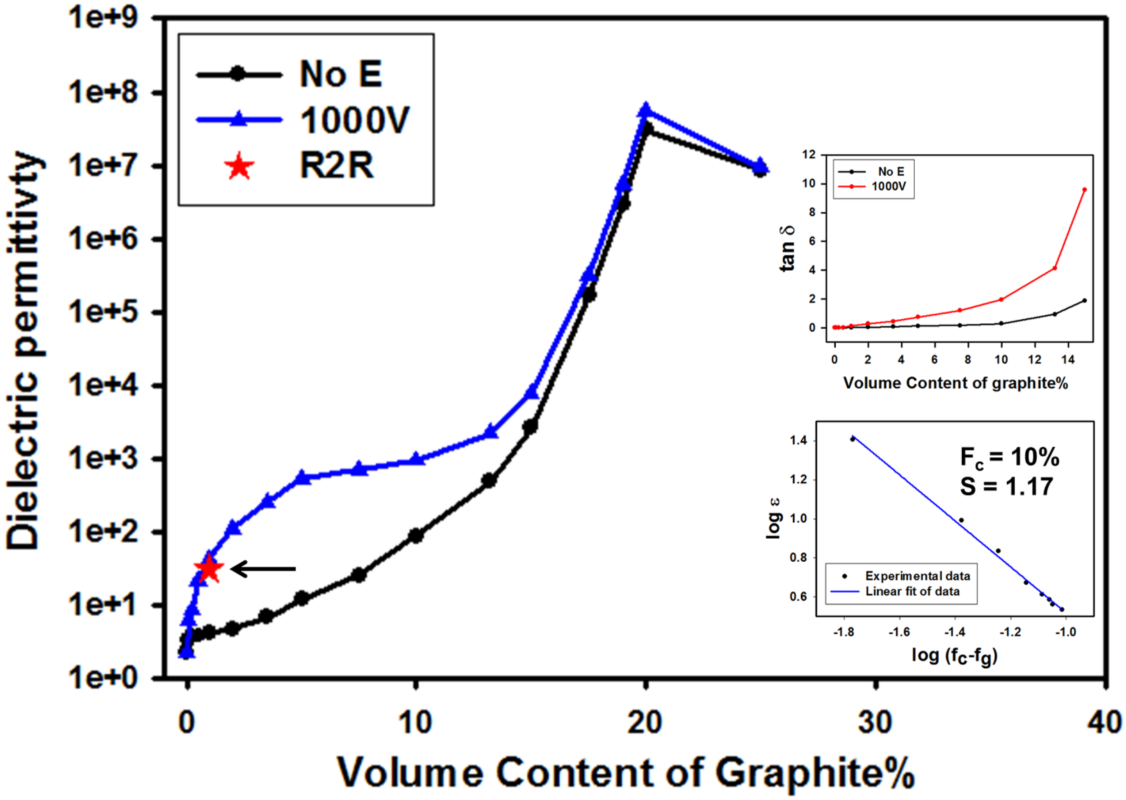

Figure 3.9 Effect of alignment on the dielectric permittivity for nanocomposites as a function of volume content at room temperature and 1000 Hz. The insets show dielectric loss as function of graphite volume fraction and the best fits of the conductivity to Equation 3.3.

On the other hand, aligned nanocomposites exhibit this fast dielectric permittivity increase at much lower particles concentration, as shown by the blue curve in Figure 3.9. At the same loading of graphite, the aligned nanocomposites have much higher value of dielectric permittivity than the isotropic samples. With merely 2 vol% of particles, the dielectric permittivity of aligned nanocomposites is improved to 111.7, which is 23 times higher than the dielectric permittivity (4.7) of the non-aligned samples, and 50 times of pure PDMS. Additionally, this value is even higher than the dielectric permittivity value (88.4) of isotropic nanocomposites at percolation threshold (10 vol%) by 26%, meaning that the percolation transmission was achieved at much lower loading of particles. Benefiting from the low loading of particles at percolation threshold, the flexibility of polymer matrix can be maintained. With dielectric permittivity of 111.7 and dielectric loss of 0.28, the aligned materials are useful for embedded capacitors working at low electric field.[17, 26] As the volume content increased to 3.5 vol%, the dielectric permittivity is increased to 258, and dielectric loss is increased to 0.45, which is still acceptable for high charge storage capacitor.[17] It is also worth mentioning that the aligned PDMS/graphite nanocomposites manufactured in this study were able to achieve similar dielectric permittivity as PVDF/graphene systems at comparable loading of particles, which were reported as 90 at 1.6 vol% particle loading and 280 at 2 vol%,[137] and two times higher than PVDF/MWCNT nanocomposites, which were reported by Xue[43] et al. as 40 and 80 at 2 vol% and 3.5 vol% particles loading, respectively. It's important to point out that graphite has the advantage of much lower cost of raw material and processing than graphene and carbon nanotubes, but it still achieve similar or even better properties after alignment. The enhancement effect in dielectric permittivity by the alignment of particles also increases with the concentration of particles and reaches the maximum at 5 vol%, with the dielectric permittivity of 524 after alignment, which is 43 times higher than that of non-aligned samples. As the volume fraction further increases, the enhancement effect diminishes, and the difference between aligned and non-aligned samples also tapers, due to the same reason as less aligned structures at higher particle concentration. The largest dielectric permittivity can be as high as 5.6×10^7 for aligned nanocomposite with 20 vol% of graphite, which is a slightly higher than that of non-aligned sample. As the graphite loading increases to 25 vol%, the dielectric permittivity decreases due to the increased electrical conductivity induced current leakage within the nanocomposite.

3.3.3 Thermal conductivity

The thermal conductivity of both aligned and non-aligned nanocomposites is shown in Figure 3.10a as a function of particle concentration. Since phonon transmission requires direct contact between the particles, this requires higher particle concentration than for electrical conduction that needs the particles to be at least at minimum tunneling distance. Both nanocomposites showed increasing thermal conductivity with increasing particle concentration thus forming thermally conductive percolated networks facilitating the transportation of photons. The aligned nanocomposites, on the other hand, having “directed percolated” nanoparticle columns exhibit substantially higher thermal conductivity than the isotropic ones. There’re two reasons for the enhancement of thermal conductivity after alignment: (1) the thermal conductivity along the basal plane of graphite particle is more than 6 times higher than that through plane direction,[138, 139] so the oriented graphite can improve the thermal conductivity more effectively, (2) the aligned graphite particle chains generate direct thermally conductive “connected” path throughout the film and the alignment creates an anisotropic structure similar to the parallel conduction structure which can achieve the highest thermal conductivity in theory for composites.[140] The highest thermal conductivity achieved is 6.05 W/m*K at 20 vol%, which is high enough for the application of thermal interface materials. Figure 3.10b shows the ratio of thermal conductivity of non-aligned (black curve) and aligned (blue curve) nanocomposite to pure polymer matrix. The thermal conductivity of aligned nanocomposites can be as high as 35 times the thermal conductivity of pure matrix. The ratio of thermal conductivity of aligned nanocomposites to non-aligned ones is shown in Figure 3.10c as a function of particle volume content. The enhancement of thermal conductivity by the alignment of particles increases with particle content and reaches maximum (~2.5) at 5 vol% graphite, and then decreases as the particle content further increases, which is consistent with the development of electrical properties as described earlier.

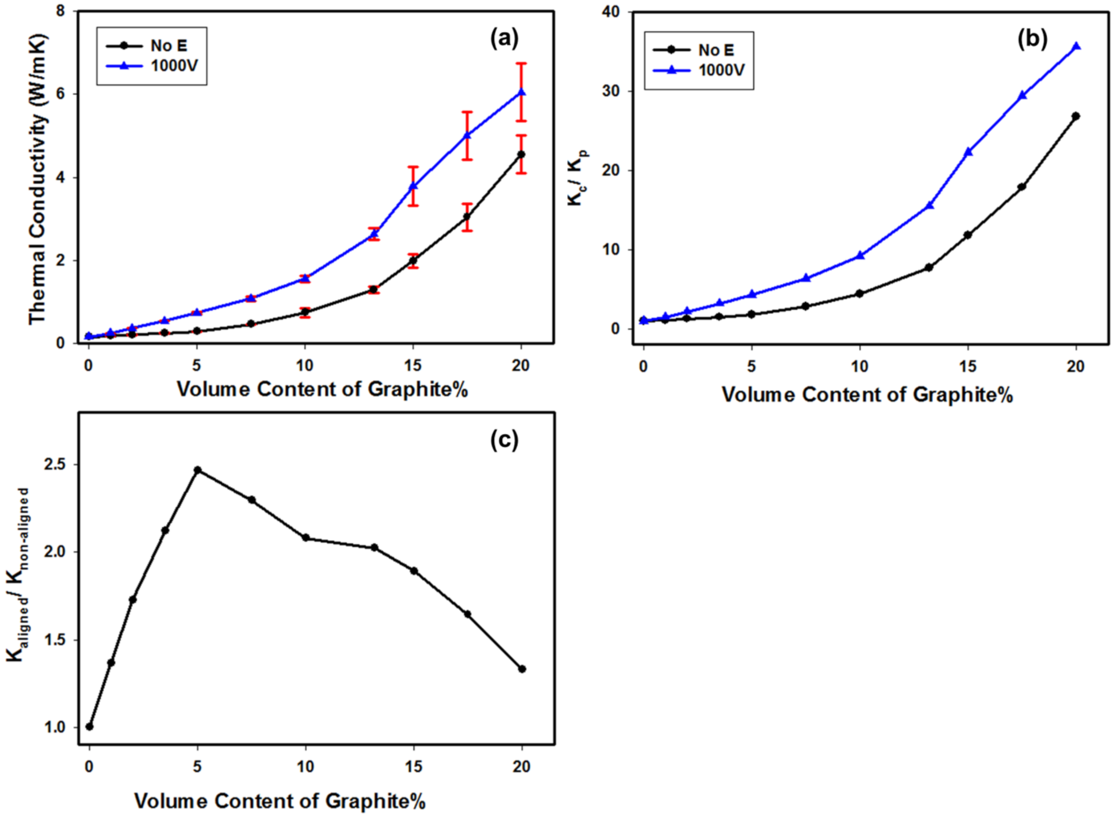

Figure 3.10 (a) Effect of alignment on the thermal conductivity for nanocomposites as a function of volume content, (b) thermal conductivity ratio of nanocomposite and polymer matrix, (c) thermal conductivity enhancement after alignment.

3.3.4 Roll to roll continuous processing

Batch process is the most common approach to manufacture nanocomposites with electric field assisted aligned particle in “Z” direction. Our group developed a roll to roll process for particle alignment to fabricate “Z” aligned functional films in previous studies.[29, 109] Nevertheless, the top electrode was adhered to the film after solidifying due to direction contact in these studies. Coating lubricants or very slow processing speed may help detaching the film from top electrode for continuous process. To solve this problem, in this study the top electrode is separated from the samples by an air gap as shown in Figure 11a and 11b, which shows the schematic drawing and actual machine of the custom built roll to roll process line for continuous manufacturing of nanocomposite films with "Z" aligned particles under electric field. This process consists of dr. blade solution casting of liquid films and electric field zone. Within the electric field zone, the front portion of the substrate was kept at room temperature (cold zone) so that the particles can move and be aligned, and the end portion was heated to desired curing temperature (hot zone) in order to cure the polymer matrix and fix the aligned structures. In a typical process, a dr. blade or slot die is used to cast thermally curable monomer mixtures with well dispersed particles into liquid film with desired thickness on transporting substrate. The liquid film is then transported into the electric field zone without touching the stainless steel plate top electrode. In the cold zone of electric field, the particles are aligned and form into chains due to dipole-dipole interactions under the electric field. Then the matrix is thermally cured to freeze the structure of particle chains as the film moves forward and passes through the hot zone. Herein, the solution of PDMS with 1 vol% graphite particle was used to demonstrate the roll to roll continuous manufacturing of nanocomposite thin film with electric field assisted "Z" aligned particle in realistic conditions. The 100µm thick liquid film (15cm wide and 6m long) was cast on PET substrate and the particles were aligned and frozen as the film pass through the cold and hot zone in electric zone at 1 cm/min speed with a 1mm thick air gap. The applied voltage was 1000V. The processing speed can also be increased in order to meet the industrial production requirements by increasing the length of the electric field zone. Figure 11c shows the cured and aligned PDMS/graphite nanocomposite film on PET substrate with 100μm thick × 15cm wide × 6m long. The cross-sectional morphology of resulting samples at selected locations was shown in the SEM images in Figure 11c, from which it can be seen that graphite particles were aligned into chains throughout the whole film. The aligned nanocomposite films prepared by roll to roll line show very close electrical conductivity and dielectric permittivity than the film prepared by batch production as shown by red stars in Figure 3.7 and 3.9, respectively.

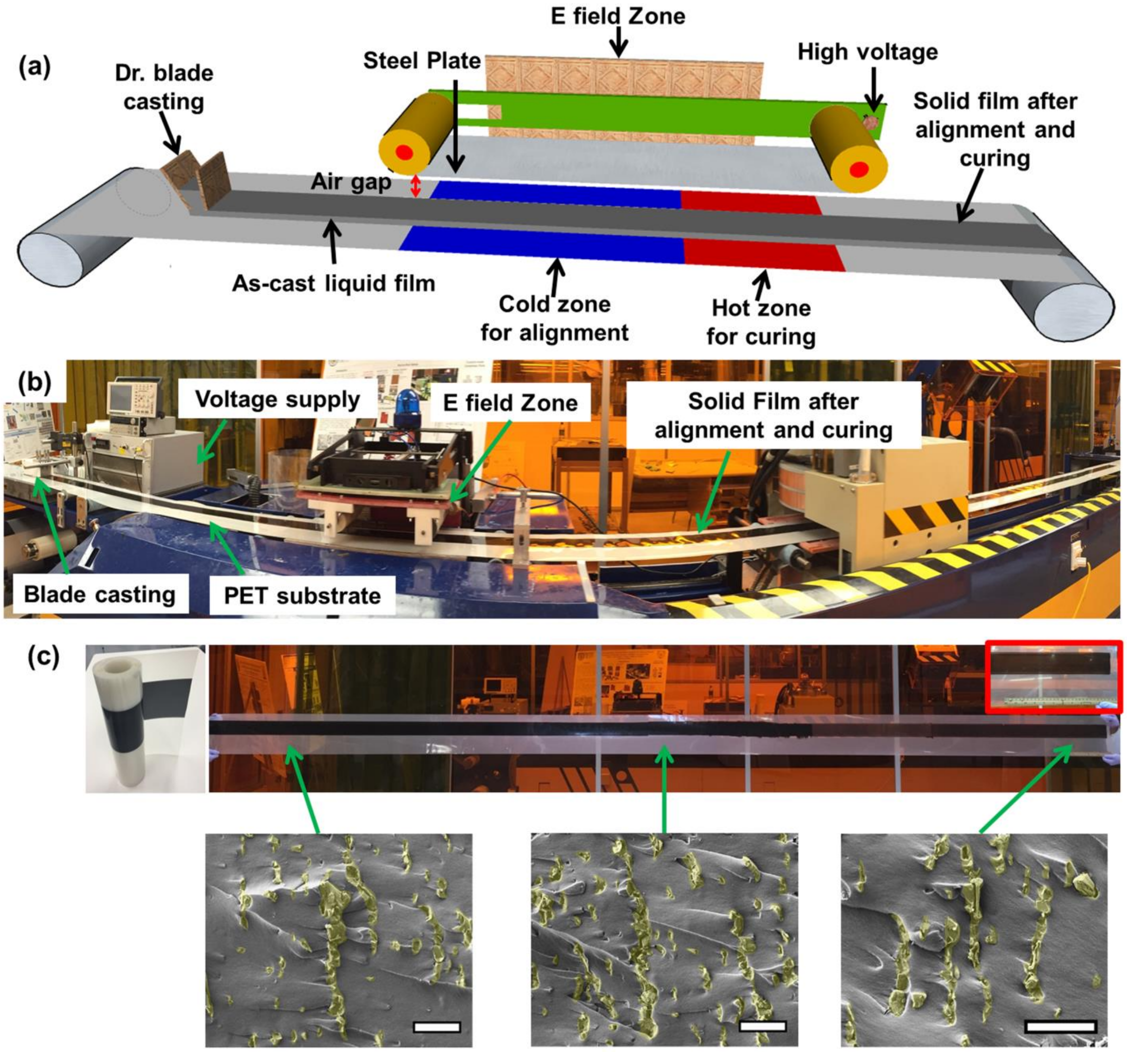

Figure 3.11. (a) schematic and (b) picture of roll to roll process for continuous manufacturing nanocomposites with electric field assisted "Z" aligned particles, (c) picture of 200µm thick, 15cm wide, 6m long film on PET substrate after alignment and curing. The Inset shows the scale with 30cm long ruler. The SEM images show the morphology of aligned particles in different location of the film (scale bar 20µm) (graphite particles were artificially colored to enhance the contrast).

3.4 Conclusion

We developed a roll to roll process to continuously produce multifunctional films with high electric, dielectric and thermal conductivities in thickness direction by aligning graphite particles along “nanocolumns” whose axes oriented in the field (thickness direction) by the application of electric field. In this study, non-contact method was introduced by adding an air gap between the top electrode and the top surface of liquid film, to rapidly manufacture these films. The kinetics of particle alignment and chain formation under electric field were studied by tracking the real-time optical light transmission, with focus on the effect of applied voltage and particle concentrations. Higher of applied voltage led to longer and thicker particle chains across the film cross-section. Aligned samples exhibited higher electrical conductivity, dielectric permittivity as well as thermal conductivity compared to non-aligned samples, and this enhancement effect first increases with particle content and then decreases as particle concentration further increases beyond 5 vol%. This is attributed to the fact that the particles were better aligned below 5 vol%, whereas frustration as a result of high particle density above 5 vol%, reduces the effect. Aligned nanocomposites achieved percolation transition at much lower, 2 vol% concentration, compared to that of non-aligned ones at10 vol%. By decreasing the percolation threshold, the flexibility of the polymer matrix was maintained while achieving similar electrical and thermal performance.   As a comparison, aligned PDMS/graphite nanocomposites were able to achieve comparable or better electrical and thermal properties than PVDF/MWCNT[43] or PVDF/graphene[137] nanocomposites at the same particle loading, yet with much lower cost and ease of processing, which are very promising for a wide range of applications such as imbedded capacitor, EM shielding, heat spreader and electrical stress control applications.

CHAPTER IV

ROLL TO ROLL ELECTRIC FIELD “Z ALIGNMENT OF NANOPARTICLES FROM POLYMER SOLUTIONS FOR MANUFACTURING MULTIFUNCTIONAL CAPACITOR FILMS

A roll to roll continuous processing method is developed for vertical alignment (“Z” alignment) of barium titanate ($BaTiO_3$) nanoparticle columns in polystyrene (PS)/toluene solutions. This is accomplished by applying electric field to a two-layer solution film cast on a carrier: one is the top sacrificial layer contacting the electrode and the second is the polymer solution dispersed with $BaTiO_3$ particles. Flexible Teflon coated mesh is utilized as the top electrode that allows the evaporation of solvent through the openings. The kinetics of particle alignment and chain buckling is studied by the custom-build instrument measuring the real time optical light transmission during electric field application and drying steps. The nanoparticles dispersed in the composite bottom layer form chains due to dipole-dipole interaction under applied electric field. In relatively weak electric fields, the particle chain axis tilts away from electric field direction due to bending caused by the shrinkage of the film during drying. The use of strong electric fields leads to maintenance of alignment of particle chains parallel to the electric field direction overcoming the compression effect. At the end of the process, the surface features of the top porous electrodes are imprinted at the top of the top sacrificial layer. By removing this layer a smooth surface film is obtained. The nanocomposite films with “Z” direction alignment of $BaTiO_3$ particles show substantially increased dielectric permittivity in the thickness direction for enhancing the performance of capacitors.

4.1 Introduction

The inclusion of nanoparticles in polymer matrix may offer enhanced properties.[141] This includes mechanical,[142] electrical,[143] thermal properties[144] and dielectric permittivity.[87, 145] In many instances, these nanocomposites require high loadings of particles to reach the percolation threshold to attain the desired physical effect. For example, more than 75 vol.% of $BaTiO_3$ particles are needed to increase the dielectric constant of polyvinylidene fluoride (PVDF) composites[146] to be larger than 100. The thermal conductivity of silicon carbide (SiC) /epoxy composites is less than 3.9 $W^*(m^*K)^{-1}$ when the particle loading is 50 vol.%.[147] At such high particle concentrations, the properties of polymers such as flexibility, transparency and ease of processing are reduced dramatically. One of the methods to achieve improvement of properties in one direction with much less loading of particles is aligning the particles to form chains under electric field.[37, 148-150] The alignment of electrically or thermally conductive particles can form a conductive pathway, so the electrical or thermal conductivity after alignment is much higher than before alignment at the same particle loading.[128] Tang[30] found that

35.7% higher dielectric permittivity of lead zirconate titanate (PZT) nanowires/PVDF nanocomposites can be achieved after aligning the nanowires in the Z direction than the composites with random nanowire due to the increased particle-particle interactions after alignment.

Thermal[7] or ultraviolet (UV) light curable[8] resins are the most commonly used matrix materials due to their ease of processing without solvent need. The particles are aligned to form chains of nanoparticles (nanocolumns) in thermal or UV light curable monomers under electric field and this formed structure is frozen in the matrix by curing the resin. There may be several drawbacks in these processes: (1) the viscosity of the precursor fluid may be too high for the particles to move to achieve the alignment due to high loading of particles. (2) UV curable matrix needs to be transparent for curing which is particularly difficult at high particle loading levels. The fluid may not be transparent when the refractive index contrast (difference) of matrix and particle is large. (3) The matrix materials are generally thermoset materials that may not be desired due to their relative brittleness. Another processing path is to use thermoplastic polymer solutions as matrix. For the polymer solution/particle system, it is easy to adjust the viscosity by modifying the concentration of solvent. Moreover, more diverse choices of thermoplastic materials with excellent performance can be chosen for the matrix materials such as PVDF, polyetherimide (PEI), polyimide (PI).

Previous studies[151, 152] have focused on the in-plane alignment of nanoparticles in polymer solution under electric field as it is relatively easy. While in the case of Z direction alignment, the use of solid top electrode prevents the evaporation of solvent, so the polymer matrix can't be solidified to freeze the developed particle chain structure. Buchanan, M.[152] studied the alignment of graphene platelets to form chains in Z direction in cellulose/1-propanol solution under electric field by using porous electrode as the top electrode. The porous electrode allows the evaporation of solvent through the opening while maintaining electrical field during solidification. When the solvent evaporates, the thickness of the polymer solution decreases which leads the top surface of polymer solution to detach from the top electrode. Direct contact of the top porous electrode and solution surface is ideal for achieving Z direction alignment of dielectric particles in polymer solutions. One method is introduced to solve the problem of detachment, which is that extra polymer solution covers the porous top electrode so that the final thickness of solid films after drying is the same as the gap between top and bottom electrode.[152] However, this method has limitations: (1) it is only suitable for batch production (0.5 cm^2 as reported[152]) and does not lend itself to continuous production. (2) After removing the porous top electrode at the end of process, the top surface of film has imprinted pattern.

In this study, Flexible Teflon coated mesh is utilized as the top electrode that allows the evaporation of solvent through the openings. While drying, the thickness of the polymer solution decreases, and the mesh remains in contact with the top surface due to its flexibility which solve the detachment problem. The kinetics of “Z direction” (thickness) alignment of particles in polymer solution during electric field application and drying is investigated by measuring optical light transmission method. A novel two-layer solution casting method is introduced to eliminate the imprinted patterned top surface. Roll to roll continuous method is introduced to produce functional films with anisotropic structure at large scale. Dielectric properties of these films are characterized.

4.2 Materials and Methods

The solution preparation, in plane alignment, preparation of cell sample, preparation of one layer film and three-layer film are described in details below.

4.2.1 Solution Preparation

30 wt. % solution of PS (Styron 685) in the toluene (anhydrous, 99.8%, Sigma-Aldrich) was prepared using a Thinky mixer for 1hr. Then 1 and 10 wt. % of barium titanate nanoparticles (average size: 500 nm, US research nanomaterials, Inc.) with respect to PS was dispersed in PS/toluene solution for 3hrs, which are denoted as 1$BaTiO_3$/30PS/Toluene and 10$BaTiO_3$/30PS/Toluene, respectively. 5 wt. % polybutadiene (BUNA CB22, LANXESS) in THF (anhydrous, 99.9%, Sigma-Aldrich) was prepared by heating at 50 ^{o}C with magnetic bar stirring for 6h.

4.2.2 In plane alignment

The 1BaTiO3/30PS/Toluene solution was loaded between two parallel copper electrodes as shown in Figure 4.1. The solution was covered by thin glass slide to minimize the evaporation of solvent or without cover. 1000V/mm electric field strength is applied between the two electrodes and images of particle alignment are taken at different time periods by optical microscope.

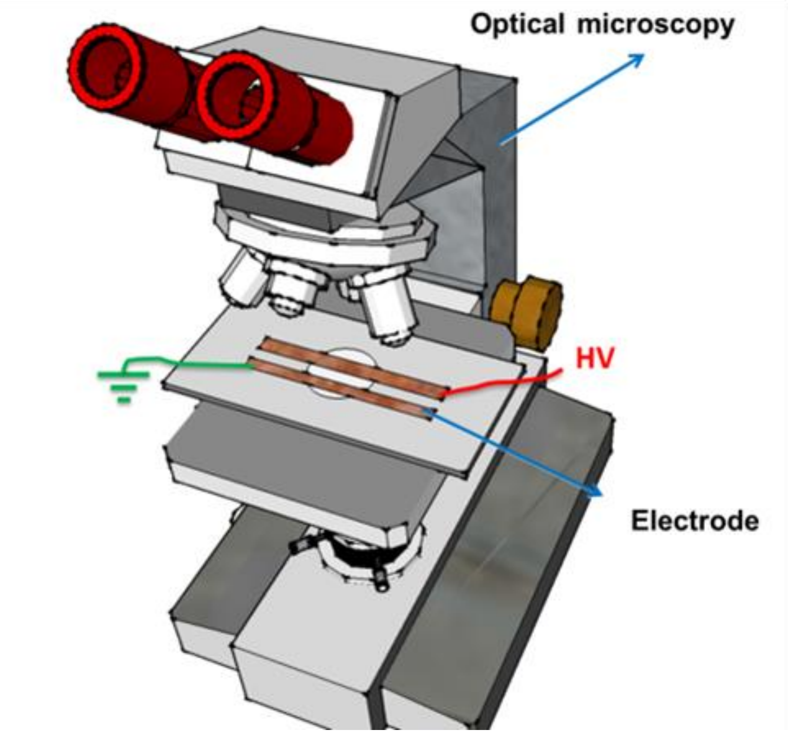

Figure 4.1 Set up for studying in-plane alignment of nanoparticles between two electrodes by optical microscopy.

4.2.3 Preparation of static (cell) sample

To prepare samples, 7 cm x 7 cm size square cell is prepared by placing a 0.5 mm thick glass slide on the top of ITO coated glass (bottom electrode). PS/toluene/barium titanate nanoparticle solution is loaded into the cell cavity slowly. The solution with 0.5 mm thickness is covered by Teflon coated mesh (325x325, TWP Inc.), and mesh is totally wetted by the solution. This set up is loaded in the real time light transmission measurement system. The initial AC (100 Hz) electric filed strengths of 500 V/mm, 1000 V/mm, 1500 V/mm and 2000 V/mm were applied between mesh and ITO glass to study their effect (all the electric field strengths mentioned in this study are initial electric field strength). The electric field is turned off until the film totally solidifies.

4.2.4 Preparation of one layer continuous casting sample

Dr. Blade solution casting method was utilized to cast 10.3 cm wide PS/toluene/barium titanate films on stainless steel substrate at the speed of 50 cm/min on a roll to roll processing line.[86] The cast film moves into the roll to roll electric field system. The diameter of the wires making up the mesh is 35 µm and the size of the opening is 40 µm. The gap of mesh and bottom electrode is adjusted slightly smaller than the thickness of cast wet solution film and the solution film is sandwiched between top mesh and bottom stainless steel substrate. Mesh and stainless steel substrate move at the same speed, thus there is no shear force is generated during the process. Electric field is applied between mesh and stainless steel substrate. After evaporating most of the solvent, the electric field is removed and the mesh is peeled off from the film.

4.2.5 Two layer continuous casting sample

Two-layer solution casting is performed by 10.3 cm wide Dr. Blade. 0.5mm thick wet solution film is cast for PS/toluene/barium titanate solution as the composite bottom layer, and 0.5mm thick wet solution film is cast for PB/THF solution as the top layer. The two layer films move into the roll to roll electric field systems. The same procedures are carried out for two layer system as the one layer system. After drying, the mesh is peeled off from the top layer film that has mesh imprints. Once this is removed the smooth surface composite bottom layer with aligned particles in Z direction was obtained.

4.2.6 Characterization

The cross section morphology of PS/$BaTiO_3$ films with and without alignment was characterized by SEM (JSM7401). The cross-section samples were prepared by freeze fracturing in liquid nitrogen. Prior to the SEM characterization, all the samples were sputter coated with silver. The film is cut into 15mm x 15mm size and sputter coated with silver on both sides. The silver coated film is sandwiched by two electrodes to measure the capacitance. The capacitance is measured by 4192A LF impedance analyzer with frequency ranging from 1 kHz to 1MHz. Based on the measured capacitance, the dielectric permittivity of film can be calculated by the following equation:

$$\varepsilon_t = \frac{Cd}{\varepsilon_0 A} \tag{4.1}$$

where ε_t is the dielectric permittivity of film, C is the measured capacitance (Farads), d is the thickness (m) of film, ε_0 is the dielectric permittivity of free space (8.854×10^{-12} Fm^{-1}) and A is the area (m^2) of capacitor electrode.

4.3 Results and Discussions

Real time electric-optical light transmission, effect of electric field and effect of drying gradient on morphology are discussed below.

4.3.1 Real time electric-optical light transmission measurement

When the nanoparticles are organized into nanocolumns in thickness direction, they create particle depletion zones between them. This leads to enhanced transparency as the light can easily transmit through these depletion zones.[64, 88] Thus the kinetics of particle alignment in solution can be easily studied by measuring the light transmission change under electric field. The custom-build measurement system (shown in Figure 4.2a) can track the real time change of weight, thickness, birefringence and optical light transmission of cast solution film during drying.[63] In this study, the solution film is sandwiched by the ITO coated glass (bottom electrode) and Teflon coated stainless steel mesh (top electrode) where the thickness is the same as the spacer (0.5mm) shown in Figure 4.2(b), and this set up is called “cell”. The light transmission is measured by directing a white light path through the solution film in normal direction, weight is measured by balance and the thickness is measured by the laser micrometer. When electric field is applied, the dispersed nanoparticles are polarized and adjacent polarized particles form chains (nanoparticle columns) due to dipole-dipole interaction whose axes are oriented in electric field (thickness).

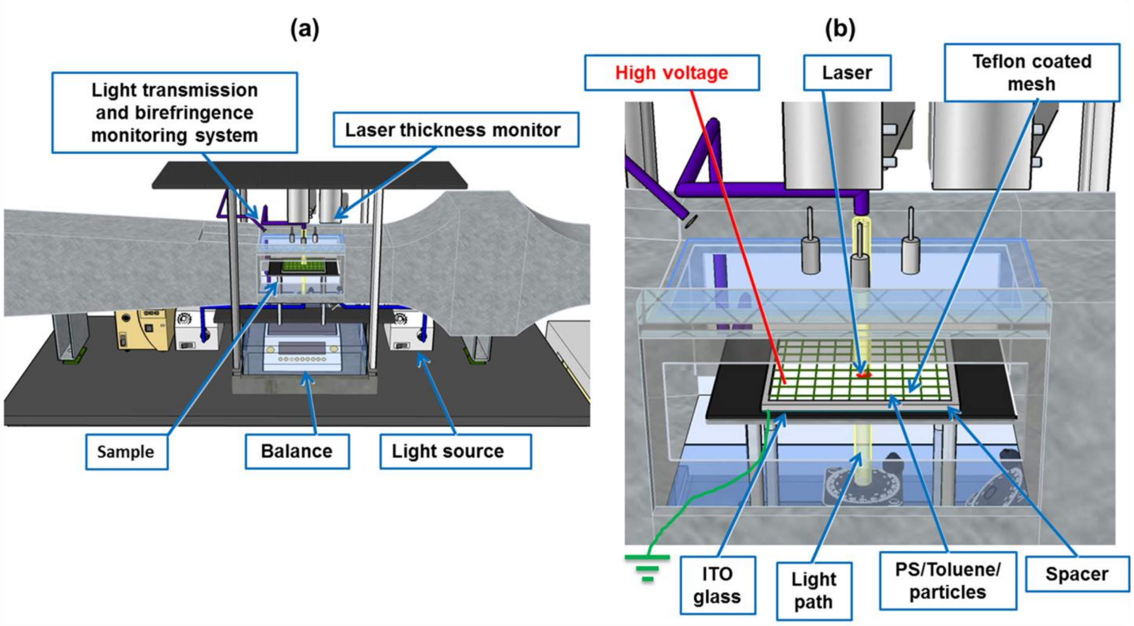

Figure 4.2 (a) Custom-build system measuring real time change of thickness, weight, birefringence and light transmission during solution drying, (b) set up to measure electric field response of light transmission.

To study the kinetics of alignment, real time light transmission measurements are performed while tracking weight and thickness on 30 wt.% PS/Toluene solution with 1 wt.% $BaTiO_3$ with respect to PS ($1BaTiO_3/30PS/Toluene$ solution) at varying initial electric field strengths (AC at 100Hz). The weight and thickness change during drying for films with and without electric field are almost the same, so only one set is shown in Figure

4.3. The weight and thickness decrease as the solvent evaporates in the beginning and then starts leveling off at the end of drying. The light transmission of solution film without electric field (red dash line) remains nearly constant during the first 1500s shown in Figure 4.3. It starts decreasing after around 2000s to lower value as the particle concentration increases as the solvent evaporates. The light transmission of the film with 1000V/mm initial electric field strength shows four-stage behavior shown Figure 4.3. At stage I, the light transmission remains constant as the particles are randomly distributed. Application of high voltage at 15s at stage II leads to very fast response of transmission changing from 12% to 17% in less than 10s as short chains of particles form concurrently with particle depletion regions in between (Figure 4.3). The formation of particle chains leads to more particle-free space between them thus leading to the rapid increase in light transmission. At stage III, the light transmission continues to increase at a lower rate. At this stage, these chains increase in length by “sweeping” the particles between chains to create wider depletion zones.[88] At stage IV, the light transmission starts decreasing gradually after critical time (960s) as the thickness decreases from 0.52 mm to around 0.40 mm and real time weight compared to the initial weight is 67%. This is due to the buckling of the formed particle chains as the thickness decreases while solvent continues to evaporate. Even with buckling of particle chains, the light transmission of the film with electric field is higher than the film without electric field after drying.

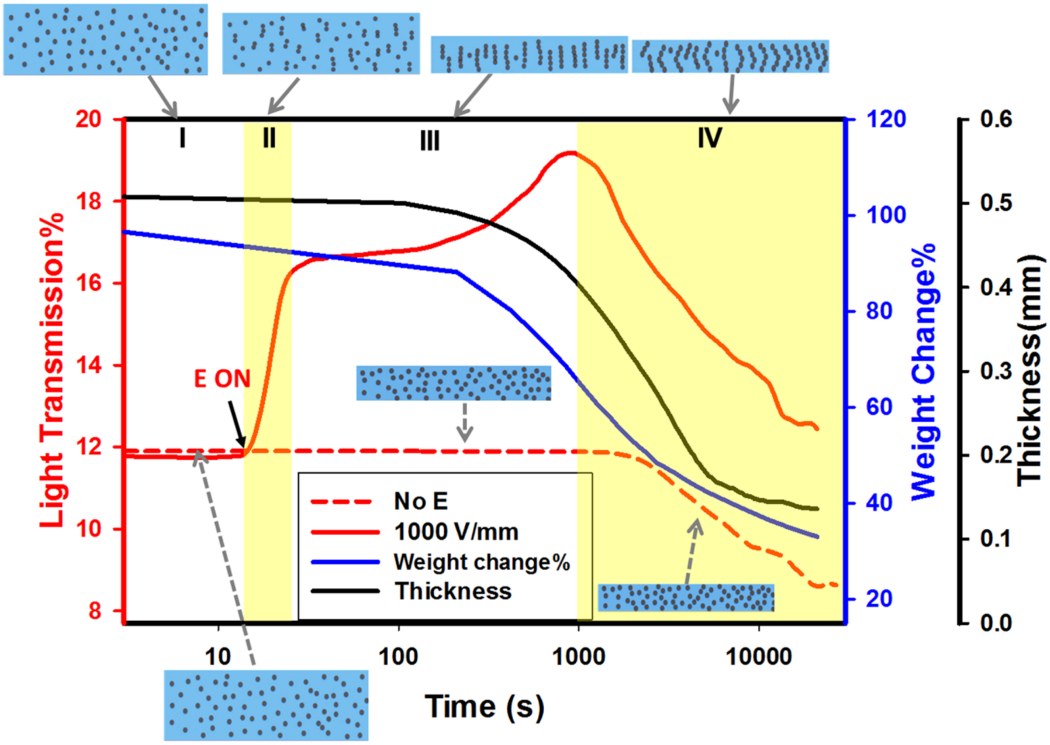

Figure 4.3 Real-time change of weight, thickness and light transmission of solution film (1BaTiO$_3$/30PS/Toluene) during drying without and with electric field (initial strength: 1000V/mm).

The effect of the electric field strength on the real time change of light transmission during drying is shown in Figure 4.4. The stronger the electric field strength, the higher light transmission achieved at the end of stage II. At stage III, the light transmission of all the films continues to increase at lower rate. At stage IV, light transmission starting decreasing occurs later with increasing electric field strength (Figure 4.4). The particle chains have stronger dielectrophoretic force to overcome the compression force caused by thickness shrinkage under stronger electric field strength leading to less buckling of these nanocolumns. After all the solvent evaporates, the films with stronger electric field have higher light transmission due to less bucking of the particle chains.

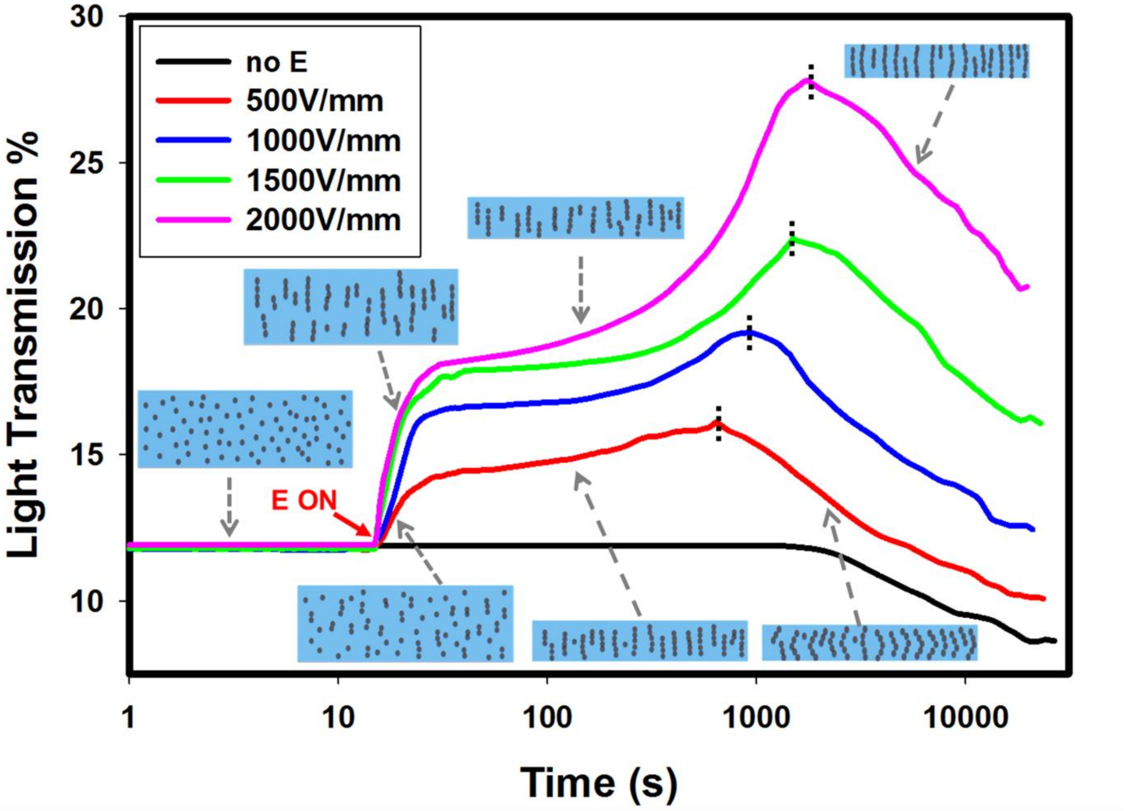

Figure 4.4 Effect of initial electric field strength on real-time change of light transmission during solution drying.

The light transmission response on electric field is explained by the hypothesis of particle alignment, chain growth and chain bucking. To prove the hypothesis, optical microscopy is utilized to observe the procedures of particle alignment and chain growing in $1BaTiO_3$/30PS/Toluene solution in-plane under electric field and SEM is used the investigate the morphology of bucking particle chains. The solution is loaded between two copper electrodes. Mesh is used as electrode for Z alignment experiment and it slows down the evaporation of solvent compared to solvent evaporation without covering. To mimic the solvent evaporation rate in Z alignment experiment, it is ideal to use mesh the cover the solution as well for in-plane experiment. However, the mesh blocks the image taking of particle alignment, so two experiments are designed: (1) the solution is covered by thin glass slide to minimize the evaporation of solvent (Figure 4.5) and (2) the solution without cover (Figure 4.6). 1000V/mm electric field strength is applied between the two electrodes and images of particle alignment are taken at various time periods. The particles are randomly distributed in the matrix at the beginning. Once the high voltage applied, short chains formed by adjacent particles can be observed in images taken in 5, 10 and 15 seconds for both of the two methods. The fast formation of short chains can explain the fast increasing of light transmission at stage II. Gradually, the chains grow longer and longer in the next hours for first method (Figure 4.5), which is a slow process and it is corresponding to the behavior of light transmission at stage III. While in the second method, the particle chains grow longer a little bit but the length of particle chains is much shorter (Figure 4.6) due to increasing viscosity caused by the fast solvent evaporation.

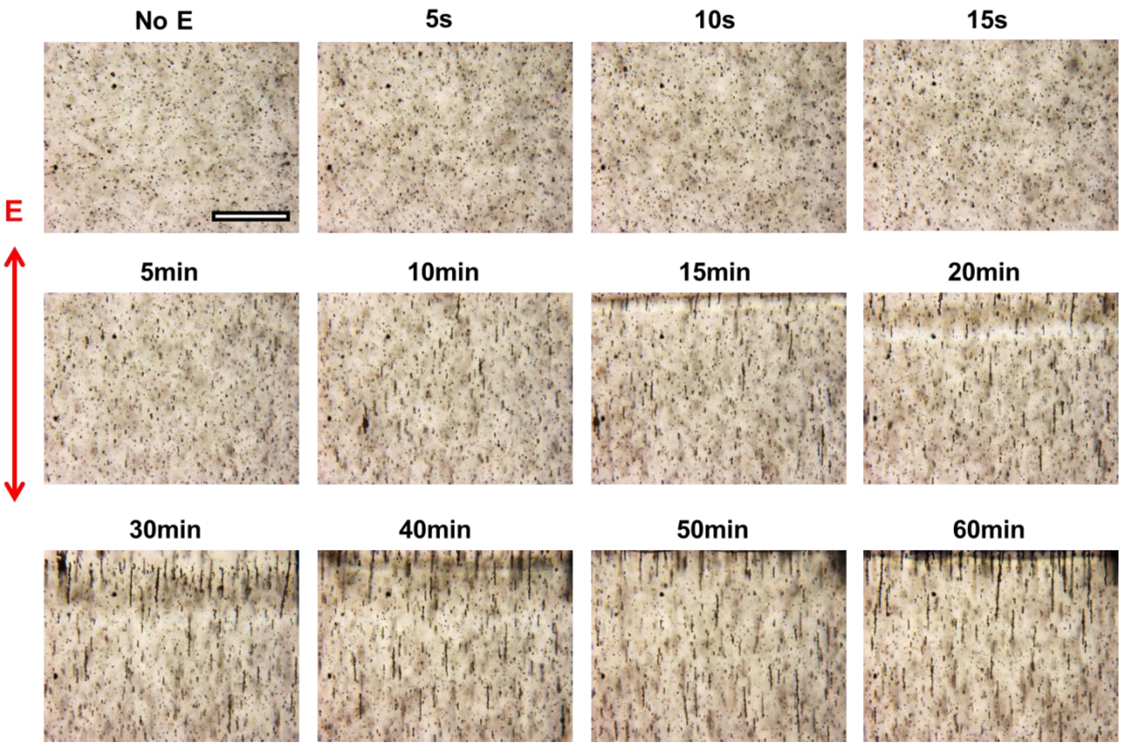

Figure 4.5 Time-evolution of nanoparticles alignment in 1$BaTiO_3$/30PS/Toluene solution covered by glass slide under electric field (1000V/mm) by optical microscopy (scale bar: 100μm).

The solvent evaporation rate in these two experiments are different with that in “Z” alignment experiment which is somewhere between the rate of these two experiments. In both of the two in-plane experiments, the images show the procedures of fast formation of short chains once applying electric field and slow growth into longer chains. Thus the chain formation in “Z” alignment must be similar, which can explain the light transmission change at stage I, II and III.

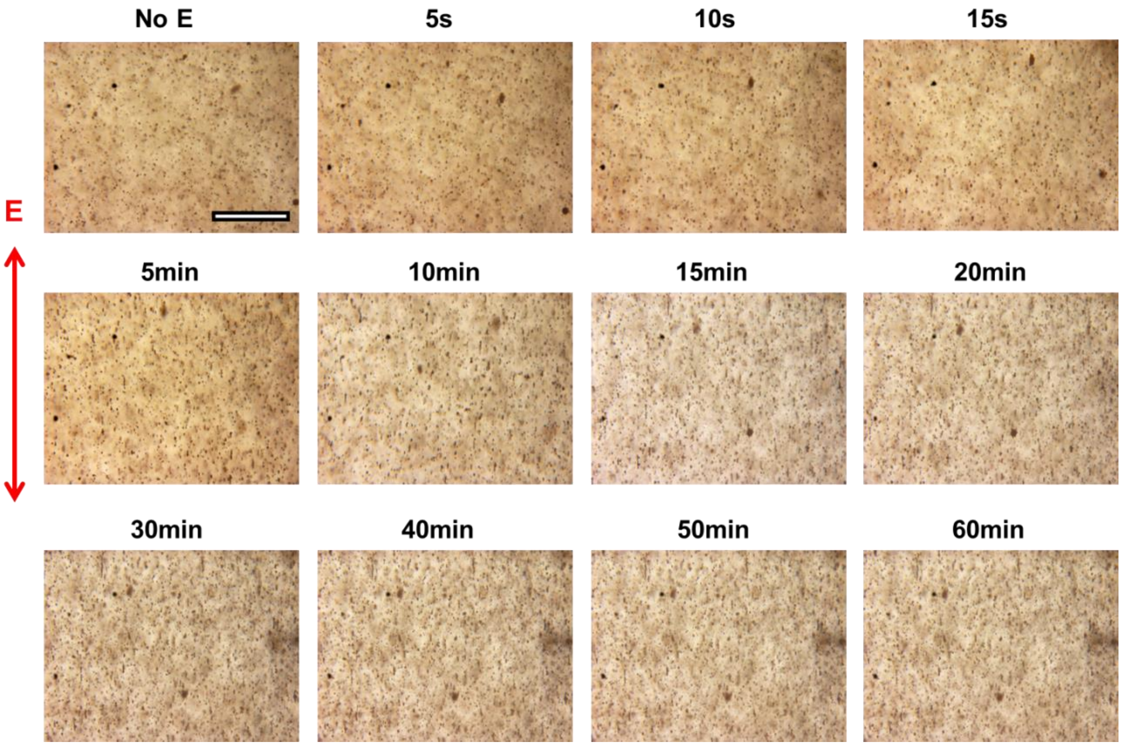

Figure 4.6 Time-evolution of nanoparticles alignment in 1BaTiO_3/30PS/Toluene solution without glass cover under electric field (1000V/mm) by optical microscopy (scale bar: 100µm).

After drying, the morphology of nanocomposite films with 1 wt.% particle content under different electric field strengths was studied in Figure 4.7-10. The morphology throughout the thickness was studied by taking a series of images from the bottom to top of the sample and creating one composite image. Transparent yellow dots are placed on all the particles to enhance their contrast. In all the samples, the particles form chains due to the dipole-dipole interaction under electric field as expected. Interestingly, the axes of particle chains are not along the electric field direction when the electric field strength is weak (500V/mm and 1000V/mm) in Figure 4.7 and 4.8, which is caused by thickness reduction during drying. There’s an angle between the axes and electric field direction and the angle become smaller as the electric field strength increases (1500V/mm) shown in Figure 4.9. Nearly vertical alignment of particles can be achieved in Figure 4.10. As electric field increases the particle chain axes become more parallel to the field direction and hence the light transmission is higher as discussed in the manuscript. Although bucking phenomena of particle chains can be observed, there’re very few particle chains throughout the thickness of film due to the low particle content (1 wt.%). To have a better understanding of the morphology, higher particle content is needed. However, the solution with higher than 1 wt.% content is too opaque for the light transmission measurements. PS/$BaTiO_3$ nanocomposite films with 10 wt.% particles are prepared to study the morphology of aligned samples (without the light transmission data), since the light transmission can’t be measured. The morphology results for these samples are discussed below in detail.

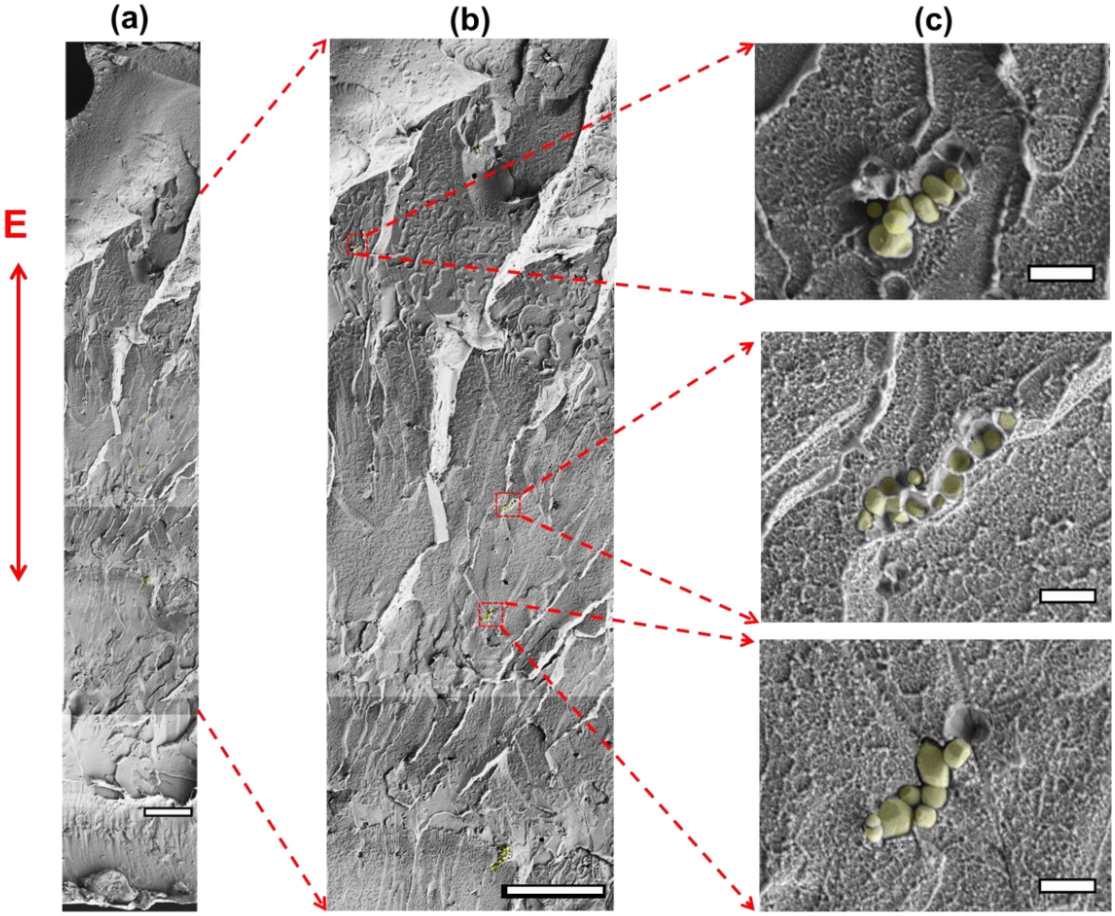

Figure 4.7 Cross sectional morphology of nanocomposite film with 1 wt.% $BaTiO_3$ in PS prepared under 500V/mm. Scale bar: (a) 10 µm, (b) 10 µm, (c) 1 µm

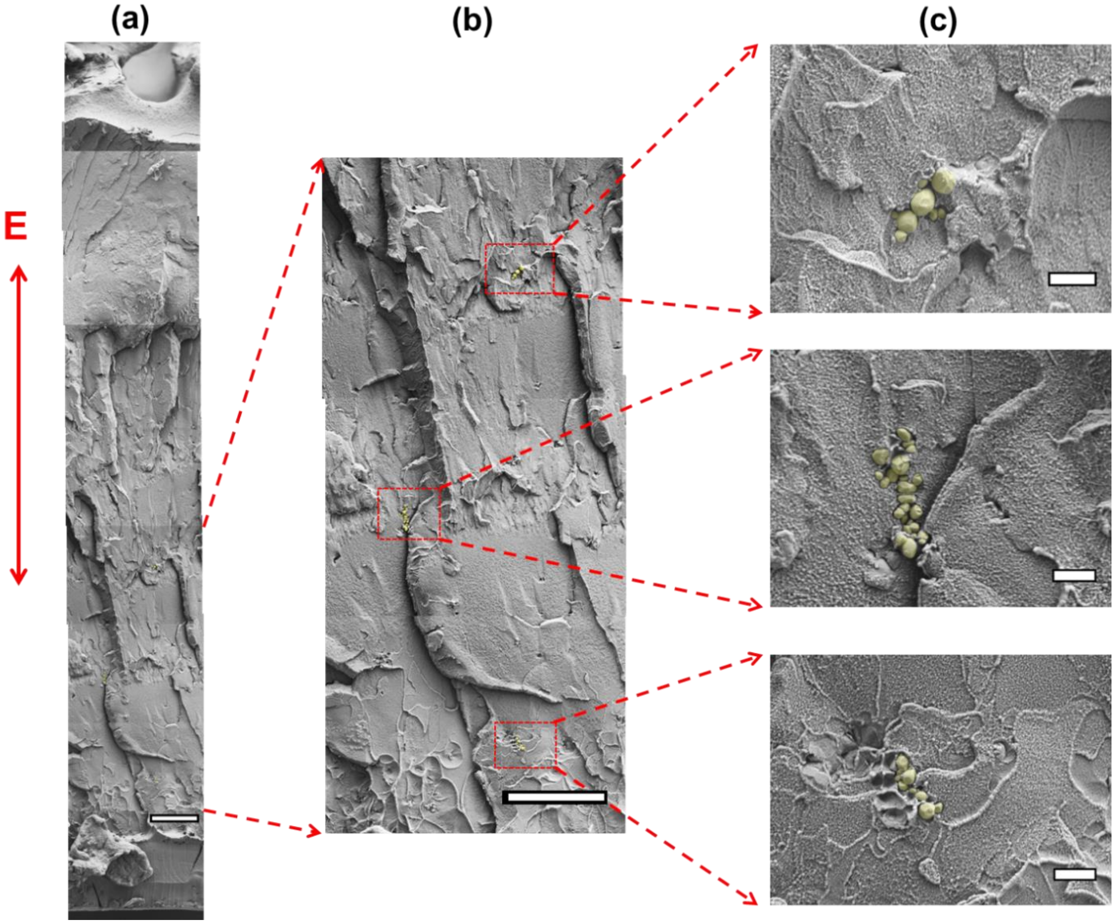

Figure 4.8 Cross sectional morphology of nanocomposite film with 1 wt.% $BaTiO_3$ in PS prepared under 1000V/mm. Scale bar: (a) 10 µm, (b) 10 µm, (c) 1 µm

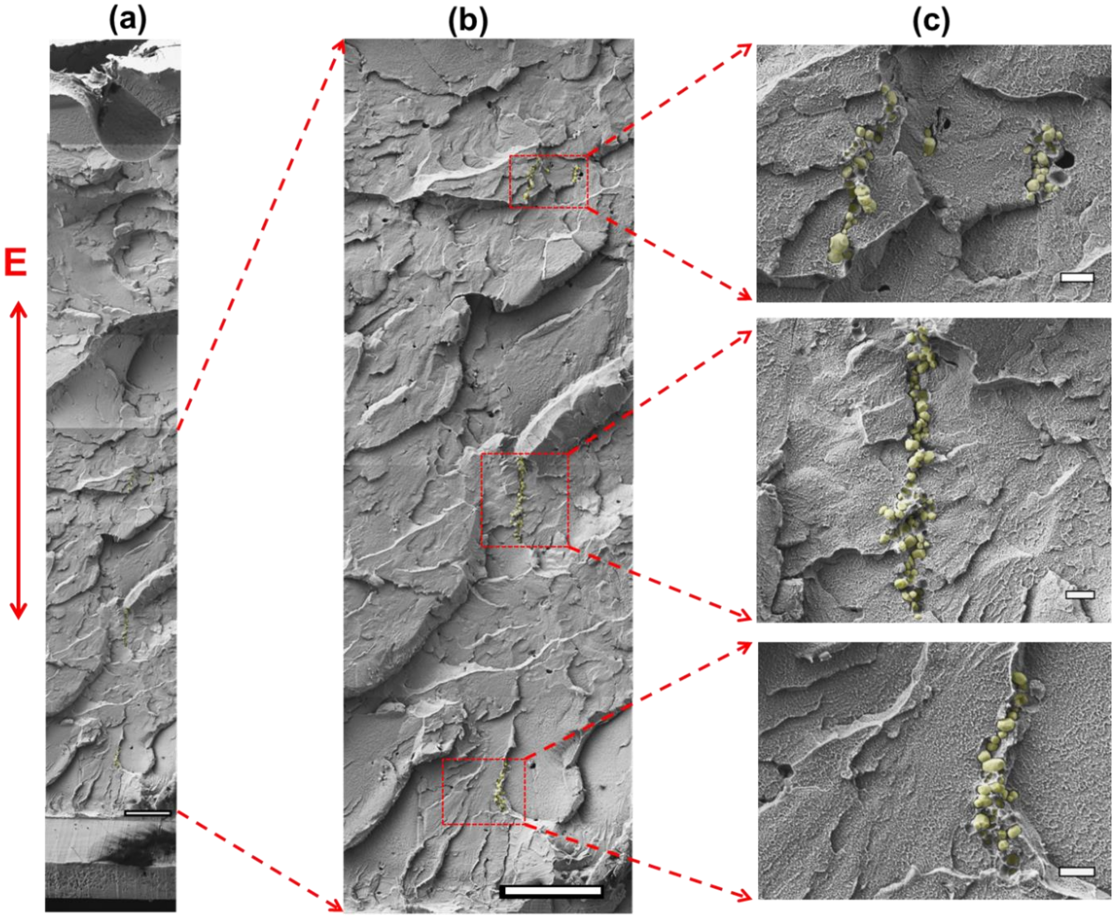

Figure 4.9 Cross sectional morphology of nanocomposite film with 1 wt.% $BaTiO_3$ in PS prepared under 1500V/mm. Scale bar: (a) 10 µm, (b) 10 µm, (c) 1 µm

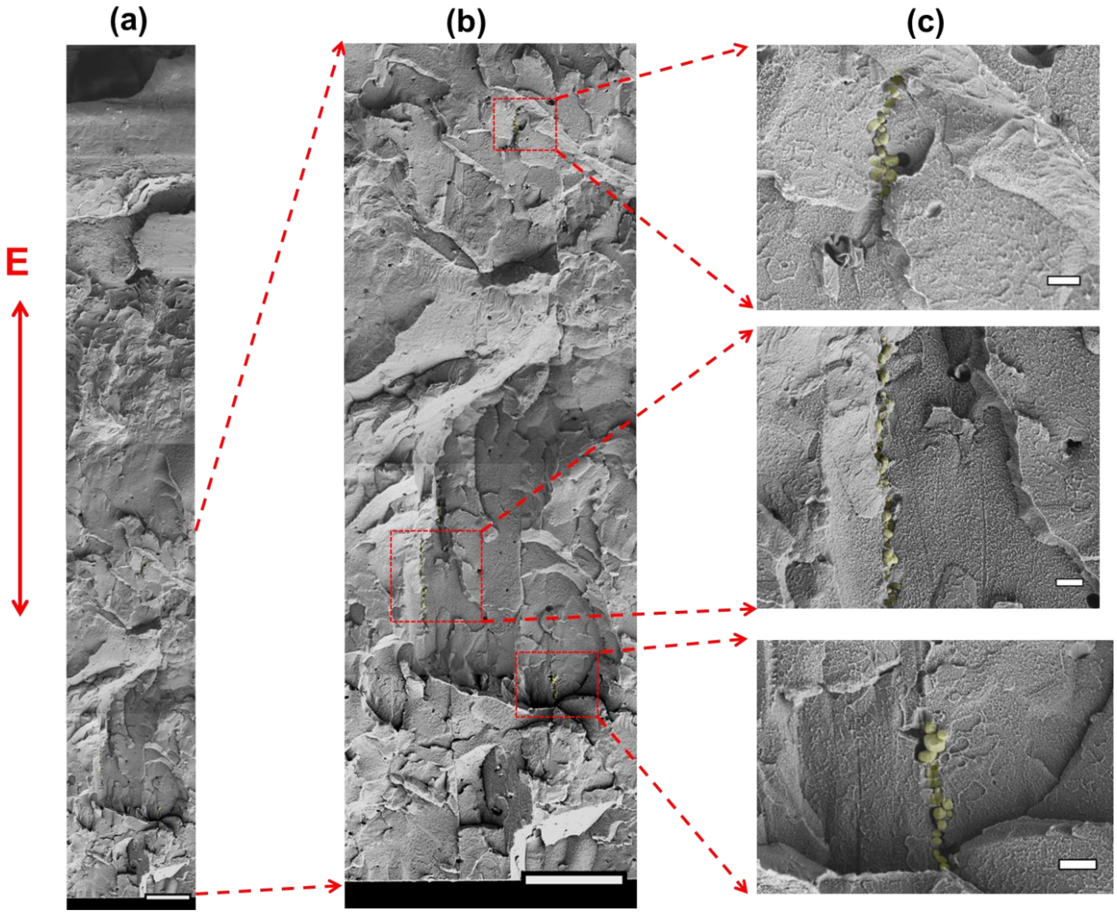

Figure 4.10 Cross sectional morphology of nanocomposite film with 1 wt.% $BaTiO_3$ in PS prepared under 2000V/mm. Scale bar: (a) 10 µm, (b) 10 µm, (c) 1 µm

4.3.2 Effect of electric field strength on particle chain morphology and orientation

PS/$BaTiO_3$ nanocomposite films with 10 wt.% particles are prepared by "cell" method under varying electric field strengths. Figure 4.11 shows the cross sectional morphology of the film prepared under 1000 V/mm. The particles are colored yellow (false) in the image to distinguish them from other features. Barium titanate particles form chains as expected under electric field due to dipole-dipole interaction. For UV light/thermal curing system, the axes of particle chains were found to orient parallel to the direction of electric field.[87, 109] As shown in this figure, for the solution system we investigated, an angle between the chain axes and the electric field vector is observed. This angle is caused by the buckling of particle chains leading to decrease in transmitted light intensity during drying discussed in the section above. Another interesting phenomenon is that the particle chains tilt towards the same direction instead of randomly in the region as shown in the enlarged image.

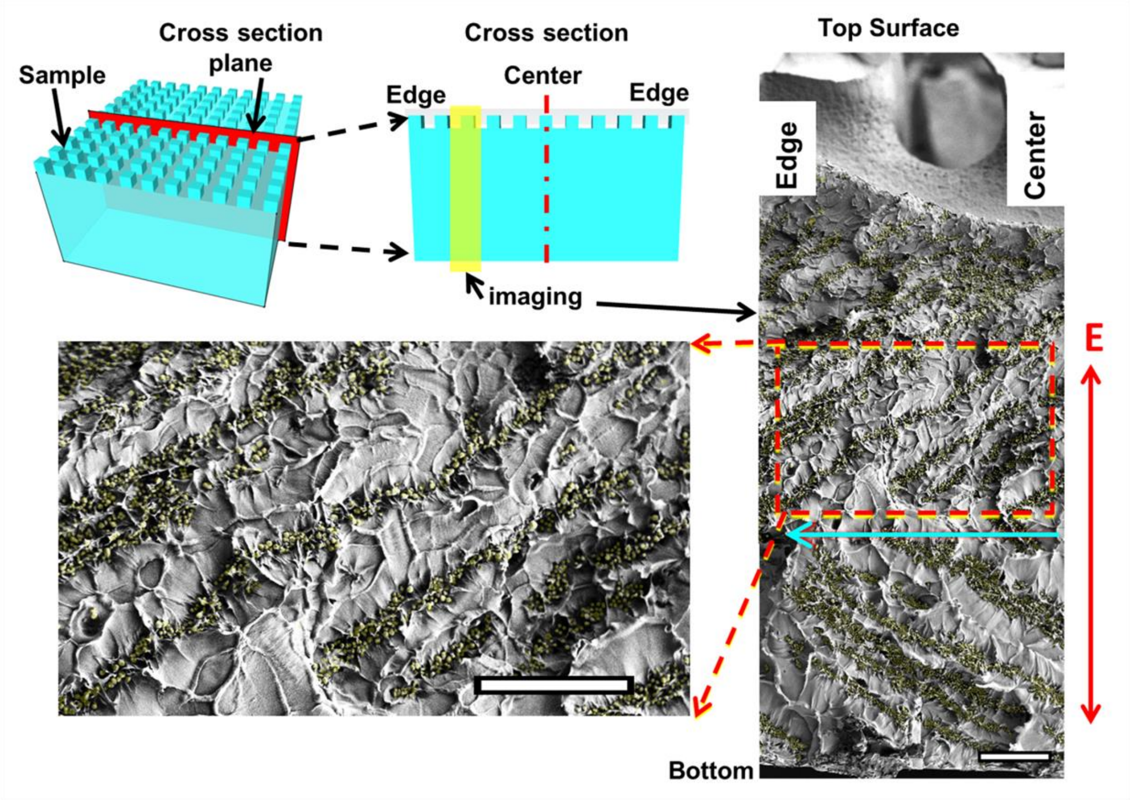

Figure 4.11 SEM cross sectional morphology of the composite film prepared by cell set up under 1000V/mm (scale bar: 40 µm).

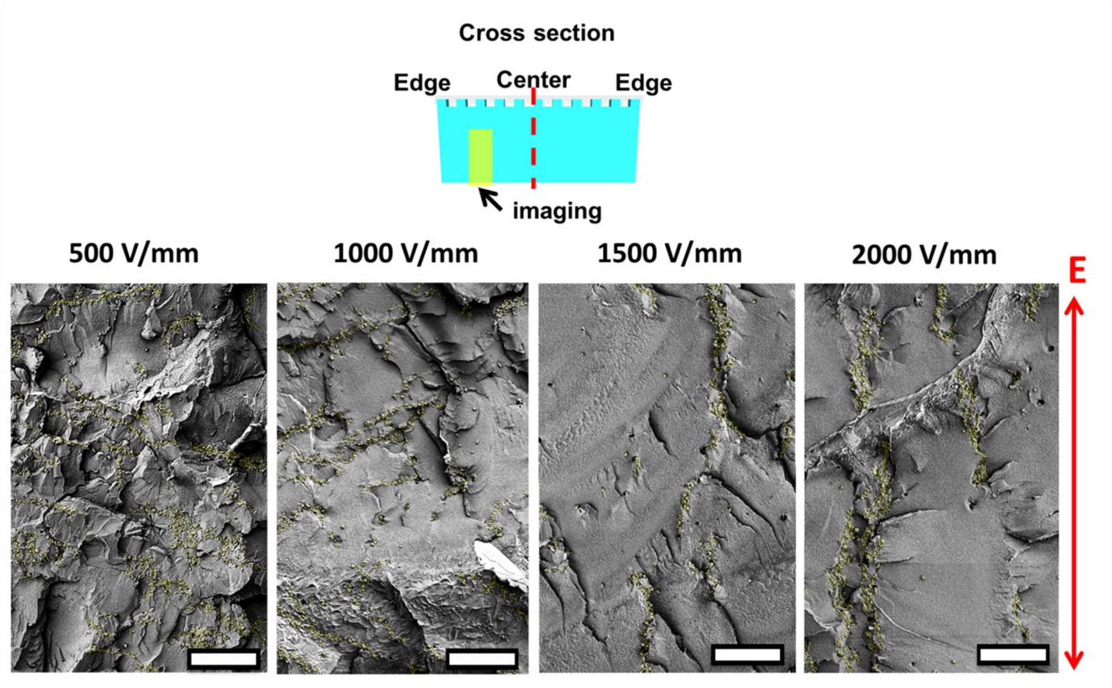

Figure 4.12 Effect of electric filed strength on the tilt angle of particle chain axes (scale bar: 20μm).

As the electric field strength increases, the particle chain axes increasingly become oriented along the electric field direction (Figure 4.12). The angle between the chain axis and electric field vector is defined as θ. The angle distribution, average angle and orientation factor of tilted chains were quantified as shown in Figure 4.13. When the initial electric field strength is low, the chain axis orientation distribution is broad. As the initial electric field strength is increased, this orientation distribution becomes narrower and the average angle decreases. Nearly vertically aligned particle chains can be achieved at stronger initial electric field strengths (1500 V/mm and 2000 V/mm), and the average angle decreases to 17 and 10°, respectively. The Herman's orientation factor[153] (defined in equation 4.1) of particle chain axes relative to the film's normal direction increases from 0.38 to 0.97 (=1 representing perfect orientation of the axes relative to the reference direction which is thickness direction in our case) with increasing electric field strength. The better maintenance of vertical alignment of particle chains under stronger electric field leads to higher light transmission observation for the film discussed in the section above. The morphology of samples with 10 wt.% particles is consistent with that of samples with 1 wt.% particle.

$$S = \frac{1}{2}(3cos^2\theta - 1) \tag{4.1}$$

where, S is the Herman's orientation factor, θ is the angle between particle chain axis and electric field vector.

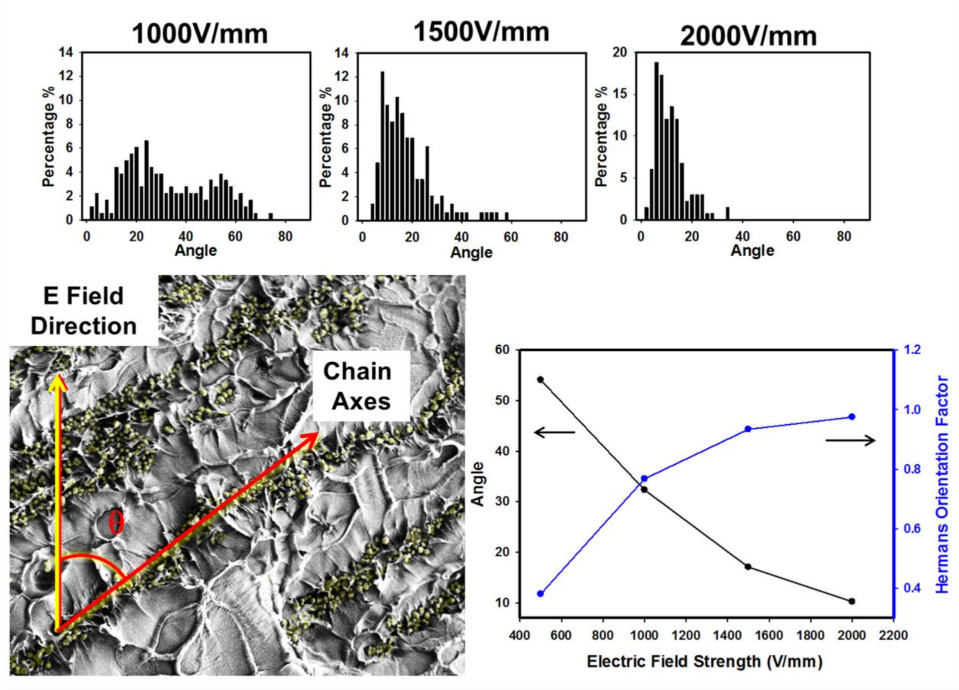

Figure 4.13 Effect of electric filed strength on average angle, angle distribution and Herman's orientation factors.

4.3.3 Drying gradient effect on the tilt direction of particle chain axes

Figure 4.11 shows cross sectional morphology of the sample prepared by “cell” method. At the surface, the chain axes tend to tilt towards the right and near bottom surface they tilt the left. There is a boundary line observed between the right tilted and left tilted chains, and these tilted chains form an arrow pointing towards the edge of the sample. As the solvent evaporates the thickness of the solution film shrinks leading to compression force on the film. Therefore, the matrix bends towards the relatively weaker side, and the particle chain tilts along the matrix, thus forming arrow pointing to one side.

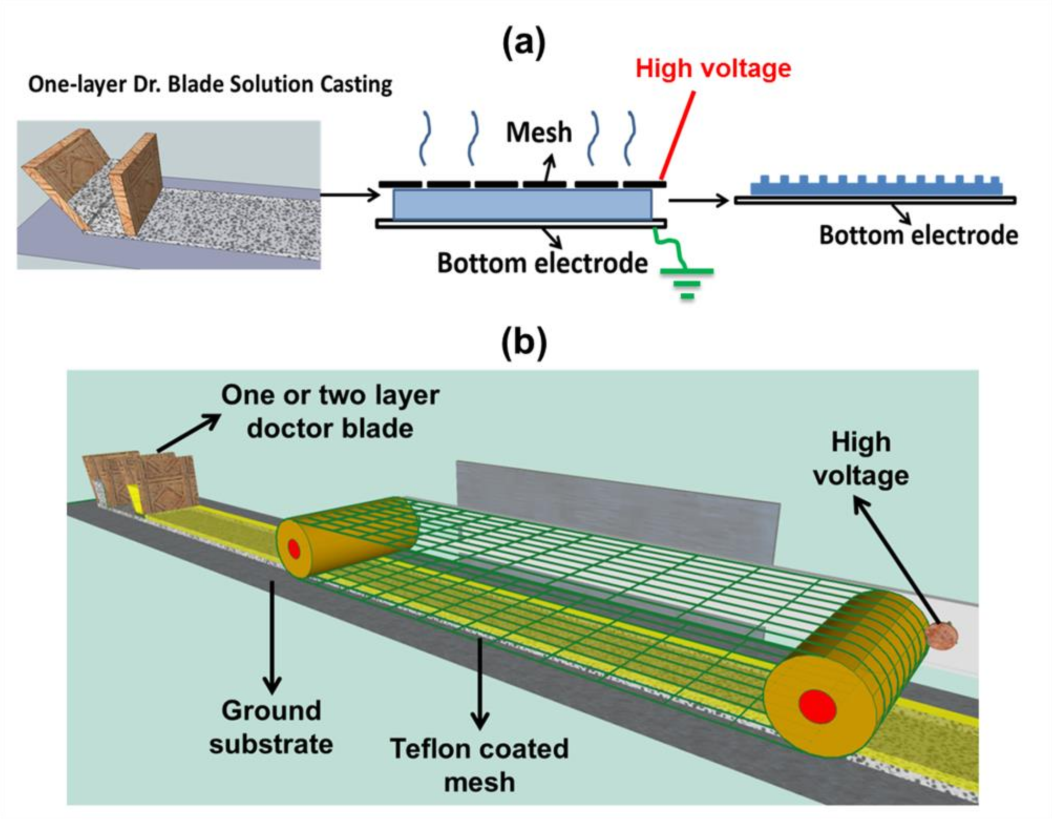

Figure 4.14. Schematic of (a) one layer solution casting method, (b) roll to roll electric field set up for one or two layer solution casting.

Roll to roll solution cast samples are fabricated by the procedures shown in Figure 4.14(a). PS/toluene/barium titanate solution is cast on the stainless steel substrate by one layer doctor blade on a roll to roll processing line.[86, 131] The cast film moves into the roll to roll electric field system shown in Figure 4.14(b). The gap of mesh and bottom electrode is adjusted slightly smaller than the thickness of cast solution film. The top surface of solution film touches and wets the mesh as the film approaching to the electric field setup. Mesh's speed (controlled by the two roller, described elsewhere[109] in detail) is adjusted the same as the speed of stainless steel substrate, thus there is no shear force is generated on the film during the process. Electric field is applied between mesh and stainless steel substrate until all the solvent evaporates. For solution cast samples, long chains form and these chains also tilt due to compression force. However, the chain axes point towards the region closer to the center of the film in the transverse direction shown in Figure 4.15, which is the opposite of the samples prepared in the stationary cell. A global widthwise look at discrete locations at the cross-section of the film along the transverse direction is shown in Figure 4.16. For the left side of the sample, the arrows point to the right, and the arrows in the right region point to the left. The chains all tilt towards the center region of the film in the transverse direction. This phenomenon can be explained by the drying gradient effect difference between these two processing methods.

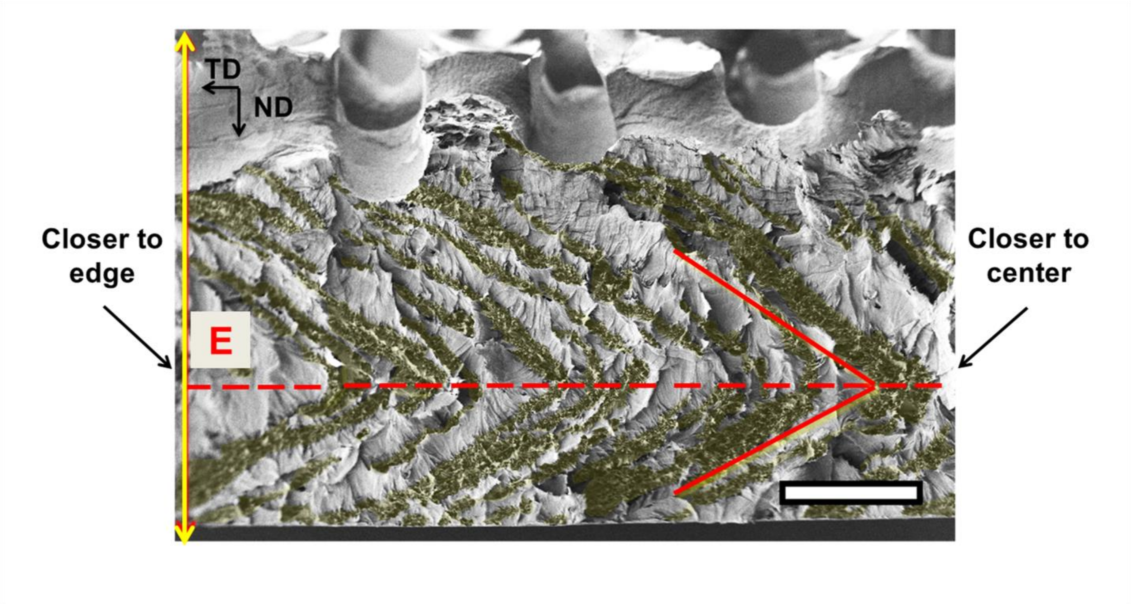

Figure 4.15 SEM cross sectional morphology of one layer casting composite film under 1000V/mm (scale bar: 50µm).

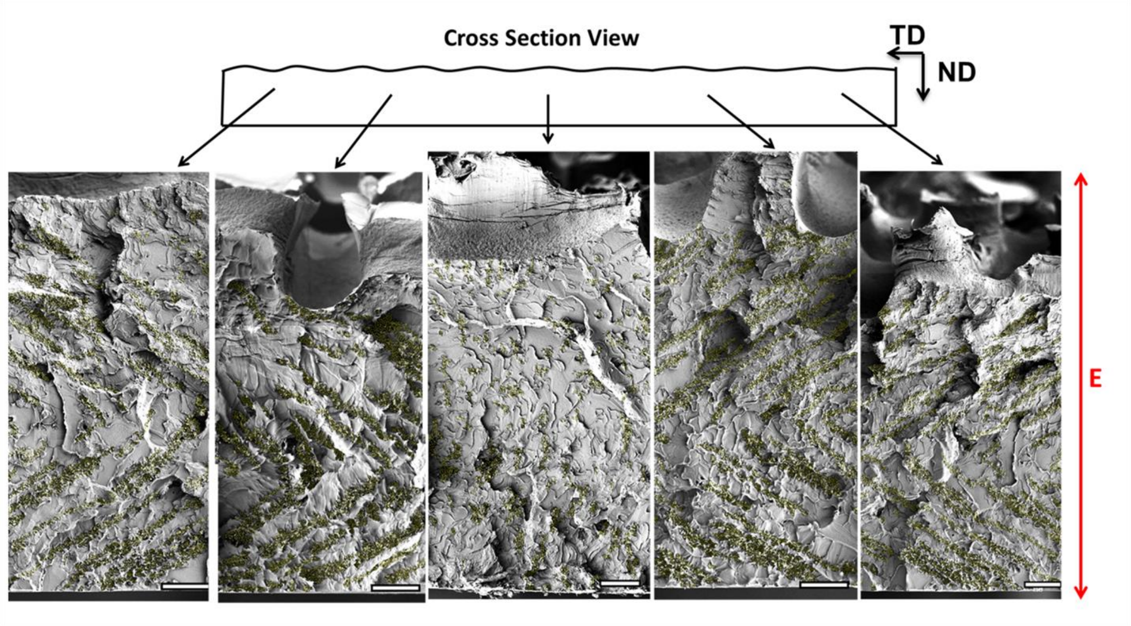

Figure 4.16 A global widthwise cross sectional morphology at discrete location along transverse direction of composites prepared by solution casting under 1000 V/m (scale bar: 30µm).

For the film prepared in the cell, the center part dries faster than the edge due to the blocking effect of the spacer[100] as shown in Figure 4.17. Under the influence of central shrinkage, the matrix film itself tends to bend towards the softer side (edge). Thus the particle chains inside the matrix bend to form an arrow pointing to the region closer to the edge, and a structure shown in Figure 4.17 can be obtained in the film prepared in cell. While for the R2R solution cast films, the drying gradient is opposite because the film is free at the edge. As shown in Figure 4.17, the edge region dries first and there is a solvent concentration gradient in width direction, thus creating a modulus gradient along the transverse direction. The chains tend to form the arrow bending towards the center region shown in Figure 4.17. By controlling the drying gradient one can control pointing direction of the arrow formed with the chain axes.

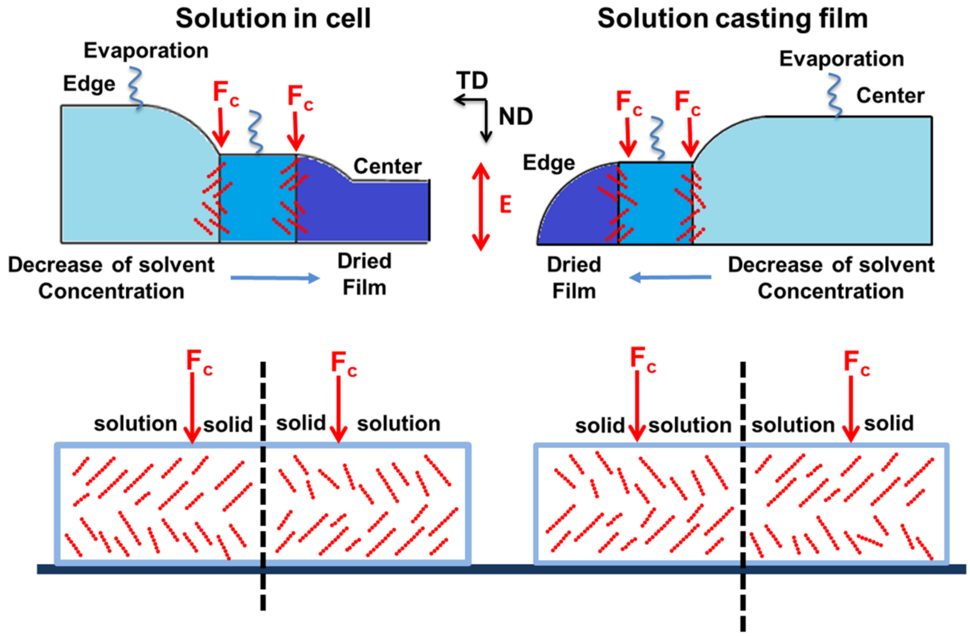

Figure 4.17 Schematic explanation of tilt direction of particle chains for cell and solution casting films.

4.3.4 Two-layer solution casting method to eliminate the imprinted pattern

After drying, the mesh can be peeled off from the film easily, but the imprint pattern is left behind on the top of the one layer film replicating the wire mesh electrode, as shown in Figure 4.18. To eliminate the top pattern, the two-layer solution casting method is developed as shown in Figure 4.19. Two-layer solution film is cast by the two layer doctor blade. The top polymer (PB) is immiscible with the bottom polymer (PS) and top solvent (THF) is miscible with the bottom solvent (toluene). Thus the top and bottom polymers are immiscible with sharp interface between them and solvent in the bottom layer can evaporate through the top layer. The mesh only touches the top layer solution so the imprint pattern only remains on the top layer which acts as sacrificial layer. The particles in the composite bottom layer can be aligned to from chains under electric field. Figure 4.20(a) shows the cross sectional morphology of two-layer composite film with aligned nanocolumns. A sharp boundary is observed between the two polymer layers and the particles are aligned to form chains in Z direction in the composite bottom layer. The cross sectional and surface morphology of the composite bottom layer peeling off the top layer are shown in Figure 4.20(b) and (c), respectively. After peeling off the top layer film, the vertically aligned particle chains still can be observed in the composite bottom layer while its top surface remains smooth from both side and top views.

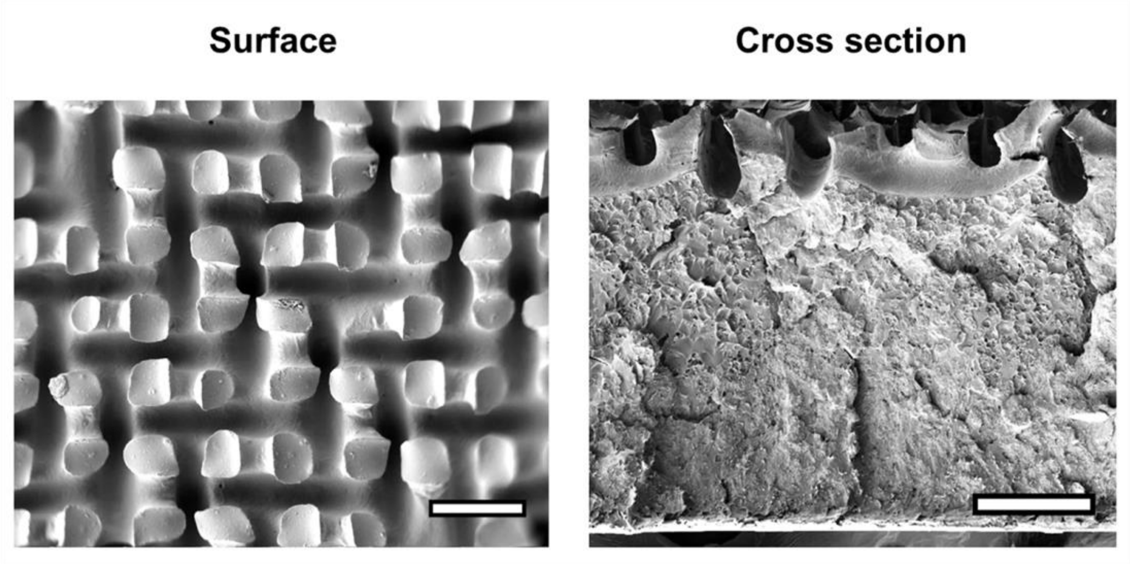

Figure 4.18 Surface and cross section morphology of one layer composite film after peeling off the mesh (scale bar: 100μm).

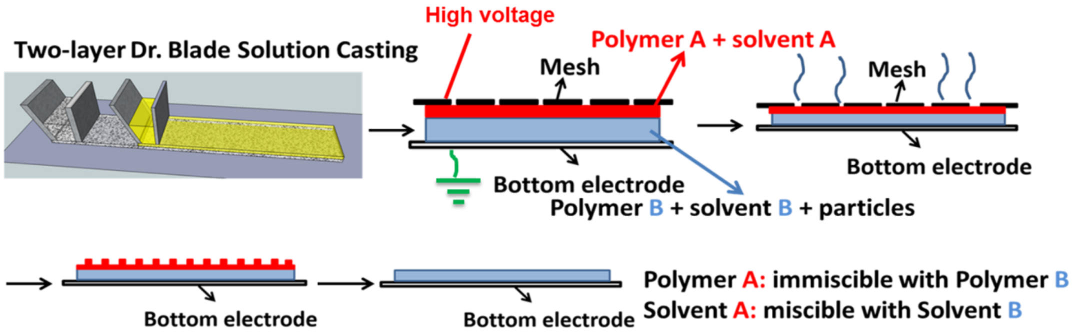

Figure 4.19 Schematic of roll to roll two-layer solution casting method.

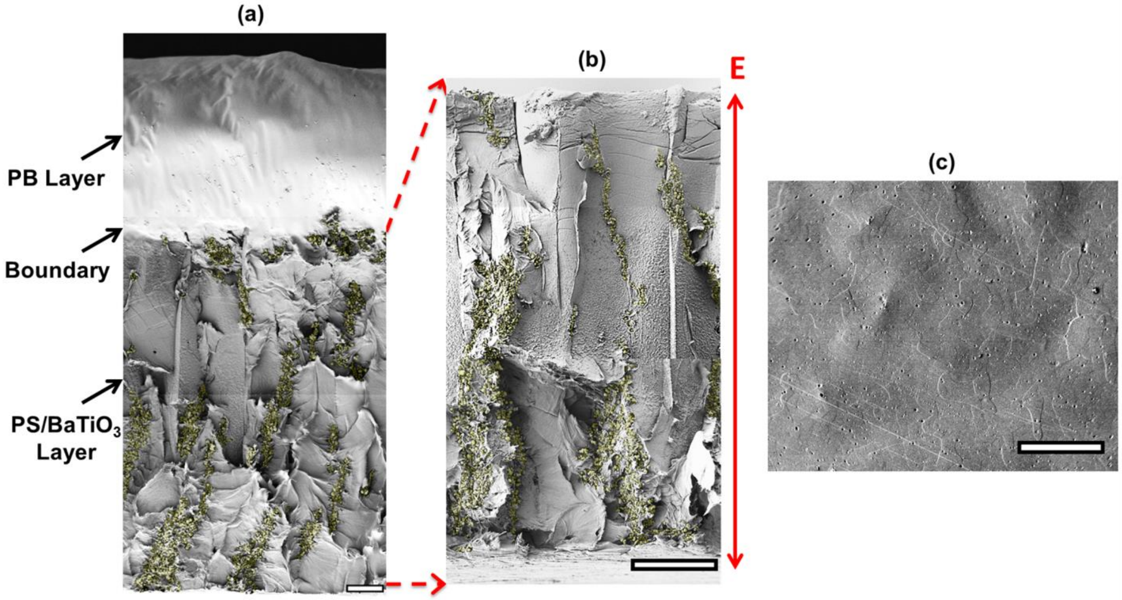

Figure 4.20 SEM cross sectional morphology of two-layer method prepared films with aligned particles (a) before and (b) after peeling off the top layer (scale bar:20µm), (c) surface of composite bottom layer after peeling off top layer (scale bar: 100µm).

4.3.5 Dielectric permittivity enhancement in aligned nanocomposites

Figure 4.21(a) shows the dielectric permittivity of pure PS film and PS/BaTiO$_3$ nanocomposite films with patterned surface from 1 kHz to 1 MHz. Pure PS film has low dielectric permittivity (2.79) at 1 kHz, and the dielectric permittivity increases to 3.28 after adding randomly distributed barium titanate particles (no E). The nanocomposites prepared under electric field have higher dielectric permittivity, and the stronger of the electric field strength, the larger dielectric permittivity as the stronger electric field strength leads to better orientation of particle chains. Figure 4.21(b) shows the effect of orientation factor of particle chains on the dielectric permittivity of nanocomposite film with patterned surface at 1 kHz. The dielectric permittivity increases with the orientation factor of particle chains. The dielectric permittivity can be increased by 43% for nanocomposite with highest orientation factor than the patterned film with random particles. The dependence of dielectric loss on the frequency is shown in Figure 4.21(c) and it shows that the dielectric loss is quite low and it increases slightly after adding random the $BaTiO_3$ particles into PS. The dielectric loss slightly increases with the higher orientation of particle chains due to the enhanced interfacial polarization between particles but remains very low less than 0.003 even at highest frequencies. Figure 4.22(a) shows the dielectric permittivity of nanocomposites with smooth surface prepared by two-layer solution casting method. The PS film with smooth surface has slightly higher dielectric permittivity (2.86) than the PS film with patterned surface. The nanocomposites with aligned nanocolumns exhibit 42% higher dielectric permittivity than the smooth film with random distribution of particles. Figure 4.22(b) shows the dependence of dielectric loss on frequency for the nanocomposite film with smooth top surface. The dielectric loss of the film with smooth surface shows smaller dielectric loss than the film with patterned surface due to fewer voids on the surface. The film with aligned particles shows larger dielectric loss than the film with random particles. The loss values are all remaining at very low levels.

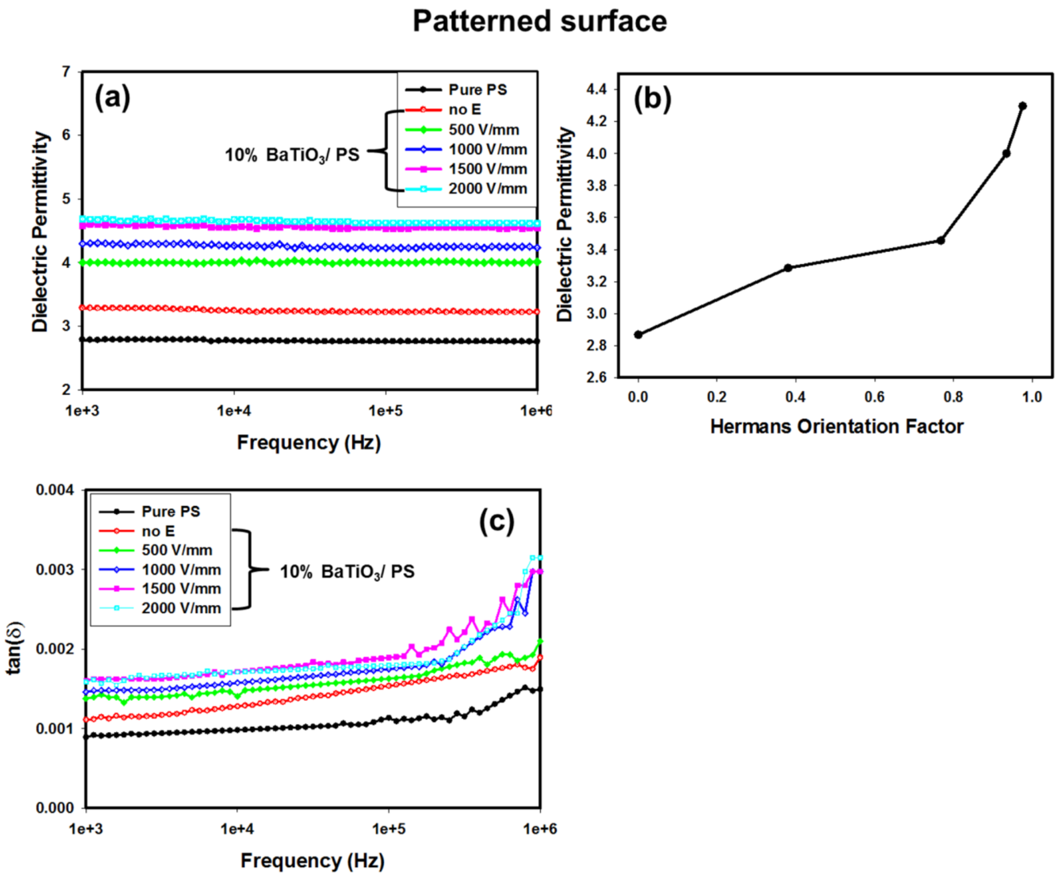

Figure 4.21 (a) Dependence of dielectric permittivity on frequency of PS/BaTiO$_3$ nanocomposites with patterned surface, (b) Effect of orientation factor of particle chains on dielectric permittivity of film with patterned surface at 1 kHz, (c) Dependence of dielectric loss tan δ on frequency of PS/BaTiO$_3$ nanocomposites.

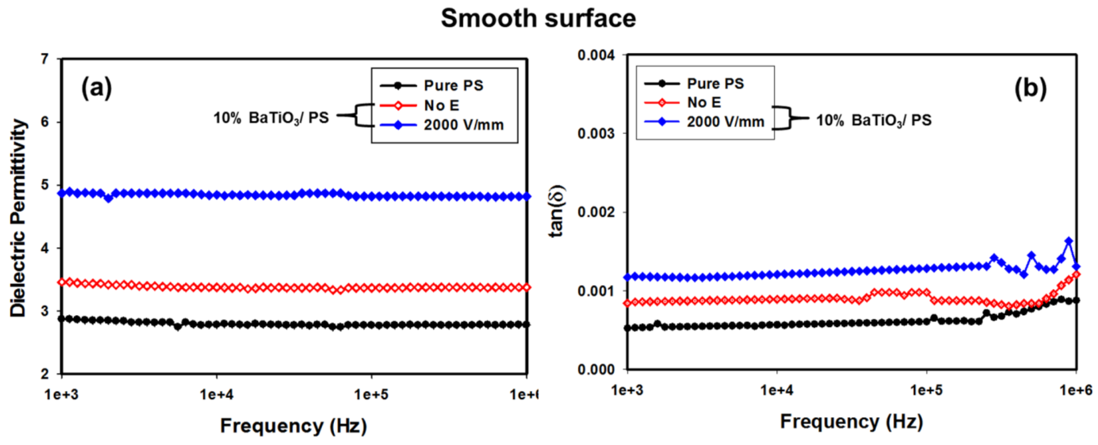

Figure 4.22 Dependence of (a) dielectric permittivity and (b) dielectric loss tan δ on frequency of PS/$BaTiO_3$ nanocomposites with smooth surface.

4.4 Conclusion

A continuous processing method is developed for aligning nanoparticles vertically under electric field in the polymer solutions. This method broadens the choice of polymers to use as matrices to produce functional films with aligned nanoparticles. The kinetics of particle organization with electric field was investigated by optical light transmission that was found to be sensitive to track nanocolumn formation and their eventual buckling as a result of solvent loss related shrinkage. The particle chain axes form first in solution and as the film dries these columns buckle at mid-section when low electric field is used. The use of high electric fields overcomes this effect and these nanocolumns remain oriented along the field direction despite the thickness direction shrinkage take place during drying. We also discovered that the direction “arrow” morphology formed of buckled columns. The tilt direction of particle chains can be controlled by the drying gradient. The patterned surface created by the porous electrodes on the top surface can be eliminated by using the two layer solution casting method that uses two immiscible polymers with solvents that are miscible with each other facilitating drying of both layers. The nanocomposites with aligned particles in Z direction show substantially enhanced dielectric permittivity in thickness direction.

Reproduced in part with permission from Guo, Y.; Batra, S.; Chen, Y.; Wang, E.; Cakmak, M. Roll to Roll Electric Field “Z” Alignment of Nanoparticles from Polymer Solutions for Manufacturing Multifunctional Capacitor Films. ACS Applied Materials & Interfaces 2016, 8, 18471. Copyright [2016] ACS Publications, Inc.

CHAPTER V

ANISOTROPIC SWELLING WOUND DRESSING WITH “Z” ALIGNED WATER ABSORPTIVE PARTICLES

Multi-layer solution casting method was utilized to fabricate three-layer wound dressing films forming wound contact layer, absorbing layer and backing layer. The absorbing layer, whose function is to absorb and retain the exudate thus providing moist environment for wound healing, was made up of super absorbent particles and thermoplastic polyurethane. In this study, the superabsorbent particles were aligned along chain structures whose axes oriented along the film thickness direction by external electric field during film formation. This lateral swelling of the absorbing layer while preferentially expanding in thickness direction during water absorption process, and therefore eliminating the lateral stress or shear induced friction between the dressing films and the wound. Compared to the films with non-aligned particles, the aligned wound dressings could achieve up to 33% smaller lateral expansion. The effect of particle shape on anisotropic swelling was also investigated, and it was found out that rod-like particles with high aspect ratio were more effective to improve anisotropic swelling and reduce lateral expansion compared to irregular shape particles. Additionally, the imprinted patterns on the contact layer resulting from the electric field alignment process promoted the efficiency of absorbing and transporting the exudate into absorbing layer.

5.1 Introduction

Wound healing is a very complex biochemical and cellular process, which comprises five overlapping stages including haemostasis, inflammation, migration, proliferation and maturation phases.[154, 155] Once the haemostasis stage is achieved, exudate that is essentially blood free of red cells and platelets is produced by the wound for both acute and chronic wound.[156, 157] The exudate plays an important role for wound healing by keeping a moist environment[158] and supplying nutrients, mitosis of epithelial cells and leucocytes to aid the wound healing as well as to prevent wound from infections.[159] In some severe cases such as deep acute wound and chronic wound, the wound produces excess amount of exudate, which to can inhibit the wound healing and corrupt the healthy skin around the wound due to the high level of proteinase enzymes.[160, 161] Traditional wound dressings such as cotton wool, natural bandage, lint and gauze were commonly used for wound care in the past.[162] These traditional wound dressings could absorb the exudate and prevent the wound from infection by bacteria, but they failed to restrain the evaporation of moisture, which resulted in the wound becoming overly dried. Furthermore, their adhesion to the wound could cause overwhelming discomfort and pain, or even more tissue damage during the removal of the wound dressings. Recent research has found out that warm and moist wound environment can help accelerate healing.[154]

Therefore, polymer-based wound dressing that is able to absorb and retain the excess exudate, hence maintaining moist environment and also show no or less adhesion to the wound is desirable.[162]

A number of polymer-based wound dressings have been developed to promote the wound healing and may be classified into: hydrocolloid dressing[163], alginate dressing[164], hydrogel dressing[165] and collagen dressing[166] based on the materials used to fabricate them. Among them, hydrocolloid dressing, which is a semi-permeable polyurethane film with absorbent particles[162, 167] is the most widely used, ascribed to the fact that the absorbent particles inside provide excellent exudate absorption capacity, and become gels after absorption to induce fast healing rate and less pain.[168, 169] In addition to absorption capacity, the ability to retain the moisture is also crucial for wound dressings. Nevertheless, traditional single layer wound dressings were insufficient to withhold the absorbed moisture due to the high moisture vapor transportation rate (MVTR), which could cause the desiccation of wound.[170] Therefore, multilayer wound dressings that consist of liquid repellent backing layer, absorbent layer and wound contact layer are developed to absorb and also to retain the exudate, benefiting from a better control on the MVTR of the backing layer.[170, 171] Currently, the remaining issue about multilayer wound dressings is that the highly absorptive layer undergoes a large lateral expansion after absorbing the exudate, which may cause lateral shearing or friction stress to the wound.

This stress hinders the wound healing and may cause further sores especially for the extremely fragile wound such as leg ulcers and pressure sores.[171]

To solve this problem, many efforts have been made to develop anisotropic polymer films for the absorbing layer to transfer the lateral expansion to vertical expansion. Tisato K. et al.[172] fabricated stearyl acrylate (SA)/ acylic acid (AA) copolymer gel film with the lamellar layer aligning parallel to film surface and alkyl chains oriented in thickness direction ("Z" direction). When such films were immersed in ethanol, their swelling ratio in "Z" direction was 40% larger than in-plane direction due to the anisotropic crystal structure. Nicholas P. et al.[173] prepared a polymer gel of nematic liquid crystalline (NLC) poly (γ-benzyl L-glutamate) (PBLG) with its helix axis oriented along the surface of film by external magnetic field,[174] the swelling ratio of which in "Z" direction was two times of in-plane swelling ratio in dichloroacetic acid. This was attributed to the fact that the mechanism of swelling in NLC state was the insertion of solvent between the parallel helix, which mainly contributed to vertical expansion.[173] However, the films in the above studies didn't show anisotropic swelling behavior in water. To achieve anisotropic swelling in water, Gudmundur S.[175] reported a multilayer wound dressing with a specially processed absorbent layer: the absorbent core was drilled with sub millimeter sized cylindrical receptacles vertically in a predetermined pattern, and these cylindrical compartments were filled with superabsorbent. The wound contacting layer was also drilled with large number of apertures so that the absorbent layer could attract exudate due to capillary action. Then the vertically aligned superabsorbent cylinders would absorb the exudate and expand to push the backing layer in Z direction. However, the preparation procedures in this method involve drilling receptacle, filling superabsorbent and laminating three layers, which are too complicated. The size of vertical cylinder is too large, in the range of sub millimeter causing nonuniformity.

In this study, multilayer wound dressings were fabricated by three-layer solution casting method consisting of wound contact layer, absorbent layer and liquid repellent layer. Irregular shape and rod like water absorptive particles were prepared by cryogrinding and electrospinning methods, respectively. The water absorptive particles were aligned in “Z” direction to form micro or nano size particle chains or cylinders in-situ in the absorbent layer under electric field instead of filling the submillimeter size superabsorbent material afterwards like Gudmundur’s work as stated above.[175] The effect of alignment on anisotropic swelling behavior was studied.

5.2 Experimental section

The materials, preparation of neutralized rods and irregular shape particles, preparation of wound dress and the characterization are described in details below.

5.2.1 Materials

The water absorptive polymers, carbopol 981NF and carbopol 907, were supplied by the Lubrizol Corporation and used to prepare water absorptive particles. The solution processing grade thermoplastic polyurethanes (TPUs), SP80A150 and HP60D20, were also provided by the Lubrizol Corporation. 1,4-dioxane (ACS reagent, ≥99.0%), N,N-dimethylacetamide (DMAc) (ACS reagent, ≥99%), polyethylene glycol (PEG) (Mn=400g/mol), sodium chloride (ACS reagent, ≥99%), calcium chloride dihydrate (ACS reagent, ≥99%) and sodium hydroxide (NaOH) (reagent grade, ≥98%, pellets) were purchased from Sigma Aldrich. Teflon coated stainless steel mesh (325×325) obtained from TWP. Inc. was used as the top electrode. Indium Tin Oxide (ITO) coated glass supplied by Structure Probe, Inc. was used as the bottom electrode. The alternating current (AC) voltage was generated by high voltage (HV) amplifier (AMP-20B20, Matsuda Precision Inc.)

5.2.2 Preparation of neutralized nanorods

12wt.% carbopol 907 (liner polyacrylic acid (PAA), non-crosslinked) aqueous solution was prepared by using paddle mixer, and this solution was neutralized by sodium hydroxide aqueous solution (18 wt.%) until the pH value of the solution was 7.0 which was denoted as 100% neutralization. The water absorptive ability of PAA increases with the percentage of neutralization, so PAA 100% neutralization has high water absorptive ability and is safe for wound dressing application. 3% wt.% PEG with respect to carbopol 907 was added into the solution above to act as the cross linker. Electrospinning technique was used to prepare 100% neutralized PAA nanofibers. The electrospinning condition was set as: 25 Gauge needle, 22 kV voltage and 13cm target distance. After collecting enough nanofibers to form a nanofiber mat, the PAA nanofiber mat was kept in oven at 190^{o}C for 7 mins to be cross linked by esterification reaction between polyacrylic acid and PEG. The cross-linked and neutralized nanofiber mat was placed in container with ceramic balls and chopped into PAA nanorods by ball grinding in Thinky mixer at 2000 rpm for 2 minutes.

5.2.3 Preparation of neutralized irregular particles

1 wt.% carbopol 981NF (partially crosslinked PAA) aqueous solution was prepared by using paddle mixer, and the solution was neutralized by sodium hydroxide aqueous solution (18 wt.%) till 100% neutralization. The solution above was cast into 3mm thick film and dried at 80 ^{o}C overnight. The dried film was ball grinded into large irregular particles in Thinky mixer at 2000r/min for 5 minutes. Then the large PAA irregular particles were grinded into smaller irregular particles by cryogrinding method.

5.2.4 Preparation of three-layer TPUs film with "Z" aligned nanorods or particles

The two-step preparation procedures were used to prepare the random or aligned three-layer TPUs films as shown in Figure 5.1. The solution of 15 wt.% HP60D20/DMAc was cast on the ITO coated glass (bottom electrode) at 0.5 mm thickness by doctor blade and dried at 50 ^{o}C for 12 hours, and this layer of film was marked as layer "A". Herein, HP60D20 and SP80A150 were denoted as TPUs1 and TPUs2, respectively. In the second step, the two-layer solution casting method was used to cast the other two-layer solution films on the top of dried TPUs1 film showing in Figure 5.1. The solution of middle layer was 19 wt.% TPUs2/dioxane solution with various concentrations of neutralized nanorods or irregular particles. The solution of top layer was 19 wt.% TPUs2/dioxane solution. Then this three-layer solution film was covered by Teflon coated mesh (top electrode).[29] 600 V/mm (AC) initial electric field was applied between mesh and ITO glass for 6 hours until all the solvent evaporated. The middle and top layer of dried film was marked as layer "B" and layer "C", respectively. The swelling ratio of TPUs1, TPUs2, nanorods and irregular particles in solution A are 0.1, 1.2, 30 and 32, respectively.

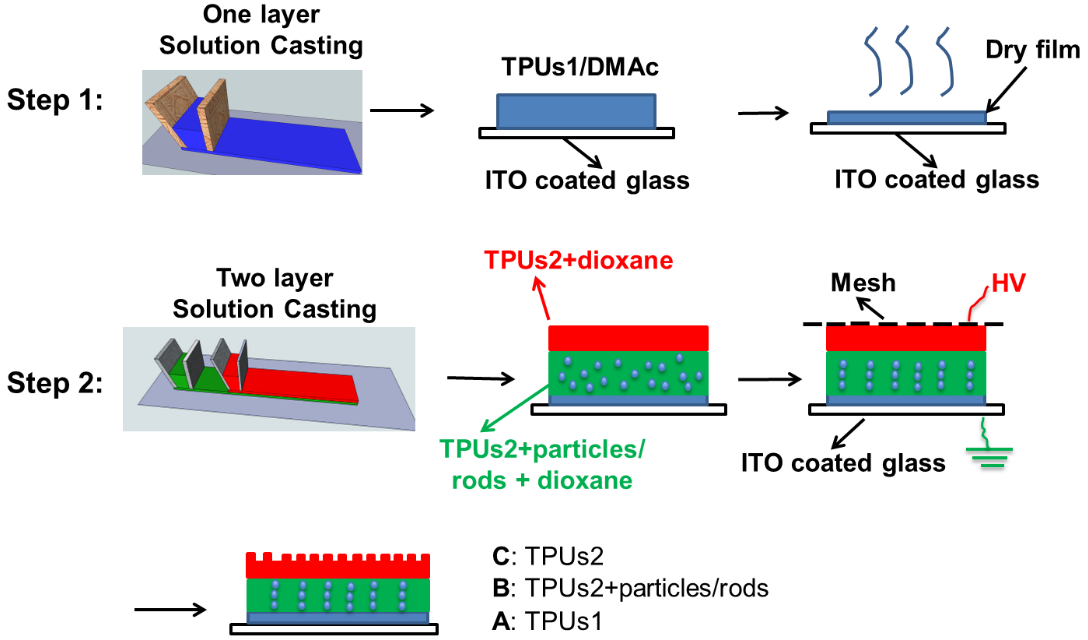

Figure 5. 1 Procedures to prepare the three-layer wound dressing.

5.2.5 Morphological characterization

The morphology of PAA nanofibers and nanorods was characterized by JEOL-7401 scanning electron microscopy (SEM). The random and aligned three-layer films were fractured in the liquid nitrogen, and the cross sectional morphology was also studied by SEM. All the samples were sputter coated with silver prior to observation. The 3D morphology of random and aligned wound dressing film was characterized by Bruker Skyscan 1172 micro-computed tomography (micro-CT).

5.2.6 Swelling test

The three-layer wound dressing films prepared above were cut into 5.0×5.0 cm square shaped samples and soaked in the solution A for 30 min at 37 ^{o}C. Solution A , an aqueous solution containing almost the same ionic composition as human serum or wound exudate and was prepared by dissolving 8.298 gram of sodium chloride and 0.368 gram of calcium chloride dihydrate in 1 litter of deionized water. The weight, thickness and length before and after swelling were measured to calculate the swelling ratio, in plan expansion ratio, out of plane expansion ratio and swelling anisotropy in equations below:

$$\text{Swelling ratio} = \frac{W_1 - W_0}{W_0} \tag{5.1}$$

$$R_{//} = \frac{L_1}{L_0} \tag{5.2}$$

$$R_{\perp} = \frac{D_1}{D_0} \tag{5.3}$$

$$\text{Swelling anisotropy} = \frac{R_{\perp}}{R_{//}} \tag{5.4}$$

where W, L and D is weight, length and thickness of the film, respectively. 0 and 1 represent before and after swelling, respectively. $R_{//}$ and $R_{\perp}$ are in plane and out of plane expansion ratio, respectively.

5.2.7 Moisture vapor transmission rate (MVTR)

The three layer wound films were sealed on the top of a cup with inner diameter 35.7 mm containing 20 ml solution A. The cup was right-side up and kept in an incubator at 37 °C and with humidity of less than 20 %. MVTR is calculated as follow:

$$\mathrm{MVTR} = \frac{(W_1 - W_2) * 1000 * 24}{T} \tag{5.5}$$

where W_1 is the mass of the cup, film and solution A, 0 and 1 represent before and after swelling, and T is the test period in hours.

5.2.8 Contact angle of three-layer films

The contact angle of the surface of casted Hi-gel solution film was studied by DSA 100. The contact angle image was taken every minute after water droplet was on the surface of the film with smooth or patterned surface.

5.3 Result and discussion

Superabsorbent materials were needed to prepare the wound dressings with high exudate absorbing ability, so the PAA were 100% neutralized to increases the water absorbing capability. The particles also needed to be crosslinked to maintain their integrity after absorbing water and in order to be aligned under electric field in solution.

In this study, two different shapes of neutralized and crosslinked particles, rod-like and irregular shape particles, were prepared to fabricate the wound dressings, noted as nanorods and irregular particles. The method to prepare PAA nanorods was electrospinning PAA nanofibers first and then mechanically chopping the electrospun nanofibers into nanorods. Figure 5.2(a) shows the SEM morphology of the as-spun nanofibers with an average diameter of about 700 nm. Since the molecules of PAA used for electrospinning was linear and non-crosslinked, the nanofibers were crosslinked afterwards at 190 ^{o}C by esterification reaction between carboxyl group of PAA and hydroxyl group of PEG, to avoid their dissolution in water. The morphology of nanofibers remained the same after crosslinking, as shown in Figure 5.2(b). In order to obtain evidence of crosslinking, the FTIR spectra of the nanofibers were recorded before and after reaction as shown in Figure 5.3. The absorption at 3390 cm^{-1}, 2930 cm^{-1}, 1450 cm^{-1} and 1101 cm^{-1} were due to the stretching vibration of O-H, C-H, CH_2 and C-O groups, respectively.[176] The peaks at 1552 cm^{-1}and 1404 cm^{-1} were assigned to asymmetric and symmetric stretching of -COO^{-}, respectively,[177, 178] because the PAA was neutralized by sodium hydroxide solution. The decrease of these two peaks was due to the conversion of the ionic bonds to ester bonds (-CO_2C-).[179] Meanwhile, the absorption band at 1691 cm^{-1} corresponding to carboxylic ester group at appears after crosslinking. To confirm the crosslinking of nanofibers further, the as-spun and crosslinked nanofiber mats were immersed in solution A for 30 minutes. As can be observed in Figure 5.2(c), the as-spun nanofibers dissolved and spread into films, whereas the crosslinked nanofibers mostly maintained their integrity despite some fibers slightly clumping together with each other as shown in Figure 5.2(d). The crosslinked nanofibers were then ball grinded into nanorods as shown Figure 5.4(a). The irregular particles were prepared by cryogrinding crosslinked PAA without further crosslinking reactions, and the morphology of the irregular particle is shown in Figure 5.4(b).

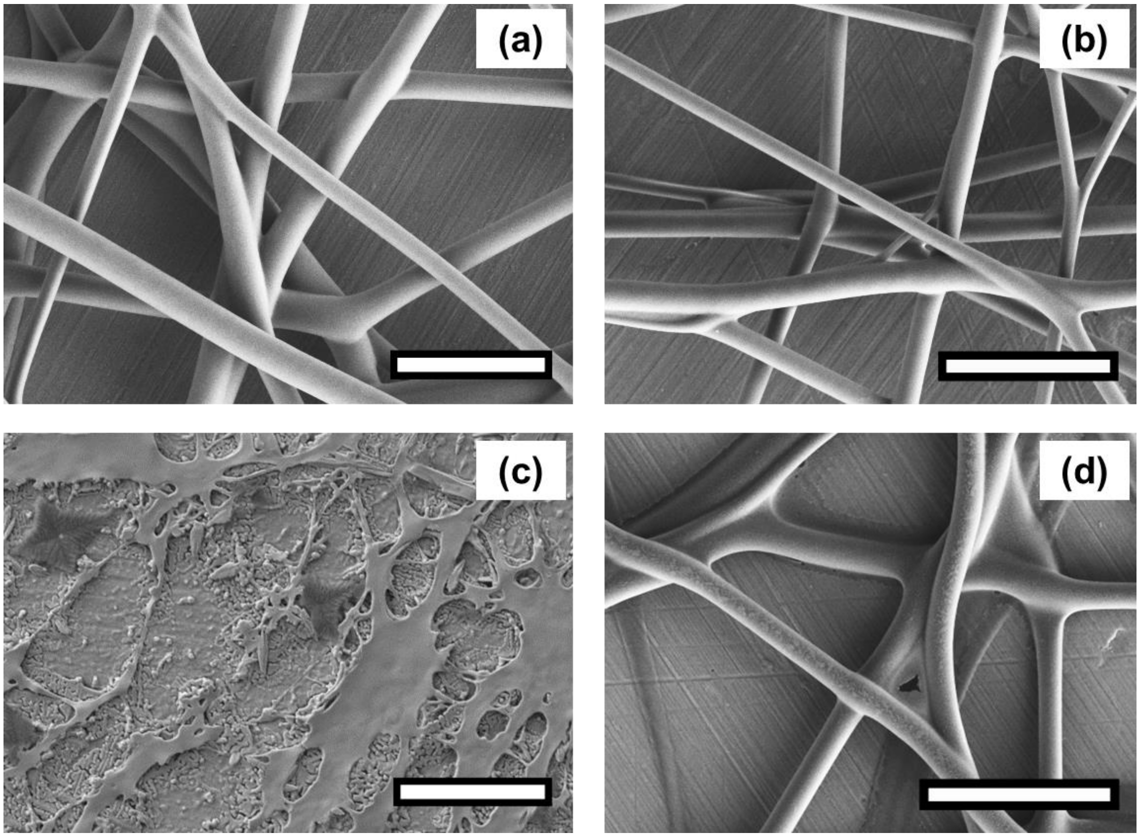

Figure 5.2 SEM morphology of neutralized PAA nanofibers (a) As-spun, (b) after cross-linking, (c) nanofibers without crosslinking after washing, (d) cross-lined nanofiber after washing.

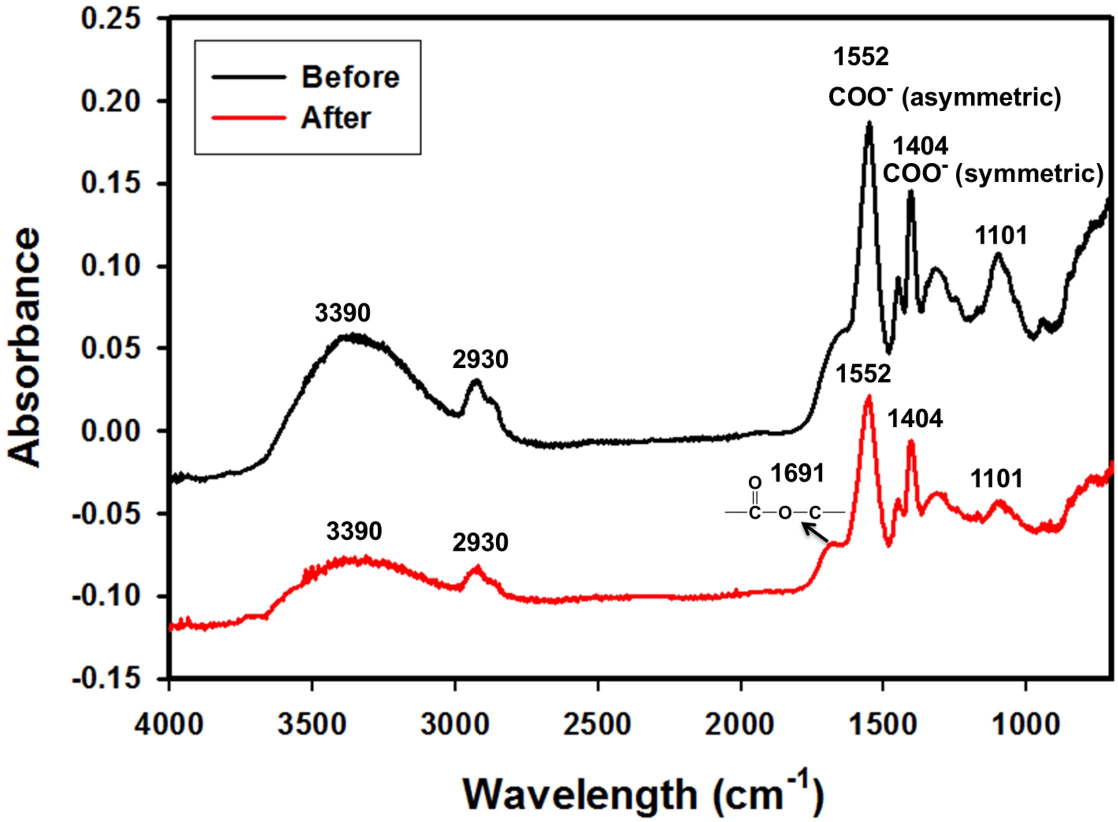

Figure 5. 3 FTIR of neutralized PAA nanofibers before and after crosslinking.

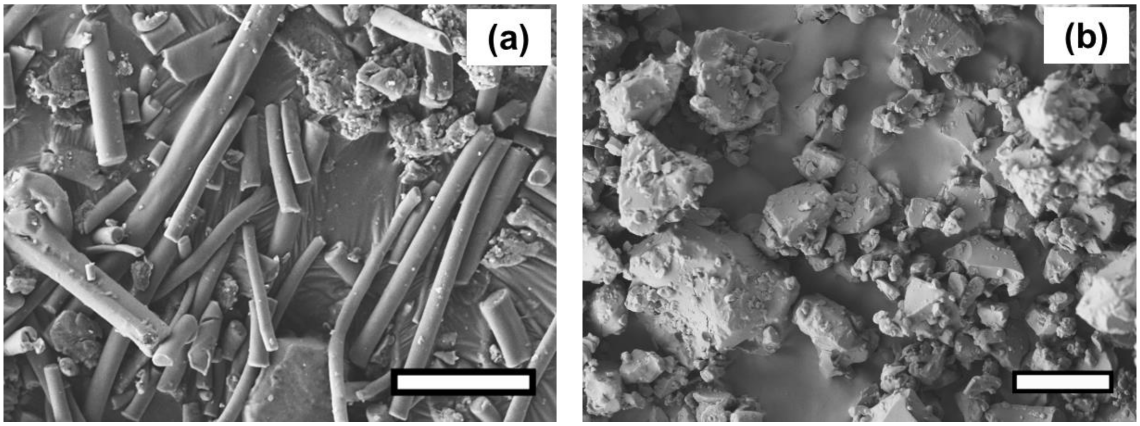

Figure 5.4 SEM morphology: (a) PAA nanorods (scale bar: 5μm), (b) PAA particles (scale bar: 10μm).

Three-layer wound dressings were prepared by solution casting method, and the in-situ alignment of nanorods or irregular particles was achieved by applying electric field in “Z” direction of film until the film was dried. SEM was utilized to characterize the cross sectional morphology of the resulting three-layer wound dressing films, as shown in Figure 5.5. This figure illustrates the control morphology of the three-layer film without the application of electric field. The nanorods were colored yellow to distinguish them from other feather. A clear three-layer structure could be seen: layer A, layer B dispersed with nanorods, and layer C with imprint patterns. Layer A was made of moisture permeable polyurethane (TPUs1), which acted as a backing layer to control the MVTR. Layer B was composed of super absorbent nanorods and polyurethane matrix (TPUs2). The nanorods were colored yellow (false color) to enhance the contrast between matrix and dispersed particles. For the wound dressing films obtained without applying electric field, the nanorods all oriented parallel to the surface of film due to development of internal compression force caused by the thickness shrinkage as the solvent evaporates.[99] On the other hand, for films aligned by electric field, the nanorods were oriented and aligned in “Z” direction as shown in Figure 5.6. This is attributed to the fact that the dielectrophoretic force overcomes the compression force during the drying resulting in maintenance of the developed orientation of the long axes of the particles in thickness direction. Some of the nanorods were not oriented perfectly in “Z” direction and a small tilting angle was observed between the electric field direction and the long axis of nanofibers due to the compressive force as the film thickness reduces,[29] but overall a clear orientation and alignment of the nanorods were obtained along the film thickness direction. Layer C is a polyurethane layer (TPUs2) with imprint patterns replicating the feature of Teflon coated mesh.

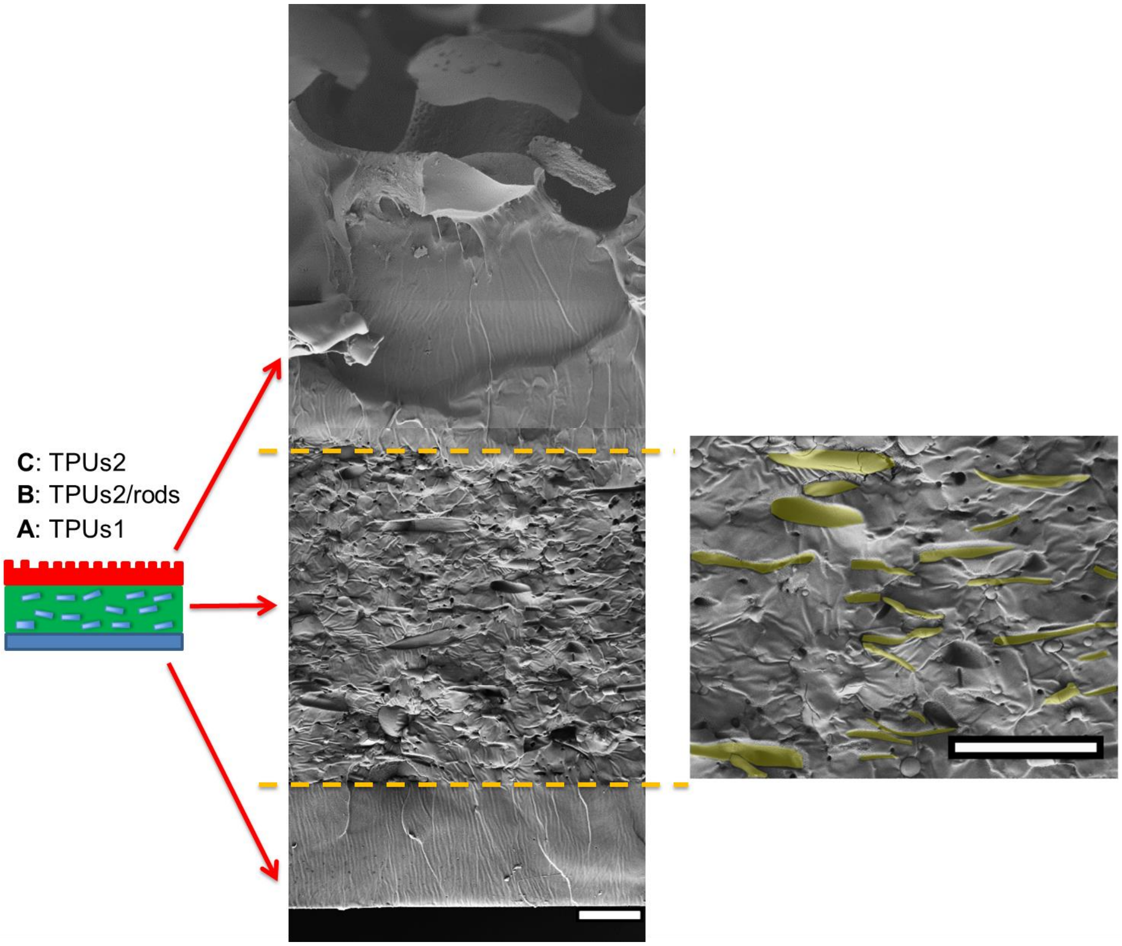

Figure 5.5 Cross sectional morphology of three-layer wound dressing without application of electric field (scale bar: 20μm).

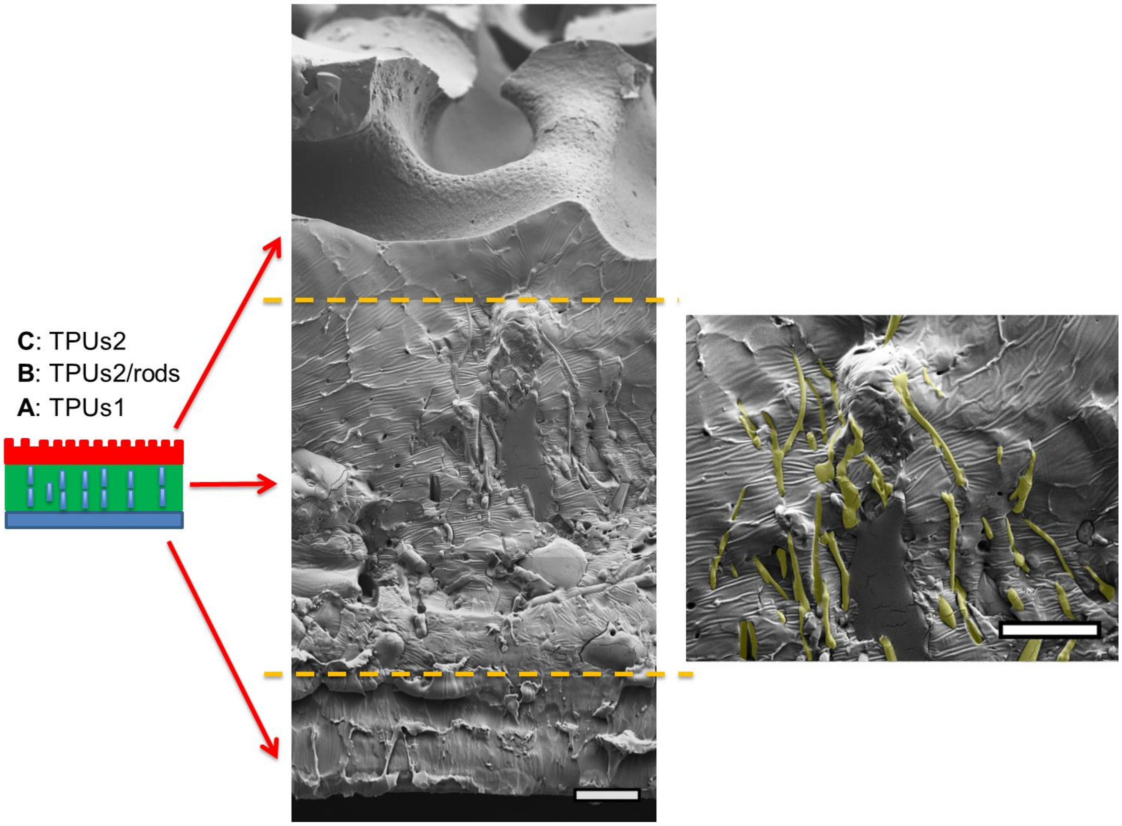

Figure 5.6 Cross sectional morphology of three-layer wound dressing with aligned nanorods (nanorods were artificially colored to enhance the contrast) (scale bar: 20μm).

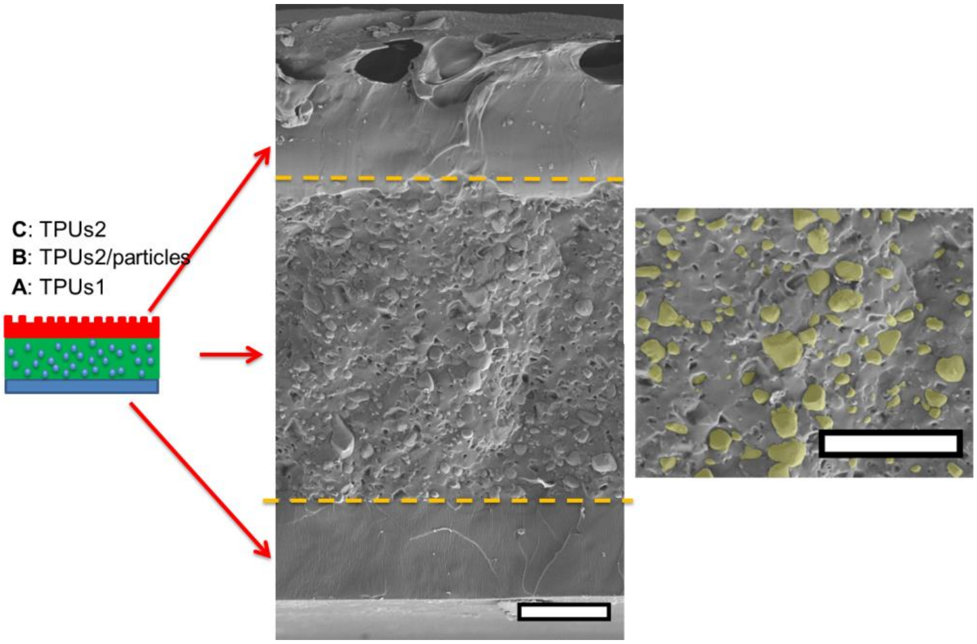

Figure 5.7 Cross sectional morphology of three-layer wound dressing with random particles (scale bar: 40μm).

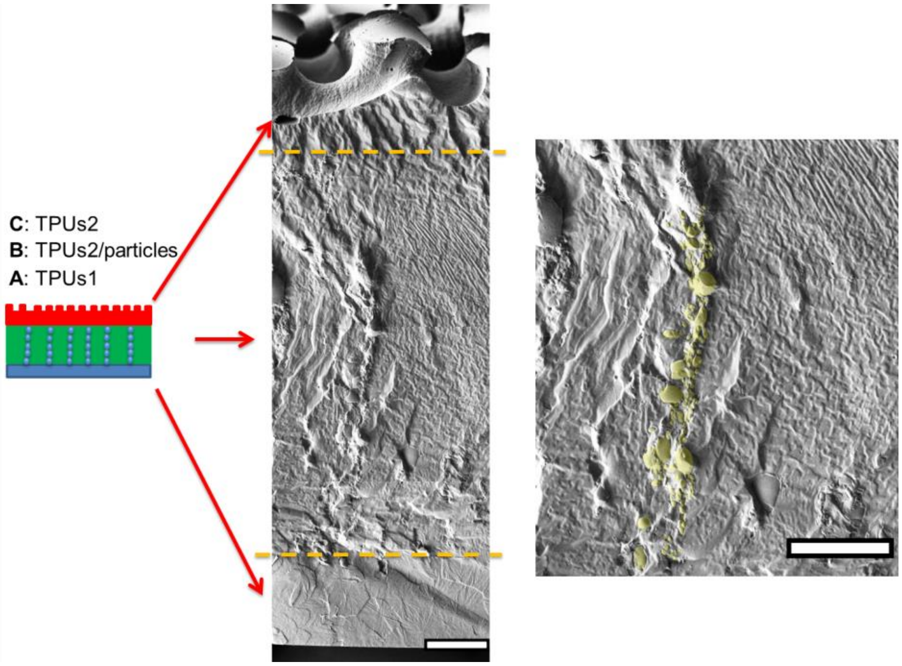

Figure 5.8 Cross sectional morphology of three-layer wound dressing with aligned particles (scale bar: 40μm).

As for irregular particles, the cross-section of resulting wound dressing films were also characterized by SEM for both non-aligned and aligned samples, illustrated in Figure 5.7 and Figure 5.8, respectively. Similar to nanorods, irregular particles were aligned in the film thickness direction, and formed chain structures in layer B for the samples with electric field on, whereas the irregular particles were randomly distributed in the films prepared without applying electric field. For a direct visual observation, the video showing the alignment of irregular particles in TPUs/dioxane solutions was provided in supporting information. Additionally, the non-aligned and aligned samples were also examined by the micro-Xray tomography system to obtain the three dimensional distribution of irregular particles, as shown in Figure 5.9. For the film prepared without applying electric field, particles were randomly distributed in layer B, whereas they were assembled into chains in the film prepared with the application of electric field. Such three-layer films, when used in wound dressing applications, were flipped upside down. Namely, the layer C with imprinted patterns becomes the layer that directly contacts the wound and transports the exudate towards layer B. Layer B is the absorbing layer which absorbs and retains the exudate. Layer A is the backing layer that allows the moisture to vaporize through but prevent ingress of liquid from outside. This allows the patient to take bath or showers while wearing the wound dressing.

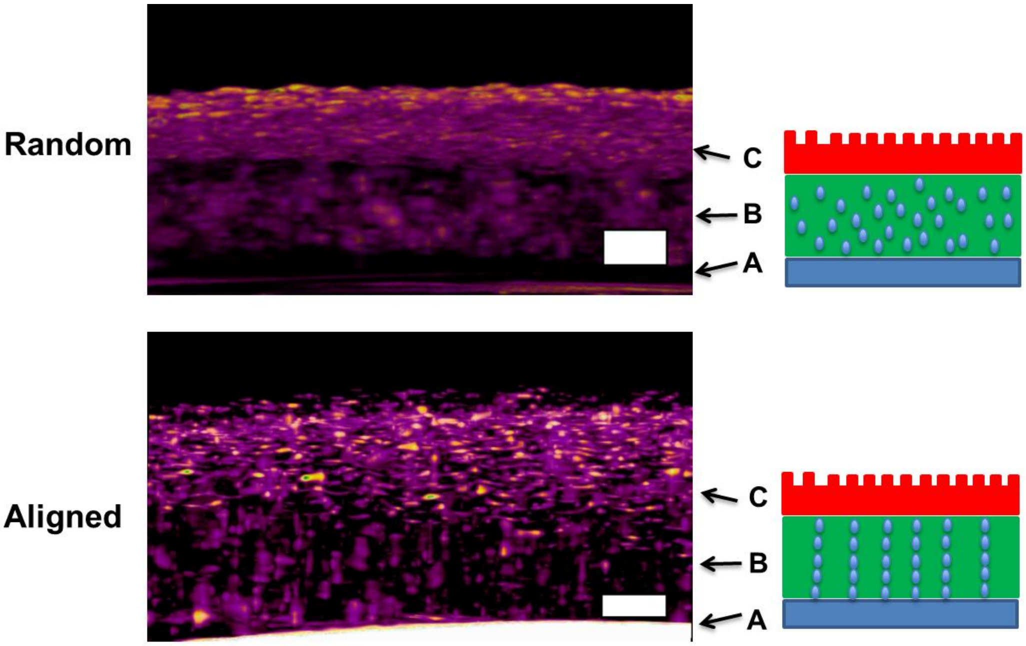

Figure 5.9 Micro-CT morphology of three layer wound dressing with random and aligned particles (scale bar: 100μm).

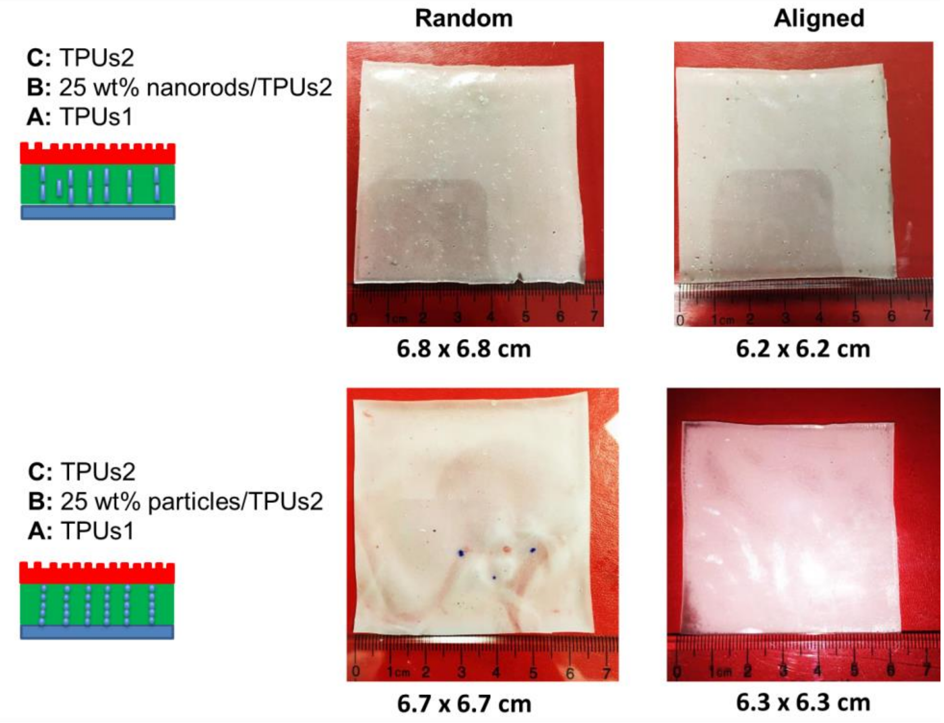

Figure 5.10 The size comparison of wound dressing with random and aligned particles or nanorods after swelling.

Table 5.1 The effect of alignment on lateral expansion on wound dressing after swelling.

Particle content (wt.%)	**Rods in TPU2 (cm)**		**Particles in TPU2 (cm)**	
	Random	**Aligned**	**Random**	**Aligned**
0	5.9	5.9	5.9	5.9
15	6.6	6.0	6.5	6.1
25	6.8	6.2	6.7	6.3
35	7.0	6.5	7.0	6.7

To study the swelling behavior of resulting films, the three-layer wound dressing films with a series of particle contents (0, 15, 25 and 35 wt.%) were cut into 5×5 cm size and soaked in solution A at 37 ^{o}C for 30 minutes. All the swollen samples were measured and samples with 25 wt.% particles are shown in Figure 5.10 as representatives. For nanorods, the non-aligned and aligned samples expanded from 5×5 cm to 6.8×6.8 cm and 6.2×6.2 cm, respectively. The lateral expansion was reduced by 33% after alignment indicating that directional swelling is actually working in these films. Since the nanorods attained much lower modulus than the polyurethane matrix in the gel state after absorbing water, the stiffer matrix that surrounds the aligned nanorod chains restrains the expansion in the lateral direction, leading to a smaller lateral deformation compared to non-aligned films. Similar effects could also be seen for irregular particles. However, less significant reduction in the lateral expansion was obtained for films with aligned irregular particles, due to their lower aspect ratio and larger particle sizes. The in-plane dimension of all swollen samples with various particle concentrations (0, 15, 25 and 35 wt.%) was provided in Table 5.1. In order to quantitatively evaluate the anisotropic swelling properties of each sample, the swelling anisotropy value, calculated as the ratio of out-of-plane expansion ratio ($R_\perp$) over in-plane expansion ($R_{//}$), and plotted as a function of particle concentration in Figure 5.11. Generally, films with aligned nanorods or irregular particles achieved dramatically higher swelling anisotropy values than the films with randomly dispersed particles, meaning that the aligned films underwent more vertical expansion than less lateral expansion in comparison to non-aligned films. Also, films with nanorods exhibited slightly higher anisotropy value than irregular particles due to their higher aspect ratios. There're much fewer number of particles needed to form chains with nanorods than irregular particles, so there's less sliding among the particles as they expand after absorbing the exudate. For films with aligned particles, the swelling anisotropy values of both nanorods and irregular particles showed first increasing then decreasing trend as the particle content increased from 0 to 35 wt.%, and the maximum swelling anisotropy value was achieved at 25 wt%. The swelling ratio of the wound dressing increases with particle content as expected in Figure 5.12(a). The MVTR of wound dressings, the MVTR of samples with various particle contents was characterized and plotted in Figure 5.12(b). Both nanorods and irregular particles demonstrated virtually identical MVTR values between aligned and non-aligned samples, which all located between 700 and 1600 $g*m^2*24h^{-1}$. The three-layer structure wound dressing were in the desired range of MVTR for ideal wound dressings to maintain moist environment but also allow reasonable evaporation to avoid frequently wound dressing replacement[170]

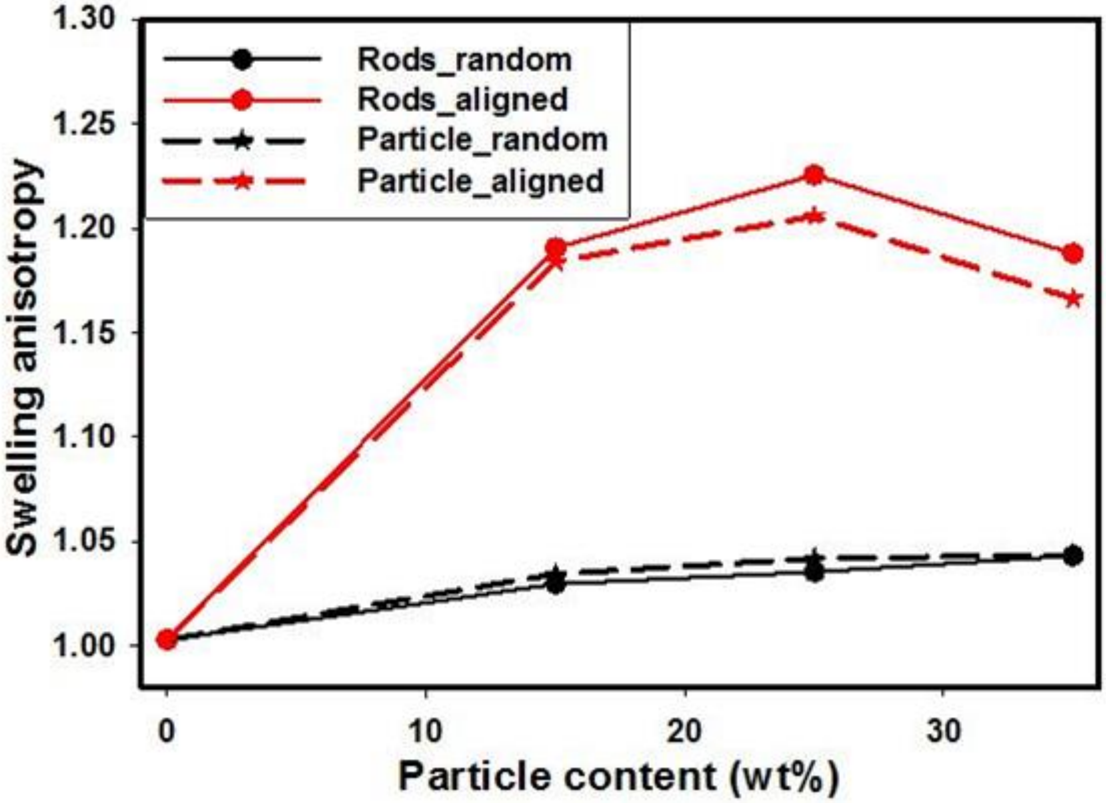

Figure 5.11 The effect of alignment and particle shape on swelling anisotropy as a function of particle content.

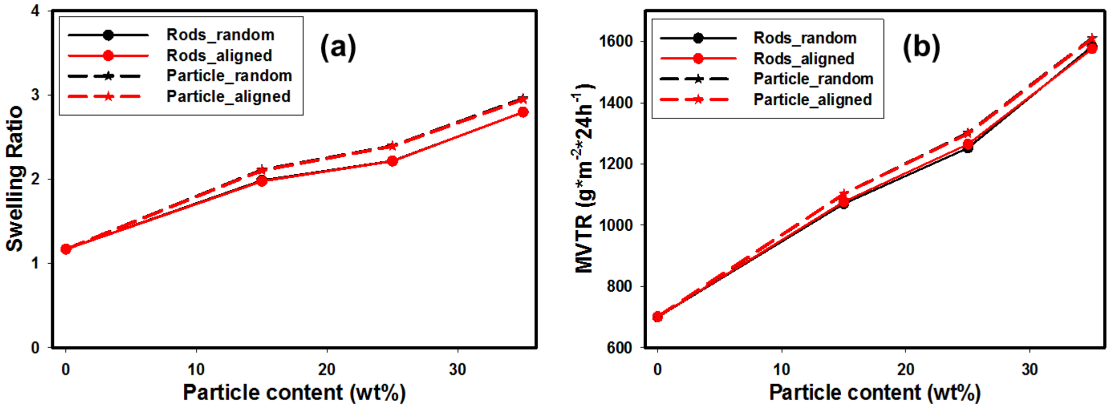

Figure 5.12 The effect of alignment on (a) swelling ratio and (b) MVTR of wound dressing after swelling.

As mentioned above, the layer (C) of aligned films were imposed on imprinted patterns from the top electrode, a conductive mesh, as shown in Figure 5.13. Since layer C was the contact layer that absorbed the excess exudate directly from the wound, it was expected to be hydrophilic and wettable for moisture to transport through. The effect of these imprinted patterns on the wettability of wound dressing films was evaluated by measuring the contact angle of water droplet on layer C, and compared to the films with smooth surface prepared without applying electric field, shown in Figure 5.13. The contact angle values were plotted vs. wetting time for both smooth and patterned surface films in Figure 5.13. It could be seen that the contact angle on the patterned surface started with slightly higher value (116 ^{o}) than smooth surface films (107 ^{o}), due to their higher roughness level as predicted by the Wenzel model. This model predicts that the contact angle of this material with rough surface increases with the roughness if the contact angle of material with smooth surface is above 90^{o}.[180, 181] However, the contact angle of patterned surface films almost instantly dropped below smooth surface films and reached a much lower value of 32^{o} at 10mins, than 83 ^{o} of smooth surface films. This is attributed to the capillary force and higher surface area induced by the patterned surface. Moreover, a higher base radius of the water droplet on the patterned surface was observed, which is consistent with previous study.[182] A combination of lower contact angle and higher base radius of water droplet indicates that the film with patterned surface has better water absorbing ability, which is benefitting from the electric field alignment.

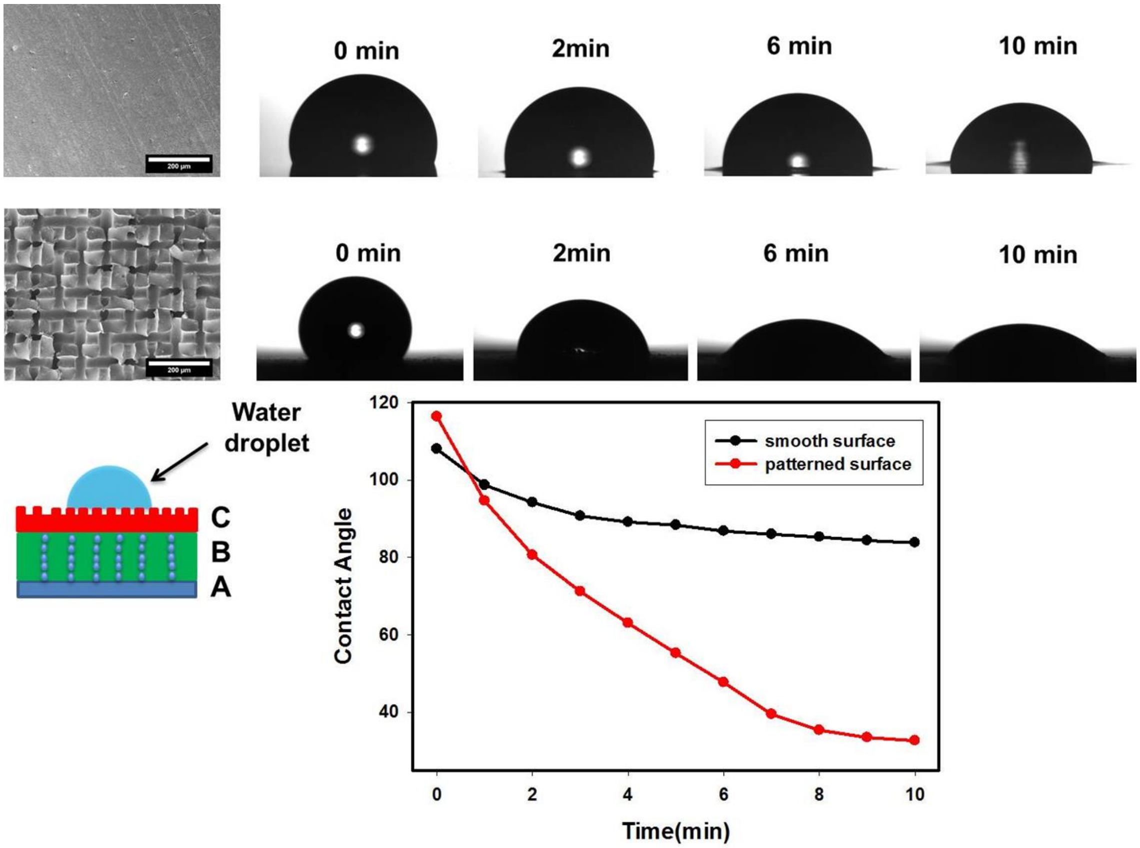

Figure 5.13 The effect of surface of pattern on the contact angle of wound dressing as a function of time.

5.4 Conclusion

The three-layer wound dressings with anisotropic swelling were prepared by preferentially aligning the absorbent particles along film thickness direction in the absorbent layer. The resulting wound dressings exhibited more vertical expansion than lateral expansion after absorbing water owing to the anisotropic structure of aligned particles. Moreover, the wound dressing films with aligned particles significantly reduced the lateral expansion compared to the films without being aligned by electric field, which could be extremely beneficial in reducing the shear stress on the wound. The particle shape also played an important role in the anisotropic swelling behavior of aligned wound dressing films. It was found that cylindrical particles (nanorods), which possessed higher aspect ratio, could further increase the anisotropic swelling ratio and reduce the lateral expansion than irregular particles. Another advantageous effect that the top layer with imprint pattern imposed by the electrode achieved lower contact angle as well as higher base radius of water droplet was also induced by the electric field alignment. Besides, the backing layer of wound dressings remained MVTR values between 700 and 1600 $g*m^2*24h^{-1}$, meaning it is liquid impervious but moisture permeable. Therefore, the three-layer wound dressings accomplished in this study have enough breathability and in the meanwhile are able to maintain a moist environment to accelerate wound healing.

CHAPTER VI

COLLOID NANOPARTICLES TRAPPED MORPHOLOGY OF POLYMER BLENDS DURING SOLVENT EVAPORATION AND ELECTRIC FIELD INDUCED VERTICAL ALIGNMENT OF NANOPARTICLE COATED PHASES

The surface of silica nanoparticles was modified by attaching PS-r-PMMA-OH copolymer brush via the condensation reaction between the hydroxyl group of copolymer and particles, in order to make them chemically neutral to PS and PMMA. During the solvent evaporation induced phase separation of PS, PMMA and silica particle blends, the dispersed and bicontinuous morphologies were stabilized by the interfacial absorption of silica nanoparticles. The resulting morphology was affected by the rate of solvent evaporation, blend compositions, particle loading and size. In symmetric blend system, dispersed phase was observed at low evaporation rate and bicontinuous morphology was obtained at high evaporation rate. The silica nanoparticles were found to be densely packed at the interface of PS and PMMA. For asymmetric blend system, only dispersed phase was observed at both low and high evaporation rates. The size of phase separated domains decreased with increasing particle loading. The silica nanoparticles with smaller size resulted in relatively smaller domain size due to their higher surface area to volume ratio. The morphology of polymer blends with dispersed nanoparticles with the application of electric field in vertical direction was investigated. The electric field resulted in the deformation of the spherical PMMA droplets into vertically oriented prolate ellipsoids with the particles segregated at the interface densely. There's no reorganization and alignment at the interface observed for silica nanoparticles due to their low dielectric constant. In contrast, the barium titanate (BT) nanoparticles with high dielectric constant were aligned to form particle chains at the interface with their primary axes oriented in the electric field direction.

6.1 Introduction

Blending two or more different polymers is a good strategy to generate new materials with desired properties by combing the unique properties of each component.[183] Fully miscible polymer blends are the ideal choice but they rarely provide such synergistic effect. Most of polymer blends tend to phase separate due to the large unfavorable enthalpy of mixing, which may lead to poor mechanical and optical properties.[184] Since the phase separation and morphology of polymer blends rely on the interface between polymer components, the addition of surfactant is a good alternative route to reduce phase separated domain size and formation of bicontinuous structure useful for creating materials with useful properties.[84, 185] The surfactants such as block and graft copolymers,[186-188] Janus particles,[189] anisotropic particles[190] and colloid nanoparticles[82, 84] are utilized to control the size scale and structure of phase separated morphology via reducing interfacial tension of two constituents and providing steric hindrance.[191]

The block copolymers can suppress the coarsening of dispersed and bicontinuous of domains in polymer blends effectively. Macosko etc. found out that the polystyrene-polyethylene (PS-PE) block copolymer can significantly hinder the coarsening of high-density polyethylene (HDPE) droplet in the polystyrene (PS) matrix with 12.7/87.3 blend ratio.[192] The PS-PE copolymer with larger PS blocks has a better effect on hindering the coalescence than one with smaller block due to its better steric repulsive interactions. The addition of 1% PS-PE block copolymer with intermediate molecular weight (40 kg/mol) into PS/HDPE blends showed the best reduction of the bicontinuous phase size and stabilization of the bicontinuous morphology during annealing compared to copolymer with lower or higher molecular weight.[187] Therefore, the balance of diffusion rate for block copolymer to reach the interface during phase separation and steric hindrance ability determines its performance.[187]

The use of Janus particles was demonstrated superior compatibilization performance compared to the corresponding triblock copolymers. The polystyrene-b-polybutadiene-b-poly(methyl methacrylate) (SBM) triblock copolymers having a tightly cross-linked polybutadiene core attached with high molecular weight PS and PMMA outer blocks functioning as corona chains form the biphasic Janus particles. The addition of SBM Janus particles into PS/PMMA polymer melt blends and poly(phenylene ether)/poly(styrene-co-acrylonitrile) (PPE/SAN) melt blends resulted in the significant decreases of dispersed phase with dense coated Janus particles at the interface.[83, 193] Bryson etc. obtained PS/PMMA bicontinuous morphology during solvent (tetrahydrofuran (TFH)) evaporation demixing, which is stabilized by the SBM Janus particles packing densely at the interface.[189] The effect of particle loading and blend composition of the morphology were investigated but the effects of controlled evaporation rate and particle size were not studied.

Colloid particle is also used as the compatibilizer to suppress the coarsening of domain and form bicontinuous morphology for polymer blend system. Chemically homogeneous colloid particles usually tend to aggregate in one of component which has preferential wetting to the particles. In order to make the colloid particles stay at the interface of polymer blends A and B, the interfacial tension between polymer A and B must exceeds the difference of the interfacial tension of the particle with each component (A B), $\gamma_{AB} > \gamma_{PA} - \gamma_{PB}$.[194] Thus the colloid particles need chemical modification to be chemically neutral to each component. The hydrophobic silica colloid nanoparticles (16nm) modified by dichlorodimethylsilane (DCDMS) were absorbed at the interface of polydimethylsiloxane (PDMS) and polyisobutylene (PIB) with 70/30 ratio, which is very similar with the Pickering emulsions for low molecular fluid.[195] The coarsening and coalescence of the dispersed PIB droplet was suppressed by the interface coated silica colloid particles.[82] Composto etc. investigated the silica colloid nanoparticles grafted with PMMA brush stabilized bicontinuous morphology during the spinodal decomposition of PMMA and poly(styrene-ran-acrylonitrile) (SAN) blends as the film was warmed above the lower critical system temperature.[84, 196] It was found out that the modified silica nanoparticles were segregated at the interface of bicontinuous phases of PMMA and SAN and domain size decreases with increasing concentration of particles. The minimum loading of silica nanoparticles to stabilize the bicontinuous morphology decreases with increasing the thickness of film. This bicontinuous morphology of polymer blends with nanoparticles trapped at interface is an extension of concept from bicontinuous interracially jammed emulsion gels (bijels)[79, 197] for low molecular weight fluids to polymer systems. This attractive bicontinuous structure provides high interfacial area for organic solar cells, fuel cell and membrane applications. The incorporating of colloid nanoparticles also introduces other functionalities such as optical, electrical and catalytic properties into polymer blends. Furthermore, selectively etching one of the phases can result in a porous polymer material with partially-exposed nanoparticles embedded at the internal pore surface, and this structure can provide high nanoparticles exposure, which has the potential to be used for filtration and catalyst applications.

For colloid particle compatibilized polymer blends, previous studies focused on the morphology of polymer blends phase separated by temperature jumping. There's no work on the colloid particle stabilized phase separated structures of polymer blends induced by the solvent evaporation. In this study, tunable domain size of both dispersed and bicontinuous structures with silica colloid particle segregated at the interface is studied for PS and PMMA blend film during solvent evaporation induced demixing. The effects of controlled evaporation, silica nanoparticle size, particle loading and blend compositions on the morphology are systematically investigated.

Polymer blends or polymer composites have attracted great attention in both academic and industrial area due to their superior properties to the single component.[198] The mechanical, chemical, optical, electrical and thermal properties of these multicomponent or multiphase polymer systems are strongly dependent on their morphologies.[119] Therefore, it is essential to design and control the morphology to tailor the properties of these systems. The morphology can be modulated by traditional processing methods such as shearing,[199] compression[142] and stretching[64] but only in the lateral direction. The vertical anisotropic morphology is becoming more and more interesting in many areas such as transistor,[200] filtration,[201] energy harvesting and storage.[202]

The external electric field is one of the most effective strategies to achieve both lateral and vertical anisotropic morphologies of polymer blends or polymer composite systems. The effect of electric field on the morphology of either phase-separated domain of polymer blends or nanoparticles have been studied separately. For example, electric field was applied on poly(2-chlorostyrene) (P2CS)/poly(vinyl methyl ether) (PVME) binary blends as the temperature was jumped into unstable region, and anisotropic morphology with deformed and aligned phases were observed along the electric field direction.[118] In case of phase-separated polymer blends solution with dispersed droplet in matrix, the electric field induced accumulation of free charges at droplet/matrix interface resulted in electrical tangential stress at the interface, which led to liquid circulation flows inside and outside of the droplets. This flow caused the electrohydrodynamic stress at the interface in addition to the electric stress.[120, 203, 204] Depending on the dielectric constant and electrical conductivity differences between two phases, the spherical droplets either retain the original shape or were deformed into prolate or oblate ellipsoids.[204] For the polyvinyl alcohol (PVA)/PS with 1/9 ratio in toluene solution, the spherical PVA droplets were stretched into prolate ellipsoids with the major axis parallel to the electric field direction and the ellipsoids were aligned to form chains in the field direction due to higher dielectric constant of PVA.[119] As the field strength increased, the ellipsoids in a pearl chain were fused together to from a long column. The PS droplets in 9/1 PVA/PS toluene solution were deformed into oblate ellipsoids due to lower dielectric constant of PS. In case of nanoparticles, the vertical alignment of barium titanate nanoparticle in PS/toluene solution was achieved under the electric field direction resulting in enchantment of dielectric properties compared to the film with random nanoparticles.[29]

Recent studies showed the electric field could lead to the elongation of Pickering emulsion or reorganization of particle at the interface. Russell and his coworkers investigated the shape deformation of water droplets in silicon oil with chemically modified polystyrene nanoparticles packing at the interface under electric field.[205] The external electric field resulted in the stretching of the spherical droplet into prolate ellipsoids with increasing surface area and absorbing more particles to the interface. The interfacial area had a little decrease after releasing the electric field but further shape change was arrested due to the jamming nanoparticle at the interface. The cross-linking among the jammed nanoparticles led to better stabilization and retaining the spherical shape under electric field. Dommersnes etc. demonstrated the electric field assisted assembly of different particles at the interface of silicon and castor oil.[206] The electric field could induce the clay particle and polyethylene particles organize into ribbons at the equator of droplets. While the silver coated glass particles were aligned to form longitudinal dipolar chains spanning the entire surface. However, the low molecular weight emulsions in these studies were not solidified to freeze the structure for further applications.

The influence of electric field on the morphology of immiscible binary polymer blends with nanoparticles was simulated by P. Millett.[207] For asymmetric polymer blends, vertical columnar channels of dispersed phase with particles coated interface were created under electric field. For the symmetric blends, the electric field resulted in the formation of vertical columnar bicontinuous structures with particles segregated at interface. After etching one of the phases, it provides porous materials with partially exposure particle on the surface of channels which is useful for filtration and catalyst applications. However, there is no experimental study on the effect of electric field on the morphology of polymer blends with particle-coated interfaces in vertical direction.

In this study, the effect of vertical electric field on the domain deformation of polymer blends with particle coated interface and the reorganization of nanoparticle at the interface will be studied. The effect of dielectric constant of particles on their behavior at the interface is also investigated. The polymer vertically aligned domains with dense particle-coated interface are demonstrated

6.2 Materials and methods

This section introduces materials, polymerization, surface modification of silica, film preparation and electric induced alignment in details.

6.2.1 Materials

Styrene (99%, Aldrich) and methyl methacrylate (MMA) 99%, Aldrich) were purified by passing through silica gels. 2,2’-Azobis(isobutyronitrile) (AIBN, Aldrich, 98%) was recrystallized from anhydrous cold ethanol and dried in vacuum. Methanol (ACS grade, Carolina), anhydrous 1,4-dioxane (99.8%, Aldrich) and the RAFT agent (4-Cyano-4-[(dodecylsulfanylthiocarbonyl)sulfanyl]pentanol) were used as received. PS (Mw: 190kg/mol), PMMA (Mw: 140kg/mol) and Tetrahydrofuran (THF) (ACS reagent, 99%) were supplied by Sigma Aldrich. Barium titanate (BT) nanoparticles were purchased from US Research Nanomaterials, Inc.

6.2.2. Polymerization Procedures

The solution of styrene, MMA, AIBN and RAFT agent with a ratio of 20/20/0.2/1 was prepared in anhydrous 1,4-dioxane in round-bottom flask following the scheme 6.1. The flask was well sealed and deoxygenated by purging nitrogen gas for 30 minutes. The flask was placed in the oil bath with magnetic bar stirring at 70 ^{o}C. After 12 hours, the reaction was stopped by quenching the solution in liquid nitrogen. The synthesized polymer was precipitated in 1/1 water/methanol solution and collected by centrifuge.

6.2.3. Surface modification of silica and BT particle by PS-r-PMMA-OH

Silica and BT particles were soaked in sulfuric acid and peroxide (7:3) mixer solution at 90 ^{o}C for 30 minutes to remove the organic and inorganic contamination on the surface[208]. The particles were rinsed and soaked in DI water to remove the residual acid. The cleaned particles were dispersed in PS-r-PMMA-OH/toluene solution with 1:2 weight ratios of silica and polymer. After evaporation of the toluene, the composite of PS-r-PMMA-OH and particles were baked at 170 ^{o}C for 2 days, which allowed the condensation reaction between hydroxyl group of copolymer and particle. The unattached copolymers were removed by rinsing in toluene for 6 times. The modified silica and BT particles were collected by centrifuge and dried in vacuum oven. Teflon coated mesh (325 × 325) was supplied by TWP Inc.

6.2.4 Film casting and drying

5 wt.% PS and PMMA homo-polymers with 50/50 ratio were dissolved in THF (slightly preferential solvent for PS) and the modified silica particles are dispersed in this solution. The solution was casted on the glass at 300 µm thickness by blade casting. Highly instrumented drying machine[63] was used to study the drying behavior of cast solution film, which can track the real time change of weight, thickness, in-plane and out of plane birefringence during the solvent evaporation. The cast solution film was put into preheated chamber (20, 100, 120 and 140^{o}C) of this instrument immediately and the

temperature was controlled by blowing hot air (air speed: 2 MPH). Different temperatures in the chamber induced different evaporation rates of the solvent.

6.2.5 In-plane alignment of phases under electric field

The nanoparticles were dispersed in 12 wt.% (50/50) PS/PMMA THF solution and this solution was dipped into the gap between two parallel copper electrodes. The electric field was applied between two electrodes in lateral direction until the film was solidified.

6.2.6 Vertical alignment of phases under electric field

A square cell with 6 cm × 6 cm size was prepared by placing four 0.5 mm thick spacer on the top of ITO coated glass (bottom electrode). The solution was loaded into the cell cavity slowly and covered by the Teflon coated mesh. The electric field was applied between mesh and ITO glass in vertical direction to study their effect of electric field on the morphology of polymer phase and particles. The electric field was turned off until the film totally solidified.

6.2.7 Characterization

NMR spectra were recorded by a Varian NMRS 300 instrument. The morphology of silica nanoparticles before and after surface modification was characterized by JEM 1200XII transmission electron microscope (TEM). Fourier transform infrared (FTIR) spectra of bare and modified silica nanoparticles were recorded on the Thermo Scientific

Nicolet 380 spectrometer. The weight loss of silica nanoparticles was characterized by TA instruments Q50 thermogravimetric analyzer (TGA). The morphology of PS/PMMA/silica nanocomposite film was characterized by JEOL JSM5310 scanning electron microscope (SEM).

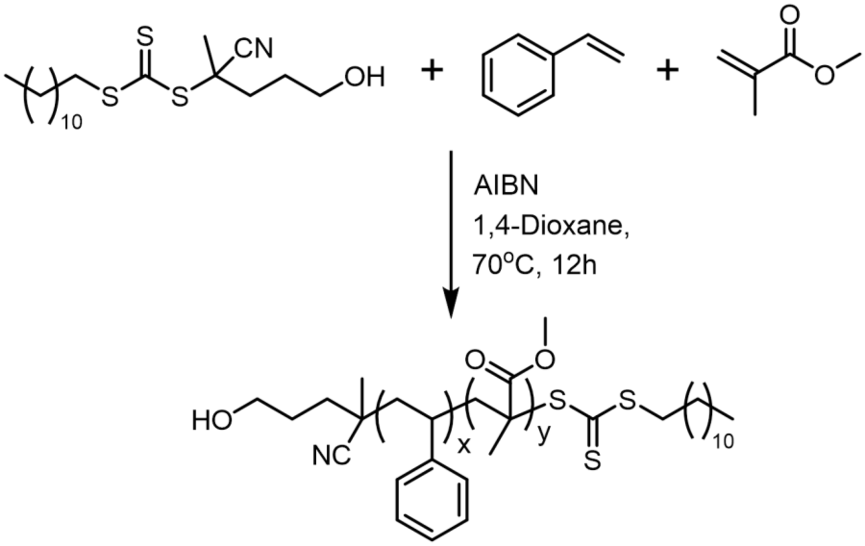

Scheme 6. 1 Synthesis of mono hydroxyl group terminated PS-r-PMMA-OH via RAFT polymerization.

6.3 Results and discussions

The polymerization, surface modification of silica and morphology of dried films are discussed in details below.

6.3.1. ^{1}H NMR spectra of synthesized polymer

The methoxy group's proton spectra is split into composite peaks grouping from δ=3.70 to 2.65 ppm showing in Figure 6.1, and this splitting of peak is caused by the current shielding effect of benzene ring of styrene unit.[209] The peak of phenyl proton resonances is split into two peaks at δ=7.2 and 6.92 ppm. The methine proton resonance of styrene unit signals around δ=2.3 ppm. The hydroxyl group resonances at δ=4.22 ppm. According to the integration of the area of peak 1, 2 and 4, the S/M ratio is close to 1. Thus mono hydroxyl group terminated PS-r-PMMA with S/M 1:1 ratio is synthesized.

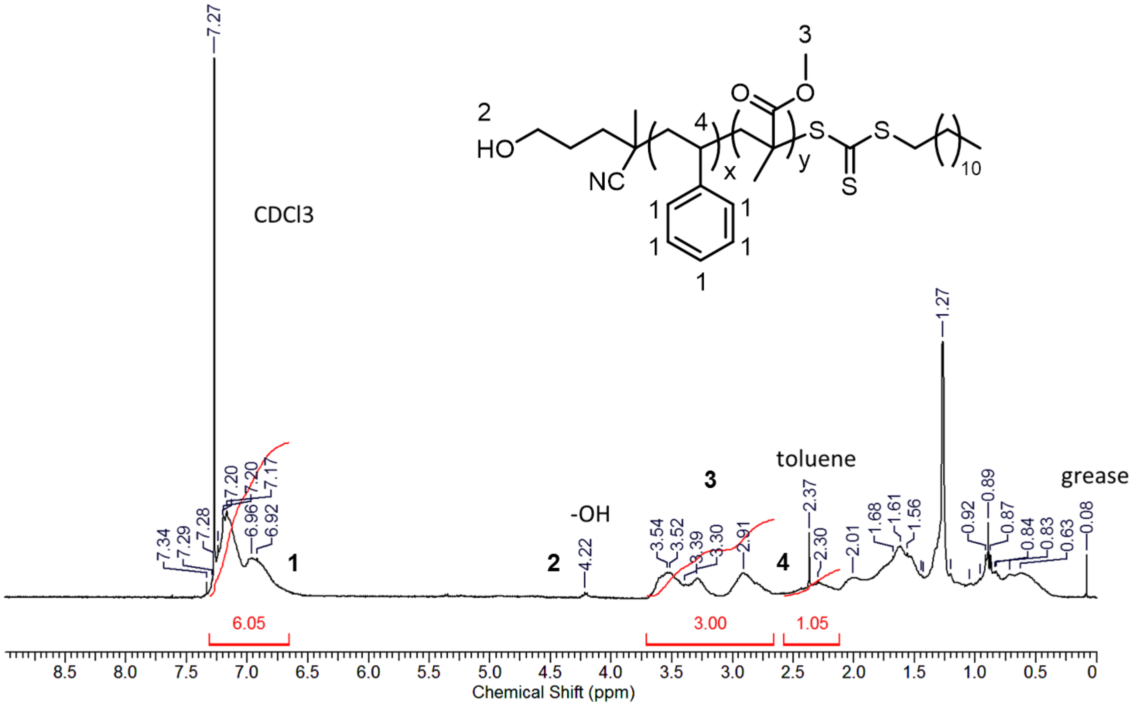

Figure 6.1 ^{1}H NMR spectrum of mono hydroxyl group terminated PS-r-PMMA.

6.3.2. Surface modification of silica nanoparticles

The morphology of silica nanoparticles (17nm) before and after surface modification was analyzed by transmission electron microscopy (TEM) shown in Figure 6.2. The nanoparticles are agglomerated, and the single nanoparticle can be observed on the edge of the agglomeration showing uniform color due to same electron absorption. Following chemical treatment we observe well separated individual silica nanoparticles with no evidence of agglomeration. The modified nanoparticles show core-shell structure with around 1.7 nm shell thickness, indicating the PS-r-PMMA-OH brush is attached to the surface of silica particles. Figure 6.3 shows the morphology of silica nanoparticles (170nm) before and after surface modifications. The bare colloid silica particles have very uniform morphology and the average diameter is around 170 nm. There is a very thin layer of coating can be observed on the surface of modified silica particles as the arrow indicates. The average diameter of the treatment nanoparticles increases slightly to 178 nm, indicating around 4nm thick coating of PS-r-PMMA-OH brush on the surface of silica nanoparticles.

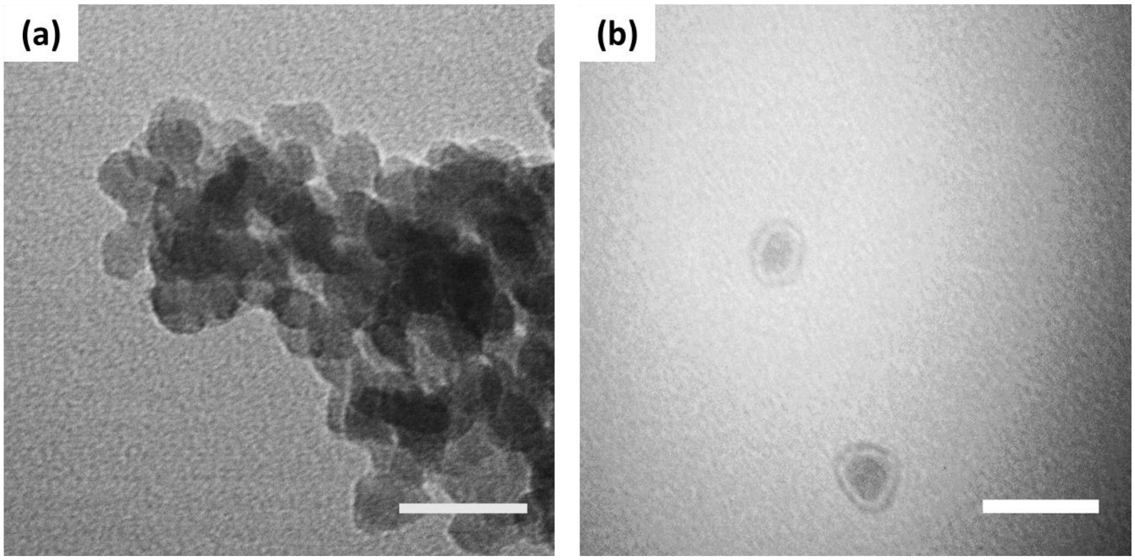

Figure 6.2 TEM image of (a) bare and modified silica nanoparticles (17 nm) (scale bar: 100nm).

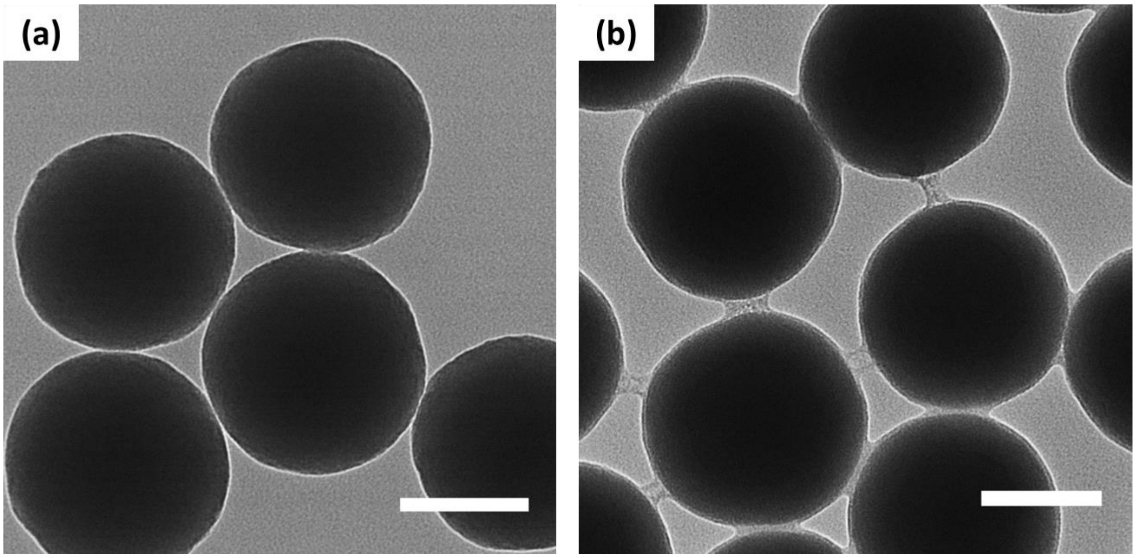

Figure 6.3 TEM image of bare and modified silica nanoparticles (170nm) (scale bar: 100nm).

Figure 6.4 shows the FTIR spectra of bare and modified silica nanoparticles. The broad band from 3000 to 3500 cm^{-1} is attributed to the O-H stretching vibration of hydroxyl group on the surface of bare silica nanoparticles. The spectra of silica nanoparticle modified with PS-r-PMMA shows two distinct peaks at 698 cm^{-1} and 1490 cm^{-1}, which are associated with the C-H bending vibration[210] and C=C stretching of aromatic rings,[211] respectively. It indicates PS-r-PMMA brushes are attached to the surface of silica nanoparticles.

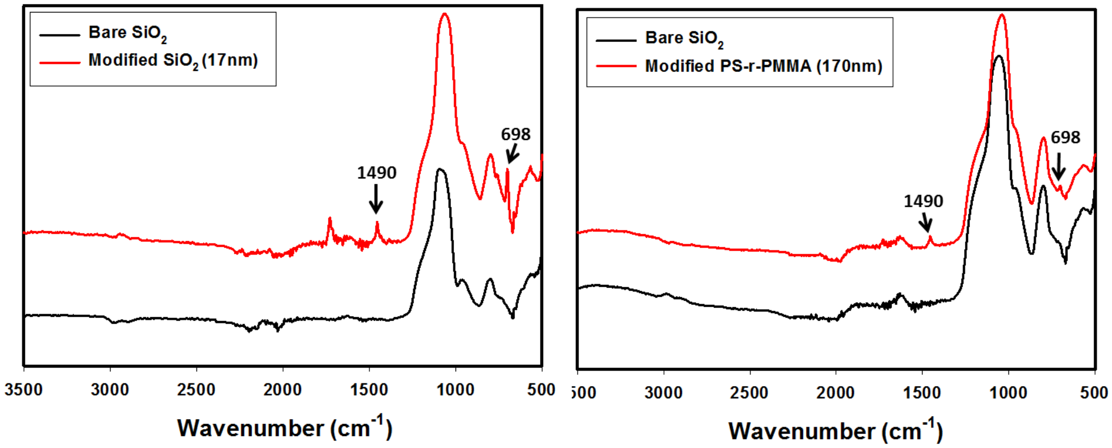

Figure 6.4 FTIR spectra of pristine and modified silica particles.

TGA was utilized to gain a better understanding of the graft density of PS-r-PMMA on the surface of the silica particles. As shown in Figure 6.5, bare and modified silica nanoparticles (17nm) with PS-r-PMMA brush have around 2.5% weight loss due to the loss of bound water on the surface of silica particle below 300 ^{o}C. The bare silica nanoparticles exhibit 6.5% loss after heating to 800 ^{o}C while the treated silica particles exhibit 33.8% weight loss due to the decomposition of attached PS-r-PMMA brush. According to the weight loss difference of bare and modified silica particles, the calculated average coating thickness is estimated to be 1.9 nm which is very close to the data from TEM. For the bare and modified silica nanoparticles (170nm), the bare silica particles have 5.5% loss after heating to 800 ^{o}C while the treated silica particles exhibit 9.7% weight loss due to the decomposition of PS-r-PMMA brush. Based on the weight loss difference of bare and modified nanoparticles, the calculated coating thickness is around 2.5 nm, which is close to the data from TEM images.

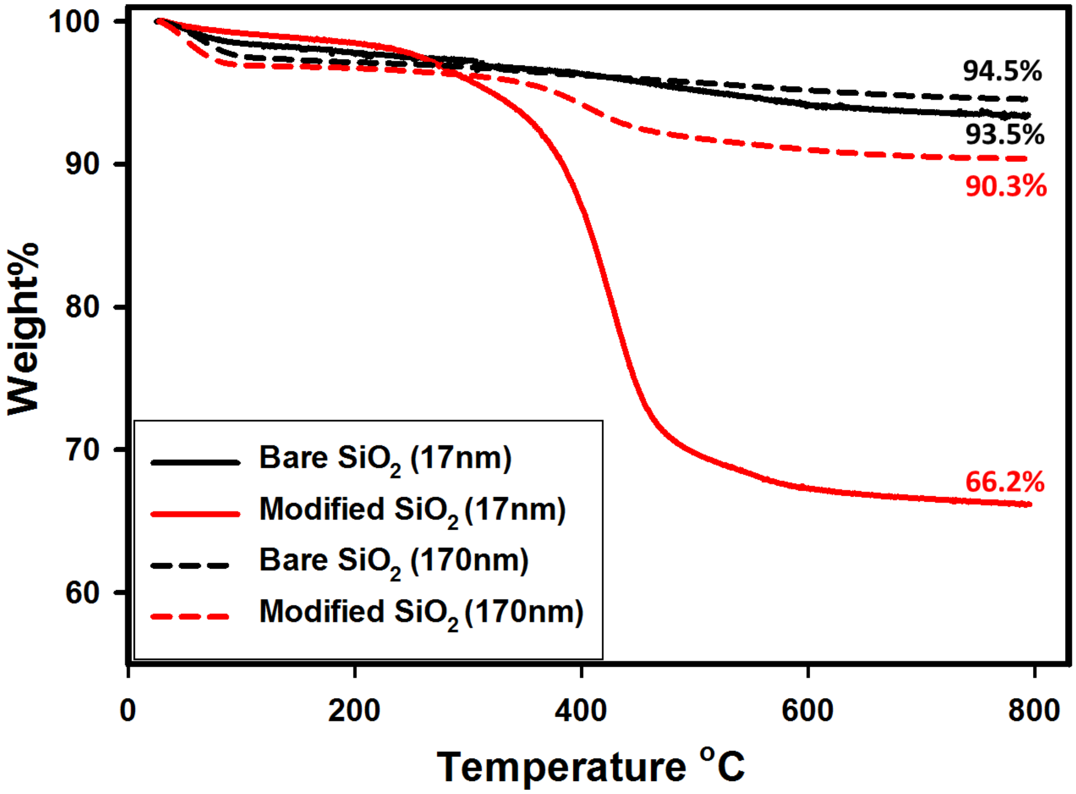

Figure 6.5 TGA curves of bare silica particle and PS-r-PMMA modified silica paticles: 17 nm (solid curve) and 170nm (dash curve).

6.3.3 Morphology of PS/PMMA/silica nanocomposite films

The effect of drying rate on the morphology and size of PS/PMMA silica nanoparticle film is studied below.

6.3.3.1 Effect of drying rate on the morphology of 50PS/50PMMA blend.

The effect of temperature on the drying rate of 50PS/50PMMA/TFH solution film was studied by measuring the real time change of weight as shown in Figure 6.6. The weight of the solution film decreases very fast due to the solvent evaporation of the THF (low boiling point: 66 ^{o}C), and the higher of the temperature, the faster evaporation rate of the solvent observed. The surface morphology of PS/PMMA blends with 50:50 ratios after drying is studied by SEM showing in Figure 6.7. PMMA spherical islands (dark region) are formed in PS matrix (light region) according to the nucleation-growth mechanism at 20 ^{o}C drying temperature. As the temperature increases to 100 ^{o}C (above the boiling point of THF), PMMA islands with relatively smaller size are formed in PS matrix due to the faster evaporation rate. The faster of the evaporation rate, the shorter time for the system to remain in metastable region between binodal and spinodal curves.[212] Thus there's less enough time for PMMA islands to grow into large islands. As the drying temperature increases to120 ^{o}C, both island and continuous PMMA domains are formed, but the size of continuous domains are large. If the temperature is further increased to 140 ^{o}C, bicontinuous morphology with small PMMA islands can be observed. This is caused by the fast evaporation rate making the system pass through the metastable region rapidly. In this case, the spinodal decomposition dominates over the nucleation of PMMA domains[212], hence the bicontinuous structure is formed.

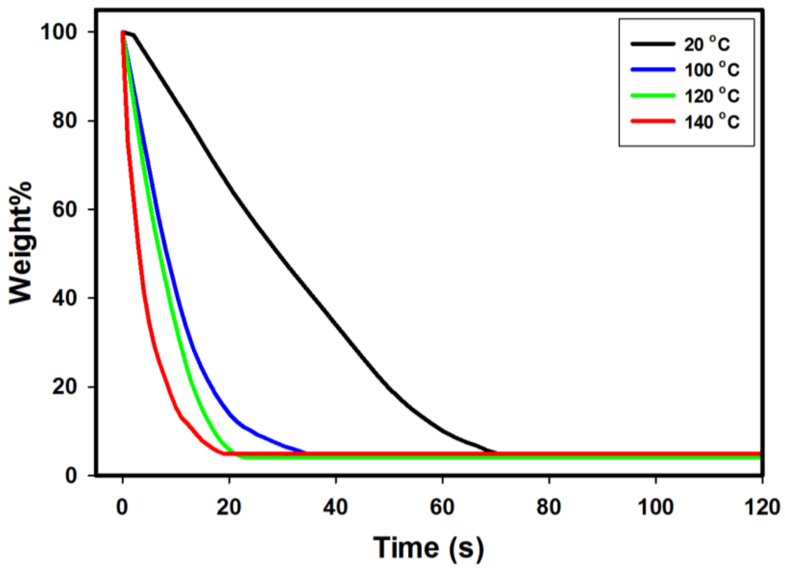

Figure 6.6 Real time change of weight change for solution cast PS/PMMA film at different temperatures.

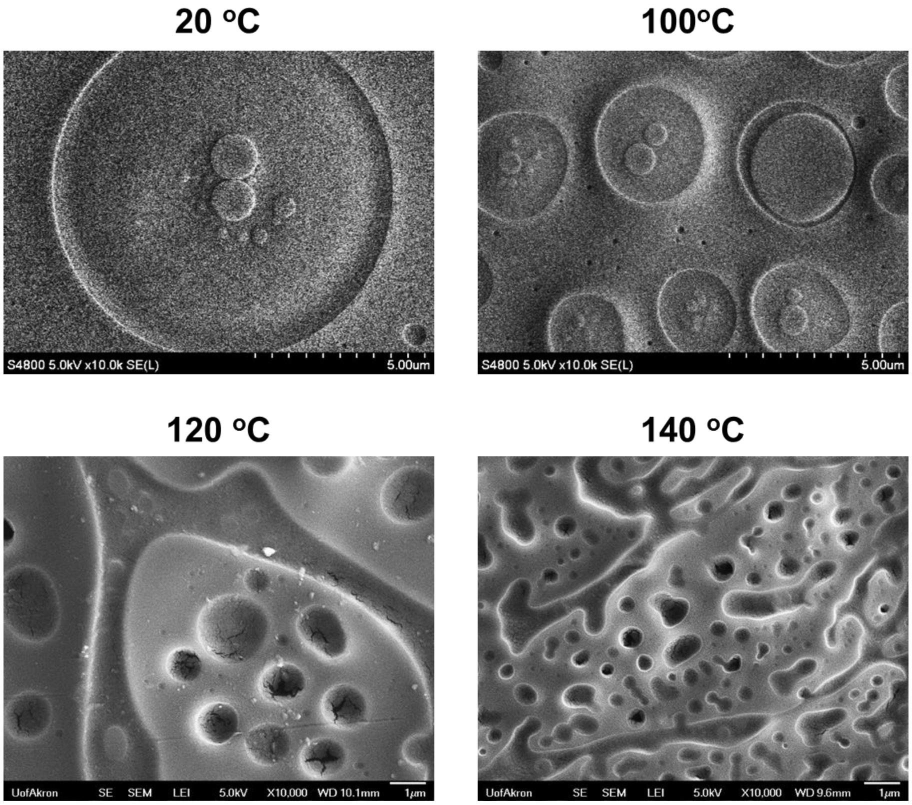

Figure 6.7 Effect of drying rate on the morphology of PS/PMMA blends with 50/50 ratio.

6.3.3.2 Effect of drying rate on the morphology of 50PS/50PMMA/silica film

The morphology of nanocomposite film with bare and modified silica nanoparticles is shown in Figure 6.8. The bare silica nanoparticles for both 170 nm and 17 nm diameter stay at the PMMA phase due to its hydrophilic surface making them preferential to PMMA as shown in Figure 6.8 (a) and (b). In contrast, the modified silica nanoparticles stay at the interface of PMMA islands and PS matrix and form particle rings (Figure 6.8 (c) and (d)) indicating that the surface of silica particle modified with PS-r-PMMA brush is chemically neutral to PS and PMMA.

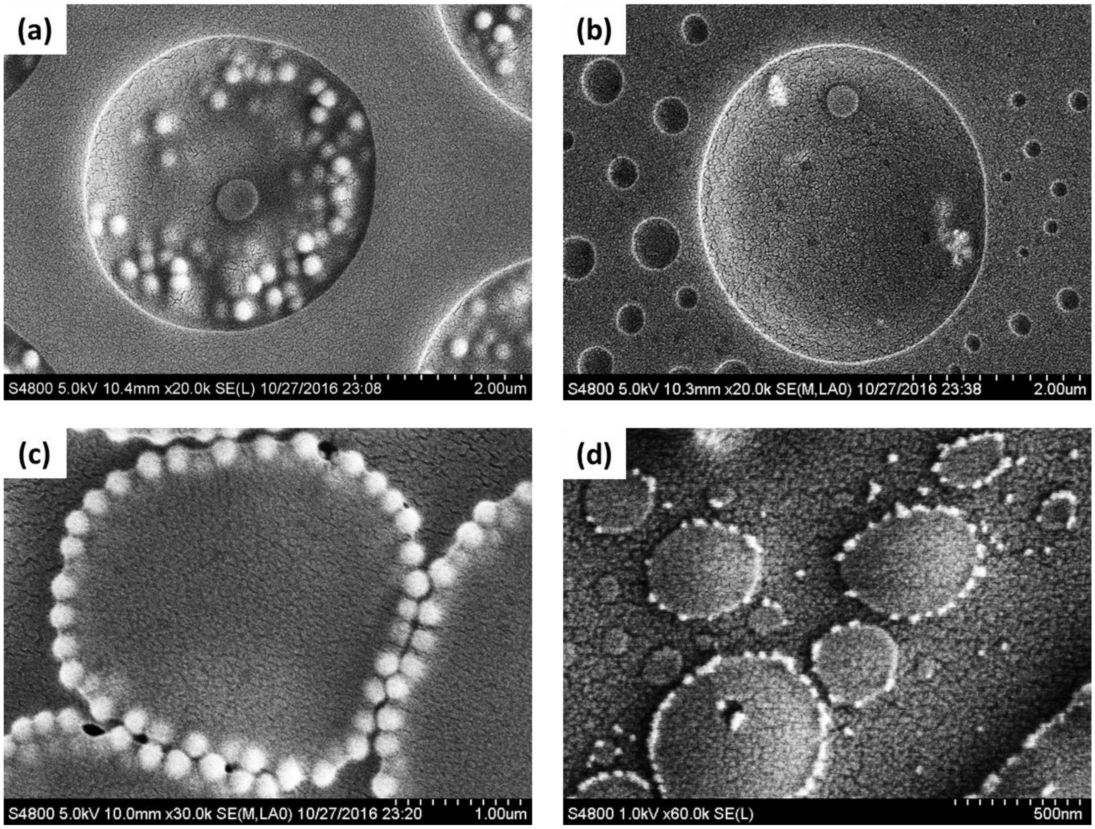

Figure 6.8 Morphology of PS/PMMA film with 10 vol% (a) bare silica nanoparticles (170nm), (b) bare (17nm), (c) modified (170nm) and (d) modified (17nm).

The effect of drying rate on morphology is studied for 50PS/50PMMA films with silica nanoparticles (170nm). The morphology of 50PS/50PMMA films with 20 vol.% silica nanoparticle dried at different temperatures is shown in Figure 6.9. The film dried at 20 ^{o}C shows island morphology due to the slow drying which gives it enough time for nucleation and growth to occur. The silica nanoparticles can be observed closely packed at the interface of PMMA islands and PS matrix and form particle rings. The film dried at 100 ^{o}C starts forming a continuous structure instead of the island structure of the pure PS/PMMA film dried at the same temperature. This is caused by the silica nanoparticles reducing the mobility of polymer chains and hindering the nucleation of PMMA phase. When the temperature is increased to 120 ^{o}C, the bicontinuous morphology with silica nanoparticles jammed at the interface can be observed. At this temperature the drying rate is so rapid that the time to pass through the metastable region is short. Since the nucleation and growth is a slow rate process, the phase separation starts according to the spinodal decomposition mechanism before the nucleation and growth happens at such a high drying rate.[213] Thus very obvious bicontinuous morphology can be observed at 80 ^{o}C. The film dried at 140 ^{o}C shows smaller bicontinuous domains with silica nanoparticle coated interface because the spinodal decomposition occurs at higher concentration at higher drying rate.[76] So the wavelength of concentration fluctuation during spinodal decomposition becomes smaller at higher evaporation rate yielding a smaller periodic distance in bicontinuous structure.[76] Compared to the domain size of pure PS/PMMA film at the same temperature, the domain size of composite film is much smaller as a result of suppression of mobility by the silica nanoparticles at the interface.

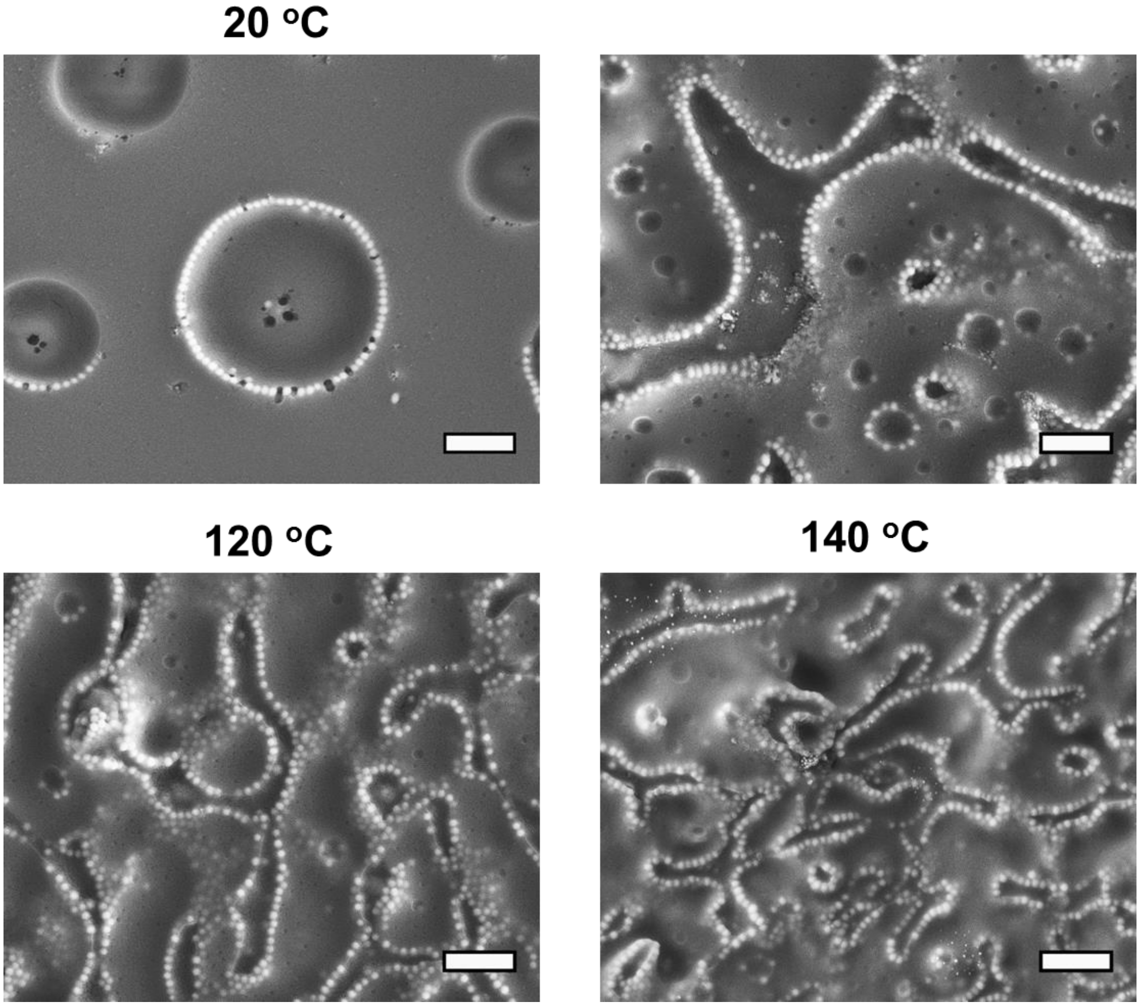

Figure 6.9 Effect of drying temperature on the morphology of PS/PMMA/20vol.% silica(170nm) film (scale bar: 2 μm).

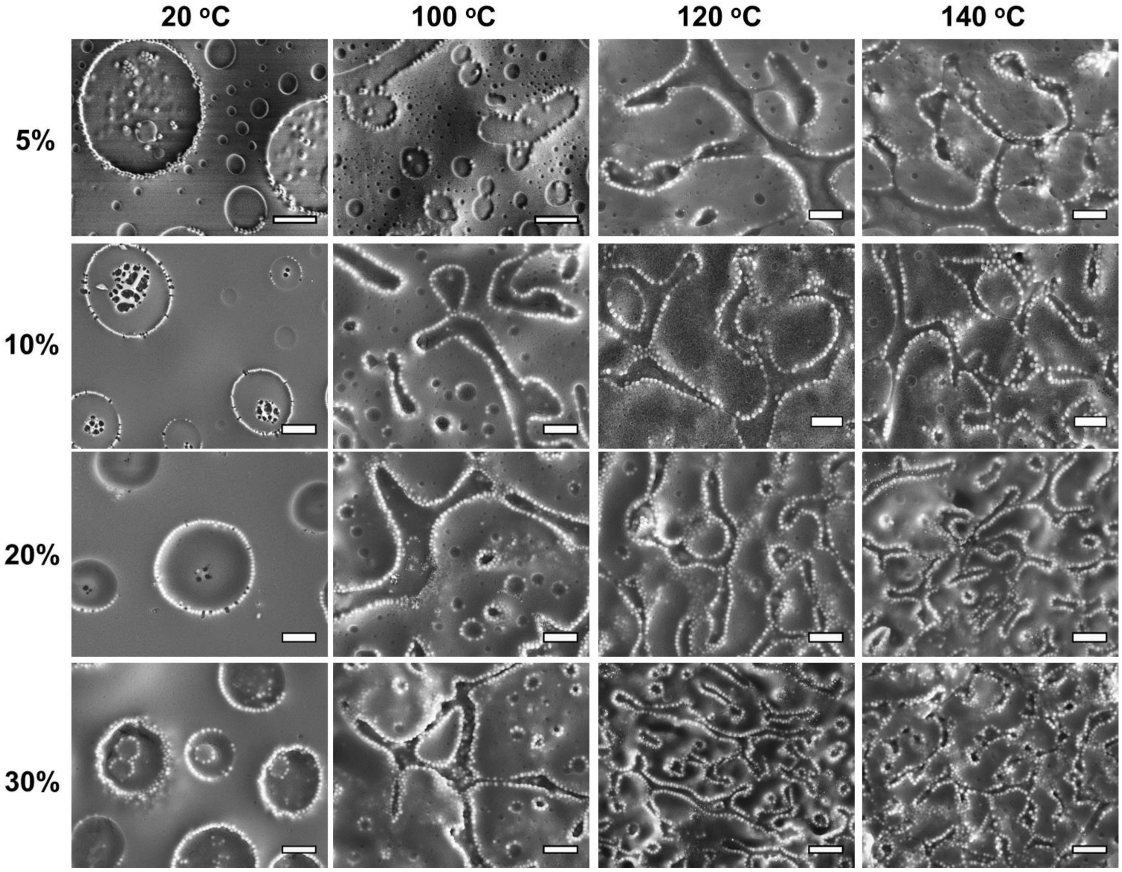

Figure 6.10 Effect of drying rate and particles' volume concentration on the morphology of PS/PMMA/silica nanoparticles (170nm) film (scale bar: 2 μm).

The effect of particle's concentration on the morphology of PS/PMMA/silica nanocomposite film is shown in Figure 6.10. The nanocomposite film form island morphology at 20 ^{o}C and the size of island decreases with increasing particle concentration because the silica nanoparticles at the interface suspend their growth. The film dried at 100 ^{o}C starts showing bicontinuous morphology as the volume concentration of silica nanoparticles increases to above 5vol%. The films dried at 120 ^{o}C and 140 ^{o}C show bicontinuous morphology with silica nanoparticle at the interface and the domain size of bicontinuous structure decreases with increasing particle concentration showing in Figure 6.11, which is attributed to the fact that there're more particles at the interface reducing the mobility of the polymer chains and restricting the coalescence process during drying. Higher drying temperature induced faster drying rate leads to smaller domain size.

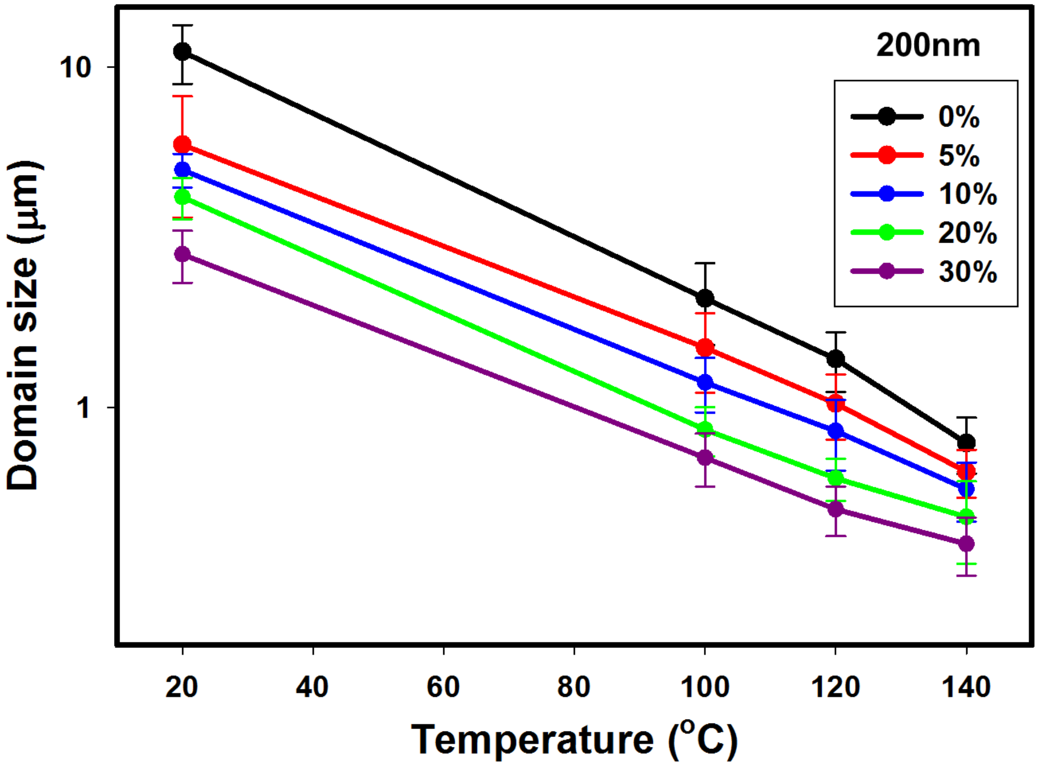

Figure 6.11 Effect of drying temperature and 200 nm size particles' volume concentration on the domain size.

6.3.3.3 Effect of particle size on the morphology of PS/PMMA/silica nanoparticle film

The morphology of PS/PMMA films with 20 vol% of silica nanoparticles (17nm) is shown in Figure 6.12. PMMA islands with silica nanoparticles closely packed at the interface are observed film dried at 20^{o}C. As the temperature is increased to 100 ^{o}C, the bicontinuous structure with silica particle coated interface can be observed and the size of domain becomes smaller compared to the film with 170 nm silica nanoparticles. This is caused by the larger numbers of nanoparticles and higher surface area for 17nm diameter silica nanoparticle than 170 nm particles resulting better hindering the mobility of polymer chains and nucleation of PMMA. As temperature increases to 120 and 140 ^{o}C, better bicontinuous structure forms with silica nanoparticles jammed at the interface and the size of domain decreases due to less time of coalescence caused by faster drying. The size bicontinuous domain is much smaller compared to film with 170 nm silica particles at the same loading of particle. The addition of silica nanoparticles with smaller size (17 nm) can halt the coalescence process earlier and trapped the bicontinuous morphology better during drying.[189, 214]

The nanocomposite films with 17nm diameter silica nanoparticles dried at 20 ^{o}C form island/matrix structure for all the samples and the size of islands decreases as the particle concentration increases showing in Figure 6.13 and Figure 6.14. As the concentration of silica nanoparticles is above 5 vol%, the film dried at 100 ^{o}C starts showing the bicontinuous morphology with nanoparticles at the interface. The bicontinuous morphology can be formed at all range of particle concentration for the film dried at 120 and 140 ^{o}C. The increase of particle concentration gives rise to the decrease of average domain size due to earlier halted coalescence process during phase separation and better stabilizing smaller scale structure for higher concentration of particles. Compared to the films with 200 nm silica particles, the films with 20 nm particles show smaller domain size at the same condition due to higher surface area to volume ratio.

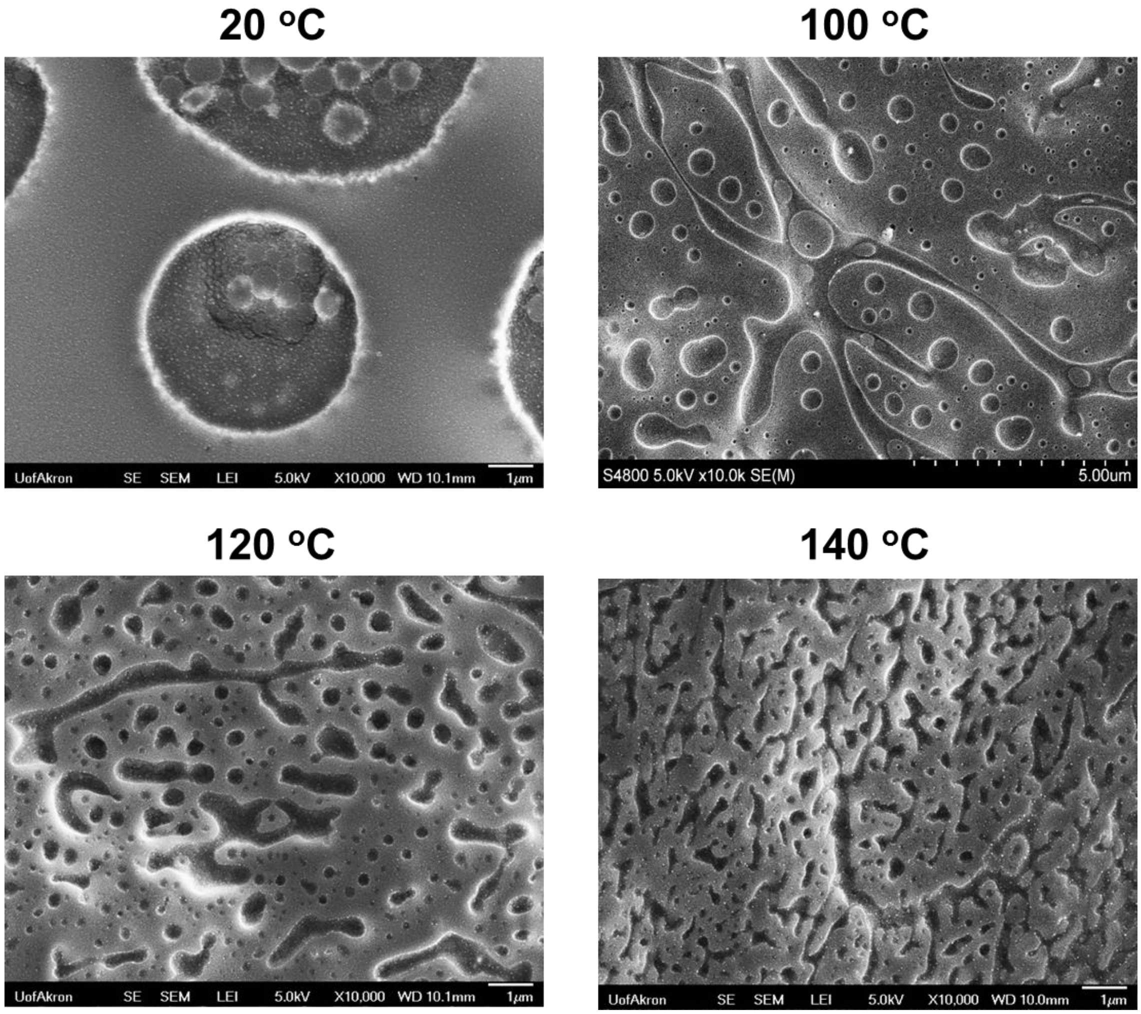

20 °C

100 °C

120 °C

140 °C

Figure 6.12 Effect of drying temperature on the morphology of PS/PMMA/20 vol.% silica(17nm) film.

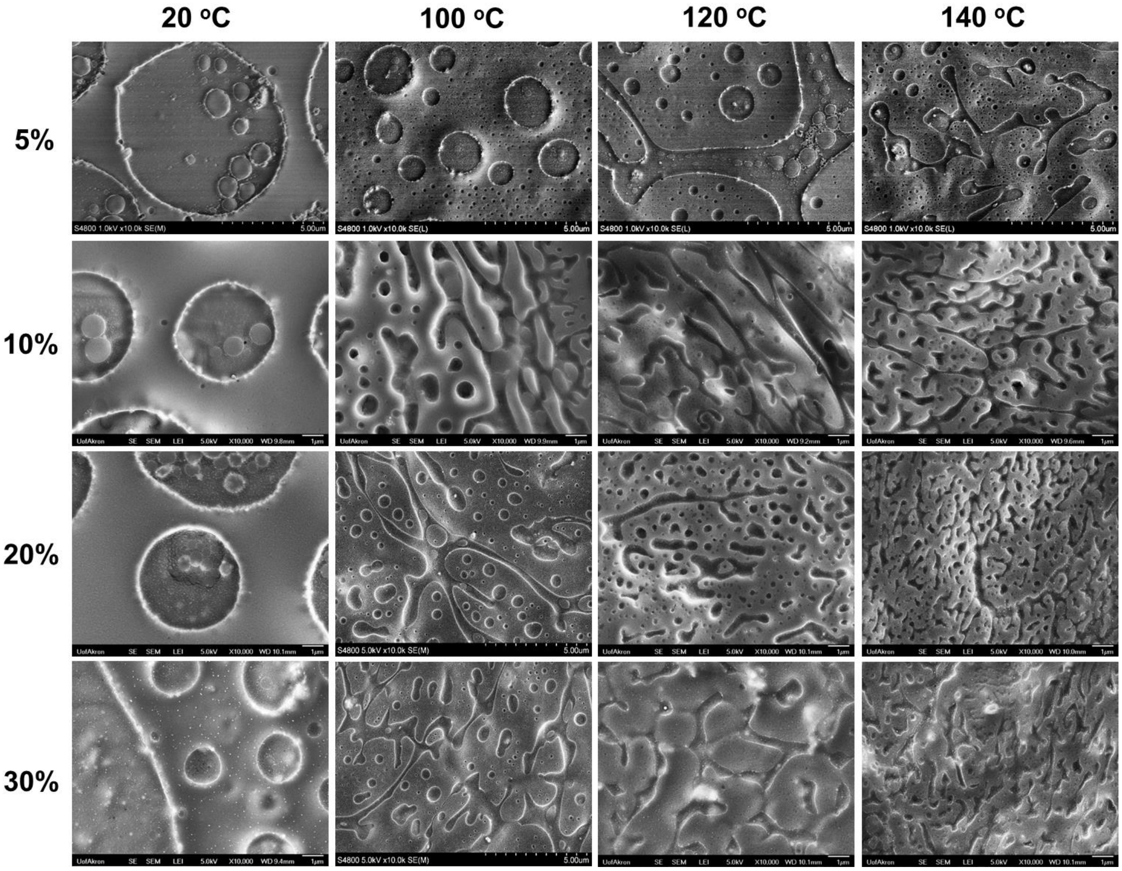

Figure 6.13 Effect of drying rate and volume concentration on the morphology of PS/PMMA/silica nanoparticles (17nm) film.

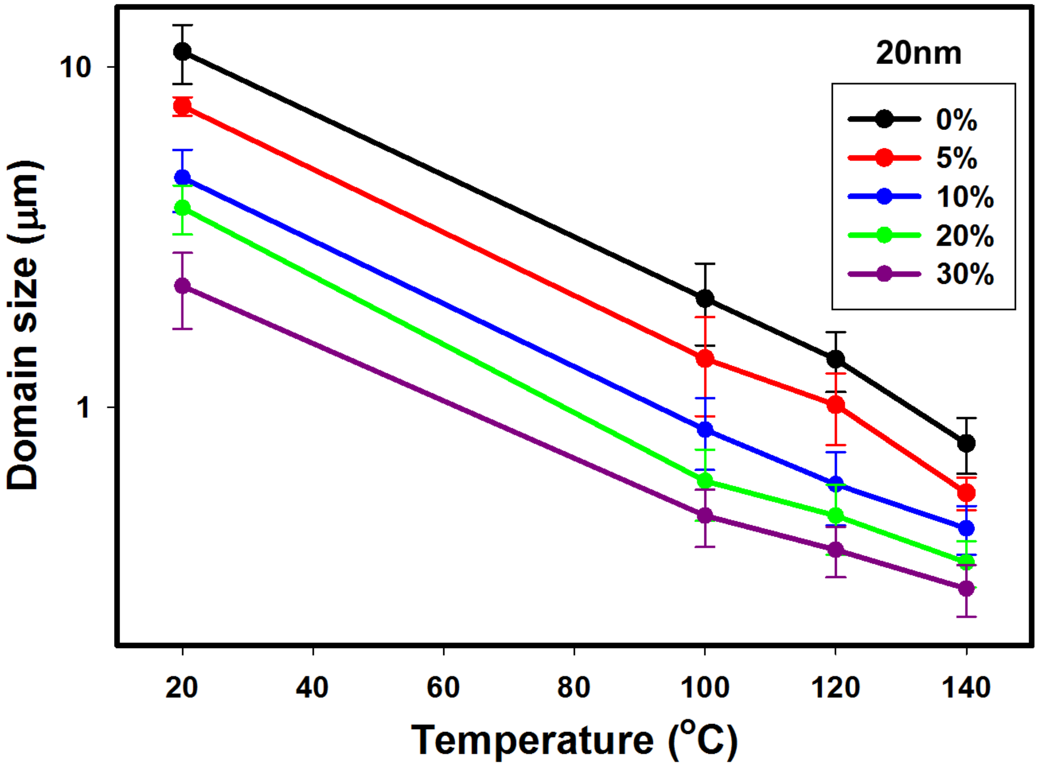

Figure 6.14 Effect of drying temperature and 20 nm size particles' volume concentration on the domain size.

6.3.3.4 Effect of polymer blend ratio on morphology

The ratio of PS and PMMA has a dramatic effect on the resulting morphology. The PS/PMMA blend films with 35/65 ratio show compact distributed PMMA islands in continuous PS matrix due to the higher ratio of PMMA as shown in Figure 6.15. For PS/PMMA films with 35/65 blend ratio, there's no transition from island to bicontinuous morphology observed as the drying temperature is 120 ^{o}C, which is observed for the films with 50/50 ratio. This indicates that this blend ratio strays away from the critical composition where the spinodal decomposition may occur. The size of PMMA island domains decreases with increasing drying temperature due to less time for nuclei to grow at higher drying rate. The effect of blend ratio on the morphology of PS/PMMA/silica nanocomposite film with 170 nm and 17nm particle diameter is shown Figure 6.16 and 6.17, respectively. At 20 ^{o}C, only island morphology is observed for both blend ratio and the film with 35/65 PS/PMMA ratio shows more compacted island than 50/50 ratio due to higher composition of PMMA. The nanocomposite films with 50/50 ratio show bicontinuous structure with silica nanoparticle segregated at the interface when the drying temperature is above 100 ^{o}C. On the contrary, the addition of silica nanoparticles doesn't make the transition from island to bicontinuous morphology occurs for the film with 35/65 PS/PMMA ratio which is away from the critical composition for spinodal decomposition.

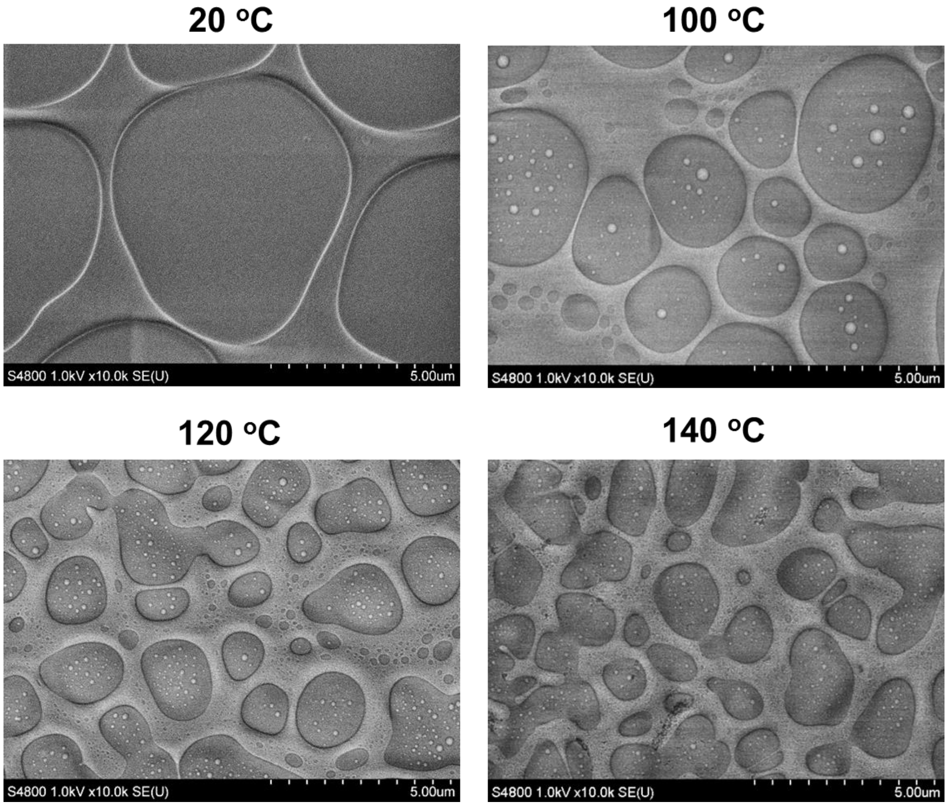

Figure 6.15 Effect of drying rate on the morphology of PS/PMMA blends film with 35/65 ratio.

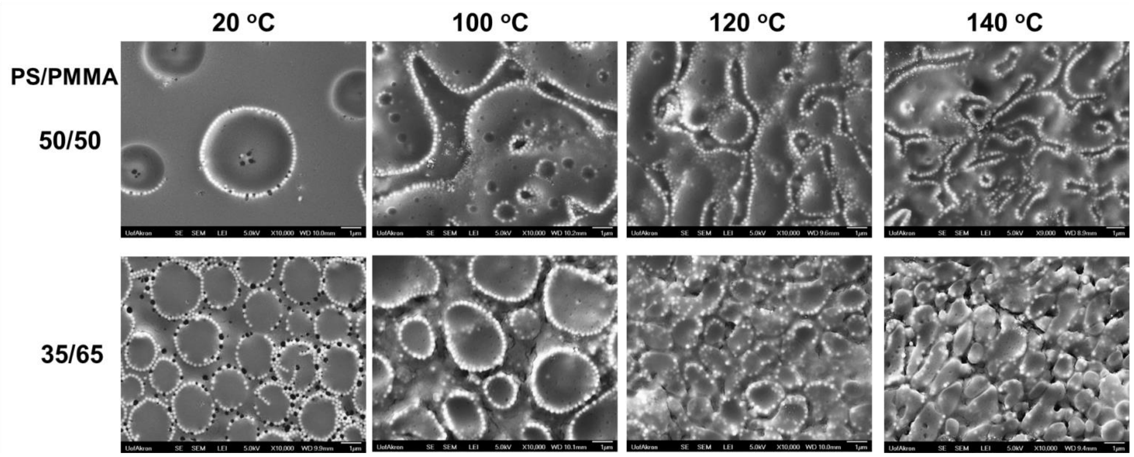

Figure 6.16 The effect of blend ratio on the morphology with 20 vol% 170 nm silica nanoparticles.

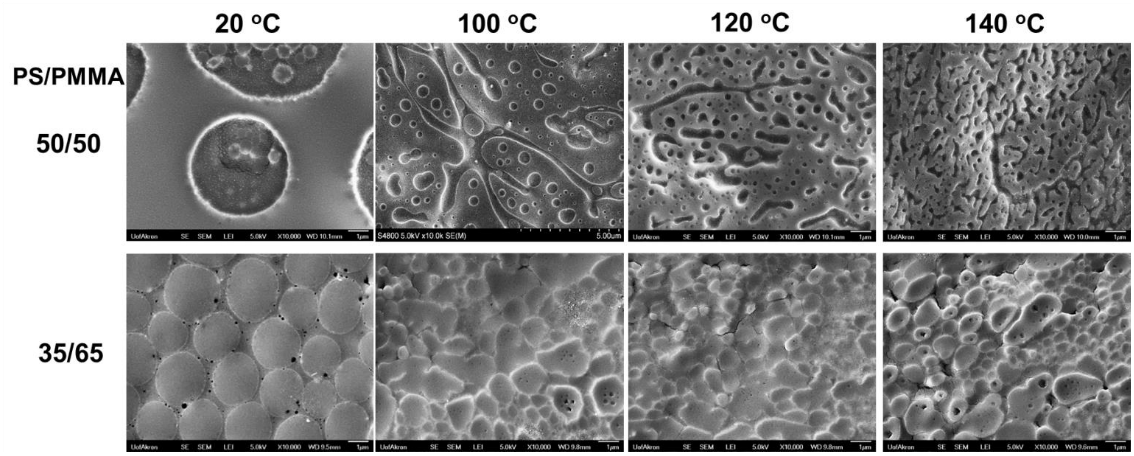

Figure 6.17 The effect of blend ratio on the morphology with 20 vol% 17 nm silica nanoparticles.

6.3.4 Effect of electric field on morphology of PS/PMMA with silica nanoparticles (low ε)

The electric field was applied in the lateral direction of the PS/PMMA/silica/THF solution once it was dripped between two electrodes. The final morphology of PS/PMMA blend film with 10% silica nanoparticles was shown in Figure 6.18. The PMMA spherical droplets with silica nanoparticles coated interface were stretched into prolate ellipsoids with the major axis along the field direction. This is consistent with previous works on pure PS/PMMA blends in toluene solution.[119] The accumulated free charges at the interface induce the tangential stress resulting in the electrohydrodynamic flow inside and outside the droplets.[206] Since PMMA (3.5) has slightly higher dielectric constant than PS (2.6), the circulation liquid flows are directed from equator to pole leading to the deformation into prolate ellipsoids.

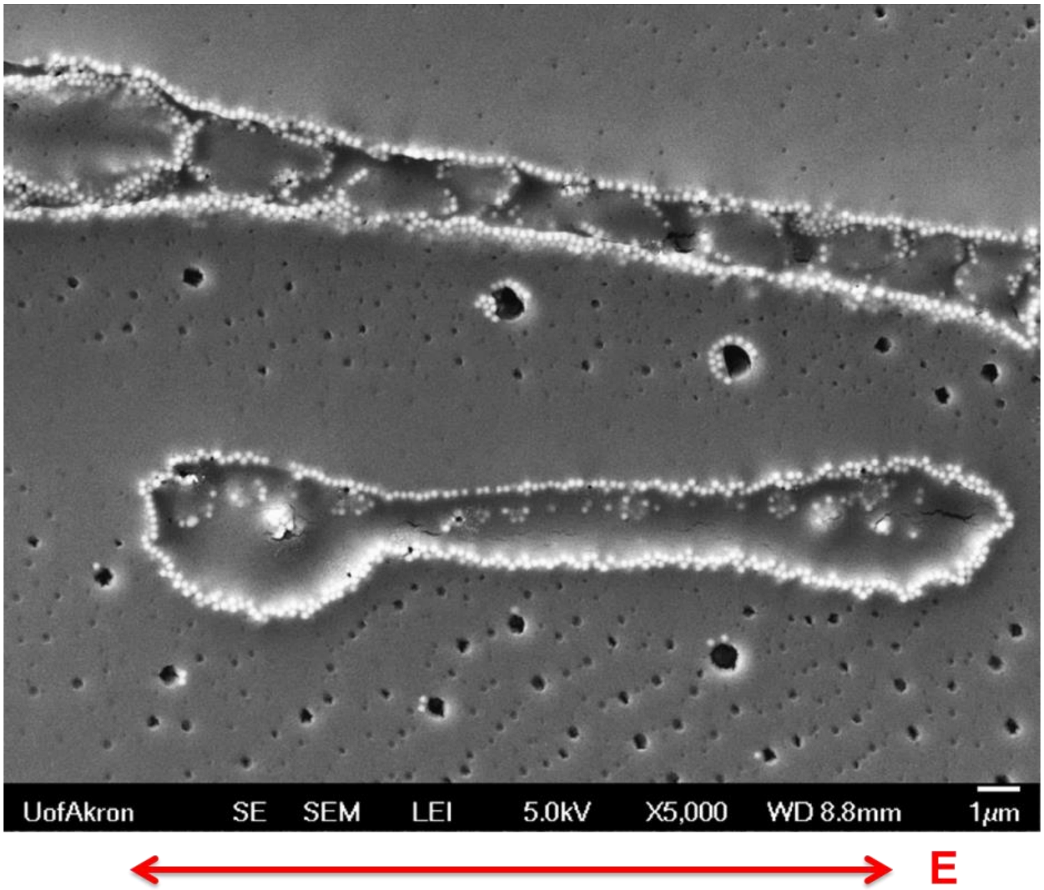

Figure 6.18 Morphology of 50/50 PS/PMMA blends with silica nanoparticles coated interface at E=/300V/mm in lateral direction.

The effect of vertical applied electric field on the morphology is also studied. The cross sectional morphology of the film without application of electric field is shown in Figure 6.19. The silica nanoparticles stay at the interface of PMMA droplets and PS matrix. The spherical droplets are compressed into elliptical domains due to the shrinkage force developed during solvent evaporation. In contrast, Figure 6.20 shows the vertical cylindrical domains with the major axis in thickness direction, namely the electric field direction, for the film applied with 300 V/mm vertical electric field. The dielectrophoresis force overcomes the shrinkage force to make the cylindrical domain vertically deformed instead of compressed in lateral direction, although there is an angle observed between the major axis and thickness direction caused by the shrinkage effect. The electric field induced deformation from spherical droplets to ellipsoids leads to the increase of surface area which is free of silica particles. The silica nanoparticles are still densely coated at the surface of droplet with hexagonal arrangement, and there is no detachment of particles from the interface observed with the application of electric field. There is no reorganization and alignment of silica particles at the interface observed because dielectric constant of silica nanoparticles (3.9) is very close that of PMMA and PS.

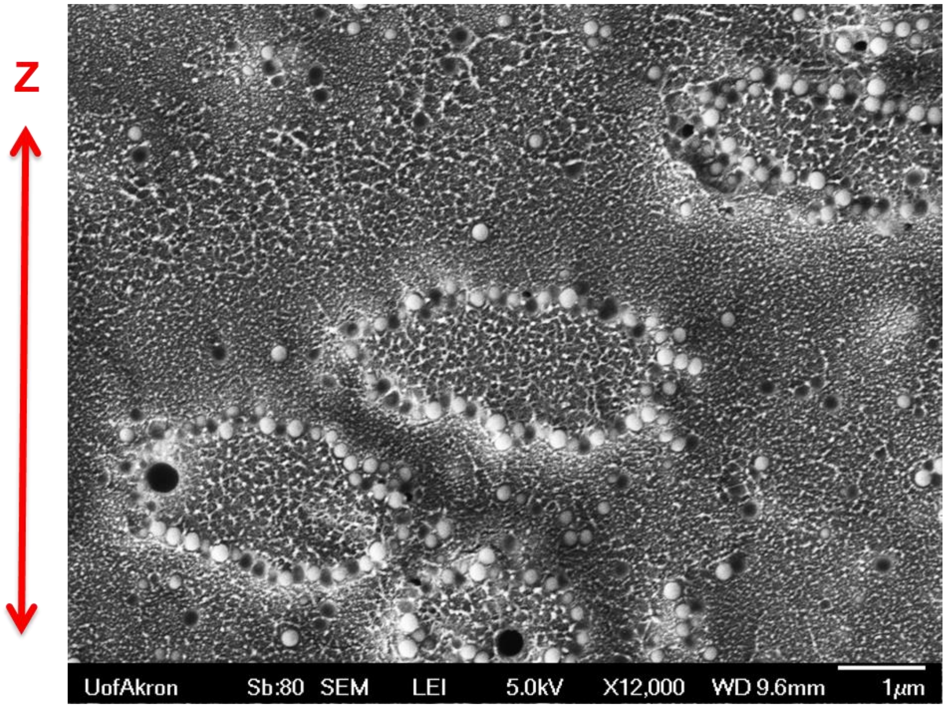

Figure 6. 19 Cross sectional morphology of 50/50 PS/PMMA blends with 10 vol% silica nanoparticles at interface without electric field.

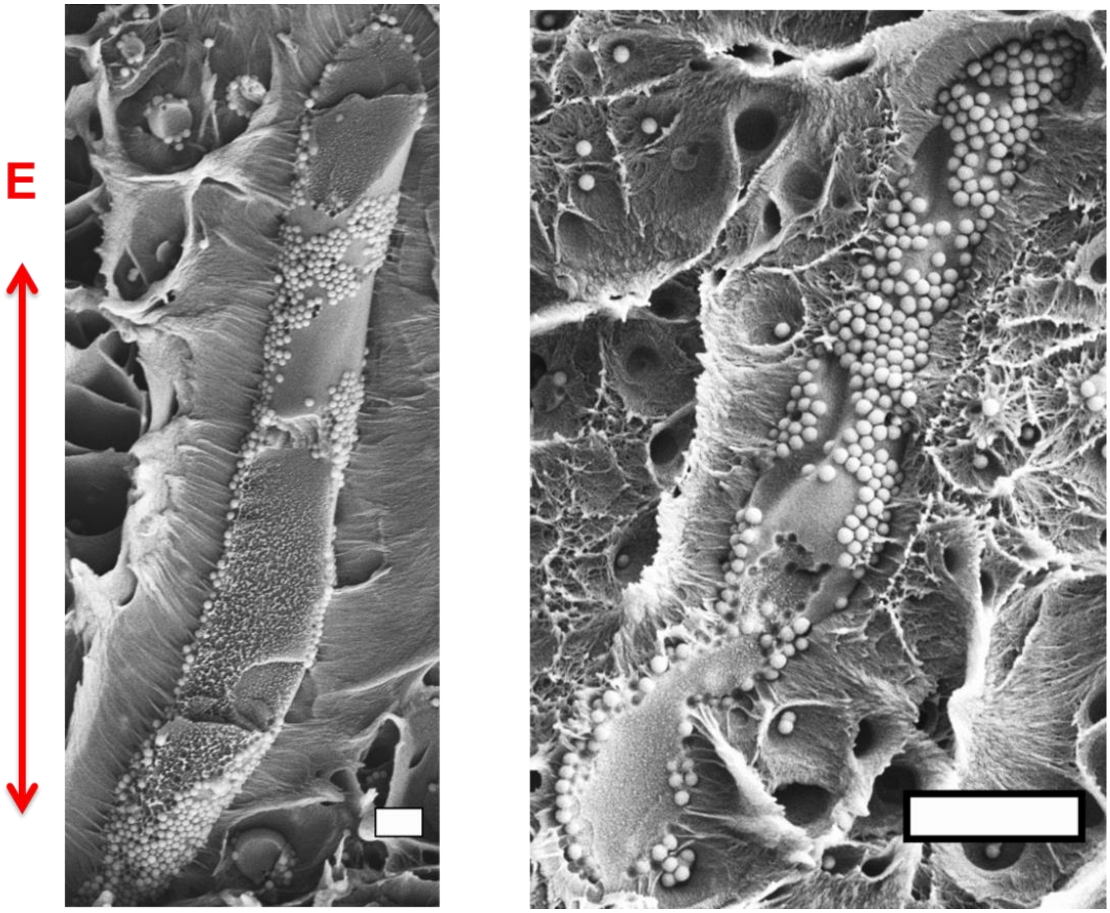

Figure 6.20 Cross sectional morphology of 50/50 PS/PMMA blends with 10 vol% silica nanoparticles coated interface at initial E=/300V/mm in vertical direction (scle bar: 2μm).

6.3.5 Effect of electric field on morphology of PS/PMMA with BT nanoparticles (high ε)

It is found that the PMMA spherical domains can be stretched into vertically oriented cylinders and the silica nanoparticles are coated at the interface densely. However, the silica nanoparticles are not aligned to from particle chains either in the matrix or at the interface. Is this caused by the limited mobility of silica nanoparticle packed at the interface or the too similar dielectric constant of nanoparticles and matrix?

To investigate the reason, the BT nanoparticles with very high dielectric constant (about 2000) are used for comparison. To make the BT nanoparticles remain at the interface of PS and PMMA, the surface modification is needed to make them chemically neutral to each component. The surface modification of BT nanoparticles was carried out by using the condensation reaction between the hydroxyl groups of BT surface and hydroxyl group terminated PS-r-PMMA. After the surface modification, the FTIR spectra of bare and modified BT nanoparticles are collected showing in Figure 6.21. Both the bare and modified BT nanoparticles show two bands at 1610 cm^{-1} and 1452 cm^{-1} indicating the asymmetric and symmetric vibrations of acetate group respectively, which is corresponding to the unreacted acetate reagent for synthesizing BT particles.[215, 216] The modified BT nanoparticles show three distinct peaks: (1) a broad peak from 1040 to 1260 cm^{-1}, which is attributed to the stretching vibration of C-O-C group; (2) the peak at 1730 cm^{-1} indicating the presence of acrylate carboxyl group; (3) two bands at 2850 and 2920 cm^{-1}, which is assigned to the C-H bond stretching vibrations of the methyl and methylene group.[217] Therefore, these distinct peaks indicates the successful surface modification of BT nanoparticles by the PS-r-PMMA copolymer brush. The TGA curve of bare and modified BT nanoparticles is shown in Figure 6.22. The bare and modified BT nanoparticles have the same weight loss (about 0.8%) below 300 ^{o}C due to the loss of bonded water. After heating to 800 ^{o}C, the modified BT nanoparticles undergo 1.2% more weight loss than bare BT particle due to the decomposition of attached PS-r-PMMA brush. The TEM image in Figure 6.23 shows the core-shell structure of modified BT nanoparticles indicating the successful surface modification of BT nanoparticles. The surface morphology of PS/PMMA with 10 vo% BT nanoparticles after the evaporation of THF is shown in Figure 6.24. All the BT nanoparticles are densely packed at the interface of PS and PMMA due to the same wetting ability of modified BT nanoparticles to each component.

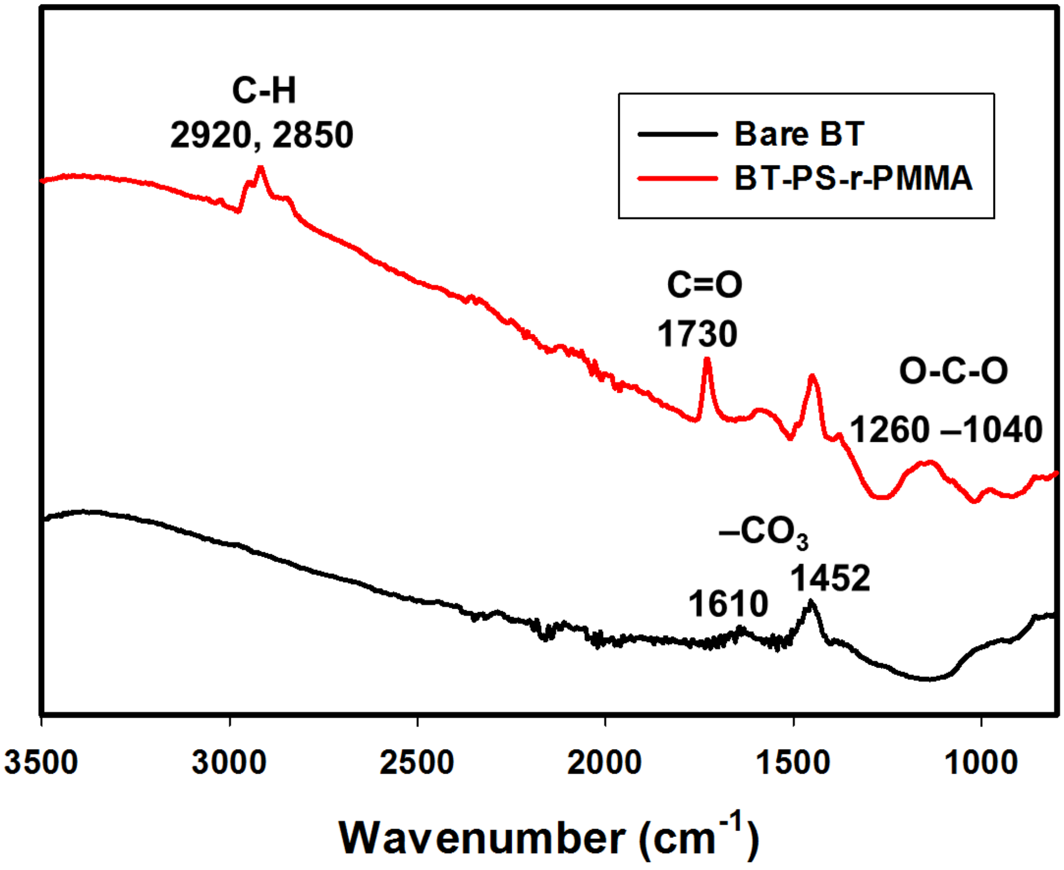

Figure 6.21 FTIR spectra of pristine and modified BT particles.

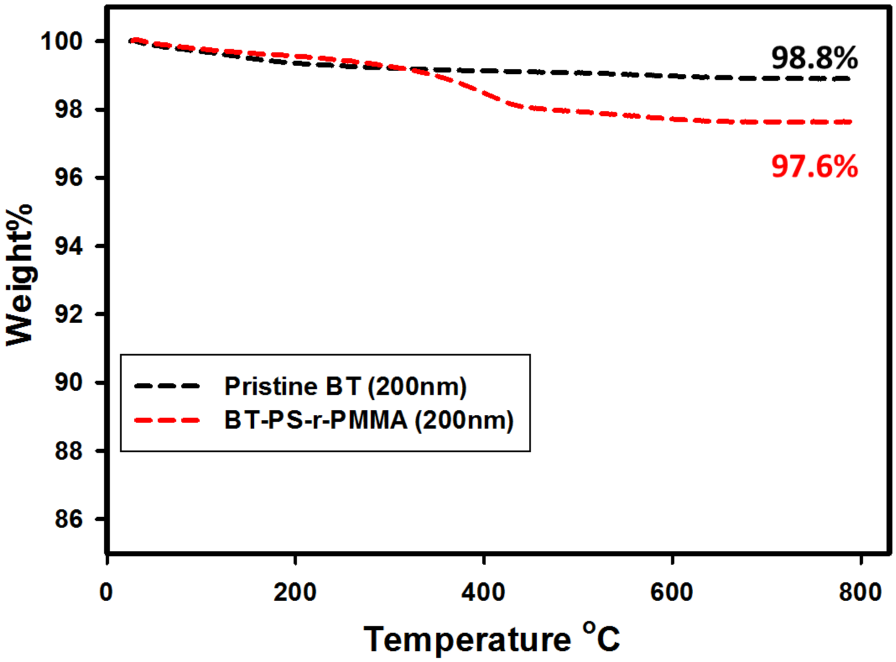

Figure 6.22 TGA curves of bare and modified BT particle.

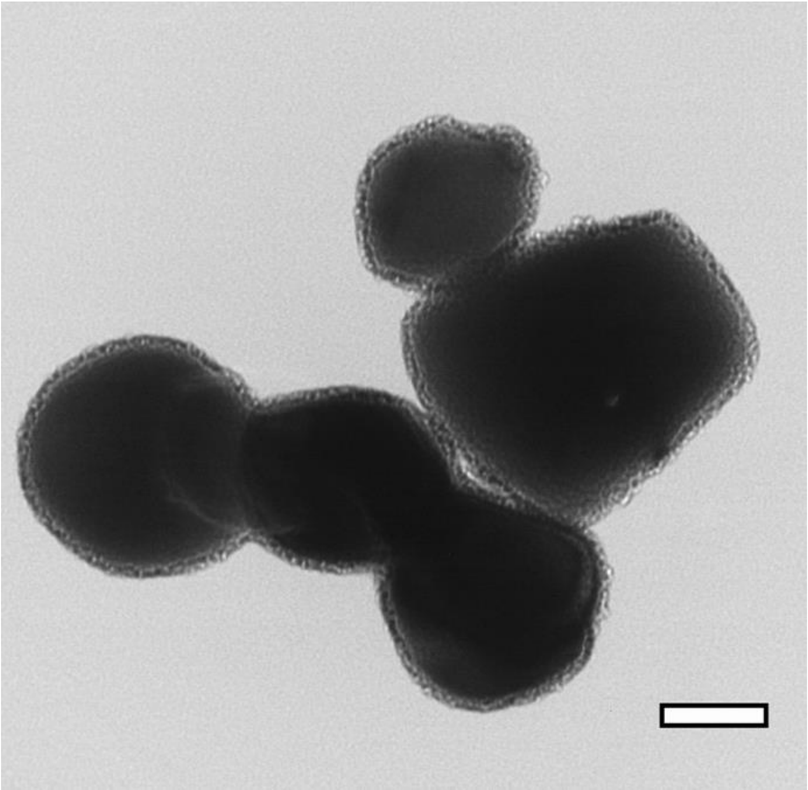

Figure 6.23 TEM image of modified BT nanoparticles (scale bar 100nm).

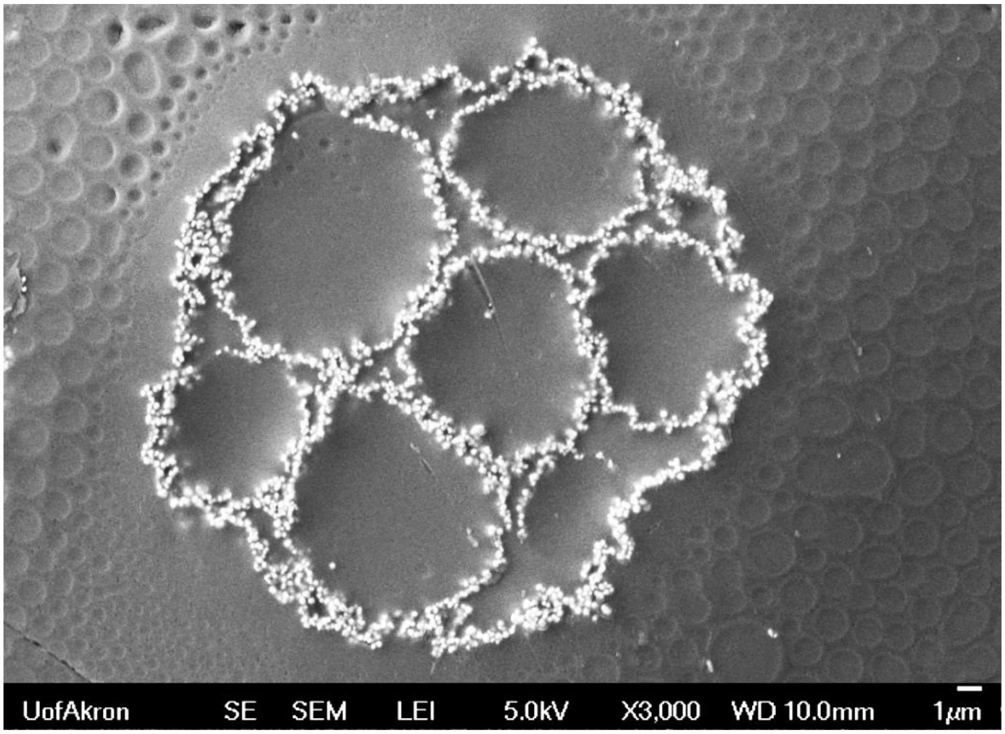

Figure 6.24 Surface morphology of PS/PMMA blend films with 10 vol% BT nanoparticles after evaporation of THF.

Figure 6.25 shows the cross sectional morphology of PS/PMMA/BT nanoparticles film without the application of electric field. The BT nanoparticles are segregated at the interface of PMMA droplet and PS matrix and the spherical PMMA droplet is compressed into elliptical shape domains due to the shrinkage forces developed during solvent evaporation. After applying vertical electric field on the film during solvent evaporation, the spherical PMMA droplet is deformed into a prolate ellipsoid in vertical direction, although there’s a tilted angle caused by the shrinkage effect showing in Figure 6.26(a). The interface absorbed BT nanoparticles are still densely packed at the interface and there is no reorganization observed, which is very similar to the morphology of

PS/PMMA/silica under electric field. In contrast, the BT nanoparticles are also aligned into pearl chains vertically at the interface of PMMA droplet and PS matrix as shown in Figure 6.26 (b). The dense packing of BT nanoparticles at the interface limits the mobility of nanoparticles to form chains under electric field in Figure 6.26(a). While in Figure 6.26(b), there are more spaces for BT nanoparticles to reorganize into chains spanning the interface. This phenomenon was observed in Pickering emulsion system with electric field induced chain formation of silver coated glass particles at castor-silicon oil interface.[206] Therefore, there is no alignment of silica nanoparticles at the interface is caused by their low dielectric constant. Figure 6.26 (c) shows the vertically aligned pearl chains of BT nanoparticles in the PS matrix due to the electric field induced dipole-dipole interactions, which is observed for homo polymer PS/BT nanoparticles system.[29]

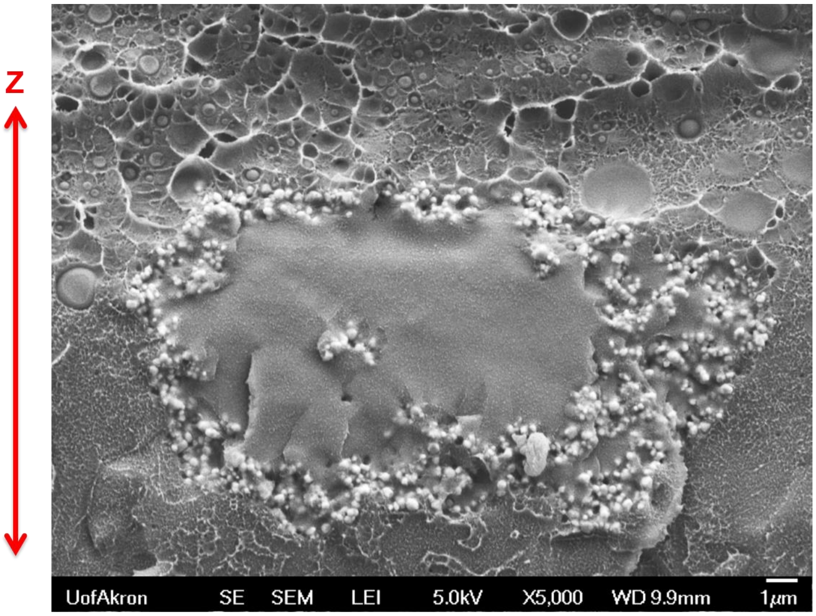

Figure 6.25 Cross sectional morphology of 50/50 PS/PMMA blends with 10 vol% BT nanoparticles at interface without electric field.

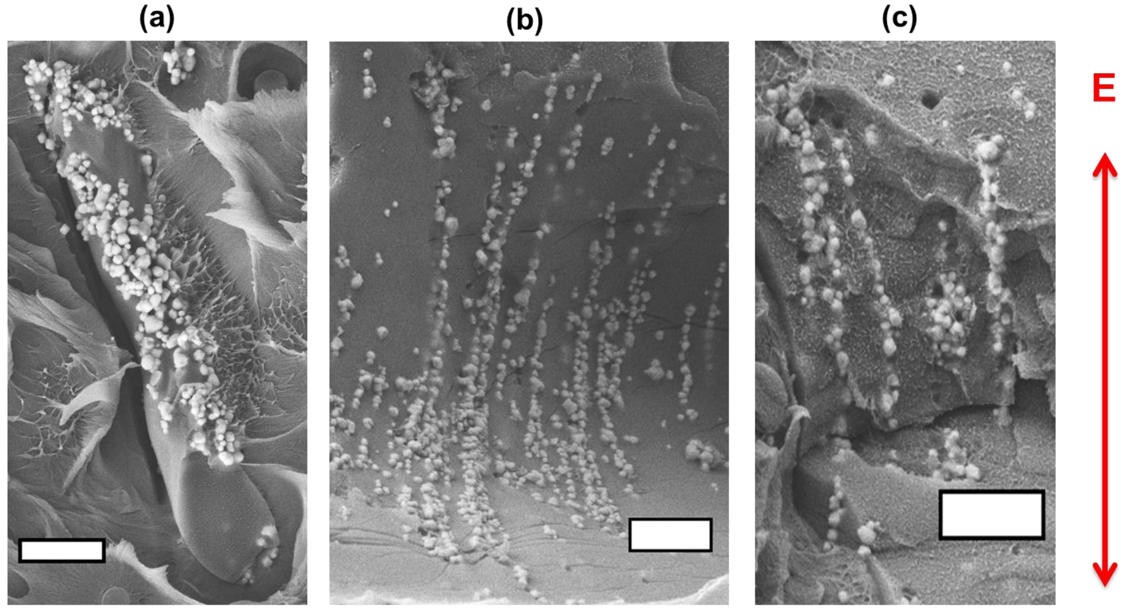

Figure 6.26 Cross sectional morphology of 50/50 PS/PMMA blends with 10 vol% BT nanoparticles at initial E=/300V/mm in vertical direction (a) vertical domains with BT particles coated at interface, (b) vertically aligned chains at the interface and (c) vertically aligned particle chains in PS matrix. (Scale bar: 2μm)

6.4 Conclusion

The RAFT polymerization synthesized PS-r-PMMA-OH copolymer was attached to the surface of silica nanoparticles to have the same wetting to PS and PMMA. After phase separation, the modified silica nanoparticles were segregated at the interface of PS and PMMA to trap both dispersed and bicontinuous morphologies. The rate of solvent evaporation, blend composition, particle loading and size determined the formation of whether dispersed or bicontinuous morphology and the size of domain after drying. The

50/50 PS/PMMA polymer blends with silica nanoparticles formed the dispersed PMMA domains in PS matrix at low evaporation rate and bicontinuous morphology at high evaporation rate at 100 ^oC drying temperature or above. The silica nanoparticles were coated at the interface for both dispersed and bicontinuous morphology. The 35/65 PS/PMMA blends can only form the dispersed phases no matter of at low and high evaporation rate because the composition was away from the critical composition in phase diagram. As the particle loading increases, the size of phase separated domain decreases because the interfacial absorbed nanoparticles halted the coarsening and coalesce of domains. The silica nanoparticles with smaller size resulted in relatively smaller domain size due to their higher surface area to volume ratio. The spherical PMMA droplets were stretched into prolate ellipsoids with the particles coated interface. The ellipsoids were oriented vertically along the electric field direction, although there is a tilted angle between the major axis of ellipsoid and filed direction caused by the shrinkage effect during solvent evaporation. The silica nanoparticles with low dielectric constant were packed densely at the interface with hexagonal arrangement, but not reorganized and aligned at the interface. The BT nanoparticles with high dielectric constant were not aligned as well at the interface if the particles were coating at the interface densely. But BT nanoparticles were aligned into particle chains at the interface if there were fewer particles at the interface.

CHAPTER VII

SUMMARY

This study develops two new processing methods for roll to roll continuous manufacturing polymer nanocomposite with electric field assisting “Z” aligned nanoparticles or phases: one is for thermoset and the other one is for thermoplastic matrix materials. Using these processing methods, the cost of large scale manufacturing can be reduced due to the directional aligned nanoparticles or phases enhancing the properties. In chapter III, non-contact alignment method was developed by adding an air gap between the top electrode and the top surface of liquid film in order to rapidly manufacture these films, which avoid the adhesion of electrode to film after solidification in previous researches. Multifunctional PDMS/graphite nanocomposite films with “Z” aligned graphite particle chains were manufactured by using this method and show high electric, dielectric and thermal conductivities in thickness direction. The kinetics of particle alignment and chain formation under electric field were studied by tracking the real-time optical light transmission, with focus on the effect of applied voltage and particle concentrations. Higher applied voltage led to faster chain formation and growth as well as longer and thicker particle chains across the film cross-section. The aligned nanocomposites exhibited higher electrical conductivity, dielectric permittivity as well as thermal conductivity compared to non-aligned samples with the same loading of particles. This enhancement effect first increases with particle content and then decreases as particle concentration is beyond 5 vol%. This is attributed to the fact that the particles were better aligned below 5 vol%, whereas bare alignment can be observed due to high viscosity and resistivity above 5 vol%. With 5 vol% graphite loading, 250 times higher electrical conductivity, 43 times higher dielectric permittivity and 1.5 times higher thermal conductivity was achieved after alignment of particle under electric field. The percolation transition occurs at much lower, 2 vol% concentration, for aligned samples compared to at 10 vol% for non-aligned ones. By decreasing the percolation threshold, the flexibility of the polymer matrix was maintained while achieving the same electrical and thermal performance.

Electric field induced vertical alignment of nanoparticles in thermoset has been well studied and developed to fabrication nanocomposites. However, there’s little study involving the thermoplastic polymers as the matrix to produce the nanocomposites with vertically aligned particles. To broaden the choice of matrix materials, Chapter IV develops a continuous processing method in the polymer/solvent solution systems for aligning nanoparticles vertically under electric field. The optical light transmission is sensitive enough to quantify the kinetics of particle organization with electric field involving nanocolumn formation and eventual buckling as a result of solvent loss related shrinkage. The nanocolumns buckle at low electric field, while the use of high electric fields overcomes the shrinkage effect to maintain nanocolumns vertically oriented along the field direction. It is also found out that the direction of buckling for the particle chains is related to the drying gradient. The patterned surface created by the porous electrodes on the top surface can be eliminated by using the two-layer solution casting method by using two immiscible polymers with solvents that are miscible with each other facilitating drying of both layers. The top layer acts as a sacrificial layer to prevent the direct touch with the composite layer. The nanocomposites with aligned particles in “Z” direction show substantially enhanced dielectric permittivity in thickness direction.

Commercialized wound dressings have an issue of too much lateral expansion after absorbing the exudate causing shearing on the fragile wound during the healing process. In Chapter V, the three-layer wound dressings are fabricated to solve this issue by preferentially aligning the absorbent particles vertically in the absorbent layer, using this newly developed processing method in previous chapter. Owing to this anisotropic structure, wound dressings undergo more vertical expansion than lateral expansion after absorbing water. Moreover, the alignment of particles significantly reduces the lateral expansion by 33% compared to the films with random particles, which is beneficial in reducing the shear stress on the wound. The cylindrical particles (nanorods) with higher aspect ratio further increase the anisotropic swelling ratio and reduce the lateral expansion than irregular particles. The imprint patterns on the top layer achieve lower contact angle as well as higher base radius of water droplet.

The PS-r-PMMA modified silica nanoparticles are absorbed at the interface of PS and PMMA blends for both dispersed and bicontinuous morphologies by solvent evaporation induced demixing in chapter VI. The formation of dispersed or bicontinuous morphology is affected by the rate of solvent evaporation, blend compositions, particle loading and size. The 50/50 PS/PMMA polymer blends form the silica nanoparticle coated dispersed PMMA domains (similar to Pickering emulsion) in PS matrix at low evaporation rate and bicontinuous morphology (similar to bijels) at high evaporation rate. The 35/65 PS/PMMA blends can only form the dispersed phases independent of evaporation rate. The size of phase separated domains decreases as the particle loading increases because the interfacial absorbed nanoparticles halts the coarsening and coalesce of domains. The spherical PMMA droplets are stretched into prolate ellipsoids with the major axis in vertical direction under electric field. The silica nanoparticles with low dielectric constant were packed densely at the interface with hexagonal arrangement, but not reorganized and aligned at the interface. While the BT nanoparticles with high dielectric constant are aligned into particle chains at the interface.

REFERENCES

1. Pandey, G.; Thostenson, E. T. Carbon Nanotube-Based Multifunctional Polymer Nanocomposites. *Polymer Reviews* 2012, 52, 355-416.

2. Thostenson, E. T.; Li, C.; Chou, T.-W. Nanocomposites in context. *Composites Science and Technology* 2005, 65, 491-516.

3. Thostenson, E. T.; Ren, Z.; Chou, T.-W. Advances in the science and technology of carbon nanotubes and their composites: a review. *Composites Science and Technology* 2001, 61, 1899-1912.

4. Riggs, B. C.; Adireddy, S.; Rehm, C. H.; Puli, V. S.; Elupula, R.; Chrisey, D. B. Polymer Nanocomposites for Energy Storage Applications. *Materials Today: Proceedings* 2015, 2, 3853-3863.

5. Alnassar, M.; Alfadhel, A.; Ivanov, Y. P.; Kosel, J. Magnetoelectric polymer nanocomposite for flexible electronics. *Journal of Applied Physics* 2015, 117, 17D711.

6. Tjong, S. C. Polymer Nanocomposites for Biomedical Applications. In *Polymer Composites with Carbonaceous Nanofillers*, Wiley-VCH Verlag GmbH & Co. KGaA: 2012; pp 285-329.

7. Martin, C. A.; Sandler, J. K. W.; Windle, A. H.; Schwarz, M. K.; Bauhofer, W.; Schulte, K.; Shaffer, M. S. P. Electric field-induced aligned multi-wall carbon nanotube networks in epoxy composites. *Polymer* 2005, 46, 877-886.

8. Knaapila, M.; Høyer, H.; Svåsand, E.; Buchanan, M.; Skjeltorp, A. T.; Helgesen, G. Aligned carbon cones in free-standing UV-Curable polymer composite. *Journal of Polymer Science Part B: Polymer Physics* 2011, 49, 399-403.

9. Fan, B. Dielectric properties of carbon nanotube-BaTiO hybrids reinforced PVDF composites. University of Paris-Saclay, 2016.

10. Kasap, S. O. *Principles of electronic materials and devices*. Mc Graw Hill Education: 2007.

11. Huang, X.; Jiang, P. Core–Shell Structured High-k Polymer Nanocomposites for Energy Storage and Dielectric Applications. *Advanced Materials* 2015, 27, 546-554.

12. Zhang, Q. M.; Li, H.; Poh, M.; Xia, F.; Cheng, Z. Y.; Xu, H.; Huang, C. An all-organic composite actuator material with a high dielectric constant. *Nature* 2002, 419, 284-287.

13. Li, J.; Sun, Z.; Yan, F. Solution Processable Low-Voltage Organic Thin Film Transistors with High-k Relaxor Ferroelectric Polymer as Gate Insulator. *Advanced Materials* 2012, 24, 88-93.

14. Hwang, S. K.; Bae, I.; Cho, S. M.; Kim, R. H.; Jung, H. J.; Park, C. High Performance Multi-Level Non-Volatile Polymer Memory with Solution-Blended Ferroelectric Polymer/High-k Insulators for Low Voltage Operation. *Advanced Functional Materials* 2013, 23, 5484-5493.

15. Eigner, A.; Semino, S. 50 years of electrical-stress control in cable accessories. *IEEE Electrical Insulation Magazine* 2013, 29, 47-55.

16. Huang, X.; Xie, L.; Yang, K.; Wu, C.; Jiang, P.; Li, S.; Wu, S.; Tatsumi, K.; Tanaka, T. Role of interface in highly filled epoxy/BaTiO₃ nanocomposites. Part I-correlation between nanoparticle surface chemistry and nanocomposite dielectric property. *IEEE Transactions on Dielectrics and Electrical Insulation* 2014, 21, 467-479.

17. He, F.; Lau, S.; Chan, H. L.; Fan, J. High Dielectric Permittivity and Low Percolation Threshold in Nanocomposites Based on Poly(vinylidene fluoride) and Exfoliated Graphite Nanoplates. *Advanced Materials* 2009, 21, 710-715.

18. Dang, Z.-M.; Yuan, J.-K.; Yao, S.-H.; Liao, R.-J. Flexible Nanodielectric Materials with High Permittivity for Power Energy Storage. *Advanced Materials* 2013, 25, 6334-6365.

19. Chu, B.; Zhou, X.; Ren, K.; Neese, B.; Lin, M.; Wang, Q.; Bauer, F.; Zhang, Q. M. A Dielectric Polymer with High Electric Energy Density and Fast Discharge Speed. *Science* 2006, 313, 334-336.

20. Nan, C.-W.; Shen, Y.; Ma, J. Physical Properties of Composites Near Percolation. *Annual Review of Materials Research* 2010, 40, 131-151.

21. Wu, L.; Chure, M.-C.; Wu, K.-K.; Chang, W.-C.; Yang, M.-J.; Liu, W.-K.; Wu, M.-J. Dielectric properties of barium titanate ceramics with different materials powder size. *Ceramics International* 2009, 35, 957-960.

22. Liu, J.; Smith, R. W.; Mei, W.-N. Synthesis of the Giant Dielectric Constant Material

CaCu3Ti4O12 by Wet-Chemistry Methods. *Chemistry of Materials* 2007, 19, 6020-6024.

23. Wu, D.; Zhou, Q.; Shung, K. K.; Bharadwaja, S. N.; Zhang, D.; Zheng, H. Dielectric and Piezoelectric Properties of PZT Composite Thick Films with Variable Solution to Powder Ratios. *Journal of the American Ceramic Society. American Ceramic Society* 2009, 92, 1276-1279.

24. Ma, R.; Sharma, V.; Baldwin, A. F.; Tefferi, M.; Offenbach, I.; Cakmak, M.; Weiss, R.; Cao, Y.; Ramprasad, R.; Sotzing, G. A. Rational design and synthesis of polythioureas as capacitor dielectrics. *Journal of Materials Chemistry A* 2015, 3, 14845-14852.

25. Dang, Z.-M.; Zhou, T.; Yao, S.-H.; Yuan, J.-K.; Zha, J.-W.; Song, H.-T.; Li, J.-Y.; Chen, Q.; Yang, W.-T.; Bai, J. Advanced Calcium Copper Titanate/Polyimide Functional Hybrid Films with High Dielectric Permittivity. *Advanced Materials* 2009, 21, 2077-2082.

26. Dang, Z.-M.; Yuan, J.-K.; Zha, J.-W.; Zhou, T.; Li, S.-T.; Hu, G.-H. Fundamentals, processes and applications of high-permittivity polymer–matrix composites. *Progress in Materials Science* 2012, 57, 660-723.

27. Dang, Z.-M.; Lin, Y.-Q.; Xu, H.-P.; Shi, C.-Y.; Li, S.-T.; Bai, J. Fabrication and Dielectric Characterization of Advanced BaTiO3/Polyimide Nanocomposite Films with High Thermal Stability. *Advanced Functional Materials* 2008, 18, 1509-1517.

28. Kuo, D.-H.; Chang, C.-C.; Su, T.-Y.; Wang, W.-K.; Lin, B.-Y. Dielectric behaviours of multi-doped BaTiO3/epoxy composites. *Journal of the European Ceramic Society* 2001, 21, 1171-1177.

29. Guo, Y.; Batra, S.; Chen, Y.; Wang, E.; Cakmak, M. Roll to Roll Electric Field “Z” Alignment of Nanoparticles from Polymer Solutions for Manufacturing Multifunctional Capacitor Films. *ACS Applied Materials & Interfaces* 2016, 8, 18471-18480.

30. Tang, H.; Lin, Y.; Sodano, H. A. Enhanced Energy Storage in Nanocomposite Capacitors through Aligned PZT Nanowires by Uniaxial Strain Assembly. *Advanced Energy Materials* 2012, 2, 469-476.

31. Looyenga, H. Dielectric constants of heterogeneous mixtures. *Physica* 1965, 31, 401-406.

32. Bobnar, V.; Vodopivec, B.; Levstik, A.; Kosec, M.; Hilczer, B.; Zhang, Q. M. Dielectric Properties of Relaxor-like Vinylidene Fluoride−Trifluoroethylene-Based Electroactive Polymers. *Macromolecules* 2003, 36, 4436-4442.

33. Choi, H.-W.; Heo, Y.-W.; Lee, J.-H.; Kim, J.-J.; Lee, H.-Y.; Park, E.-T.; Chung, Y.-K.

EFFECTS OF Ni PARTICLE SIZE ON DIELECTRIC PROPERTIES OF PMMA-Ni-BaTiO3 COMPOSITES. *Integrated Ferroelectrics* 2007, 87, 85-93.

34. Tomer, V.; Randall, C. A.; Polizos, G.; Kostelnick, J.; Manias, E. High- and low-field dielectric characteristics of dielectrophoretically aligned ceramic/polymer nanocomposites. *Journal of Applied Physics* 2008, 103, -.

35. Bowen, C. P.; Newnham, R. E.; Randall, C. A. Dielectric properties of dielectrophoretically assembled particulate-polymer composites. *Journal of Materials Research* 1998, 13, 205-210.

36. van den Ende, D. A.; van Kempen, S. E.; Wu, X.; Groen, W. A.; Randall, C. A.; van der Zwaag, S. Dielectrophoretically structured piezoelectric composites with high aspect ratio piezoelectric particles inclusions. *Journal of Applied Physics* 2012, 111, 124107.

37. van den Ende, D. A.; Bory, B. F.; Groen, W. A.; van der Zwaag, S. Improving the d33 and g33 properties of 0-3 piezoelectric composites by dielectrophoresis. *Journal of Applied Physics* 2010, 107, 024107.

38. ZHANG, L.; CHENG, Z.-Y. DEVELOPMENT OF POLYMER-BASED 0–3 COMPOSITES WITH HIGH DIELECTRIC CONSTANT. *Journal of Advanced Dielectrics* 2011, 01, 389-406.

39. Bergman, D. J.; Imry, Y. Critical Behavior of the Complex Dielectric Constant near the Percolation Threshold of a Heterogeneous Material. *Physical Review Letters* 1977, 39, 1222-1225.

40. Pecharromán, C.; Moya, J. S. Experimental Evidence of a Giant Capacitance in Insulator–Conductor Composites at the Percolation Threshold. *Advanced Materials* 2000, 12, 294-297.

41. Wu, S.; Ladani, R. B.; Zhang, J.; Bafekrpour, E.; Ghorbani, K.; Mouritz, A. P.; Kinloch, A. J.; Wang, C. H. Aligning multilayer graphene flakes with an external electric field to improve multifunctional properties of epoxy nanocomposites. *Carbon* 2015, 94, 607-618.

42. Dang, Z. M.; Lin, Y. H.; Nan, C. W. Novel Ferroelectric Polymer Composites with High Dielectric Constants. *Advanced Materials* 2003, 15, 1625-1629.

43. Li, Q.; Xue, Q.; Hao, L.; Gao, X.; Zheng, Q. Large dielectric constant of the chemically functionalized carbon nanotube/polymer composites. *Composites Science and Technology* 2008, 68, 2290-2296.

44. McCulloch, I.; Man, H.-T.; Song, K.; Yoon, H. Mechanical failure in thin-film

nonlinear optical polymers: Structure and processing issues. *Journal of Applied Polymer Science* 1994, 53, 665-676.

45. Parikh, T.; Gupta, S. S.; Meena, A. K.; Vitez, I.; Mahajan, N.; Serajuddin, A. T. M. Application of Film-Casting Technique to Investigate Drug–Polymer Miscibility in Solid Dispersion and Hot-Melt Extrudate. *Journal of Pharmaceutical Sciences* 2015, 104, 2142-2152.

46. Kowel, S. T.; Selfridge, R.; Eldering, C.; Matloff, N.; Stroeve, P.; Higgins, B. G.; Srinivasan, M. P.; Coleman, L. B. Future applications of ordered polymeric thin films. *Thin Solid Films* 1987, 152, 377-403.

47. Kanai, T.; White, J. L. Kinematics, dynamics and stability of the tubular film extrusion of various polyethylenes. *Polymer Engineering & Science* 1984, 24, 1185-1201.

48. Maniruzzaman, M.; Boateng, J. S.; Snowden, M. J.; Douroumis, D. A Review of Hot-Melt Extrusion: Process Technology to Pharmaceutical Products. *ISRN Pharmaceutics* 2012, 2012, 9.

49. Chokshi, R.; Zia, H. Hot-Melt Extrusion Technique: A Review. *Iranian Journal of Pharmaceutical Research* 2010, Volume 3, 3-16.

50. Reale, A.; La Notte, L.; Salamandra, L.; Polino, G.; Susanna, G.; Brown, T. M.; Brunetti, F.; Di Carlo, A. Spray Coating for Polymer Solar Cells: An Up-to-Date Overview. *Energy Technology* 2015, 3, 385-406.

51. Siemann, U. Solvent cast technology – a versatile tool for thin film production. In *Scattering Methods and the Properties of Polymer Materials,* Springer Berlin Heidelberg: Berlin, Heidelberg, 2005; pp 1-14.

52. Sata, H.; Murayama, M.; Shimamoto, S. 5.4 Properties and applications of cellulose triacetate film. *Macromolecular Symposia* 2004, 208, 323-334.

53. HOSOI, M. T. L. M. F.; NAGOSHI, T. T. L. Optical films and process for producing the same. Google Patents: 2000.

54. Unsal, E.; Cakmak, M. Molecular mechanism of temporal physico/chemical changes that take place during imidization of polyamic acid: Coupled real-time rheo-optical and IR dichroism measurements. *Polymer* 2014, 55, 6569-6576.

55. Unsal, E.; Cakmak, M. Real-Time Characterization of Physical Changes in Polyimide Film Formation: From Casting to Imidization. *Macromolecules* 2013, 46, 8616-8627.

56. Shams Es-haghi, S.; Cakmak, M. On the thermal diffusion in polymer solutions: Case study on bicomponent film drying. *Polymer* 2015, 79, 110-118.

57. Shams Es-haghi, S. Modeling and Simulation of Diffusion in Evaporating Polymer Solutions. University of Akron, 2015.

58. Powers, G. W. The Effect of Temperature on the Solvent Removal from Solution-cast Thin Polymer Films/. Ohio University, 1988.

59. Chen, P.-J.; Liu, T.-J.; Wu, P.-Y.; Tseng, C.-F.; Leu, C.-M. Drying-induced birefringence of polyimide optical films. *AIChE Journal* 2010, 56, 790-800.

60. Sudduth, R. D.; Rogers, C. E. Structure of cellulose acetate desalination membranes. *Journal of Polymer Science: Polymer Letters Edition* 1973, 11, 603-608.

61. Prest, W. M.; Luca, D. J. The alignment of polymers during the solvent-coating process. *Journal of Applied Physics* 1980, 51, 5170-5174.

62. Prest, W. M.; Luca, D. J. The origin of the optical anisotropy of solvent cast polymeric films. *Journal of Applied Physics* 1979, 50, 6067-6071.

63. Unsal, E.; Drum, J.; Yucel, O.; Nugay, I. I.; Yalcin, B.; Cakmak, M. Real-time measurement system for tracking birefringence, weight, thickness, and surface temperature during drying of solution cast coatings and films. *Review of Scientific Instruments* 2012, 83, 025114.

64. Chen, Y.; Guo, Y.; Batra, S.; Wang, E.; Wang, Y.; Liu, X.; Wang, Y.; Cakmak, M. Transparent and through thickness conductive polystyrene films using external magnetic fields for "Z" alignment of nickel nanoparticles. *Nanoscale* 2015, 7, 14636-14642.

65. Yucel, O.; Unsal, E.; Cakmak, M. Temporal Evolution of Optical Gradients during Drying in Cast Polymer Solutions. *Macromolecules* 2013, 46, 7112-7117.

66. Zhang, W. Phase Behavior and Phase Separation Kinetics in Polymer Solutions under High Pressure. Virginia Polytechnic Institute and State University, 2005.

67. Qian, C.; Mumby, S. J.; Eichinger, B. E. Phase diagrams of binary polymer solutions and blends. *Macromolecules* 1991, 24, 1655-1661.

68. Kamide, K.; Matsuda, S.; Saito, M. Evaluation of Concentration Dependence of [chi]-Parameter, Flory Temperature and Entropy Parameter for Polymer-Solvent System from Their Critical Solution Temperature and Concentration Data. *Polym J* 1985, 17, 1013-1027.

69. Siow, K. S.; Delmas, G.; Patterson, D. Cloud-Point Curves in Polymer Solutions with Adjacent Upper and Lower Critical Solution Temperatures. *Macromolecules* 1972, 5, 29-34.

70. Elias, H. G. *Macromolecules*. Plenum Press: New York, 1983; Vol. 1.

71. Manias, E.; Utracki, L. A. Thermodynamics of Polymer Blends. In *Polymer Blends Handbook*, Utracki, L. A.; Wilkie, C. A., Eds. Springer Netherlands: Dordrecht, 2014; pp 171-289.

72. Thanh, N. T. K.; Maclean, N.; Mahiddine, S. Mechanisms of Nucleation and Growth of Nanoparticles in Solution. *Chemical Reviews* 2014, 114, 7610-7630.

73. Binder, K.; Fratzl, P. Spinodal Decomposition. In *Phase Transformations in Materials*, Wiley-VCH Verlag GmbH & Co. KGaA: 2005; pp 409-480.

74. Vladimir, P. S.; Skripov, A. V. Spinodal decomposition (phase transitions via unstable states). *Soviet Physics Uspekhi* 1979, 22, 389.

75. van de Witte, P.; Dijkstra, P. J.; van den Berg, J. W. A.; Feijen, J. Phase separation processes in polymer solutions in relation to membrane formation. *Journal of Membrane Science* 1996, 117, 1-31.

76. Inoue, T.; Ougizawa, T.; Yasuda, O.; Miyasaka, K. Development of modulated structure during solution casting of polymer blends. *Macromolecules* 1985, 18, 57-63.

77. Flory, P. J. *Principles of Polymer Chemistry*. Cornell University Press: Ithaca, NY, 1953.

78. van Aartsen, J. J. Theoretical observations on spinodal decomposition of polymer solutions. *European Polymer Journal* 1970, 6, 919-924.

79. Stratford, K.; Adhikari, R.; Pagonabarraga, I.; Desplat, J.-C.; Cates, M. E. Colloidal Jamming at Interfaces: A Route to Fluid-Bicontinuous Gels. *Science* 2005, 309, 2198-2201.

80. Herzig, E. M.; White, K. A.; Schofield, A. B.; Poon, W. C. K.; Clegg, P. S. Bicontinuous emulsions stabilized solely by colloidal particles. *Nat Mater* 2007, 6, 966-971.

81. Clegg, P. S.; Herzig, E. M.; Schofield, A. B.; Egelhaaf, S. U.; Horozov, T. S.; Binks, B. P.; Cates, M. E.; Poon, W. C. K. Emulsification of Partially Miscible Liquids Using Colloidal Particles: Nonspherical and Extended Domain Structures. *Langmuir* 2007, 23, 5984-5994.

82. Vermant, J.; Cioccolo, G.; Golapan Nair, K.; Moldenaers, P. Coalescence suppression in model immiscible polymer blends by nano-sized colloidal particles. *Rheologica Acta* 2004, 43, 529-538.

83. Bahrami, R.; Löbling, T. I.; Gröschel, A. H.; Schmalz, H.; Müller, A. H. E.; Altstädt, V. The Impact of Janus Nanoparticles on the Compatibilization of Immiscible Polymer Blends under Technologically Relevant Conditions. *ACS Nano* 2014, 8, 10048-10056.

84. Gam, S.; Corlu, A.; Chung, H.-J.; Ohno, K.; Hore, M. J. A.; Composto, R. J. A jamming morphology map of polymer blend nanocomposite films. *Soft Matter* 2011, 7, 7262-7268.

85. Willmann, J.; Stocker, D.; Dörsam, E. Characteristics and evaluation criteria of substrate-based manufacturing. Is roll-to-roll the best solution for printed electronics? *Organic Electronics* 2014, 15, 1631-1640.

86. Cakmak, M.; Batra, S.; Yalcin, B. Field assisted self-assembly for preferential through thickness ("z-direction") alignment of particles and phases by electric, magnetic, and thermal fields using a novel roll-to-roll processing line. *Polymer Engineering & Science* 2015, 55, 34-46.

87. Batra, S.; Cakmak, M. Ultra-capacitor flexible films with tailored dielectric constants using electric field assisted assembly of nanoparticles. *Nanoscale* 2015, 7, 20571-20583.

88. Chen, Y.; Guo, Y.; Batra, S.; Unsal, E.; Wang, E.; Wang, Y.; Liu, X.; Wang, Y.; Cakmak, M. Large-scale R2R fabrication of piezoresistive films (Ni/PDMS) with enhanced through thickness electrical and thermal properties by applying a magnetic field. *RSC Advances* 2015, 5, 92071-92079.

89. Singh, G.; Batra, S.; Zhang, R.; Yuan, H.; Yager, K. G.; Cakmak, M.; Berry, B.; Karim, A. Large-Scale Roll-to-Roll Fabrication of Vertically Oriented Block Copolymer Thin Films. *ACS Nano* 2013, 7, 5291-5299.

90. Teschler, L. U.S. plays catch-up with flexible electronics. http://www.powerelectronictips.com/u-s-plays-catch-up-with-flexible-electronics/.

91. Søndergaard, R. R.; Hösel, M.; Krebs, F. C. Roll-to-Roll fabrication of large area functional organic materials. *Journal of Polymer Science Part B: Polymer Physics* 2013, 51, 16-34.

92. Füredi, A. A.; Valentine, R. C. Factors involved in the orientation of microscopic particles in suspensions influenced by radio frequency fields. *Biochimica et Biophysica Acta* 1962, 56, 33-42.

93. Klingenberg, D. J.; van Swol, F.; Zukoski, C. F. Dynamic simulation of electrorheological suspensions. *The Journal of Chemical Physics* 1989, 91, 7888-7895.

94. Parthasarathy, M.; Klingenberg, D. J. Electrorheology: Mechanisms and models. *Materials Science and Engineering: R: Reports* 1996, 17, 57-103.

95. Qian, C.; Huang, H.; Chen, L.; Li, X.; Ge, Z.; Chen, T.; Yang, Z.; Sun, L. Dielectrophoresis for Bioparticle Manipulation. *International Journal of Molecular Sciences* 2014, 15, 18281-18309.

96. Davis, L. C. Finite-element analysis of particle-particle forces in electrorheological fluids. *Applied Physics Letters* 1992, 60, 319-321.

97. Lei, H.; Francis, L. F.; Gerberich, W. W.; Scriven, L. E. Stress development in drying coatings after solidification. *AIChE Journal* 2002, 48, 437-451.

98. Francis, L. F.; Mccormick, A. V.; Vaessen, D. M.; Payne, J. A. Development and measurement of stress in polymer coatings. *Journal of Materials Science* 2002, 37, 4717-4731.

99. Croll, S. G. The origin of residual internal stress in solvent-cast thermoplastic coatings. *Journal of Applied Polymer Science* 1979, 23, 847-858.

100. Ma, Y.; Davis, H. T.; Scriven, L. E. Microstructure development in drying latex coatings. *Progress in Organic Coatings* 2005, 52, 46-62.

101. Vanderhoff, J. W.; Bradford, E. B.; Carrington, W. K. The transport of water through latex films. *Journal of Polymer Science: Polymer Symposia* 1973, 41, 155-174.

102. Hoffman, R. W. Stress distributions and thin film mechanical properties. *Surface and Interface Analysis* 1981, 3, 62-66.

103. Watarai, H.; Sakamoto, T.; Tsukahara, S. In Situ Measurement of Dielectrophoretic Mobility of Single Polystyrene Microparticles. *Langmuir* 1997, 13, 2417-2420.

104. Park, C.; Robertson, R. E. Alignment of particles by an electric field. *Materials Science and Engineering: A* 1998, 257, 295-311.

105. Zhang, X. POLYMER FILMS WITH ENHANCED THROUGH THICKNESS OPTICAL TRANSMISSION AND COMPRESSION MODULUS WITH ELECTRIC FIELD ALIGNED GLASS FIBER/BUBBLES. University of Akron, 2016.

106. Jones, T. B.; Jones, T. B. *Electromechanics of Particles*. Cambridge University

Press: 2005.

107. Lumsdon, S. O.; Scott, D. M. Assembly of Colloidal Particles into Microwires Using an Alternating Electric Field. *Langmuir* 2005, 21, 4874-4880.

108. Jones, T. B. Basic theory of dielectrophoresis and electrorotation. *IEEE Engineering in Medicine and Biology Magazine* 2003, 22, 33-42.

109. Batra, S.; Unsal, E.; Cakmak, M. Directed Electric Field Z-Alignment Kinetics of Anisotropic Nanoparticles for Enhanced Ionic Conductivity. *Advanced Functional Materials* 2014, 24, 7698-7708.

110. Deng, S.; Zhang, J.; Ye, L. Halloysite–epoxy nanocomposites with improved particle dispersion through ball mill homogenisation and chemical treatments. *Composites Science and Technology* 2009, 69, 2497-2505.

111. Pan, S. “Z”-Alignment Of Halloysite Nanotubes In Norland 65. University of Akron, 2016.

112. Li, P.; Martin, C.; Yeung, K. K.; Xue, W. Dielectrophoresis Aligned Single-Walled Carbon Nanotubes as pH Sensors. *Biosensors* 2011, 1, 23.

113. Moriya, S.; Adachi, K.; Kotaka, T. Deformation of droplets suspended in viscous media in an electric field. 1. Rate of deformation. *Langmuir* 1986, 2, 155-160.

114. Moriya, S.; Adachi, K.; Kotaka, T. Deformation of droplets suspended in viscous media in an electric field. 2. Burst behavior. *Langmuir* 1986, 2, 161-165.

115. Venugopal, G.; Krause, S.; Wnek, G. E. Modification of polymer blend morphology using electric fields. *Journal of Polymer Science Part C: Polymer Letters* 1989, 27, 497-501.

116. Venugopal, G.; Krause, S. Development of phase morphologies of poly(methyl methacrylate)-polystyrene-toluene mixtures in electric fields. *Macromolecules* 1992, 25, 4626-4634.

117. Venugopal, G.; Krause, S.; Wnek, G. E. Morphological variations in polymer blends made in electric fields. *Chemistry of Materials* 1992, 4, 1334-1343.

118. Hori, H.; Urakawa, O.; Yano, O.; Tran-Cong-Miyata, Q. Phase Separation of Binary Polymer Mixtures under an Electric Field. *Macromolecules* 2007, 40, 389-394.

119. Xi, K.; Krause, S. Droplet Deformation and Structure Formation in Two-Phase Polymer/Polymer/Toluene Mixtures in an Electric Field. *Macromolecules* 1998, 31,

3974-3984.

120. Torza, S.; Cox, R. G.; Mason, S. G. Electrohydrodynamic Deformation and Burst of Liquid Drops. *Philosophical Transactions of the Royal Society of London. Series A, Mathematical and Physical Sciences* 1971, 269, 295-319.

121. Garton, C. G.; Krasucki, Z. Bubbles in Insulating Liquids: Stability in an Electric Field. *Proceedings of the Royal Society of London. Series A. Mathematical and Physical Sciences* 1964, 280, 211-226.

122. Wei, C.; Dai, L.; Roy, A.; Tolle, T. B. Multifunctional Chemical Vapor Sensors of Aligned Carbon Nanotube and Polymer Composites. *Journal of the American Chemical Society* 2006, 128, 1412-1413.

123. Arjmand, M.; Mahmoodi, M.; Gelves, G. A.; Park, S.; Sundararaj, U. Electrical and electromagnetic interference shielding properties of flow-induced oriented carbon nanotubes in polycarbonate. *Carbon* 2011, 49, 3430-3440.

124. Garimella, S. V.; Fleischer, A. S.; Murthy, J. Y.; Keshavarzi, A.; Prasher, R.; Patel, C.; Bhavnani, S. H.; Venkatasubramanian, R.; Mahajan, R.; Joshi, Y.; Sammakia, B.; Myers, B. A.; Chorosinski, L.; Baelmans, M.; Sathyamurthy, P.; Raad, P. E. Thermal Challenges in Next-Generation Electronic Systems. *IEEE Transactions on Components and Packaging Technologies* 2008, 31, 801-815.

125. Chen, H.; Ginzburg, V. V.; Yang, J.; Yang, Y.; Liu, W.; Huang, Y.; Du, L.; Chen, B. Thermal conductivity of polymer-based composites: Fundamentals and applications. *Progress in Polymer Science*.

126. Haggenmueller, R.; Guthy, C.; Lukes, J. R.; Fischer, J. E.; Winey, K. I. Single Wall Carbon Nanotube/Polyethylene Nanocomposites: Thermal and Electrical Conductivity. *Macromolecules* 2007, 40, 2417-2421.

127. Shahil, K. M. F.; Balandin, A. A. Graphene–Multilayer Graphene Nanocomposites as Highly Efficient Thermal Interface Materials. *Nano Letters* 2012, 12, 861-867.

128. Knaapila, M.; Rømoen, O. T.; Svåsand, E.; Pinheiro, J. P.; Martinsen, Ø. G.; Buchanan, M.; Skjeltorp, A. T.; Helgesen, G. Conductivity Enhancement in Carbon Nanocone Adhesive by Electric Field Induced Formation of Aligned Assemblies. *ACS Applied Materials & Interfaces* 2011, 3, 378-384.

129. Cho, H.-B.; Konno, A.; Fujihara, T.; Suzuki, T.; Tanaka, S.; Jiang, W.; Suematsu, H.; Niihara, K.; Nakayama, T. Self-assemblies of linearly aligned diamond fillers in

polysiloxane/diamond composite films with enhanced thermal conductivity. *Composites Science and Technology* 2011, 72, 112-118.

130. BATRA, S.; Cakmak, M.; GUO, Y. Alignement selon un champ électrique dans des solutions polymères. Google Patents: 2016.

131. Qiang, Z.; Guo, Y.; Liu, H.; Cheng, S. Z. D.; Cakmak, M.; Cavicchi, K. A.; Vogt, B. D. Large-Scale Roll-to-Roll Fabrication of Ordered Mesoporous Materials using Resol-Assisted Cooperative Assembly. *ACS Applied Materials & Interfaces* 2015, 7, 4306-4310.

132. Amarandei, G.; Beltrame, P.; Clancy, I.; O'Dwyer, C.; Arshak, A.; Steiner, U.; Corcoran, D.; Thiele, U. Pattern formation induced by an electric field in a polymer-air-polymer thin film system. *Soft Matter* 2012, 8, 6333-6349.

133. Verma, R.; Sharma, A.; Kargupta, K.; Bhaumik, J. Electric Field Induced Instability and Pattern Formation in Thin Liquid Films. *Langmuir* 2005, 21, 3710-3721.

134. Kirkpatrick, S. Percolation and Conduction. *Reviews of Modern Physics* 1973, 45, 574-588.

135. Sheng, P.; Sichel, E. K.; Gittleman, J. I. Fluctuation-Induced Tunneling Conduction in Carbon-Polyvinylchloride Composites. *Physical Review Letters* 1978, 40, 1197-1200.

136. Nan, C.-W. Physics of inhomogeneous inorganic materials. *Progress in Materials Science* 1993, 37, 1-116.

137. Tang, H.; Ehlert, G. J.; Lin, Y.; Sodano, H. A. Highly Efficient Synthesis of Graphene Nanocomposites. *Nano Letters* 2012, 12, 84-90.

138. Slack, G. A. Anisotropic Thermal Conductivity of Pyrolytic Graphite. *Physical Review* 1962, 127, 694-701.

139. Berman, R. The Thermal Conductivity of some Polycrystalline Solids at Low Temperatures. *Proceedings of the Physical Society. Section A* 1952, 65, 1029.

140. Agari, Y.; Uno, T. Estimation on thermal conductivities of filled polymers. *Journal of Applied Polymer Science* 1986, 32, 5705-5712.

141. Potts, J. R.; Dreyer, D. R.; Bielawski, C. W.; Ruoff, R. S. Graphene-based polymer nanocomposites. *Polymer* 2011, 52, 5-25.

142. Liang, Y.; Guo, Y.; Wang, E.; Cakmak, M. Details of Molecular Organization

during Strain-Induced Crystallization in Natural Rubber/Clay Systems As Revealed by Real-Time Mechano-Optical Behavior. *Macromolecules* 2015, 48, 2299-2304.

143. Vlassiouk, I.; Polizos, G.; Cooper, R.; Ivanov, I.; Keum, J. K.; Paulauskas, F.; Datskos, P.; Smirnov, S. Strong and Electrically Conductive Graphene-Based Composite Fibers and Laminates. *ACS Applied Materials & Interfaces* 2015, 7, 10702-10709.

144. Wang, M.; Hu, N.; Zhou, L.; Yan, C. Enhanced interfacial thermal transport across graphene–polymer interfaces by grafting polymer chains. *Carbon* 2015, 85, 414-421.

145. Ning, N.; Ma, Q.; Liu, S.; Tian, M.; Zhang, L.; Nishi, T. Tailoring Dielectric and Actuated Properties of Elastomer Composites by Bioinspired Poly(dopamine) Encapsulated Graphene Oxide. *ACS Applied Materials & Interfaces* 2015, 7, 10755-10762.

146. Dang, Z.-M.; Wang, H.-Y.; Zhang, Y.-H.; Qi, J.-Q. Morphology and Dielectric Property of Homogenous BaTiO3/PVDF Nanocomposites Prepared via the Natural Adsorption Action of Nanosized BaTiO3. *Macromolecular Rapid Communications* 2005, 26, 1185-1189.

147. Hill, R. F.; Supancic, P. H. Thermal Conductivity of Platelet-Filled Polymer Composites. *Journal of the American Ceramic Society* 2002, 85, 851-857.

148. Ladani, R. B.; Wu, S.; Kinloch, A. J.; Ghorbani, K.; Zhang, J.; Mouritz, A. P.; Wang, C. H. Improving the toughness and electrical conductivity of epoxy nanocomposites by using aligned carbon nanofibres. *Composites Science and Technology* 2015, 117, 146-158.

149. Sarker, B. K.; Shekhar, S.; Khondaker, S. I. Semiconducting Enriched Carbon Nanotube Aligned Arrays of Tunable Density and Their Electrical Transport Properties. *ACS Nano* 2011, 5, 6297-6305.

150. Shekhar, S.; Stokes, P.; Khondaker, S. I. Ultrahigh Density Alignment of Carbon Nanotube Arrays by Dielectrophoresis. *ACS Nano* 2011, 5, 1739-1746.

151. Kretschmer, R.; Fritzsche, W. Pearl Chain Formation of Nanoparticles in Microelectrode Gaps by Dielectrophoresis. *Langmuir* 2004, 20, 11797-11801.

152. Helgesen, G.; Knaapila, M.; Buchanan, M. Method for forming an anisotropic conductive paper and a paper thus formed. Google Patents: 2013.

153. Lovell, R.; Mitchell, G. R. Molecular orientation distribution derived from an arbitrary reflection. *Acta Crystallographica Section A* 1981, 37, 135-137.

154. Boateng, J. S.; Matthews, K. H.; Stevens, H. N. E.; Eccleston, G. M. Wound healing dressings and drug delivery systems: A review. *Journal of Pharmaceutical Sciences* 2008, 97, 2892-2923.

155. Russell, L. Understanding physiology of wound healing and how dressings help. *British Journal of Nursing* 2000, 9, 10-21.

156. Deetjen. Untersuchungen über die Blutplättchen. *Archiv für pathologische Anatomie und Physiologie und für klinische Medicin* 1901, 164, 239-263.

157. Cutting, K. F. Wound exudate: composition and functions. *British Journal of Community Nursing* 2003, 8, S4-S9.

158. Eaglstein, W. H.; Davis, S. C.; Mehle, A. L.; Mertz, P. M. Optimal use of an occlusive dressing to enhance healing: Effect of delayed application and early removal on wound healing. *Archives of Dermatology* 1988, 124, 392-395.

159. Quick, A. Dressing choices. *Nursing times* 1994, 90, 68.

160. Cutting, K. F.; White, R. J. Maceration of the skin and wound bed 1: its nature and causes. *Journal of Wound Care* 2002, 11, 275-278.

161. Chen, W. Y. J.; Rogers, A. A.; Lydon, M. J. Characterization of Biologic Properties of Wound Fluid Collected During Early Stages of Wound Healing. *Journal of Investigative Dermatology* 1992, 99, 559-564.

162. Zahedi, P.; Rezaeian, I.; Ranaei-Siadat, S.-O.; Jafari, S.-H.; Supaphol, P. A review on wound dressings with an emphasis on electrospun nanofibrous polymeric bandages. *Polymers for Advanced Technologies* 2010, 21, 77-95.

163. Dealey, C. Role of hydrocolloids in wound management. *Br J Nurs* 1993, 2, 358, 360, 362 passim.

164. Wang, L.; Shelton, R. M.; Cooper, P. R.; Lawson, M.; Triffitt, J. T.; Barralet, J. E. Evaluation of sodium alginate for bone marrow cell tissue engineering. *Biomaterials* 2003, 24, 3475-3481.

165. Lay-Flurrie, K. The properties of hydrogel dressings and their impact on wound healing. *Prof Nurse* 2004, 19, 269-273.

166. Ramos-e-Silva, M.; Ribeiro de Castro, M. C. New dressings, including tissue-engineered living skin. *Clinics in Dermatology* 2002, 20, 715-723.

167. Heenan, A. *World Wide Wounds* 1998, 1, 1.

168. Cadier MA, C. J. Dermasorb versus Jelonet in patients with burns skin graft donor sites. *Journal of Burn Care & Rehabilitation* 1996, 17, 246–251.

169. Hoekstra, M. J.; Hermans, M. H. E.; Richters, C. D.; Dutrieux, R. P. A histological comparison of acute inflammatory responses with a hydrofibre or tulle gauze dressing. *Journal of Wound Care* 2002, 11, 113-117.

170. Bishop, S. M.; Griffiths, B.; Linnane, P. G.; Lydon, M. J.; Shaw, H. Multi layered wound dressing. Google Patents: 2010.

171. Gundersen, B. Wound Dressing. Google Patents: 2008.

172. He, X.; Takahara, A.; Kajiyama, T. Anisotropic swelling behavior of copolymeric gel film with crystalline oriented side chains. *Polymer Gels and Networks* 1997, 5, 429-438.

173. Kishi, R.; Sisido, M.; Tazuke, S. Liquid-crystalline polymer gels. 2. Anisotropic swelling of poly(γ-benzyl L-glutamate) gel crosslinked under a magnetic field. *Macromolecules* 1990, 23, 3868-3870.

174. Panar, M.; Phillips, W. D. Magnetic ordering of poly(.gamma.-benzyl L-glutamate) solutions. *Journal of the American Chemical Society* 1968, 90, 3880-3882.

175. Sigurjonsson, G. Wound dressing. Google Patents: 2004.

176. Liang, R.; Yuan, H.; Xi, G.; Zhou, Q. Synthesis of wheat straw-g-poly(acrylic acid) superabsorbent composites and release of urea from it. *Carbohydrate Polymers* 2009, 77, 181-187.

177. Kirwan, L. J.; Fawell, P. D.; van Bronswijk, W. In Situ FTIR-ATR Examination of Poly(acrylic acid) Adsorbed onto Hematite at Low pH. *Langmuir* 2003, 19, 5802-5807.

178. Zhang, M.; Cheng, Z.; Zhao, T.; Liu, M.; Hu, M.; Li, J. Synthesis, Characterization, and Swelling Behaviors of Salt-Sensitive Maize Bran–Poly(acrylic acid) Superabsorbent Hydrogel. *Journal of Agricultural and Food Chemistry* 2014, 62, 8867-8874.

179. Luo, H.; Chen, J.; Luo, G.; Chen, Y.; Cao, W. Self-assembly films from diazoresin and carboxy-containing polyelectrolytes. *Journal of Materials Chemistry* 2001, 11, 419-422.

180. Nosonovsky, M.; Bhushan, B. Roughness optimization for biomimetic superhydrophobic surfaces. *Microsystem Technologies* 2005, 11, 535-549.

181. Bhushan, B.; Jung, Y. C.; Koch, K. Micro-, nano- and hierarchical structures for superhydrophobicity, self-cleaning and low adhesion. *Philosophical Transactions of the Royal Society A: Mathematical, Physical and Engineering Sciences* 2009, 367, 1631-1672.

182. Chen, X.; Weibel, J. A.; Garimella, S. V. Water and Ethanol Droplet Wetting Transition during Evaporation on Omniphobic Surfaces. *Scientific Reports* 2015, 5, 17110.

183. Paul, D. R.; Barlow, J. W. Polymer Blends. *Journal of Macromolecular Science, Part C* 1980, 18, 109-168.

184. Higgins, J. S.; Lipson, J. E. G.; White, R. P. A simple approach to polymer mixture miscibility. *Philosophical transactions. Series A, Mathematical, physical, and engineering sciences* 2010, 368, 1009-1025.

185. Pötschke, P.; Paul, D. R. Formation of Co-continuous Structures in Melt-Mixed Immiscible Polymer Blends. *Journal of Macromolecular Science, Part C* 2003, 43, 87-141.

186. Lepers, J.-C.; Favis, B. D.; Lacroix, C. The influence of partial emulsification on coalescence suppression and interfacial tension reduction in PP/PET blends. *Journal of Polymer Science Part B: Polymer Physics* 1999, 37, 939-951.

187. Galloway, J. A.; Jeon, H. K.; Bell, J. R.; Macosko, C. W. Block copolymer compatibilization of cocontinuous polymer blends. *Polymer* 2005, 46, 183-191.

188. Trifkovic, M.; Hedegaard, A.; Huston, K.; Sheikhzadeh, M.; Macosko, C. W. Porous Films via PE/PEO Cocontinuous Blends. *Macromolecules* 2012, 45, 6036-6044.

189. Bryson, K. C.; Löbling, T. I.; Müller, A. H. E.; Russell, T. P.; Hayward, R. C. Using Janus Nanoparticles To Trap Polymer Blend Morphologies during Solvent-Evaporation-Induced Demixing. *Macromolecules* 2015, 48, 4220-4227.

190. Si, M.; Araki, T.; Ade, H.; Kilcoyne, A. L. D.; Fisher, R.; Sokolov, J. C.; Rafailovich, M. H. Compatibilizing Bulk Polymer Blends by Using Organoclays. *Macromolecules* 2006, 39, 4793-4801.

191. Jones, R. A. L. Polymer interfaces and the molecular basis of adhesion. *Current Opinion in Solid State and Materials Science* 1997, 2, 673-677.

192. Lyu, S.; Jones, T. D.; Bates, F. S.; Macosko, C. W. Role of Block Copolymers on Suppression of Droplet Coalescence. *Macromolecules* 2002, 35, 7845-7855.

193. Walther, A.; Matussek, K.; Müller, A. H. E. Engineering Nanostructured Polymer Blends with Controlled Nanoparticle Location using Janus Particles. *ACS Nano* 2008, 2, 1167-1178.

194. Dinsmore, A. D.; Hsu, M. F.; Nikolaides, M. G.; Marquez, M.; Bausch, A. R.; Weitz, D. A. Colloidosomes: Selectively Permeable Capsules Composed of Colloidal Particles. *Science* 2002, 298, 1006-1009.

195. Thareja, P.; Velankar, S. Particle-induced bridging in immiscible polymer blends. *Rheologica Acta* 2007, 46, 405-412.

196. Chung, H.-j.; Ohno, K.; Fukuda, T.; Composto, R. J. Self-Regulated Structures in Nanocomposites by Directed Nanoparticle Assembly. *Nano Letters* 2005, 5, 1878-1882.

197. Frijters, S.; Günther, F.; Harting, J. Domain and droplet sizes in emulsions stabilized by colloidal particles. *Physical Review E* 2014, 90, 042307.

198. Imagawa, A.; Tran-Cong, Q. Structure-Property Relationship of Polymer Blends with Co-Continuous Structures Prepared by Photo-Crosslinking. *Macromolecules* 1995, 28, 8388-8394.

199. Möller, M. W.; Kunz, D. A.; Lunkenbein, T.; Sommer, S.; Nennemann, A.; Breu, J. UV-Cured, Flexible, and Transparent Nanocomposite Coating with Remarkable Oxygen Barrier. *Advanced Materials* 2012, 24, 2142-2147.

200. Chen, X. L.; Lovinger, A. J.; Bao, Z.; Sapjeta, J. Morphological and Transistor Studies of Organic Molecular Semiconductors with Anisotropic Electrical Characteristics. *Chemistry of Materials* 2001, 13, 1341-1348.

201. Ulbricht, M.; Schuster, O.; Ansorge, W.; Ruetering, M.; Steiger, P. Influence of the strongly anisotropic cross-section morphology of a novel polyethersulfone microfiltration membrane on filtration performance. *Separation and Purification Technology* 2007, 57, 63-73.

202. Nour, E. S.; Chey, C. O.; Willander, M.; Nur, O. A flexible anisotropic self-powered piezoelectric direction sensor based on double sided ZnO nanowires configuration. *Nanotechnology* 2015, 26, 095502.

203. Taylor, G. Studies in Electrohydrodynamics. I. The Circulation Produced in a Drop by Electrical Field. *Proceedings of the Royal Society of London. Series A. Mathematical and Physical Sciences* 1966, 291, 159-166.

204. Baygents, J. C.; Saville, D. A. The circulation produced in a drop by an electric

field: A high field strength electrokinetic model. *AIP Conference Proceedings* 1990, 197, 7-17.

205. Cui, M.; Emrick, T.; Russell, T. P. Stabilizing Liquid Drops in Nonequilibrium Shapes by the Interfacial Jamming of Nanoparticles. *Science* 2013, 342, 460-463.

206. Dommersnes, P.; Rozynek, Z.; Mikkelsen, A.; Castberg, R.; Kjerstad, K.; Hersvik, K.; Otto Fossum, J. Active structuring of colloidal armour on liquid drops. *Nature Communications* 2013, 4, 2066.

207. Millett, P. C. Electric-field induced alignment of nanoparticle-coated channels in thin-film polymer membranes. *The Journal of Chemical Physics* 2014, 140, 144903.

208. Tsui, O. K. C.; Russell, T. P.; Hawker, C. J. Effect of Interfacial Interactions on the Glass Transition of Polymer Thin Films. *Macromolecules* 2001, 34, 5535-5539.

209. Brar, A. S.; Puneeta. Synthesis of styrene/methyl methacrylate copolymers by atom transfer radical polymerization: 2D NMR investigations. *Journal of Polymer Science Part A: Polymer Chemistry* 2006, 44, 2076-2085.

210. Huang, C.; Gao, J.; Yu, W.; Zhou, C. Phase Separation of Poly(methyl methacrylate)/Poly(styrene-co-acrylonitrile) Blends with Controlled Distribution of Silica Nanoparticles. *Macromolecules* 2012, 45, 8420-8429.

211. Yang, Y.; Yang, Z.; Zhao, Q.; Cheng, X.; Tjong, S. C.; Li, R. K. Y.; Wang, X.; Xie, X. Immobilization of RAFT agents on silica nanoparticles utilizing an alternative functional group and subsequent surface-initiated RAFT polymerization. *Journal of Polymer Science Part A: Polymer Chemistry* 2009, 47, 467-484.

212. Kumacheva, E.; Li, L.; Winnik, M. A.; Shinozaki, D. M.; Cheng, P. C. Direct Imaging of Surface and Bulk Structures in Solvent Cast Polymer Blend Films. *Langmuir* 1997, 13, 2483-2489.

213. McMaster, L. P. Aspects of Liquid-Liquid Phase Transition Phenomena in Multicomponent Polymeric Systems. In *Copolymers, Polyblends, and Composites*, AMERICAN CHEMICAL SOCIETY: 1975; Vol. 142, pp 43-65.

214. Minelli, C.; Frommen, C.; Hinderling, C.; Pugin, R.; Heinzelmann, H.; Liley, M. The influence of nanoparticle fillers on the morphology of a spin-cast thin film polymer blend. *Colloid and Polymer Science* 2006, 284, 482-488.

215. Tangwiwat, S.; Milne, S. J. Barium titanate sols prepared by a diol-based sol–gel route. *Journal of Non-Crystalline Solids* 2005, 351, 976-980.

216. Ashiri, R. Detailed FT-IR spectroscopy characterization and thermal analysis of synthesis of barium titanate nanoscale particles through a newly developed process. *Vibrational Spectroscopy* 2013, 66, 24-29.

217. Duan, G.; Zhang, C.; Li, A.; Yang, X.; Lu, L.; Wang, X. Preparation and Characterization of Mesoporous Zirconia Made by Using a Poly (methyl methacrylate) Template. *Nanoscale Research Letters* 2008, 3, 118.